Extreme Hydrodynamic impact onto buildings

PAR

Davide WÜTHRICH

acceptée sur proposition du jury:

Prof. E. Brühwiler, président du jury
Prof. A. Schleiss, Dr M. Pfister, directeurs de thèse
Prof. I. Nistor, rapporteur
Prof. N. Goseberg , rapporteur
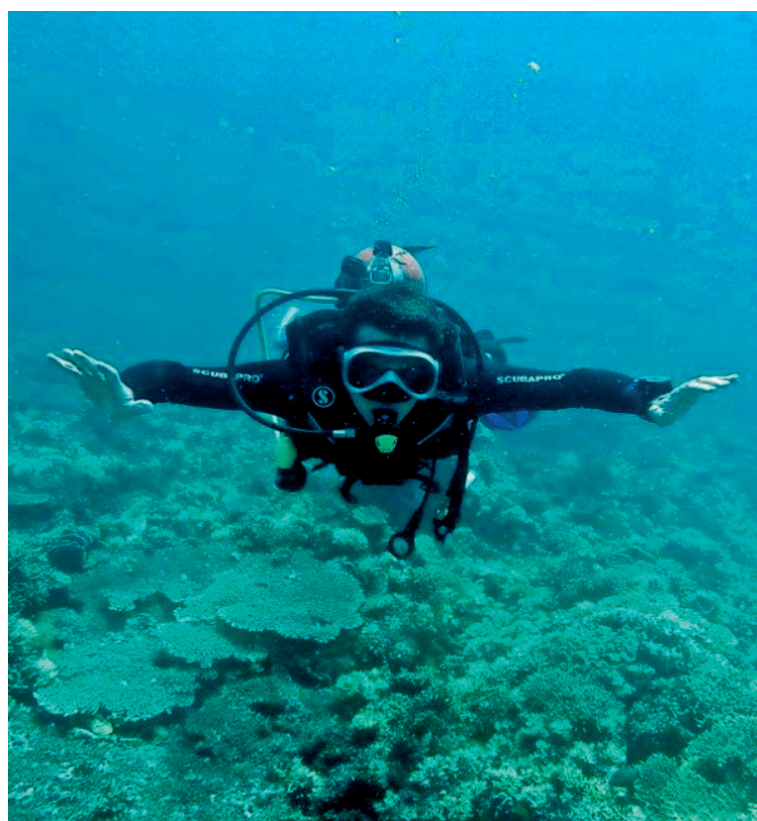Prof. W. H. Hager, rapporteur

ÉCOLE POLYTECHNIQUE
FÉDÉRALE DE LAUSANNE

Suisse
2018

We are like the OCEAN:

pretty enough on the surface,
but DIVE down into its depths,
and you'll find beauty most people never see.

— Ellen Hopkins

Abstract

Dam failures, impulse waves, tsunamis and storm surges are natural disasters that challenge humanity, often leading to massive casualties and important economic losses. These events generate highly unsteady flow conditions in the form of surges or turbulent bores, associated with extreme loading on infrastructure. In the past, the impact on these flows on buildings was considered too rare and wave induced forces were neglected in the design process. However, recent events showed that some measures can guarantee human safety and reduce reconstruction costs. As such, vertical shelters able to withstand extreme loading are fundamental and an estimation of induced forces is necessary. Field studies showed that buildings with openings perform better during wave impact. The objective of this research is to evaluate and analyse damage potential of resilient buildings hit by both surges and bores. In particular, the influence of openings as a mitigation measure on the loading process is addressed and quantified.

The research is based on an experimental approach. Wave formation is achieved through the vertical release of a water volume from an upper reservoir, generating dry bed surges or wet bed bores in the downstream horizontal channel. A variation of the released discharge results into waves with different hydrodynamic properties. A detailed methodology to hydraulically characterize the generated waves in terms of their water depths and flow velocities is presented and good agreement with the classical dam-break case for both dry bed surges and wet bed bores is demonstrated. Particular attention is given to wave front celerity and velocity profiles measured behind the wave front, showing some features typical of open channel flows.

Free-standing buildings were reproduced using aluminium structures installed on a force plate, providing a detailed time history of impact forces and moments. The impact was characterised by high splashes, followed by a quasi-steady flow around the building. For the impervious buildings (without openings), dry bed surges resulted into horizontal forces proportional to the momentum flux. For wet bed bores, an attenuation of the peak force was constantly observed and the introduction of a reduction coefficient was necessary to achieve a realistic force estimation.

In this study the effect of openings and overflow were tested. First, four building configurations with seven opening values ranging from 0 (impervious) to 84% were investigated using 12 standard waves. The flow through the structure reduced the upstream water depths, providing safer vertical shelters. In terms of loading, the openings produced a linear reduction of the maximum horizontal force, if compared to the impervious case. The configuration with an

Abstract

impervious back wall showed similar results to the impervious building. Openings on the side walls had no influence on the resulting maximum load. Analysis in terms of peak time, wave height at maximum force and impulse pointed out some key differences on the loading process between surges and bores. The time occurrence of the maximum tilting moment corresponded to the maximum horizontal force and the resulting cantilever arm was constant for all opening configurations. Second, in case of overflow, milder loading conditions were constantly measured.

Finally, a combination of theoretical approach with empiric adjustments, lead to new formulae to estimate the hydrodynamic load are introduced, taking into account the effect of openings within an adapted resistance coefficient, providing relevant information for the design of safer infrastructures.

Key words: *dam-break waves, impulse waves, tsunamis, wave impact, hydrodynamic loading, vertical shelters, openings, overflow.*

Résumé

Les ruptures de barrages, les vagues d'impulsion, les tsunamis et les inondations dues aux ouragans, représentent des calamités naturelles qui menacent l'humanité, provoquant souvent de nombreuses victimes et d'importantes pertes économiques. Ces évènements induisent des écoulements transitoires sous forme de vagues, menant à des sollicitations extrêmes contre les infrastructures. Dans le passé, l'impact de ces écoulements contre les bâtiments était considéré comme trop rare et les forces provoquées par les vagues étaient négligées en phase de projet. Cependant, des évènements récents ont montré que des mesures constructives peuvent garantir la sécurité des personnes et réduire les couts de reconstruction. Par conséquent, des refuges verticaux capables de résister à des charges extrêmes sont fondamentaux et une estimation des forces induites nécessaire. De plus, des observations sur le terrain ont montré que les bâtiments avec ouvertures résistent mieux à l'impact des vagues et l'objectif de cette recherche est d'évaluer et d'analyser le dommage potentiel des bâtiments frappés par des vagues. En particulier, cette recherche vise à considérer et quantifier l'influence des ouvertures comme mesure d'atténuation dans le processus de charge.

Cette recherche est basée sur une approche expérimentale. La formation des vagues est obtenue à travers un lâché vertical d'un volume d'eau depuis un réservoir supérieur, produisant des vagues dans le canal à l'aval. La variation du débit relâché produit des vagues avec des propriétés hydrodynamiques différentes. Cette recherche présente une méthodologie détaillée pour la caractérisation hydrodynamique des vagues en termes de hauteur d'eau et de vitesse d'écoulement, en démontrant un bon accord avec la théorie classique de rupture de barrage sur fond sec et sur fond mouillé. Une attention particulière est donnée à la vitesse du front et aux profils de vitesse mesurés derrière le front, montrant des caractéristiques typiques des écoulements à surface libre.

Les bâtiments ont été reproduits avec des structures en aluminium, installées sur une plaque dynamométrique, qui fournit le développement temporel des forces et des moments. L'impact était caractérisé par des hautes éclaboussures, suivies pas un écoulement quasi-uniforme autour du bâtiment. Pour les structures imperméables (sans ouvertures), les vagues sur fond sec ont généré des forces proportionnelles au flux de quantité de mouvement. Les vagues sur fond mouillé ont constamment montré une atténuation du pic de la force et l'introduction d'un coefficient de réduction était alors nécessaire pour obtenir une estimation fiable de la force.

Résumé

Plus précisément, cette étude se focalise sur l'effet des ouvertures et de la submersion. Quatre configurations avec sept ouvertures entre 0 (imperméable) et 84% ont été testées avec douze vagues standards. L'écoulement à travers la structure a mené à une diminution de la hauteur d'eau à l'amont, générant des refuges verticaux plus sûrs. En termes de charges, les ouvertures ont produit une réduction linéaire de la force maximale horizontale par rapport à la structure imperméable. La configuration avec la façade arrière imperméable a montré un comportement similaire à celui du bâtiment entièrement imperméable. Les ouvertures sur les côtés ont démontré de ne pas avoir une influence sur la force maximale résultante. Une analyse en termes de temps de pic, de hauteur d'eau pendant la force maximale et d'impulsion a montré des différences clés entre les forces provoquées par les vagues sur fond sec et celles sur fond mouillé. L'occurrence du moment maximal correspondait au pic de la force horizontal et le bras de levier était constant pout toutes configurations. En cas de submersion du bâtiment, des conditions de charge plus légères ont été à chaque fois mesurées.

En conclusion, cette étude introduit des formules pour prédire la charge hydrodynamique sur un bâtiment, en tenant en compte l'effet des ouvertures à travers un coefficient de résistance adapté. Ces résultats fournissent des informations importantes pour le dimensionnement d'infrastructures plus sures.

Mots clés: *Vague de rupture de barrage, vague impulsive, tsunami, impact hydrodynamique, refuge vertical, ouverture, submersion.*

Sintesi

Il collasso di una diga, la formazione di onde impulsive, gli tsunami e le inondazioni post-uragani rappresentano calamità naturali che mettono a dura prova l'umanità, spesso provocando numerose vittime ed ingenti perdite economiche. Questi eventi generano moti transitori sotto forma di onde, con conseguenti sollecitazioni estreme sulle infrastrutture. In passato, l'impatto di queste onde contro gli edifici era considerato un evento particolarmente raro e, di conseguenza, le forze indotte da tali flussi venivano trascurate in fase di progetto. Tuttavia, alcuni recenti studi hanno dimostrato che particolari misure architettoniche possono sia garantire incolumità delle persone, sia ridurre i costi di ricostruzione. Per tali ragioni, la stima delle forze indotte dall'impatto di onde impulsive sugli edifici interessati risulta necessaria per la corretta progettazione di rifugi verticali capaci di sopportare carichi estremi. Osservazioni sul campo hanno mostrato che gli edifici con aperture resistono in modo più efficace all'impatto di un'onda rispetto ad edifici senza aperture. Lo scopo di questo progetto è quello di stimare ed analizzare i potenziali danni agli edifici strategici. In particolare, questa ricerca si pone l'obiettivo di considerare e quantificare l'effetto delle aperture come misura di attenuazione sul processo di carico.

Questo progetto di ricerca si basa su un approccio sperimentale con prove su modello fisico. La formazione delle onde è riprodotta tramite il rilascio verticale di un certo volume d'acqua da un serbatoio superiore, generando onde nel canale inferiore. La variazione della portata rilasciata produce onde con proprietà idrodinamiche diverse. In particolare, questa ricerca è caratterizzata da una metodologia fortemente dettagliata per analizzare il comportamento idraulico delle onde di piena prodotte, in termini di altezza idrica e velocità, dimostrando compatibilità con la classica teoria sulla rottura istantanea di dighe su fondo secco e su fondo bagnato. E' stata data particolare attenzione alla celerità del fronte d'onda ed ai profili di velocità misurati dietro il fonte, mostrando alcune caratteristiche tipiche delle correnti a pelo libero.

Gli edifici sono stati riprodotti tramite strutture in alluminio, installate su una placca dinamometrica che fornisce lo sviluppo temporale delle forze e dei momenti. L'impatto è caratterizzato da alti schizzi, seguiti da un moto quasi-uniforme attorno all'edificio. Per le strutture impermeabili (senza aperture), le onde su fondo secco hanno generato forze proporzionali al flusso della quantità di moto. Le onde su fondo bagnato hanno costantemente mostrato un'attenuazione del picco della forza e l'introduzione di un coefficiente di riduzione é stata necessaria per ottenere una stima realistica della forza stessa.

Sintesi

Questo studio si focalizza sull'effetto delle aperture e della sommersione. Quattro configurazioni con sette gradi di apertura compresi tra 0 (impermeabile) e 84% sono state testate con dodici onde standard. Il flusso attraverso la struttura ha portato ad una diminuzione dell'altezza idrica a monte, generando rifugi verticali più sicuri. In termini dicarico, le aperture hanno prodotto una riduzione lineare della massima forza orizzontale rispetto a quella che sollecita la struttura impermeabile. La configurazione con la facciata posteriore impermeabile ha mostrato un comportamento simile a quello dell'edificio interamente impermeabile. Le aperture sulle facciate laterali hanno dimostrato di non avere alcuna influenza sulla risultante forza di picco. Un'analisi in termini di tempo di picco, altezza idrica durante la sollecitazione massima ed impulso hanno dimostrato alcune differenze chiave tra le forze provocate da onde su fondo secco e quelle su fondo bagnato. L'occorrenza del massimo momento ribaltante è risultata corrispondere al picco della forza orizzontale ed il conseguente braccio di leva è risultato costante per tutte le configurazioni. In caso di sommersione dell'edificio, condizioni di carico più tenue sono state costantemente misurate.

In conclusione, questo studio introduce delle formule per predire il carico idrodinamico su un edificio, tenendo conto dell'effetto delle aperture. Tale effetto è stato inglobato in un coefficiente di resistenza adattato. Questi risultati forniscono informazioni importanti per la progettazione di infrastrutture più sicure.

Parole chiave: *Collasso di diga, onde di piena, onde impulsive, tsunami, impatto idrodinamico, rifugi verticali, aperture, sommersione.*

Zusammenfassung

Dammbrüche, Impulswellen, Tsunamis und Sturmfluten sind Naturkatastrophen, welche die Menschheit herausfordern. Oftmals führen sie zu zahlreichen Opfern und bewirken bedeutende wirtschaftliche Verluste. Diese Ereignisse erzeugen instationäre Strömungsbedingungen in Form von Schwall- oder Flutwellen, die mit einer extremen Belastung der Infrastruktur verbunden sind. In der Vergangenheit wurden solche Belastungen bei Gebäudeauslegungen ungenügend berücksichtigt. Die jüngsten Ereignisse haben jedoch gezeigt, dass diesbezügliche Massnahmen die Sicherheit der Menschen gewährleisten und die Wiederaufbaukosten senken können. Daher sind vertikale Refugien, die extremen Belastungen standhalten können, von grosser Bedeutung und eine Abschätzung der induzierten Kräfte notwendig. Erfahrungen haben gezeigt, dass Gebäude mit vielen Öffnungen wie Fenster in der Fassade beim Wellenaufprall besser widerstehen. Ziel der vorliegenden Forschungsarbeit ist es, das Schadenspotenzial von Gebäuden, die durch Schwall- oder Flutwellen betroffen sind, zu bewerten und zu analysieren. Insbesondere wird der Einfluss von Öffnungen als Abschwächungsmassnahme auf den Belastungsprozess untersucht und quantifiziert.

Im Rahmen einer systematischen experimentellen Studie wird die Schwallwelle durch die vertikale Freisetzung eines Wasservolumens aus einem oberen Reservoir ausgelöst, wodurch Wellen auf trockener oder benetzter Unterlage im horizontalen Kanal erzeugt werden. Eine Variation des freigesetzten Abflusses führt zu Wellen mit unterschiedlichen hydrodynamischen Eigenschaften. Eine detaillierte Methodik zur hydraulischen Charakterisierung der erzeugten Wellen in Bezug auf deren Wassertiefen und Strömungsgeschwindigkeiten wird vorgestellt. Es konnte eine gute Übereinstimmung mit den klassischen Theorien des Talsperrenversagens sowohl auf trockener als auch auf benetzter Sohle nachgewiesen werden. Besondere Aufmerksamkeit wird den Fliessgeschwindigkeiten der Wellenfront und den dahinter gemessen Wellengeschwindigkeitsprofilen gewidmet.

Freistehende Gebäude wurden mit Aluminiumstrukturen reproduziert und auf einer Kraftmessplatte installiert, welche eine detaillierte zeitliche Aufzeichnung der Stosskräfte und -momente erlaubte. Der Aufprall war durch hoch aufsteigende Wassermassen gekennzeichnet, gefolgt von einer quasi-gleichförmiger Strömung um das Gebäude herum. Für die undurchlässigen Strukturen (ohne Öffnungen) ergaben sich horizontale Kräfte proportional zum Impulsfluss auf trockener Sohle. Bei benetzter Sohle wurde eine anhaltende Abschwächung der Maximalbelastung beobachtet. Die Einführung eines Reduktionskoeffizienten war für eine realitätsgetreue Belastungsabschätzung notwendig.

Zusammenfassung

Der Einfluss von Gebäudeöffnungen und einer Überströmung wurde systematisch untersucht. Vier Gebäudekonfigurationen mit sieben Durchlässigkeiten von 0 (undurchlässig) bis 84% wurden mit 12 Standardwellen untersucht. Der Durchfluss durch die Struktur reduzierte die Wassertiefen oberstrom und sorgte für sichereren vertikalen Schutz. Hinsichtlich der Belastung erzeugten die Öffnungen eine lineare Verringerung der maximalen horizontalen Kraft auf das Gebäude im Vergleich zum undurchlässigen Fall. Für die Konfiguration mit einer undurchlässigen Rückwand ergaben sich ähnliche Ergebnisse wie für das undurchlässige Gebäude. Öffnungen an den Seitenwänden hatten keinen Einfluss auf die resultierende maximale Belastung. Die Analyse bezüglich des Zeitpunkts der höchsten Belastung, der Wellenhöhe bei maximaler Kraft und des Impulses, zeigte Unterschiede des Belastungsprozesses zwischen Schwall- und Flutwellen. Das maximale Kippmoment trat zur gleichen Zeit wie die maximale Horizontalkraft auf. Der resultierende Hebelarm war für alle Öffnungskonfigurationen konstant. Im Falle einer Überströmung des Gebäudes wurden konstant geringere Belastungsbedingungen gemessen.

Schließlich werden neue Formeln zur Abschätzung der hydrodynamischen Belastung von Gebäuden erarbeitet, welche die Auswirkungen von Öffnungen mittels eines angepassten Widerstandskoeffizienten berücksichtigen. Diese können relevante Informationen für die Gestaltung sicherer Infrastrukturen liefern.

Schlüsselwörter: *Talsperrenversagen, Impulswellen, Tsunamis, Wellenschlag, hydrodynamische Belastung, vertikale Schutzvorrichtungen, Öffnungen in Gebäuden, Überströmung.*

Contents

Contents

Contents

List of Symbols

These symbols are used throughout the report:

Roman letters

a	deceleration behind the wave front [Eq. 4.13]	[m/s^2]
a'	US sensors calibration coefficient	[m/V]
A	wave amplitude	[m]
A_o	surface of openings on the buildings	[m^2]
A_P	cross-sectional area of the pipes	[m^2]
b	coefficient [Eq. 4.10]	[-]
b'	US sensors calibration coefficient	[m]
B	building width and depth, $B = 0.3$ m	[m]
c	coefficient [Eq. 4.10]	[-]
C_D	drag coefficient	[-]
C_m	inertia coefficient	[-]
C_H	hydrostatic empirical coefficient [Eq. C.2]	[-]
C_R	resistance coefficient	[-]
$C_\mathrm{R,0}$	resistance coefficient for the impervious, reference, configuration	[-]
$C_\mathrm{R,S}$	resistance coefficient for submerged structure, $C_\mathrm{R,S}=1.5$	[-]
Ca	Cauchy number, Ca $= \rho\, v^2 / K$ [Eq. 3.6]	[-]
d_0	impoundment depth for the classical dam-break scenario	[m]
D	distance of buildings from the coastline [Eq. 2.36]	[m]
D_H	hydraulic diameter, $D_\mathrm{H} = 4 \cdot R_\mathrm{H}$	[m]
E	elastic modulus	[N/m^2]
f	frequency	[Hz]
f_DW	Darcy-Weissbach friction factor	[-]
F	generic force	[N]
F_1	first order correction factor for flow resistance, [Eq. B.5]	[N]
F_D	hydrodynamic (drag) force [Eq. 2.24]	[N]
F_HS	hydrostatic force	[N]
F_I	inertia force [Eq. 2.23]	[N]

List of Symbols

F_S	surge force	[N]
F_x	measured horizontal hydrodynamic force in x direction	[N]
$F_{x,D}$	predicted horizontal hydrodynamic force	[N]
$F_{x,max}$	maximum measured horizontal force	[N]
$F_{x,D,max}$	maximum predicted horizontal force	[N]
F_y	transversal force in y direction	[N]
F_z	total vertical force in z direction	[N]
$F_{z,B}$	buoyant vertical force (uplift), [Eq. 7.7]	[N]
$F_{z,g}$	gravitational vertical force , [Eq. 7.7]	[N]
Fr	Froude number, $\mathrm{Fr} = v/(gh)^{0.5}$ [Eq. 4.14]	[-]
$\mathrm{Fr}_{1,2}$	Froude number for the up- and downstream flow conditions	[-]
Fr_B	bore Froude number, $\mathrm{Fr}_B = (U + V_0)/(gh_0)^{0.5}$ [Eq. B.1]	[-]
g	gravity constant ($g = 9.81$ m/s^2)	[m/s^2]
h	wave height without the building or water depth	[m]
h_0	initial still water depth in the channel	[m]
h_2	height of the plateau according to Stoker (1957), [Eq. 2.16]	[m]
h_i	height of the profile i	[m]
h_M	ratio between the wave height when M_{max} occurs and h_{max}	[-]
h_{max}	maximum wave height value	[m]
H	have height with the structure (run-up height)	[m]
H_B	building height , $H_B = 0.3$ and 0.6 m	[m]
H_{eq}	equivalent water depth obtained from F_z through Eq. 3.8	[m]
H_R	water depth in the upper reservoir for the vertical release technique	[m]
$H_{R,0}$	water depth in the upper reservoir before the gate opening ($t < t_0$)	[m]
i	index	[-]
I	impulse	[Ns]
I^*	relative impulse $I^* = I_{peak}/I_{tot}$	[Ns]
I_{peak}	peak impulse	[Ns]
I_{tot}	total impulse	[Ns]
I_{tsu}	tsunami importance factor, $I_{tsu} = 1$, [Eq. 2.43]	[-]
k	building stiffness	[N/m]
k_s	channel roughness	[m]
k_w	wave number, defined as $k_w = 2\pi/\lambda$	[m^{-1}]
k_ρ	fluid density factor for soil and debris, $k_\rho = 1.1$	[-]
K	modulus representing the elasticity of the fluid	[kg/ms^2]
L	channel length, $L = 15.5$m	[m]
L_r	length of the roller for wet bed bores	[m]
L_z	cantilever arm $L_z = M_y/F_x$	[m]
m	mass	[kg]
M	momentum flux per unit width, $M = hv^2$	[m^3/s^2]
M^*	modified momentum flux per unit width, [Eq. 5.5]	[m^3/s^2]
M_{max}	maximum momentum per unit width	[m^3/s^2]

M_x	moment around the x-axis	[Nm]
M_y	moment around the y-axis	[Nm]
M_z	moment around the z-axis	[Nm]
n	number of points in the vertical direction per velocity profile	[-]
N	exponent	[-]
p	pressure	[N/m^2]
p_{max}	maximum pressure	[N/m^2]
P	general porosity $P = A_o/B^2$	[-]
$P_{h,max}$	porosity at $h = h_{max}$	[-]
P_{tot}	total porosity at $h = H_B$	[-]
q	unit discharge, $q = h \cdot V_m$	[m^2/s]
Q_0	initial discharge released into the channel	[m^3/s]
R	ground elevation at maximum tsunami penetration	[m]
R_H	hydraulic radius	[m]
Re	Reynolds number, Re $= (v \cdot D_H)/v$ [Eq. 3.5]	[-]
s	sensitivity term in force plate measurements [Eq. 3.2]	[N^{-1}]
S	submergence coefficient [Eq. 6.2]	[-]
St	Strouhal number, St $= f \cdot B/U$	[-]
t	time	[s]
t_0	reference time at which the wave reaches the measurement location	[s]
T	shifted time, defined as $T = t - t_0$	[s]
T^*	time after which constant discharge assumption is no longer valid	[-]
Tu	turbulent intensity [Eq. 4.9]	[-]
u_x	velocity component in the horizontal x-direction	[m/s]
u_z	velocity component in the vertical z-direction	[m/s]
U	wave front celerity	[m/s]
Ur	Ursell number, Ur $= A\lambda^2/h^3$	[-]
v	generic velocity	[m/s]
V	voltage measured in the calibration of the US sensors	[V]
$\dot{V}$	velocity gradient, calculated through Eq. 4.12	[-]
$\forall$	volume	[m^3]
V_0	flow velocity of the initial still water depth	[m/s]
V_2	bore velocity behind the front, calculated through Eq. 2.22	[m/s]
V_m	depth-averaged profile velocity	[m/s]
V_P	flow velocity through the pipes	[m/s]
W	channel width, $W = 1.4$ m	[m]
We	Weber number, We $= v^2 \rho h/\sigma_T$	[-]
x	streamwise coordinate along the channel	[m]
x_s	wave front location along the x-axis	[m]
y	transversal coordinate	[m]
z	vertical coordinate	[m]

Greek letters

α	velocity coefficient	[-]
β	blockage ratio, $\beta = W/B$	[-]
γ	relative wave length, $\gamma = \lambda/h$	[-]
δ	deflection [Eq. 3.3]	[m]
ϵ	relative wave height, $\epsilon = A/h$	[-]
$\eta(x,t)$	function describing the water surface elevation in space and time	[m]
θ	orientation angle	[°]
λ	wave length	[m]
λ_{F}	coefficient function of the blockage ratio [Eq. 2.41]	[m]
Λ	scaling ratio	[-]
ν	water kinematic viscosity, $\nu = 10^6 \, \mathrm{m^2/s}$	[m^2/s]
ξ	head loss at the inlet of the pipes, $\xi = 0.5$	[-]
π	constant, $\pi = 3.14$	[-]
Π	porosity coefficient [Eq. 7.3]	[-]
ρ	water density, $\rho = 1000 \, \mathrm{kg/m^3}$	[kg/m^3]
σ	standard deviation	[-]
σ_{T}	surface tension	[kg/s^2]
$\tau_{\max}$	shifted time at which $F_{\mathrm{x,max}}$ occurs	[s]
Φ	velocity potential	[m^2/s]
χ	wet bed reduction coefficient	[-]
ω	angular frequency, $\omega = 2\pi/T$	[Hz]

Abbreviations

ADV	Acoustic Doppler Velocimeter
DPIV	Digital Particle Image Velocimeter
EPFL	Ecole Polytechnique Fédérale de Lausanne
ETH	Swiss Federal Institute of Technology in Zürich
FEM	Finite Element Method
FFT	Fourier Fast Transform
ICOLD	International Commission on Large Dams
LCH	Laboratoire de Constructions Hydrauliques of EPFL
LDV	Laser Doppler Velocimeter
PIV	Particle Image Velocimeter
Rep.	Repetitions
SNSF	Swiss National Science Foundation
US	Ultrasonic distance Sensors
UVP	Ultrasonic Velocity Profiler
VAW	Laboratory of Hydraulics, Hydrology and Glaciology of ETH Zürich

1 Introduction

1.1 Motivation/Overview

In the context of global climate change, in the last few years the world was hit by an increasing number of catastrophic events such as tsunamis, impulse waves, hurricanes, storm surges or extreme floods responsible for the collapse of dams. These events showed severe devastation, damages to the build environment and important human losses. Furthermore, post-event field observations and surveys showed that most infrastructures, including critical buildings hit by such hydrodynamic events, were destroyed or highly damaged. Nevertheless, because of the rarity of these events, most building codes or guidelines do not include design criteria for such hydrodynamic forces and these phenomena remain neglected in the design phase.

In nature the sudden release of a large amount of water can be found in the following events:

1. **Dam break waves** - produced by the collapse of a man-made dam or natural reservoir
2. **Impulse waves** - generated by a landslide falling inside a water reservoir
3. **Tidal bores** - take place after a sudden increase in water depth due to tidal activity
4. **Tsunamis** - provoked by an underwater earthquake
5. **Storm surges** - generated by tropical cyclones with strong winds and high water levels

1.1.1 Dam-break waves

Dam breaks are rare but catastrophic events. Independently from its causes, such a failure results into a sudden release of an important amount of water that propagates downstream, creating an hydrodynamic wave responsible for flooding, devastation and serious damages. The propagating wave has a high level of energy capable of severe destruction. A similar process can be observed in case of failure of a river weir, a dyke, accumulation dams or natural lakes (moraines and glacial lakes), also called with the Icelandic word *jökulhlaup*.

In the world there are approximatively 58 000 large dams according to ICOLD registry, but in history only few structures collapsed, among which it is worth recalling: (1) Sweetwater Dam

(USA), 30 January 1916; (2) Gleno (Italy) 1923; (3) Malpasset (France) 2 September 1959 and (4) Taum Sauk Dam (USA), 14 December 2005. Pictures of the remaining structures are presented in Figure 1.1. In Switzerland it is well known the collapse of the glacial dam of Giétro (glacier lake break out), in Valais, near Mauvoisin, that provoked the death of 44 people in 1818. A summary of some of the major catastrophes in history is presented in Table 1.1.

(a)

(b)

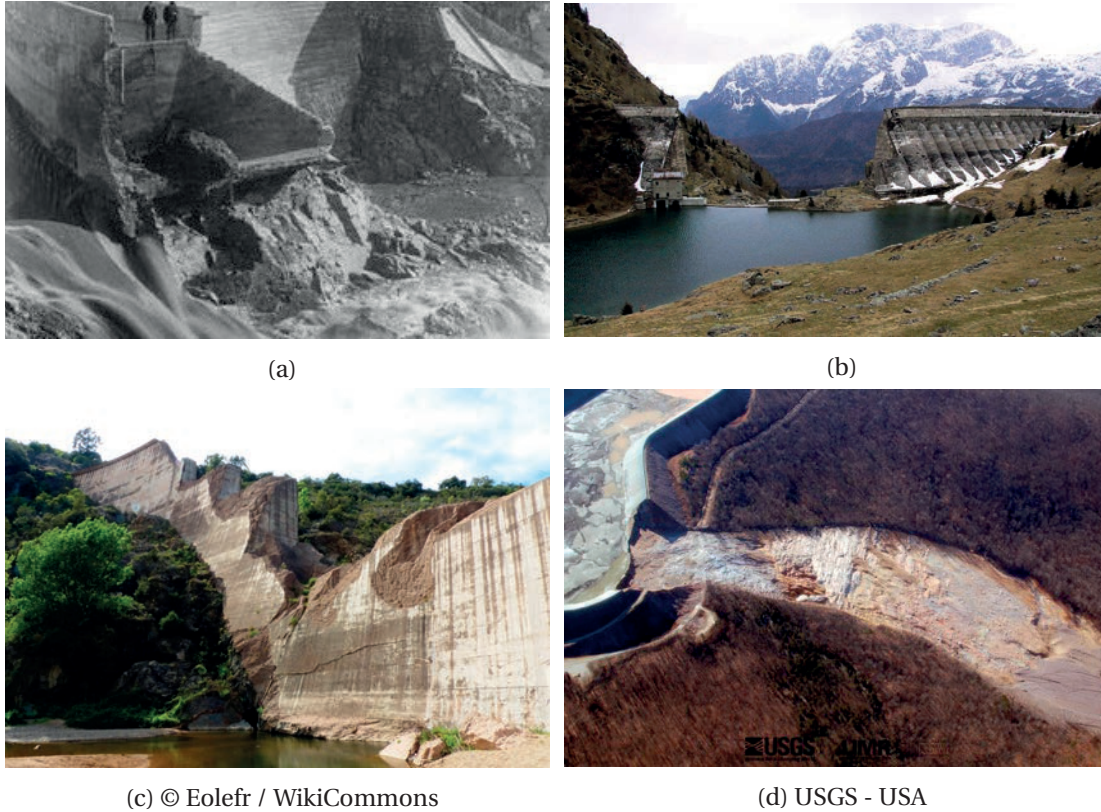

(c) © Eolefr / WikiCommons

(d) USGS - USA

Figure 1.1 – Collapsed dams in history : (a) Sweetwater, USA (1916) ; (b) Gleno, Italy (1923) ; (c) Malpasset, France (1959); (d) Taum Sauk Dam, USA (2005) [source: WikiCommons]

Date	Location	Dam type	Height	Fatalities
16 June 1818	Giétro (Switzerland)	Natural glacial lake	~60 m	44
30 January 1916	Sweetwater Dam (USA)	Masonry arch	27.4 m	-
1 December 1923	Gleno Dam (Italy)	Multi-arch concrete	43 m	356
12 March 1928	St. Francis Dam (USA)	Concrete gravity	56 m	600
13 August 1935	Molare (Italy)	Concrete gravity	35 m	111
2 September 1959	Malpasset (France)	Concrete arch	60 m	423
8 August 1975	Banqiao Dam (China)	Embankment (clay)	24.5 m	171 000
11 August 1979	Machchhu dam (India)	Embankment	31 m	5 000
14 December 2005	Taum Sauk Dam (USA)	Rockfill	27.4 m	-

Table 1.1 – Examples of dam-break events in history

1.1.2 Impulse waves

Impulse waves are caused by a landslide, a rockfall or an avalanche falling inside a water reservoir, producing a wave in the opposite direction. These events are characterised by three main phases, *i.e.* wave formation, propagation and run-up (Figure 1.2). Because of the extreme height that these waves can reach, they are also called *Mega-tsunamis*. The generation and propagation of such waves were the object of different research projects at VAW, ETH, Zürich, including Fritz (2002), Heller (2007) and Fuchs (2013).
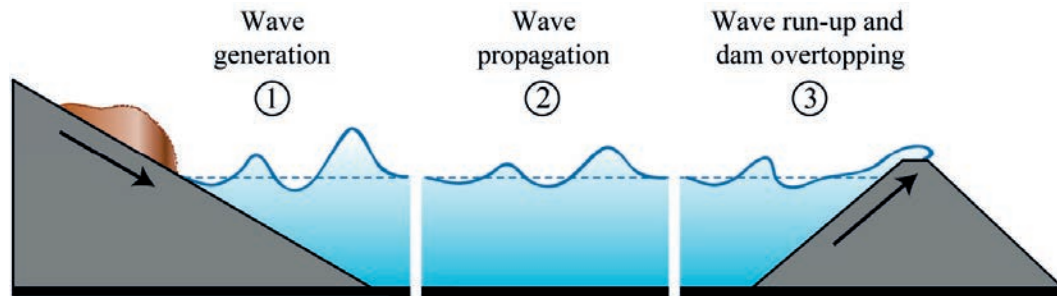

Figure 1.2 – The three phases of an impulse wave (Heller, 2007)

Well known is the event that took place in Lituya Bay (USA), where on July 9th 1958 a wave of 524 m overpassed the opposite mountains, as shown in Figure 1.3c. The Vajont dam (Italy), on 9 October 1963, experienced a 70-meter-wave that completely destroyed the village of Longarone, killing about 2 000 people during the night, leaving the dam almost undamaged (Figure 1.3b). In Switzerland impulse waves were observed in 563 a.d. on Lake Geneva (*tsunami du lac Léman*, Figure 1.3d), with inundation depths of 13 m in Lausanne and 8 m in Geneva. Furthermore, in 1806 in the Lauerz Lake (Goldau) a landslide produced the death of 450 people and in 2007 on the shores of Lake Lucerne, waves of ≈ 6 m were observed. In 2009, close to Grindelwald (BE), Switzerland, more than 300 000 m^3 of rock entered a glacial lake generating an impulse wave that reached 70 m (Figure 1.3a). A list of major impulse waves observed in the past is summarized in Table 1.2.

Date	Location	Volume	Run-up height
563 a.d.	Léman Lake (Switzerland)	$25 \cdot 10^6$ m^3	3-13 m
9 July 1958	Lituya Bay (USA)	$30 \cdot 10^6$ m^3	524 m
9 October 1963	Vajont (Italy)	$250 \cdot 10^6$ m^3	≈200 m
18 May 1980	Spirit Lake (USA)	$56 \cdot 10^6$ m^3	≈60 m
20 July 2007	Lake Lucerne (Switzerland)	$8 \cdot 10^3$ m^3	≈6 m
4 December 2007	Lake Chehalis (Canada)	$3 \cdot 10^6$ m^3	38 m
22 May 2009	Grindelwald Glacier (Switzerland)	$8 \cdot 10^3$ m^3	≈10 m
September 2011	Nagatono (Japan)	$3 \cdot 10^6$ m^3	≈50 m

Table 1.2 – Examples of impulse waves in history
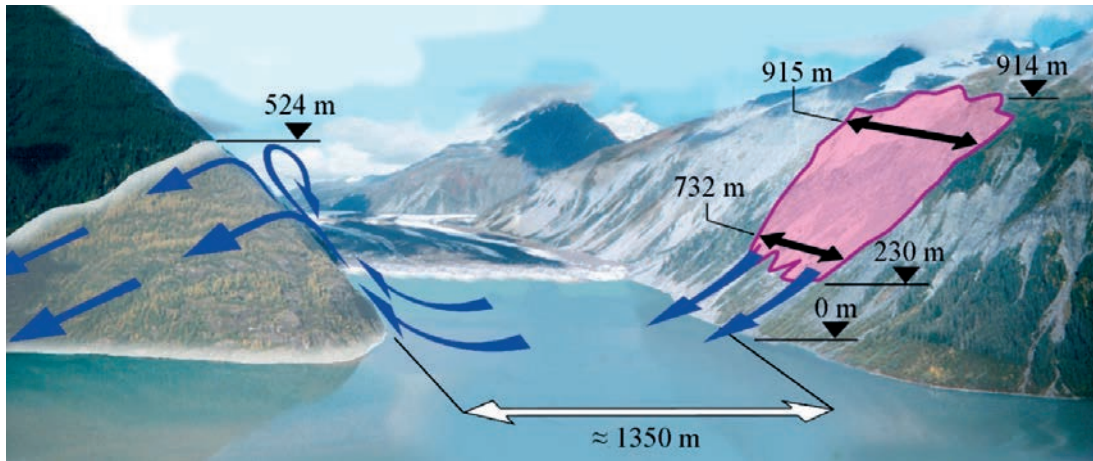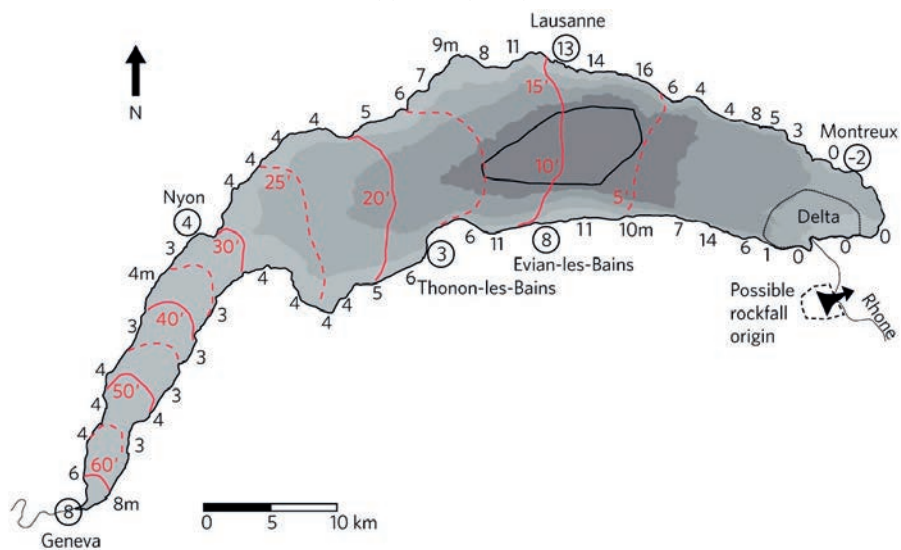
(a) H-R.Burgener

(b) D. Wüthrich

(c) Fritz (2002)

(d) Kremer et al. (2012)

Figure 1.3 – Examples of impulse waves: (a) Lake Grindelwaldgletscher, Switzerland; (b) Vajont, Italy; (c) Lituya Bay, USA and (d) *Tsunami du Lac Léman*, Geneva Lake, Switzerland.

1.1.3 Tidal bore

A tidal bore is a wave that propagates in the river mouth as the tide coming from the sea increases. These are particularly intense during spring tides, when the tidal range exceeds 4 to 6 m and the rising tidewater is confined to the narrow funnelled estuary (Chanson, 2012). This phenomenon can be observed in all continents (besides Antarctica) and it is estimated that more than 400 river estuaries are effected by tidal bores. For this, there exist different names to identify the same phenomenon such as *Aegir* (Trent River, UK), *Eagre* (UK), *Mascaret* (France), *Pororoca* (Amazon River) and *Silver dragon* on the Qiantang River in China.

Visually, a tidal bore appears as a series of waves propagating upstream, as shown in Figure 1.4 for the *Mascaret* on the Garonne River in France. Depending on the Froude number, a tidal bore can appear as undular waves or broken, fully aerated, bores (Chanson, 2012). During its propagation, these tidal bores hit multiple bridge piers and there have been cases of human losses due to arrival of these waves.

(a) (b)

(c) (d)

Figure 1.4 – Examples of tidal bores on the Garonne River (France): (a) Arcins, 28 October 2015 16h23; (b) Boisson, 28 October 2015 17h45; (c) Port de Saint Pardon, 29 October 2015 17h38; (d) Boisson, 29 October 2015 18h35. [pictures: Davide Wüthrich]

1.1.4 Tsunami

Tsunami is a Japanese word that literally means "harbour wave" and it is defined as a pressure, or shock, wave travelling at high speed in the ocean, caused by an undersea earthquake, subsidence, coastal landslide, volcanic activity or other disturbance (Source: *IATE*). The wave amplitude is relatively small in the middle of the ocean (0.5 to 1 m), which makes them difficult to detect. Tsunamis travel extremely fast, with common velocities of 200 m/s; they are characterized by very long wave-lengths and periods ($\lambda \approx 1 - 100$ km) and the wave-length to water-depth ratio ($\lambda/h < 1$) classifies them as *shallow water waves* (Section 2.1). The extremely long wave-length of these waves reduces the energy dissipation during the propagation phase and tsunamis can cause damages and destruction far away from their place of origin. When the wave approaches the shore the velocity decreases following the square root of the water depth. Even near the coastline the period of the wave is relatively long compared to wind-generated waves, whose typical values vary between 5 and 20 seconds. This implies that a draw-down of the water surface level is followed, after a relative long time, by a massive wave; furthermore tsunamis may take minutes before they reach full height. The increase of wave height near the shore is due to the conservation of energy, which is dependent on both its wave speed and wave height. Since the wave only provokes a translation of water mass, the variation in amplitude cannot be due to the conservation of mass. (Margaritondo, 2005).

The interest in tsunami research was regained after some recent catastrophic events, including the Indian Ocean tsunami in 2004 and the 2011 Tohoku earthquake in Japan, sadly known for the damages caused to the nuclear power plant of Fukushima. Some of the most devastating tsunamis in history are presented in Table 1.3. Closely followed by media, the last events deeply touched the public opinion all over the world. Pictures of these events are shown in Figures 1.6, where Figure 1.6a shows a tsunami reaching the coast-line, and Figure 1.6b the interaction with buildings located near the coast. Figure 1.5 shows some of the signs used in Thailand and in South America to convey people to designated tsunami-safe zones.

Date	Location	Deaths	Damages (CHF)
20 September 1498	Enshunada Sea, Japan	31 000	
27 January 1703	Boso Peninsula, Japan	100 000	
1 November 1755	Lisboa, Portugal	60 000	
13 August 1868	Arica, Chile	25 000	300 million
27 August 1883	Krakatoa, Indonesia	36 000	
26 December 2004	Sumatra (Indian Ocean)	280 000	11 billion
27 February 2010	Valparaiso, Chile	525	30 billion
11 March 2011	Tohoku, Japan	15 889	226 billion

Table 1.3 – Most devastating tsunamis experienced in the past (Chanson, 2005b) and World Bank

Figure 1.5 – Tsunami protection signs in Antofagasta (Chile), Ko Phi Phi (Thailand) and Lima (Peru) [pictures: Davide Wüthrich]

Visual observations and field surveys showed that, during the Indian Ocean tsunami in December 2004, coastal inundation heights reached 4 to 7 m in the southern part of Khao Lak (Dias et al., 2006; Matsutomi et al., 2006) and wave front velocities were estimated between 3 to 4 m/s in Kumala Beach and 6 to 8 m/s in Khao Lak, Thailand (Rossetto et al., 2007). From debris watermarks and eyewitness Fritz and Okal (2008) concluded that along the shores of Socotra Island, Indonesia, run-up heights reached up to 6.1 m. During the 2011 Tohoku Tsunami event in Japan, onshore inundation velocities up to 8 m/s were recorded in Sendai (Hayashi and Koshimura, 2013) while values of 10 to 13 m/s were observed near the Sendai Airport (Jaffe et al., 2012). The Japanese Port and Airport Research Institute (PARI) reported inundation heights of up to 15 m in the City of Onagawa, with an average of 8 to 9 m along certain coastal areas. Fritz et al. (2012) estimated from video post-processing flow depths of 9 m and flow velocities up to 11 m/s were recorded in Kesennuma Bay, with an average increase in the water level rate of 1m/min and a Froude number of approximately 1. They also pointed out that the return (outflow) current velocity diminished from 3 m/s to 11 m/s in little over 2 minutes. A comprehensive study of tsunami front velocities during the Tohoku event was presented by Chock et al. (2012), based on aerial video analysis, showing average values of 3 to 9 m/s.

(a) D. Rydevik / WikiCommons

(b) courtesy of J.M. Thomson

Figure 1.6 – Examples of tsunami waves during the Indian Ocean 2004 event: (a) wave arrival in Ao Nang (Thailand); (b) wave propagating in Khao Lak (Thailand).

1.1.5 Storm surge

A storm surge (or storm tide) is a coastal flood with rising water levels associated with low pressure weather such as *cyclones* (Indian Ocean), *typhoons* (Pacific Ocean) and *hurricanes* (Atlantic Ocean). These events are characterised by a long strong fetch of winds spiralling inward and a low-pressure-induced dome of water drawn up under the storm's centre. The surge amplifies to a considerable extent as it approaches the shore (Figure 1.7), causing disastrous floods along the coast (Murty et al., 1986). During cyclones, typhoons and hurricanes most casualties occur as a result of the rising storm surges and the majority of damages are observed on structures located along the coast. Similarities between tsunami-likes waves and storm surges were discussed by Roeber and Bricker (2015). Some examples of major catastrophes observed in the recent past are presented in Table 1.4. Areas particularly affected by these phenomena are the bay of Bengal in the Indian Ocean, the gulf of Mexico, Japan and the archipelago of the Philippines. Although only 1% of all tropical cyclones that form each year strike Bangladesh, that nation has suffered 53% of all world fatalities due to tropical cyclones (Ali, 1999). The highest surge ever recorded was produced by Cyclone Mahina in Bathurst Bay in Australia, where according to Whittingham (1958), depths of 13-14.6 m were produced.
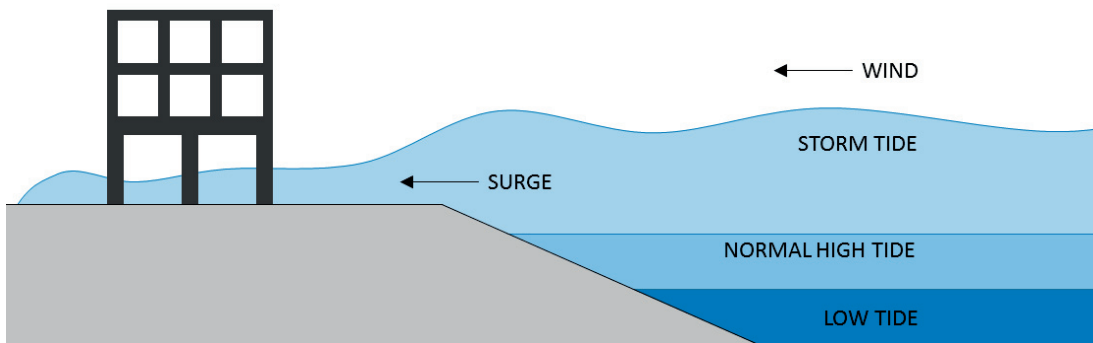

Figure 1.7 – Storm surge propagating inland

Type	Year	Location	Surge height	Deaths
Cyclone (Mahina)	March 1899	Bathurst Bay, Australia	14.6 m	307
Typhoon (Ida)	September 1958	China, Japan	1.1 m	1 269
Hurricane (Carla)	September 1961	Port Lavaca (TX), USA	6.9 m	43
Cyclone (Bhola)	November 1970	Chittagong, Bangladesh	10.6 m	300 000
Hurricane (Andrew)	August 1992	Miami (FL), USA	5.2 m	65
Cyclone (Sidr)	November 2007	Barguna, Bangladesh	6.0 m	3 500
Hurricane (Katrina)	September 2005	Mobile (AL), USA	7.5 m	1 836
Typhoon (Yolanda)	November 2013	Philippines	7.5 m	11 801
Hurricane (Irma)	September 2017	Charleston (SC), USA	3.0 m	134

Table 1.4 – Selected examples of storm surges in recent history

1.2 Resilient structures and buildings

Coastal communities have experienced natural calamities for centuries and it is well known that a specific design can reduce the hydrodynamic load on the structure, allowing it to resist to strong floods (Kreibich et al., 2005). This not only reduces reconstructions costs, but it also guarantees safety and protection to human beings through the construction of specific shelters. It is the case for **amphibious, hurricane-resistant, structures** in the Gulf of Mexico (English et al., 2017), where stilt houses are built on columns, avoiding any contact between the living space and the ground, as shown in Figure 1.8a. Similarly, in Bangladesh, some cyclone shelters with higher openings on the lower portion of the structure were conceived to guarantee safety to the people in the upper levels (Figure 1.8b). There exist some perforated houses in the west coast of the Philippines, where the higher porosity concentrated in the lower part of structure allows the passage of the storm surge, combined with a inclined roof for wind protection. This design is particularly suitable in case of typhoons, which are associated with a storm surge and strong winds (Figure 1.8c).

Practical surveys showed that for inundation depths lower than 2 m, almost no damages were observed, however, for heights larger than 4-5 m, almost all buildings were destroyed (Koshimura et al., 2009). Nevertheless, events that took place along the western and northern coasts of Sumatra Island (Indonesia, 2004), central coast of Chile (2010) and in Tohoku, Japan (2011), showed that, even for tsunamis, specific design features of infrastructures can help saving lives. For example, some 500 people successfully sought refuge at three specifically-designed buildings in Ishinomaki, Japan (2011), proving thus that **vertical shelters** are essential in tsunami-prone coastal areas, where access to higher elevation is limited or distant. An example of a similar vertical shelter can be observed in Figure 1.8d, representing a dormitory also designated as a tsunami refuge centre in Minamisanriku (Japan).

Furthermore, post-tsunami forensic engineering surveys showed that some structures behave better than others; moreover, **buildings with openings** seem to resist better under hydrodynamic impact (Chock et al., 2012). Currently, buildings located on the shoreline are seldom impervious cubes, but most often characterized by openings such as windows and doors, similar to the one presented in Figure 1.8e. If correctly designed, these can also act as vertical shelter during tsunami events. The effectiveness of openings on the stability of the structure was proved by the Banda Aceh Mosque and some other surrounding structures (Figure 1.8f). The role of engineers and researchers is therefore to develop and design infrastructures able to withstand natural disasters and protect human lives. In this context, the understanding of the effect of openings as a mitigation measure on coastal structures is essential.

(a) Davide Wüthrich

(b) Karim and Mimura (2008)

(c) Davide Wüthrich

(d) courtesy of Prof. Ioan Nistor

(e) Davide Wüthrich

(f) M.L. Bak / WikiCommons

Figure 1.8 – Examples of resilient buildings specifically designed to withstand natural catastrophes: (a) amphibious, hurricane-resistant house in Florida (USA); (b) cyclone shelter in the west coast of Bangladesh; (c) typhoon resistant house in the Philippines; (d) coastal structure designed as vertical shelter in Minamisanriku (Japan) after the 2011 Tohoku event; (e) buildings on the coast of Viña del Mar (Chile) and (f) building in Bandah Aceh (Indonesia) after the 2004 Indian Ocean tsunami.

1.3 Objectives

The construction of resilient structures and buildings capable to withstand natural calamities is essential. For this, the evaluation of resulting forces and moments is fundamental for a specific design. Although some specific research was carried out in the last 10 years, the phenomenon of wave impact against a building is poorly understood and the estimation of wave-induced forces is rough and subject to high uncertainties. In addition most construction codes do not include design guidelines for waves-induced forces. Improvement is therefore needed.

When looking at damaged buildings, one has the impression that some structures are more resistant than others. In particular, buildings with openings let the wave pass without collapsing under hydrodynamic impact. Some recent studies on tsunami-proof houses showed that architectural features are a key parameter in reducing impact forces (Thusyanthan and Madabhushi, 2008), however no systematic study was carried out and Wilson et al. (2009) concluded their study with the remark that very little research in this area exists. In this context, the purpose of this research project is to deepen the knowledge in the domain of wave-structure interaction, mainly focusing on the interaction between the impacting waves and buildings with openings. Also, some practical guidelines for a better estimation of wave induced forces are provided.

The main objectives of this research project can be summarized as follows:

1. To characterise the wet bed bores and dry bed surges produced with the vertical release technique in terms of their hydrodynamic behaviour, namely depth profiles and flow velocities.

2. To identify the magnitude and application point of the horizontal force exerted by the incoming bores and surges on the reference impervious free-standing building without overflow.

3. To estimate the consequences of building overflow on the loading process.

4. To investigate the effect of building openings on the resulting hydrodynamic loading for different configurations.

These objectives are derived from a gap in knowledge that emerged from the State of the Art presented in Chapter 2 and summarized in Section 2.6.

1.4   Structure of the report

This report is divided into 8 chapters. The first presents a broad overview of the main natural events considered in the present study, outlining the motivation behind the research project. Techniques used in the past to reduce the impact of these events on the local communities are also presented. In Chapter 2 a comprehensive literature review of both the physics of shallow water waves and major studies carried out in the past to estimated the resulting horizontal forces on both impervious and porous structures is presented. The experimental set-up, the instruments used and the experimental methodology are detailed in Chapter 3. Chapter 4 focuses on the hydrodynamic properties of the generated waves with the vertical release technique. The resulting forces produced on an impervious free-standing structure are presented and discussed in Chapter 5. The effect of building overflow on the impervious structures is presented in Chapter 6. The influence of openings for multiple configurations is fully addressed in Chapter 7. Finally Chapter 8 summarize the key findings and presents an outline for the future work. More detailed studies and additional, exploratory, research is presented in the Appendix section of this report. Note that Chapters 4, 5, 6 and 7 were conceived and prepared as journal papers.
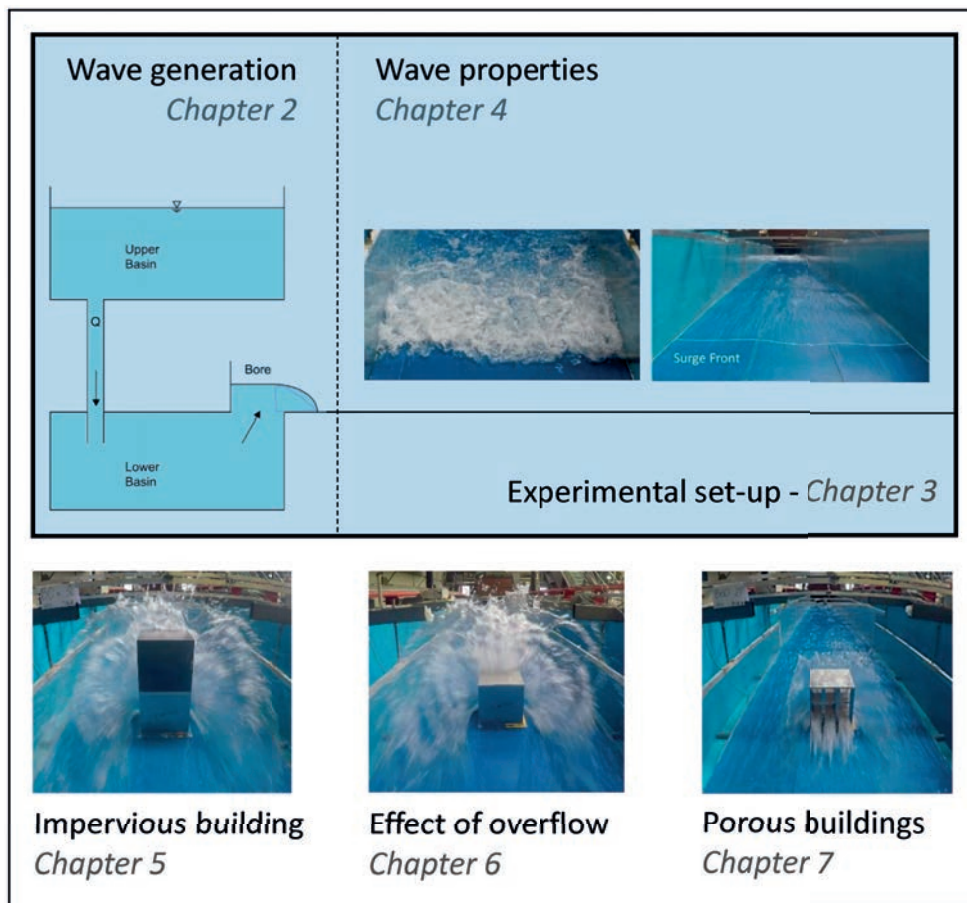
2 State of the Art

2.1 Wave theory

A *Wave* is a disturbance produced in a body of water that propagates at a certain speed. Such disturbance is the result of all forces acting on the surrounding volume. Waves often have an oscillating nature and they are characterized by a positive and a negative peak, called respectively *ridge* (or crest) and *trough*. The wave length can vary from less than a centimetre to kilometres, as it is the case for tides, the longest known water ways (Dean and Dalrymple, 1991). The main parameters that are used to define a wave are length (λ), height or amplitude, (A) and the water depth below the wave (h). All other quantities can be obtained from these parameters. The definition of all parameters is presented in Figure 2.1.
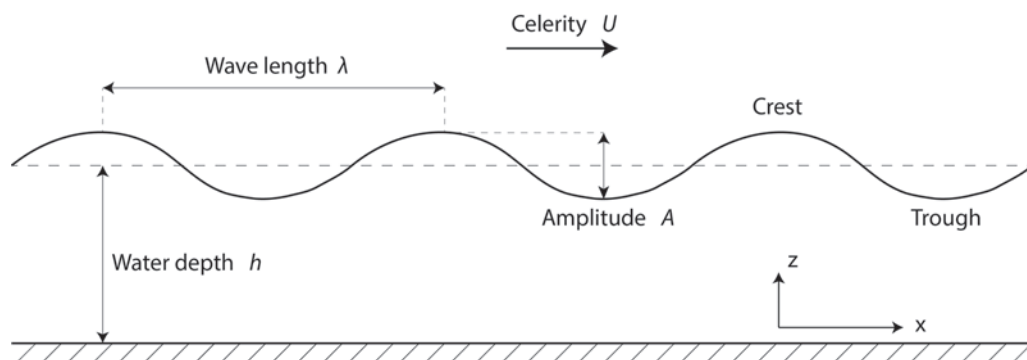
Figure 2.1 – Definition sketch of the main wave parameters

Waves are a complex and non-linear phenomenon, however, under certain circumstances, a linear approximation is acceptable. The most common theory used to describe the behaviour of gravity wave is the the **Airy wave model**, with the following assumptions:

$$\frac{\partial \rho}{\partial t} = 0 \qquad\qquad \nabla \times \mathbf{u} \qquad\qquad (2.1)$$

These imply, respectively, an incompressible and irrotational flow. In addition, the bed underneath the flow is considered impermeable.

Through the definition of a velocity potential $\Phi(x, z)$ such that:

$$\frac{\partial \Phi}{\partial x} = u_x \qquad\qquad \frac{\partial \Phi}{\partial z} = u_z \tag{2.2}$$

From the governing equation (Laplace equation) $\nabla^2 \Phi = 0$, the equation of surface waves can be obtained:

$$\frac{\partial^2 \Phi}{\partial t^2} + g\frac{\partial \Phi}{\partial z} = 0 \tag{2.3}$$

A linear and sinusoidal solution can be mathematically described by the equation:

$$\eta(x, t) = \frac{A}{2}\sin(k_w x - \omega t + \phi) \tag{2.4}$$

where A is the wave amplitude, k_w the wave-number, defined as $k_w = 2\pi/\lambda$, ω the angular frequency, defined as $\omega = 2\pi/T$ and ϕ the phase constant. $\eta(x,t)$ is the function that describes both in time and space the elevation of the wave. More complex phenomena are usually represented using a superposition of multiple sinusoids.

The **celerity** (U) can be approximated by:

$$U = \sqrt{\frac{g\lambda}{2\pi}\tanh\left(\frac{2\pi h}{\lambda}\right)} \tag{2.5}$$

Two main classes of waves can be recognised according to their behaviour:

Shallow-water waves	Deep-water waves
Waves with length longer than 20 water depths	Waves having a length shorter that two time the water depth. $L < 2h$
$\frac{h}{\lambda} > \frac{1}{20}$	$\frac{h}{\lambda} > \frac{1}{2}$
$U = \lim_{\lambda/h \to \infty} U = \sqrt{gh}$	$U = \sqrt{\frac{g\lambda}{2\pi}}$ with $\tanh\left(\frac{2\pi h}{\lambda}\right) \to 1$

Waves between these two categories are called *Intermediate depth waves.*

The **Ursell number (Ur)** is commonly used to distinguish waves for which linear approximation can be used. It is defined as the product between the relative wave height ($\epsilon = A/h$) and the square of the relative wave length ($\gamma = \lambda/h$):

$$\text{Ur} = \epsilon\frac{1}{\gamma^2} = \frac{A}{h}\left(\frac{\lambda}{h}\right)^2 = \frac{A\lambda^2}{h^3} \tag{2.6}$$

For long waves ($\lambda >> h$) with small values of Ur, typically Ur < 100, a linear approximation such as the Airy Model can be used (Ursell, 1953) and shallow water waves belong to this

category. The latter is of interest since it includes tsunamis and bores. These waves can be described by a single sinusoid and the celerity depends only on water depth (h), and it is no longer a function of the period and the wavelength (λ). For shallow-water waves the energy between two sections is conserved and a relationship between the change in water depth and water height can be determined using Green's law (Green, 1837), where W_1 and W_1 are some typical width at the two sections:

$$\frac{A_2}{A_1} = \sqrt{\frac{W_1}{W_2}} \sqrt[4]{\frac{h_1}{h_2}} \tag{2.7}$$

This formula allows the prediction of the wave height when approaching the shore. When the wave height becomes too high, the wave breaks over itself, orginating a broken bore. Through this process, called *shoaling*, some of the energy is dissipated (Li and Raichlen, 2003).

2.2 Long-wave generation techniques

As presented in Chapter 1, in nature there exist a wide range of physical phenomena resulting into flows with similar hazardous consequences on the built environment. This diversity and heterogeneity is reflected in the several generation techniques currently used to reproduce these flows in a laboratory environment, including:

- Piston-type generators
- Landslide-generators
- Pump-driven generators
- Gate closure
- Vertical releases
- Dam-break gates

The main driving principles of these techniques are schematized in Figure 2.2 and briefly described in the following sections. A comprehensive literature review of these techniques was presented by Liu (2008). A non-exhaustive list of major techniques used in selected previous studies, along with the resulting wave heights and channel dimensions is presented in Table 2.1.

2.2.1 Piston-type generators

In coastal engineering the use of piston-type, automatic, wave generators is widely used to generate solitary waves. This technique transfers energy to the water by horizontally moving a wave paddle (Dean and Dalrymple, 1991), as shown in Figure 2.2a. Solitary waves of different amplitude are generated by varying the speed and the extension of the wave paddle. The transition between solitary waves and overland flow was addressed by Fuchs and Hager (2015). In the past solitary waves produced with wave paddles were used to tsunamis-like flows,

(a) Piston-type generator

(b) Landslide generator

(c) Vertical release

(d) Dam-break gate

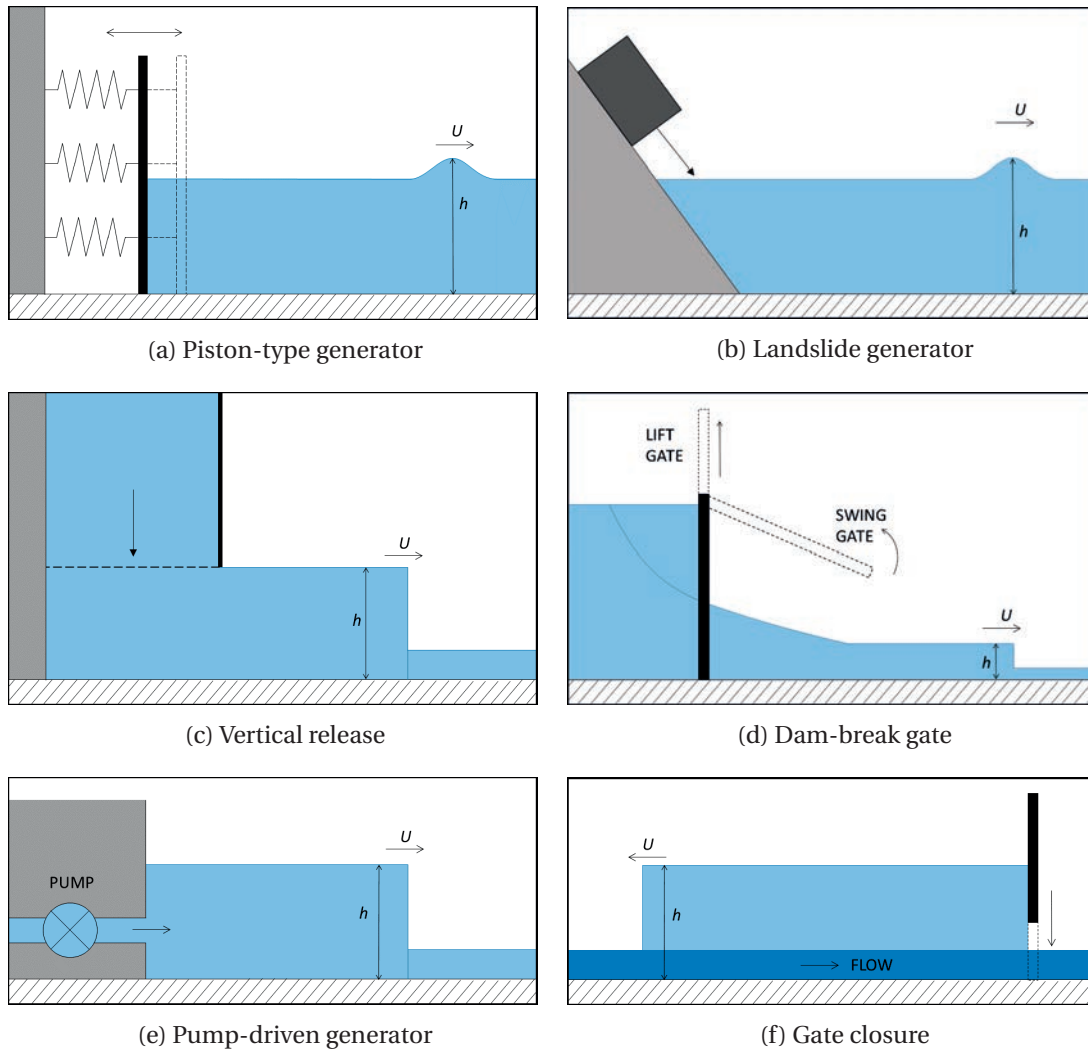(e) Pump-driven generator

(f) Gate closure

Figure 2.2 – Wave generation techniques

including Ramsden (1993), Van de Lindt et al. (2009), Wilson et al. (2009), Chen et al. (2012) and Fuchs (2013) among others. Nevertheless, Madsen et al. (2008) criticized this approach because of the short wave length and period when compared with real tsunami waves. This is known in literature as the *solitary wave paradigm* and the use of solitary wave leads to some errors in the order of a magnitude in both temporal and spatial duration. Therefore, for tsunami-like flows, waves with longer durations are necessary.

2.2.2 Landslide generators

Landslide-generated waves are reproduced through the sudden drop of a solid, granular, or liquid body into the water, producing a wave travelling in the opposite direction, as shown in Figure 2.2b. This technique is particularly suitable to reproduce impulse waves, generated in nature by a landslide falling inside a lake or a reservoir. A landslide generator can function

either manually, by dropping a solid, rectangular block (100 kg) inside the water (Thusyanthan and Madabhushi, 2008), or using a more sophisticated mechanism such as a pneumatic landslide generator (Fritz, 2002; Fuchs et al., 2010). The drop of a granular body inside the reservoir was previously used by Huber (1980), Fritz (2002) and Evers and Hager (2015) among others. Hinwood and Mackenzie (2011) used a inclined piston-type generator, pointing out some similarities between landslide and piston-type generators.

2.2.3 Pump-driven generators

Goseberg et al. (2013) introduced the concept of pump-driven long waves generation technique. This represents an alternative approach to generate single sinusoidal, prolonged solitary and N-waves characterised by long wave periods. A schematic representation of this technique is presented in Figure 2.2e. Pump-driven generators operate on the basis of accelerated and decelerated water volumes in both positive and negative directions, in a closed-circuit wave flume. This technique is particularly suitable to reproduce tsunami-like flows with longer wave periods.

2.2.4 Gate closure

A propagating surge or bore can also be generated by the sudden closure of a downstream gate (Koch and Chanson, 2009; Leng and Chanson, 2015, 2017a,b), as shown in Figure 2.2f. By obstructing the initial steady-state flow, the gate produces a positive surge/bore which propagates in the upstream direction. This technique is particularly appropriate to reproduce positive surges and bores in rivers and man-made channels, as well as tidal bores.

2.2.5 Vertical release

A different approach was introduced by Chanson et al. (1999, 2002, 2003). Both surges and bores were generated by the sudden vertical drop of a known amount of water through a rectangular, sharp-crested orifice into a lower channel (Figure 2.3a). High splashes were observed and great velocities found in the first part of the channel. After an initial development, time velocities were similar to the ones given by the formula for rough surfaces presented by Whitham (1955). Further studies were carried out with an improved facility using a funnel-like structure to avoid air entrainment and splashes (Figure 2.3b).

An improvement of this set-up was used by Meile (2007) and Meile et al. (2011, 2013) to simulate unsteady-flows in rivers subject to hydro-peaking. The use of a combination of multiple pipes with various diameters allowed the reproduction of a wider spectrum of waves with different properties. In the coastal engineering domain, a sudden release of water through a controlled gate was used by Lukkunaprasit et al. (2009a,b) to simulate tsunami flows similar to those observed in Kamala (Phuket, Thailand) during the 2004 Indian ocean event. In addition, Rossetto et al. (2011) used an upward pneumatic wave generator to produce a

vertical displacement of water through a low pressure head pump. The stored volume was then released into the channel, generating waves with long periods, led either by a crest or a trough, as shown in Figure 2.4. Nowadays, some of the newest large-scale facilities apply similar concepts to reproduce tsunami-like waves with controlled long-period waves using pneumatic Tsunami Simulators (Allsop et al., 2014; Chandler et al., 2016; Foster et al., 2017).
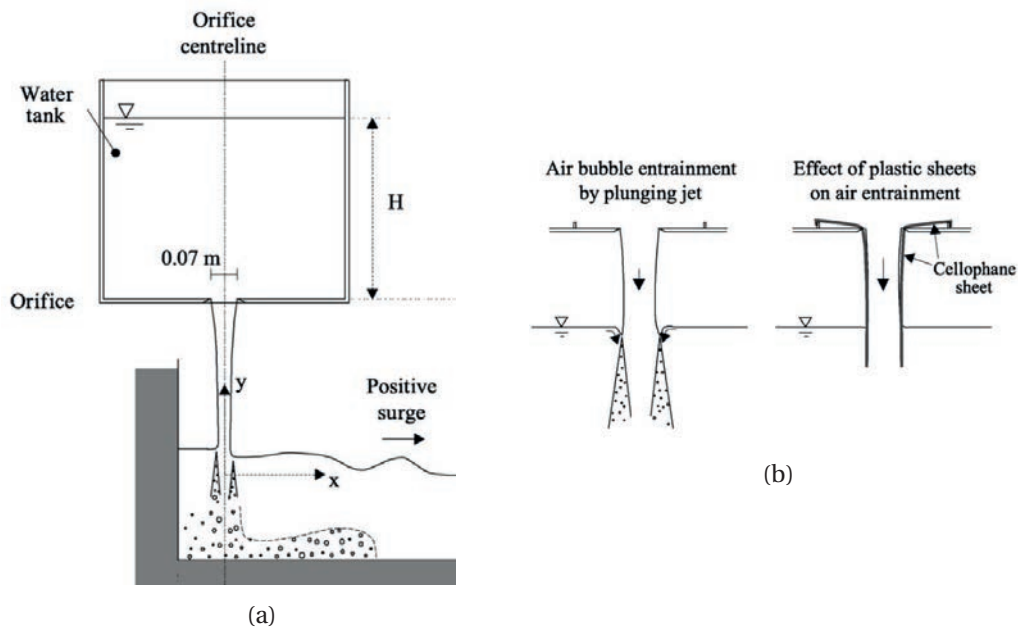

Figure 2.3 – Experimental set up used by Chanson et al. (2002) without (a) and with funnel (b) to reproduce waves with a vertical release technique
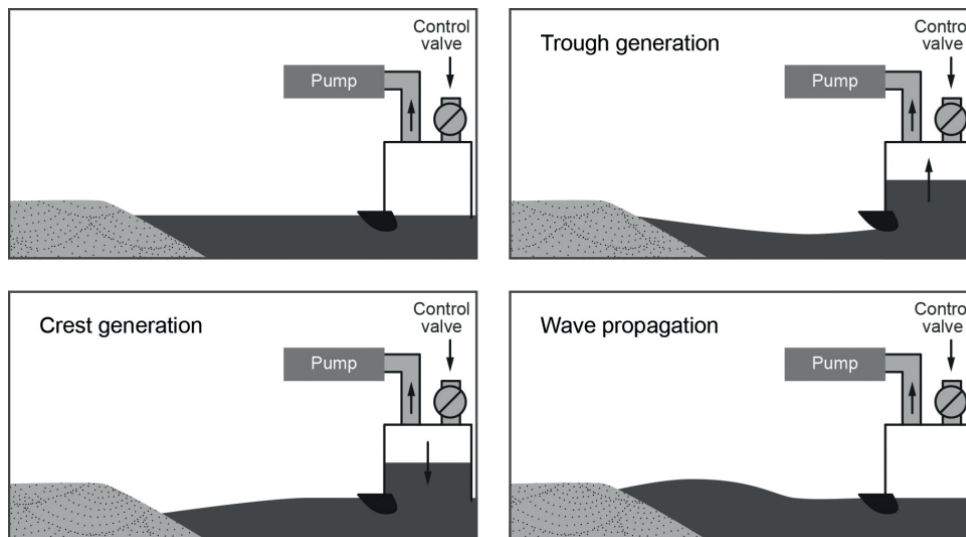
Figure 2.4 – Basic principals of the Tsunami Pneumatic Generator through a vertical release technique (Chandler et al., 2016)

Author	Technique	Wave [cm]	Channel size [m]
Cross (1967)	Dam break (lift gate)	$d_0 = 36$ $h = 6.70$	$L = 6.8$ $W = 0.15$
Ramsden and Raichlen (1990)	Tilting wave tank (solitary waves)	$4.7 < h < 20.2$	$L = 40.0$ $W = 1.1$
Ramsden (1993, 1996)	Tilting wave tank (solitary waves)	$h_{max} = 17.86$	$L = 36.6$ $W = 0.4$
	Pneumatic gate (dry bed surges)	$15.28 < d_0 < 50.92$	
	Pneumatic gate (ondular bores)	$22.88 < d_0 < 64.64$ $13.45 < h < 14.28$	
	Pneumatic gate (wet bed bores)	$25.99 < d_0 < 48.01$ $0.28 < h < 12.69$	
Lauber and Hager (1998)	Dam-break (lift gate)	$15 < d_0 < 60$	$L = 14.0$ $W = 0.5$
Chanson et al. (1999, 2002, 2003)	Vertical release	$H_R = 207$	$L = 12.8$, $W = 0.8$
Fritz (2002) Fritz et al. (2004)	Pneumatic landslide generator (45°)	$h < 68$	$L = 11.0$ $W = 0.5$
Meile (2007) Meile et al. (2011)	Vertical release	$H_R = 207$ $h = 10$	$L = 38.3$ $W = 0.5$
Thusyanthan and Madabhushi (2008)	Drop of a rectangular block (110kg)	$h = 10$	$L = 4.5$ $W = 1.0$
Van de Lindt et al. (2009) Wilson et al. (2009)	Tsunami wave basin (Oregon State University)	$h = 10 - 60$	$L = 32.5$
Lukkunaprasit et al. (2009a,b)	Vertical release	$h = 4, 6$ and 8	$L = 40.0$ $W = 1.0$
Fujima et al. (2009)	Piston-type generator	$h = 10, 15$ and 20	$L = 11.0$ $W = 5.9$
Arnason et al. (2009)	Dam break (lift gate)	$10 < d_0 < 30$ $5 < h < 10$	$L = 16.6$ $W = 0.6$
Fuchs et al. (2010)	Pneumatic landslide generator	$h_{max} = 11.6, 16.8$ and 18.5	$L = 6.5$ $W = 0.5$
Nouri et al. (2010) Al-Faesly et al. (2012)	Dam break (swing gate)	$d_0 = 50, 75, 85$ 85 and 100	$L = 10.6$ $W = 2.7$
Hinwood and Mackenzie (2011)	Inclined piston-type	$h < 60$	$L = 40.0$ $W = 1.0$
Kisacik et al. (2012)	Wave paddle	$3.5 < h < 18.5$	$L = 22.5$
Rossetto et al. (2011)	Pneumatic vertical release generator	$2.7 < h < 12.0$	$L = 28.9$ $W = 1.2$
Chen et al. (2012)	Piston-type generator	$h = 6$	$L = 32$ $W = 0.7$
Goseberg et al. (2013)	Pump-driven generator	$3.1 < h < 10$	$L = 19.0$ $W = 1.0$
Shafiei et al. (2016)	Dam break (lift gate)	$40 < d_0 < 60$ $14 < h < 21$	$L = 14.0$ $W = 1.2$
Chandler et al. (2016) Foster et al. (2017)	Pneumatic vertical release generator	$3.6 < h < 7.5$	$L = 100.0$ $W = 1.8$
Goseberg et al. (2017)	Dam break (swing gate)	$20 < d_0 < 40$	$L = 8.4$ $W = 1.5$
Present study	Vertical release	$40 < d_0 < 82$ $13 < h < 25$	$L = 15.5$ $W = 1.4$

Table 2.1 – Wave production techniques for selected studies in literature

2.2.6 Dam-break gates

Dry bed surges and wet bed bores are commonly reproduced using dam-break gates. The sudden opening of a vertical gate, and the subsequent release of an impounded volume, results into an unsteady flow propagating in the downstream channel. This approach is based on the theory of Ritter (1892) and further explanations are given in Section 2.3. A schematic representation of the process is presented in Figure 2.2d. This technique was used by several authors, including Cross (1967); Yeh et al. (1989); Lauber and Hager (1998); Arnason et al. (2009); Nistor et al. (2009); O'Donoghue et al. (2010); Al-Faesly et al. (2012); Duricic et al. (2013); Shafiei et al. (2016); Goseberg et al. (2017). Currently, the use of dam-break waves is considered a more appropriate method to reproduce inundations generated by tsunamis and impulse waves (Chanson, 2005b, 2006).

The sudden opening of the gate can be achieved through vertical lift gates (Lauber and Hager, 1998) or swing gates (Goseberg et al., 2017). The minimal opening velocity of a vertically-moving gate, was proposed by Lauber and Hager (1998) :

$$t\sqrt{\frac{g}{d_0}} = \sqrt{2} \tag{2.8}$$

Goseberg et al. (2017) pointed out that the construction of vertical lifts becomes less economical for flumes with larger widths. For these, rapidly-swinging gate mechanisms were found to me more appropriate to initiate the dam break wave.

2.3 Physics of dam-break waves

The dam-break is a unsteady phenomenon that was widely studied by many authors, including Ritter (1892), Whitham (1955), Stoker (1957) Hunt (1982), Lauber and Hager (1998) and Chanson (2005a). The latter also described tsunamis as very similar to dam-break waves. The propagation of a wave generated from the sudden removal of a vertical gate is an unsteady phenomenon described by the equations presented by St. Venant (1871). For this, the system can be described at any point and any time using two main variables: velocity (v) and flow depth (h).

$$\frac{\partial v}{\partial t} + u\frac{\partial v}{\partial x} = -g\frac{\partial h}{\partial x} \tag{2.9a}$$

$$\frac{\partial h}{\partial t} + \frac{\partial vh}{\partial x} = 0 \tag{2.9b}$$

These equations, known as the St.Venant equations, are non-linear and thus can not be solved analytically. A mathematical technique such as the method of characteristics must therefore be used to solve them.

The main hydrodynamic properties of the propagating wave are affected by the dry or wet

bed conditions of the channel. The difference in behaviour between dry and wet surfaces was shown experimentally by Ramsden (1993), Lauber and Hager (1998) and Nouri et al. (2010), among others. A wave propagating on dry bed is commonly called a *surge*, whereas, due to its turbulent and aerated appearance, a wave on wet bed is termed a *bore*. An example in nature of such difference can be observed in Figure 1.4b, which illustrates the case of a tidal bore propagating upstream the Garonne River in France on both dry (left) and wet (right) bed conditions.

For this reason, a distinction between the dam-break wave propagating on dry and wet bed has to be made:

1. wave propagating on dry bed → **Dry bed surge**
2. wave propagating on wet bed → **Wet bed bore**

Thus the scenario on dry bed is presented in Section 2.3.1 and the one on wet bed in Section 2.3.2

2.3.1 Dry bed surges

A solution of the St. Venant equations (Eq. 2.9) in one direction, for the dry bed condition was presented by Ritter (1892) using the method of characteristics. This theory is based on the following assumptions:

1. Infinite upstream reservoir
2. Ideal fluid
3. Wave is propagating on horizontal, frictionless channel.

The sudden removal of the vertical gate produces a dam break wave in the downstream direction (positive characteristic) and a negative wave propagating in the upstream direction (negative characteristic). For a given reservoir depth d_0, expressions for water depth h and flow velocity v at location x and time t were found:

$$h = \frac{1}{9g} \left[2\sqrt{gd_0} - \frac{x}{t} \right]^2 \tag{2.10a}$$

$$v = \frac{2}{3} \left[\sqrt{gd_0} + \frac{x}{t} \right] \tag{2.10b}$$

A schematic representation of the propagating waves is presented in Figure 2.5.

For $x = 0$ a constant water height h and discharge Q_0 are found, as shown in Eqs. 2.11

$$h(x = 0) = \frac{4}{9} d_0 \tag{2.11a}$$

$$Q_0(x = 0) = \frac{8}{27} \sqrt{gd_0^3} \tag{2.11b}$$

21
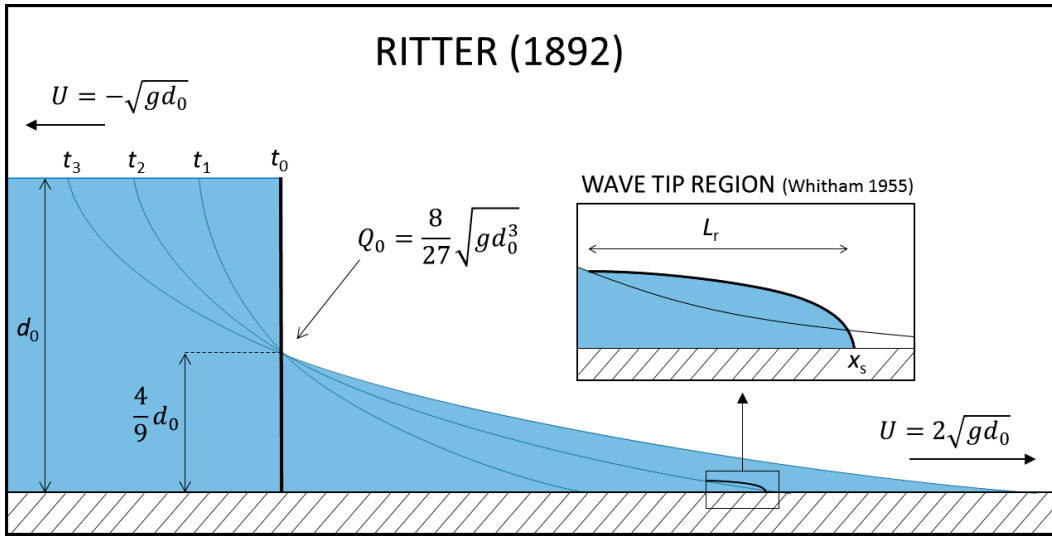
Figure 2.5 – Dam-break wave theory on dry bed [based on Ritter (1892) and Whitham (1955)]

The theory developed by Ritter (1892) (ideal fluid flow, horizontal channel and semi-infinite reservoir) is quite restrictive and hardly applicable to reality. Therefore, there exist other theories removing some of the key assumptions, including: **Dressler (1952)** and **Whitham (1955)** (real fluid on a horizontal plane with semi-infinite reservoir) and **Hunt (1982)** (real fluid on a slope).

The analytical solution proposed by Whitham (1955) added friction to the propagating channel. According to this theory, in the dam break wave two main parts can be distinguished: (1) a main body and (2) a wave tip/edge region. In the main body, the Ritter theory can be applied and the water behaves like an ideal fluid, whereas the wave tip region is dominated by friction with negligible inertia terms, resulting into a rounded shape with lower velocities. Whitham (1955) developed an analytical solution based upon the Pohlhausen technique and the integral treatment of the boundary layer (Chanson, 2005a). This solution made the assumption that in the wave tip/edge region the velocity distribution was constant. The resulting equation is presented in Eq. 2.12.

$$\frac{x - x_s}{h_0} = -\frac{f}{8} \cdot \frac{U^2}{g \cdot h_0} \cdot \left(\frac{g}{\partial U / \partial t}\right)^2 \cdot \left[\ln\left(1 + \frac{8}{f} \cdot \frac{h/h_0}{U^2/g h_0} \cdot \frac{\partial U/\partial t}{g}\right) - \frac{8}{f} \cdot \frac{h/h_0}{U^2/g h_0} \cdot \frac{\partial U/\partial t}{g}\right] \quad (2.12)$$

where x_s is the position of the front, d_0 is the initial reservoir depth, f is the friction factor, U is the tip/edge celerity and while $\partial U/\partial t$ is the deceleration of the wave along the channel.

According to Freeman and LéMehauté (1964) the dynamic wave equation in the wave tip region is reduced into:

$$\frac{\partial h}{\partial x} + \frac{f}{8} \cdot \frac{U^2}{g d_0} = 0 \quad (2.13)$$

and its integration leads to an analytical expression for the shape front (Chanson, 2006, 2009)

$$\frac{h}{d_0} = \sqrt{\frac{f}{4} \cdot \left(\frac{U}{\sqrt{g\,d_0}}\right)^2 \cdot \left(\frac{x - x_s}{d_0}\right)} \tag{2.14}$$

leading to the following set of equations to characterize the free surface profile for a dam break wave propagating on an horizontal channel with bed friction f:

$$\frac{h}{d_0} = \frac{1}{9} \cdot \left(2 - \frac{x}{t \cdot \sqrt{g\,d_0}}\right)^2 \qquad -\sqrt{\frac{g}{d_0}} \cdot t \le \frac{x}{d_0} \le \left(\frac{3}{2} \cdot \frac{U}{\sqrt{g\,d_0}} - 1\right) \cdot \sqrt{\frac{g}{d_0}} \cdot t \tag{2.15a}$$

$$\frac{h}{d_0} = \sqrt{\frac{f}{4} \cdot \left(\frac{U}{\sqrt{g\,d_0}}\right)^2 \cdot \left(\frac{x - x_s}{d_0}\right)} \qquad \left(\frac{3}{2} \cdot \frac{U}{\sqrt{g\,d_0}} - 1\right) \le \frac{x}{d_0} \le \frac{x_s}{d_0} \tag{2.15b}$$

Chanson (2006) also compared the validity of Eqs. 2.15 with field observation in Banda Aceh during the Indian ocean tsunami (26 December 2004). The good agreement observed in Figure 2.6, indicated that Eq. 2.15 is suitable to represent the front shape of tsunamis flows propagating inland.
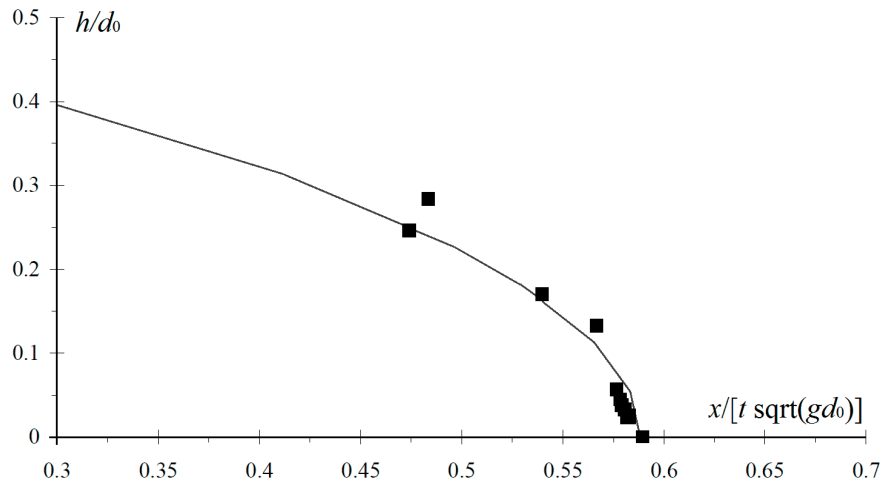
Figure 2.6 – Comparison between Eq. 2.15 and the field data obtained from the 2004 Indian Ocean tsunami in Banda Aceh [adapted from Chanson (2006)].

2.3.2 Wet bed bores

A dam-break wave propagating on a wet channel with an initial still water depth h_0 has a different behaviour if compared to the dry bed scenario presented in Section 2.3.1. Their properties are best described by the theory presented by Stoker (1957) for an infinite reservoir and water initially at rest ($v = 0$) on both sides of the dam. This phenomenon is characterised by the propagation of a negative surge in the upstream direction and an aerated bore in the downstream direction, as shown in Figure 2.7. The temporal evolution of a dam-break bore propagating over a wet bed can be divided into 5 main regions (downstream to up-stream): (0) the initial still water depth h_0; (1) the turbulent bore front; (2) a "*plateau*", *i.e.* a region with almost constant water height h_2; (3) a far-back region where the Ritter (1892) theory for a surge propagating on dry bed can be applied, and (4) the upstream reservoir where $h = d_0$.

Stoker (1957) showed that for values of $h_0/d_0 < 0.1384$, the water depth h, the velocity v and the discharge Q_0 were independent of the initial still water depth h_0. Therefore, Eqs. 2.11 derived for the Ritter (1892) theory at $x = 0$ can be applied to zone (3). For values of $h_0/d_0 > 0.1384$, all main parameters become a function of h_0.

Zone (2) is characterized by a constant water depth (h_2) called *plateau height*. The exact value of h_2, observed in Figure 2.7, can be obtained graphically from Stoker (1957) or numerically with the numerical approximation proposed by Chanson et al. (2000) in Eq. 2.16 as a function of h_0/d_0.

$$\frac{h_2}{d_0} = 0.932 \left(\frac{h_0}{d_0}\right)^{0.371} \tag{2.16}$$
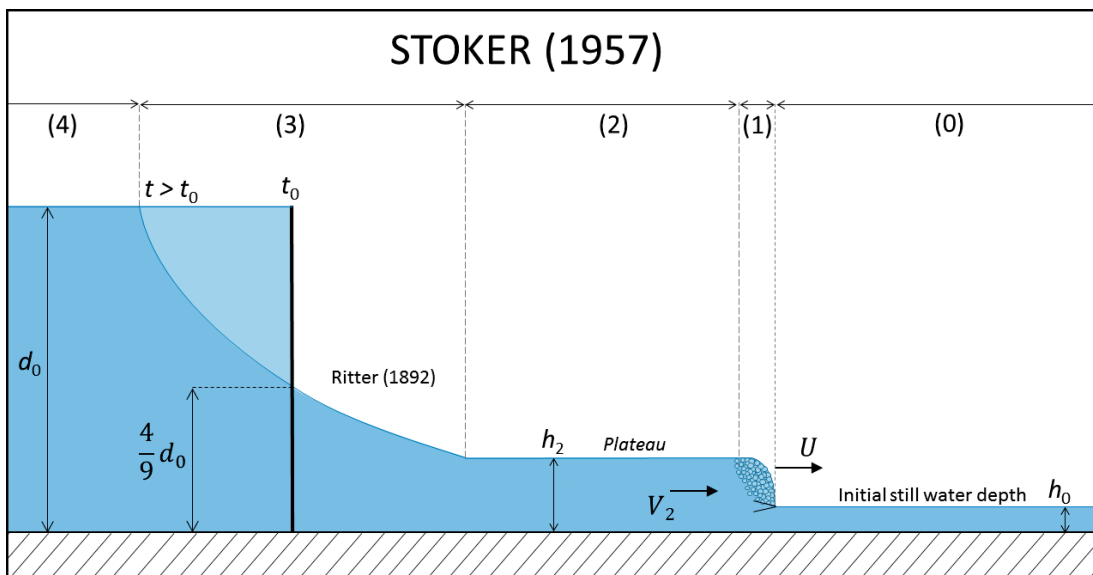
Figure 2.7 – Dam-break wave theory on wet bed [based on Ritter (1892) and Stoker (1957)]

Both Continuity and Momentum equations can be applied to the propagating wave, resulting into the following expressions:

$$h_0 \cdot U = h_2 \cdot (U - V_2) \tag{2.17a}$$

$$h_2 \cdot (U - V_2)^2 - h_0 \cdot U^2 = \frac{1}{2} g h_0^2 - \frac{1}{2} g h_2^2 \tag{2.17b}$$

The front region in zone (1) visually appears as an aerated and recirculating roller, similar to a translating hydraulic jump (Figure 4.7). According to Yeh and Mok (1990) the roller was formed by the flow separation initiated at the front toe resulting from the streamline divergence caused by the sudden raise in water depth. In the roller, a "*generation-advection cycle*" was observed, suggesting that eddies formed inside the roller were later advected in the flow, where a turbulence stretching in the slanting vertical direction was detected. Air is entrained behind the bore front for a length of L_r, whereas further behind mainly clear water can be observed. For wet bed bores the shape of the front can be predicted using the following equation:

$$\frac{h - h_0}{h_2 - h_0} = \left(\frac{x - x_s}{L_r} \right)^N \tag{2.18}$$

where x_s is the position of the wave front and L_r the length of the roller. Chanson (2011) proposed an exponent value $N = 0.441$ and Wang and Chanson (2015) $N = 0.540$ for hydraulic jumps.

2.3.3 Front celerity

In wave hydrodynamics, the computation of the front celerity U is fundamental to estimate the forces induced by the wave on the buildings. Nevertheless, Nistor et al. (2009) showed that the highest uncertainty in the computation of the hydrodynamic force (drag) derives from the estimation of the wave celerity, as there is no agreement in literature on one single value for the velocity of a tsunami approaching the shore. For this reason, the next sections focus on the most common techniques used to estimate the front celerity for both dry bed surges and wet bed bores.

Dry bed surge

The St. Venant equations (Eq. 2.9) can be solved using the theory of Ritter (1892) presented in Section 2.3.1. This predicts a front celerity of $U = 2\sqrt{g d_0}$ for a horizontal frictionless channel. This theoretical upper limit also coincides with the value suggested by the Federal Emergency Management Agency (FEMA) 55. Lauber and Hager (1998) showed that, for small times, the maximum wave velocity is located at the positive wave front and that a linear deceleration until the negative wave front. Furthermore, the location of maximum velocity and maximum flow depth do not coincide. The front celerity of a surge propagating on dry bed is commonly

Study	Formula	Note
CCH (2000)	$U = h$	Lower limit
FEMA55 (2000)	$U = 2\sqrt{gh}$	Upper limit ($\alpha = 2$)
Iizuka and Matsutomi (2000)	$U = 1.1\sqrt{gh}$	$\alpha = 1.1$
Kirkoz (1983)	$U = \sqrt{2gh}$	$\alpha = \sqrt{2}$
Fukui et al. (1963)	$U = 1.83\sqrt{gh}$	$\alpha = 1.83$
Bryant (2001)	$U = 1.67h^{0.7}$	
Matsutomi and Okamoto (2010)	$U = 0.66\sqrt{gh}$	$\alpha = 0.66$
Shafiei et al. (2016)	$U = 1.7\sqrt{gh}$	$\alpha = 1.7$

Table 2.2 – Celerity coefficient α in Eq.2.19 for dry bed surges.

presented in the form

$$U = \alpha \cdot \sqrt{gd_0} \tag{2.19}$$

where α is a velocity coefficient whose value is coved by high incertitudes. The most common values found in literature are summarised in Table 2.2. Nevertheless the coefficient α is a function of the friction factor f, as shown by both Dressler (1952) and Whitham (1955). More information concerning the influence of bed roughness on the propagating surge are presented in Apprendix B.4.

Wet bed bores

For wet bed bores the front celerity can be numerically obtained as a function of h_0/d_0 from the momentum equation in Eq. 2.20 presented by Stoker (1957):

$$\frac{U}{gd_0} = \sqrt{\frac{1}{8} \cdot \left[\left(2\frac{h_2}{h_0} + 1\right)^2 - 1\right]} \tag{2.20}$$

and with the approximation of Montes (1998), presented by Chanson (2004) in Eq. 2.21:

$$\frac{U}{\sqrt{gd_0}} = \frac{0.63545 + 0.3286\left(\frac{h_0}{d_0}\right)^{0.65167}}{0.00251 + \left(\frac{h_0}{d_0}\right)^{0.65167}} \tag{2.21}$$

where d_0 is the impoundment depth, h_0 is the initial still water depth and h_2 is the plateau height obtained from Eq. 2.16. Behind the bore front, in the plateau region h_2 (zone 2), a velocity $V_2 < U$ is observed. This value can be obtained through a rearrangement of the Continuity equation (Eq. 2.17):

$$V_2 = U \cdot \left(\frac{h_2 - h_0}{h_2}\right) \tag{2.22}$$

2.3.4 Velocity profiles

In the analytical solution that led to Eq. 2.12, Whitham (1955) made the assumption that in the wave tip/edge region the velocity distribution was constant over the entire wave depth. Lauber and Hager (1998) performed some Particle Image Velocimetry (PIV) tests on dam-break waves on horizontal bed, showing the existence of a thin boundary layer.

Arnason (2005) measured the velocity field of a dam-break wave impacting against a vertical obstacle in a horizontal two-dimensional plane using a Digital Particle Image Velocimeter (DPIV). In addition, Laser Doppler Velocimeter (LDV) were used to acquire velocity profiles in bores of different sizes. This showed a deceleration of the average velocity behind the wave front for large bores.

The quasi-instantaneous velocity profile for passing bore fronts was obtained by Meile et al. (2008) through some Acoustic Doppler Velocimeters (ADV) measurements. (Figure 2.8). Note that 2.8 showed that before and after the passage of the wave, the flow had a logarithmic profile, thus indicating a quasi-uniform flow distribution. During this time, the flow showed a *"two-layer-type"* velocity profile, in which the lower layer accelerated to comply with the different mean velocities before and after the wave front (Figure 2.8, profile 3). It was estimated that it took less than 0.2 s for the quasi-uniform flow to be re-established.
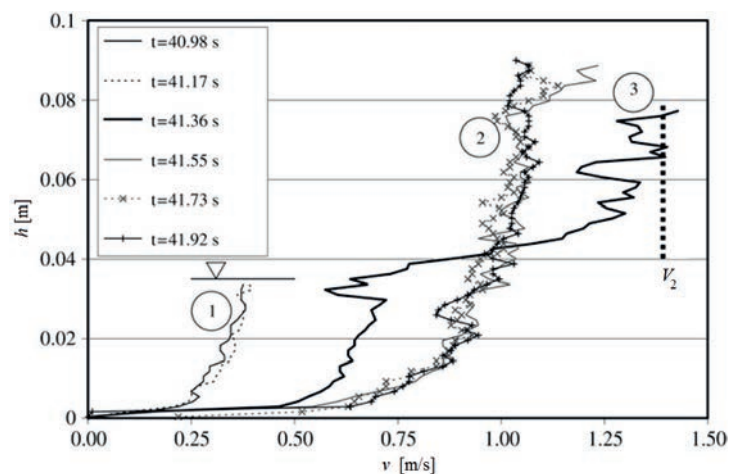
Figure 2.8 – Quasi-instantaneous velocity profiles measured before (1), during (3) and after (2) passage of the bore front (adapted from Meile et al. (2008))

Most recently, Leng and Chanson (2017a,b) performed studies on the velocity profiles on turbulent bores and positive surges comparing three measurement techniques: Vectrino II Profiler, Nortek™ acoustic Doppler velocimeter (ADV) Vectrino+ and Prandtl Pitot tubes. Results showed close agreement between all instruments, with instantaneous velocity fluctuations of the same order of magnitude were recorded. All velocity measurements showed a strong deceleration during the passage of the bore front, as well as large velocity fluctuations for the three velocity components at all elevations.

2.4 Frontal impact on impervious buildings

The hydrodynamic impact of a wave against a structure is a complex phenomenon and the resulting force is difficult to evaluate. Inundation depth, flow velocity and direction are key parameters in the estimation process and they are all covered by a high level of incertitude. In literature no common agreement is found on this subject (Dean and Dalrymple, 1991) and several empirical formulae were proposed. A summary of major previous studies focusing on impact forces is presented in Table 2.3 and presented hereafter in chronological order. Despite the work performed to date, the number of empirical or semi-empirical formulas available and their significant scattering suggest that the behaviour of structures under such extreme loading remains challenging to describe and difficult to properly quantify.

Reference	Wave type	Wave height [m]	Wave celerity [m/s]	Building geometry [m]	Block ratio β	Force frequency [kHz]
Ramsden (1996)	Solitary wave Dam-break	0.05-0.2	0.7-1.3	Wall W=1.1 H_B=0.6	1.00	1.0
Arnason et al. (2009)	Dam-break	0.05-0.1	0.9-1.8	B=0.12 H_B=0.45	5.00	0.3
Lukkunaprasit et al. (2009)	Vertical release	0.04-0.08	1.4-2.5	B=0.15 H_B=0.45	6.67	0.5
Nouri et al. (2010)	Dam-break	0.5-0.85	2.6-4.6	B=0.20 H_B=0.60	6.50	1.0
Santo and Robertson (2010)	Solitary wave	0.12-1.28	2.6-6.8	Wall W=2.1 B=0.05 B=0.15 B=0.30 H_B=0.61	1.00 42.6 14.2 7.10	1.0
Al-Faesly et al. (2012)	Dam-break	0.25-0.45	2.6-5.1	B=0.30 H_B=1.40	4.33	1.0
Linton et al. (2012)	Solitary wave	0.1-1.04	2.3-4.9	Wall W=3.7 H_B=4.57	1.00	1.0
Robertson et al. (2013)	Solitary wave	0.23-1.28	2.6-6.8	Wall W=3.7 H_B=1.83	1.00	1.0
Rahman et al. (2014)	Dam-break	0.01-0.03	-	Wall W=0.6 H_B=0.04,0.08	1.00	-
Shafiei et al. (2016)	Dam-break	0.14-0.21	2.0-2.4	B=0.30 H_B=0.6	4.00	1.0
Foster et al. (2017)	Pneumatic generator	0.03-0.1	1.5-4.6	B=0.18 B=1.08 B=1.44 H_B=0.2	10.0 1.67 1.25	Not specified
Present study	Vertical release	0.13-0.25	1.9-3.7	B=0.30 H_B=0.6	4.67	1.0

Table 2.3 – Main parameters of selected studies involving wave/dam-break-induced loading on impervious structures with side B and height H_B, installed in a channel with width W.

The most generic case is represented by Eq. 2.23, proposed by Morison et al. (1950). This equation includes both inertia and drag forces:

$$F = F_{\text{I}} + F_{\text{D}} = \rho C_{\text{m}} \forall \frac{\mathrm{d}v}{\mathrm{d}t} + \frac{1}{2}\rho C_{\text{D}} B h v^2 \tag{2.23}$$

where: F_{I} is the inertia force and F_{D} the hydrodynamic (drag) force; ρ the water density, C_{m} the inertia coefficient, $\forall$ the volume, $\mathrm{d}v/\mathrm{d}t$ the flow acceleration, C_{D} the drag coefficient, B the width of the obstacle, h the water depth and v the velocity of the flow.

Since tsunamis and dam-break waves have really long wave-periods, the inertia term is considered important only at the tip of the bore when impacting against a structure; this component is usually called *surge force* (F_{S}) (Yeh, 2007).

2.4.1 Hydrodynamic force

The hydrodynamic force (or drag force) is the resistance force that any obstacle, including buildings, imposes to a moving fluid. This force is conventionally described using a drag coefficient (C_{D}). The hydrodynamic force (F_{D}) can be calculated assuming independence from Mach number (Ma<<1, and therefore $v << v_{\text{sound}}$) :

$$F_D = \frac{1}{2}C_{\text{D}}\rho B h v^2 \tag{2.24}$$

The drag force resulting from the impact of moving fluid against a solid obstacle is described by Blevins (1984) for steady flow conditions. The drag coefficient depends on the shape of the obstacle, the blockage ratio (*i.e.* B/W, where B is the building side and W the channel width), the ratio between flow depth and obstacle side (*i.e.* h/B) and the Froude number of the impinging flow (Qi et al., 2014) . The dependence of C_{D} on the Reynolds number is commonly assumed to be weak because of the turbulent nature of most open-channel flows, both in the laboratory and in the field. The drag coefficient is typically defined for low Froude numbers (sub-critical regimes) with similar upstream and downstream flow depths. Furthermore, most values of the drag coefficient were derived from the loss of momentum flux through flow depths measurements (Henderson, 1966). More information on the drag coefficient can be found in Appendix C.

For squared obstacles, values of $C_{\text{D}} \approx 2$ are commonly found in literature and design codes.

2.4.2 Impact force

While investigating wave-pile interaction, Snodgrass et al. (1951) pointed out that the force produced by a broken wave (bore) was higher compared to that produced by unbroken waves (surge). Ever since, many authors have given their contribution to the domain and research mostly focused on tsunamis, the most catastrophic and common of all hydrodynamic bores.

Some of the first authors to investigate tsunamis were Fukui et al. (1963) who found that the most influential factor on impulsive pressures is velocity; they suggested that maximum pressure is proportional to the velocity to the power 4.

$$p_{\text{max}} = \frac{1}{2}\frac{\gamma v^4}{g^2 h} \tag{2.25}$$

Although with some scattering, they proved that for vertical walls, the pressure distribution was linear from the base of the wall to 1.5 times the wave height.

Cross (1967) verified the reliability of the force predicted by the momentum equation for a uniform and steady flow. The result is a simple theory to estimate the force exerted by a surge travelling on a dry bed impinging on a vertical wall.

$$F = F_{\text{HS}} + F_{\text{D}} = \frac{1}{2}\rho g B h^2 + \rho b h v^2 \tag{2.26}$$

Ramsden (1996) analysed the forces produced by a translatory turbulent bore against a vertical wall. The force computed from the maximum measured run-up height on the wall, assuming hydrostatic condition, exceeded the maximum measured force. Ramsden (1996) also compared the behaviour of of a turbulent bore over wet bed (offshore structure or second wave) and a dry bed surge (inshore, first wave) with similar celerity. Results showed that the turbulent bore was constantly associated with a higher water depth and with a steeper front, thus resulting into larger run-up heights, higher pressures and forces (Figure 2.9). The propagation velocity of the turbulent bore was similar to the celerity of moving hydraulic jump in still water (Stoker, 1957):

$$\frac{v^2}{gh} = \frac{1}{8}\left[\left(2\frac{A}{h}+3\right)^2 - 1\right] \tag{2.27}$$

where h is the effective water depth and A the maximum wave amplitude. For all scenarios a hydrostatic condition was found after the bore. The following formulas were presented by Ramsden (1993)

$$\frac{F}{F_1} = 1.325 + 0.347\left(\frac{A}{h}\right) + \frac{1}{58.5}\left(\frac{A}{h}\right)^2 + \frac{1}{7160}\left(\frac{A}{h}\right)^3 \tag{2.28a}$$

$$\frac{M}{M_1} = 1.923 + 0.454\left(\frac{A}{h}\right) + \frac{1}{8.21}\left(\frac{A}{h}\right)^2 + \frac{1}{808}\left(\frac{A}{h}\right)^3 \tag{2.28b}$$

where F_1 is the force obtained assuming a linear pressure distribution due to a run-up that is twice the wave amplitude (A):

$$F_1 = \frac{1}{2}\rho g B(2A+h)^2 \tag{2.29}$$

Results showed that the results of Cross (1967) and Ramsden (1993) both overestimated the force by, respectively, 20-50% and 30-40%.
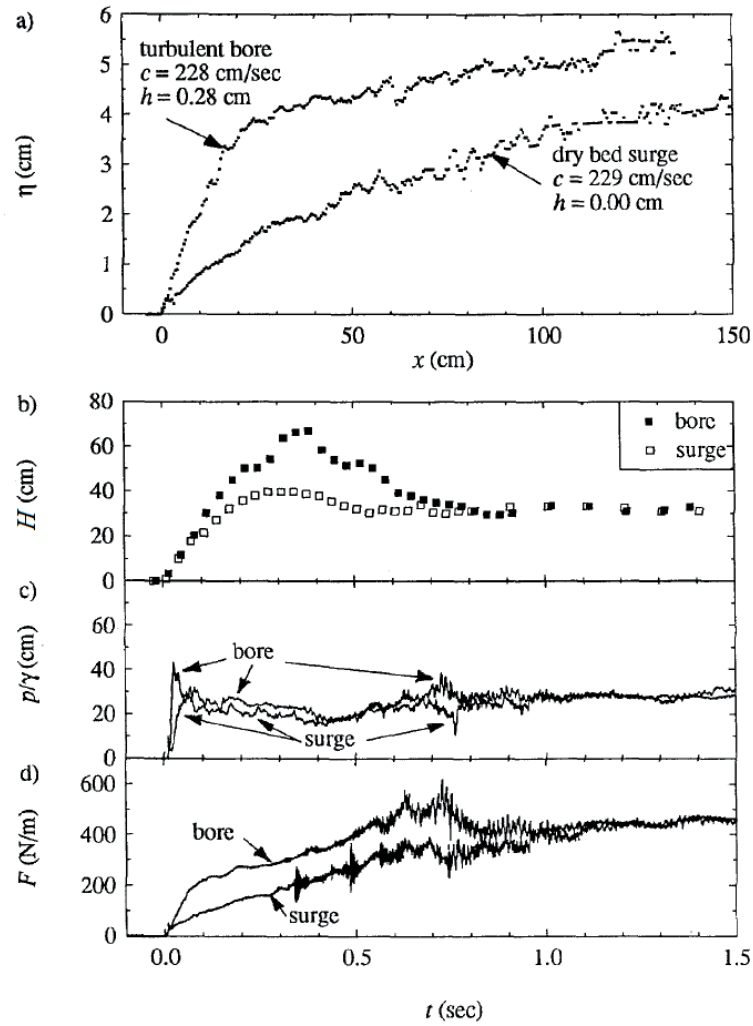
Figure 2.9 – comparison of dry bes surge and wet turbulent bore (a) wave height (η), (b) run-up height (H), (c) pressure (p) and (d) force (F) (Ramsden, 1993)

Asakura et al. (2000) proposed the following formula to estimate the pressure (p) against the structure, where h_{max} represents the maximum inundation depth.

$$p = \rho g B (3 h_{max} - z) \tag{2.30}$$

Its integration gives the formula used by the City and Council of Honolulu (CCH 2000) to quantify the surge force:

$$F_S = \int_0^{3h_{max}} \rho g B (3 h_{max} - z) \, dz = \frac{1}{2} \rho g B (3 h_{max})^2 = 4.5 \rho g B h_{max}^2 \tag{2.31}$$

Okada et al. (2005) proposed a method to evaluate tsunami load (surge force) against structures, making a difference between broken and unbroken waves:

- **Unbroken waves** : the force is given by an hydrostatic pressure with three times the wave height h. The resulting force is therefore 9 times the hydrostatic pressure of the wave.

$$F_S = 9 \cdot \left(\frac{1}{2} \rho g h^2 \right) \tag{2.32}$$

- **Broken waves** : an additional pressure is added over a height that is equal to 0.8h. This pressure has a value of $2.4\rho g h$ at the base. The resulting force is therefore 11 times the hydrostatic pressure of the wave.

$$F_S = 11 \cdot \left(\frac{1}{2} \rho g h^2 \right) \tag{2.33}$$

For both cases if the building is not high enough, the pressure distribution is considered until the end of the structure. This is in agreement with the findings of Nakano (2008) presented in Section 2.4.4

Arnason (2005) tested some free-standing buildings with different geometries and orientation. This study showed that an initial overshot was only observed for rectangular shaped buildings impacted by waves with relatively small height. For cylindrical, rhomboidal structures and large waves, no overshot was observed.

<div align="center">(a)   (b)</div>
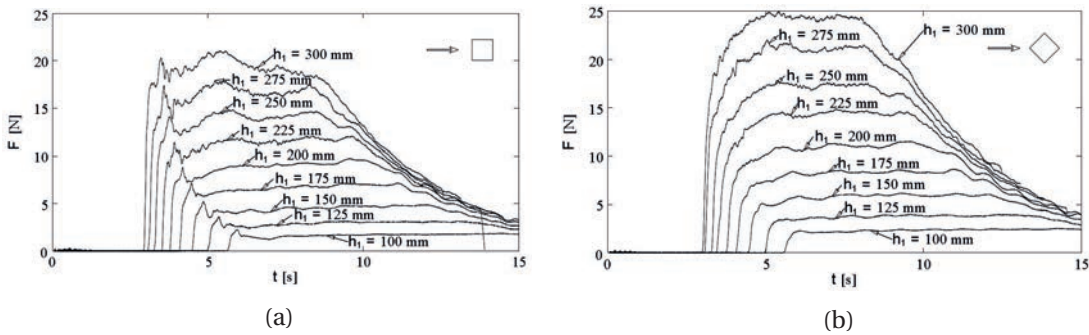
<div align="center">Figure 2.10 – Forces measured for rectangular structures (Arnason, 2005)</div>

As previously discussed, during the impact phase, various components of the total force can be identified, including an initial surge force, hydrodynamic (or drag) and hydrostatic components. Since the process is highly unsteady and rapidly varied, these components are difficult to isolate and estimate. Thus, similarly to Gupta and Goyal (1975), Arnason (2005) and Arnason et al. (2009) used a resistance coefficient C_R, taking into account the surge, hydrostatic and hydrodynamic components. This coefficient is defined as:

$$C_R = \frac{2 \cdot F_x}{\rho B h v^2} \tag{2.34}$$

Eq. 2.34 is similar to the drag coefficient C_D in Eq. 2.24 for the computation of the hydrostatic component. However, C_R is a function of time rather than a constant value.

Dias and Mallikarachchi (2006) consider 3 components of the total force: hydrostatic, hydrodynamic and impact load:

Hydrostatic	**Hydrodynamic**	**Impact Load**
$F_S = \frac{1}{2}\rho g B h^2$	$F_D = \frac{1}{2}C_D\rho B h v^2$	$F_L = \frac{1}{2}C_T\rho B h v^2$

Finally, the total force can reach a maximum upper bound of 18 times the static pressure.

Yeh et al. (2005), on behalf of the Washington State Department of Natural Resources published some guidelines for structures that serve as tsunami vertical evacuation sites. Two years later Prof. H. Yeh published a paper giving specific guidelines on evaluating tsunami forces. Yeh (2007) states that both hydrostatic and buoyant forces can be easily identified once the inundation depth is known, whereas hydrodynamic forces are complicated to determine due to the incertitude linked to the velocities. Yeh (2007) proposed the following method:

- **Hydrodynamic force** $F_D = \frac{1}{2}C_D\rho B(hv^2)_{\max}$, where h and v are respectively the maximum inundation depth and the maximum inundation velocity, that might not take place at the same time. He also suggested the following formula to evaluate hv^2 based on a constant and uniform run-up slope:

$$\frac{(hv^2)_{\max}}{gR^2} = 0.125 - 0.325\frac{z}{R} + 0.11\left(\frac{z}{R}\right)^2 \tag{2.35}$$

  where R is the ground elevation at the maximum tsunami penetration, measured from the initial shoreline, z is the ground elevation of the location of interest.

- **Surge Force** The author questioned the validity of equation 2.31 proposed by CCH, Okada et al. (2005) and Asakura et al. (2000) to evaluate the surge force produced by a tsunami. This formula was derived by adding the hydrostatic force and the change in linear momentum in the impact zone between a surge and a vertical wall, with a steady flow velocity of $2\sqrt{gh}$. In addition the maximum inundation height is hard to define. Since an important overshot is not observed for dry bed surges (Ramsden, 1996; Arnason, 2005), Yeh (2007) suggested to include the surge force inside the hydrodynamic force by using a drag coefficient $C_D = 3$, 1.5 times higher than the usual value.

Koshimura et al. (2009) statistically analysed tsunami damages and showed that for inundation depths $h < 2$ m, 90% of the structures resisted. For $h > 4$ m, 90% of the buildings collapsed.

Fujima et al. (2009) experimentally tested different buildings located at multiple distances from the coastline. They proposed to use the theory suggested by Yeh (2007) with an expression of the drag coefficient as a function of h/D, where D is the distance from the coastline:

$$C_D = 2.0 + 5.4\left(\frac{h}{D}\right) \tag{2.36}$$

The increase of C_D near the coast line might indicate that the inertia term in Morison Equation (Eq. 2.23) is no longer negligible. They conclude that for structures that are located far from the coastline (h/D small), the hydrodynamic formulas should be used. For buildings that are close to the shoreline (h/D large) hydrostatic formulas, such as Eq. 2.31 are more appropriate. Similarly Duricic et al. (2013) used statistical techniques to estimated the mean normalised force produced by an impacting bore against various structures through the definition of a drag coefficient taking into account the shape and the geometry of the obstacle. In addition, for bores, Fujima et al. (2009) also proposed an expression similar to Asakura et al. (2000), but based on the maximum inundation depth:

$$F_{\text{x,D}} = 1.3\rho B(h_2 - h_0)U^2 \tag{2.37}$$

Overseas Coastal Area Development Institute OCADI (2009) of the Ports and Harbours Bureau of Japan, proposed a triangular pressure distribution above the still water level with height $3h$ and base pressure given by $2.2\rho gh$. This base pressure is maintained constant throughout the depth of the still water h_0. The resulting force on the wall is given by :

$$F_{\text{x,D}} = 3.3\rho gB(h_2 - h_0)^2 + 2.2\rho gB(h_2 - h_0) \cdot h_0 \tag{2.38}$$

Nouri et al. (2010) carried out similar investigations on free standing buildings, testing both circular and rectangular shapes. They also tested the effect of constrictions on flow characteristics. The buildings were equipped with both a force plate and pressure sensors distributed along the height of the structure. Results showed the presence of a surge force; the latter was greater than the hydrodynamic force only for higher waves. The induced force was assumed to be a function of the bore front steepness and the pressure sensors showed a non hydrostatic distribution. Similarly, Al-Faesly et al. (2012) experimentally found that larger flow depths induced higher forces compared to shallower ones. Furthermore, they showed that the initial bed condition (wet or dry) influenced the magnitude of the impulsive force during the initial impact with the structural model, while the post-peak quasi-steady flow was similar for both bed conditions. Lastly, comparison of experimental values with existing codes such as FEMA P646 and SMBTR (Section 2.4.5), showed an overestimation of the predicted forces up to 136%.

At Oregon State University, Robertson et al. (2013) experimentally tested the impact of an *"offshore"* solitary wave against a vertical wall installed on the whole width of the channel. As a result a design formula in Eq. 2.39 was derived and successfully validated with the field survey of Chock et al. (2012). This expression is also included in the ASCE7-06 (2016).

$$F_{\text{x,D}} = \rho B\left\{\frac{1}{2}gh_2^2 + (h_2 - h_0)U^2 + g^{1/3} \cdot [(h_2 - h_0)U]^{4/3}\right\} \tag{2.39}$$

Shafiei et al. (2016) also tested experimentally the impact of bores produced with a dam-break technique on free-standing rectangular structures. This study pointed out that the hydrodynamic pressure is dominant and that the pressure distributions tended to have a slope similar to that of the hydrostatic pressure. In addition, some oriented structures ranging

from 0 to 135° were also tested, showing that increasing the structure orientation to the flow decreased the total pressure.

Most recently Foster et al. (2017) tested the impact of tsunami-like waves produced through the newly developed pneumatic-type tsunami generator against free-standing structures. In this study, it was concluded that for waves with long periods, no impulsive component was observed and an hydrostatic pressure distribution was observed. The quasi-steady flow conditions presented by Qi et al. (2014), discussed in Appendix C, can be applied to tsunami-like flows, resulting into the following set of equations as a function of the upstream Froude number Fr_1 and the blockage ratio B/W.

$$
F_D = \begin{cases} \frac{1}{2} C_D \rho B h v^2, & \text{if } Fr_2 < 1 \text{ (subcritical)} \\ \lambda_F \rho B g^{1/3} v^{4/3} h^{4/3}, & \text{if } Fr_2 > 1 \text{ (choked)} \end{cases} \tag{2.40}
$$

where λ_F is a function of the blockage ratio B/W and the upstream Froude number (Eq. C.6). Foster et al. (2017) proposed an approximation of λ_F based on their experimental results:

$$
\lambda_F = 1.37 - 1.35 \left(\frac{B}{W} \right) + 1.37 \left(\frac{B}{W} \right)^2 \tag{2.41}
$$

2.4.3 Effect of bore aeration

As shown in the previous sections, bores propagating on wet bed are characterized by the presence of a recirculating roller with intense aeration. In broken waves the air can be either entrapped or entrained (Bullock et al., 2001). The compressibility of the air inside the flow affects the dynamic of the impact, reducing the maximum pressure because of a cushioning effect. However, the presence of a compressible mixture also redistributes the impact pressures more widely, leading to similar overall forces (Peregrine et al., 2005). Furthermore, Bullock et al. (2007) showed that a high level of aeration does not always reduce the peak pressure, but it tends to increase both the rise times and the duration.

Bullock et al. (2001) also performed some tests with both freshwater and salt water. Fresh water is known to have less air entrainment than seawater, resulting into larger bubble size, coalescing more easily. This implies that it is easier for air to escape in freshwater than in seawater. Finally, the same authors concluded that freshwater resulted into higher peak forces, with a lower rise times.

2.4.4 Effect of building overflow

In the past, the effect of overflow on the loading process was poorly addressed as it represented an undesirable scenario, to be avoided. Nevertheless, the increasing number of low-rise residential houses built on the coastline, suggested that this issue should be addressed. In literature the case of building overflow was addressed by Nakano (2008), based on the results

of the experimental work of Asakura et al. (2000). For structures without submergence (Case 1), the Japanese design guideline (SMBTR) suggested Eq. 2.31, leading to a value equal to 9 times the hydrostatic pressure. For structure with submergence, the same pressure is assumed at the bottom of the structure, however it is only applied to the actual height of the structure, leading to Eq. 2.42. Their findings are summarized in Figure 2.11.

$$F_{x,D} = \frac{1}{2}\rho g B \left(6 h_{max} - H_B\right) \cdot H_B \tag{2.42}$$

Most recently, Esteban et al. (2017) investigated the effect of tsunami overtop on concrete coastal structures, focusing on inundation depths behind the structures.
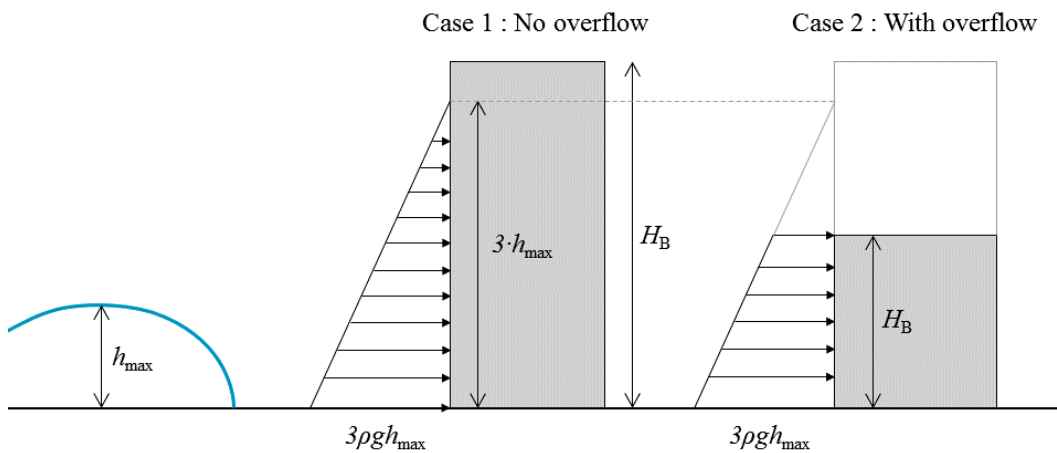
Figure 2.11 – Forces with and without overflow (Asakura et al. (2000) and Nakano (2008))

2.4.5 Design codes

Buildings are designed to resist to an extraordinary lateral load induced by seismic action or strong winds. Onshore structures are rarely designed to withstand hydrostatic or hydrodynamic loads. The purpose of current tsunami-related studies is to quantify the horizontal loading due to wave-induced impacts on buildings located near the shoreline and combine it with the already existing seismic design guidelines. Nevertheless, some basic differences in building failure modes due to seismic loads, associated with high-frequency dynamic effects and tsunami loads have been identified and discussed (Nistor et al., 2009). Tsunami waves and associated inland inundation have long-periods and are highly transitory. As such, they generate sustained forces whose magnitudes depend on the inundation depth and the flow velocity (ASCE, 2016).

The large amount of formulae available in literature presented in Section 2.4.2 clearly showed a lack of knowledge in the bore-structure interaction process (Nistor et al., 2009). The exact magnitude of the forces applied is unknown and values have to be derived based on vague empirical formulas. Most design codes across the world are based on the sum of various components: (1) hydrostatic force (F_{HS}), (2) buoyant force (F_B), (3) hydrodynamic force (F_D)

(4) and surge force (F_S). The greatest incertitudes concern the surge force and the flow velocity in the computation of the hydrodynamic force (Nistor et al., 2009). At present time, the major design guidelines and codes dealing with hydrodynamic impact against structures are:

1. CCH - City and County of Honolulu Building Code, Chapter 16, Article 11. (2000). The code was developed by the Department of Planning and Permitting of Honolulu, Hawaii based on the results of Dames and Moore (1980). The sum of hydrostatic (F_{HS}), hydrodynamic (F_D) and surge (F_S) forces is recommended. The surge force is evaluated using Equation 2.31 and the velocity in the computation of the hydrodynamic force is equal to the height ($v = h$)

2. FEMA 55 – Federal Emergency Management Agency, USA (2011). These guidelines neglect the surge component (F_S), however the the hydrodynamic force is computed using Equation 2.24 with a velocity that is twice the theoretical value ($v = 2\sqrt{gh}$).

3. SMBTR – Structural Design Method of Buildings for Tsunami Resistance. This method is recommended by the Building Centre of Japan and it is based on the results of Asakura et al. (2000), Okada et al. (2005) and Nakano (2008). Similarly to CCH the surge force is evaluated using Eq. 2.31 and Eq. 2.42 for buildings with and without overflow.

4. Development of Guidelines for Structures that serve as Tsunami Vertical Evacuation Sites, developed by Yeh et al. (2005) for the Washington State Department of Natural Resources.

5. Most recently, the 2016 edition of the ASCE-7 standard entitled *"Minimum design loads for buildings and other structures"* introduced a specific Chapter 6, *"Tsunami loads and effects"* (ASCE7-06, 2016; Chock, 2016; Robertson, 2016). The latter identifies tsunami building categories depending on their importance. The present study mostly focuses on buildings belonging to Tsunami Risk Category II, *i.e.* structures acting as vertical shelters with an elevation higher than 19.8 m at prototype level. The maximum hydrodynamic loads are assumed to occur for the Load Case 2, when $h = 2/3 h_{max}$, assuming a conservative Froude number of $\sqrt{2}$:

$$F_{x,D} = 1.5 \cdot \frac{1}{2} k_\rho \rho I_{tsu} C_D B (h v^2)_{max} \rightarrow F_{x,D} = k_\rho \rho I_{tsu} B h_{max}^2 \qquad (2.43)$$

where k_ρ is fluid density factor taking into account the effect of soil and debris (typically $k_\rho = 1.1$), ρ is flow density, ($\rho = 1000 \, kg/m^3$), I_{tsu} is the importance factor, herein assumed $I_{tsu} = 1$ and C_D is the drag coefficient, herein $C_D = 2$. According to ASCE 7 Chapter 6, the wave velocity is computed using:

$$v = \sqrt{2} \cdot \sqrt{g \cdot \frac{2}{3} h_{max}} \qquad (2.44)$$

If a more conservative approach is used, then Eq. 2.43 becomes:

$$F_{x,D} = 1.6 \cdot k_\rho \rho g I_{tsu} B h_{max}^2 \qquad (2.45)$$

ASCE 7 Chapter 6 also suggests to use the Eq. 2.39 derived by Robertson et al. (2013).

2.5 Impact on porous buildings

As detailed in Section 2.4, many research projects were carried out on impervious structures. On the contrary, little importance was given to the effect of building openings on the resulting forces, shown by the limited amount of studies available in literature. A selection of the main studies involving buildings with openings is presented in Table 2.4.

Reference	Wave type	Wave height [m]	Wave celerity [m/s]	Building geometry [m]	Porosity [%]	Block ratio β
Thusyanthan and Madabhushi (2008)	Impulse wave (block drop)	0.08-0.11	1.0-2.2	B=0.2m H_B=0.15m	Tsunami resistant house	3.33
Van de Lindt et al. (2009)	Solitary wave	0.1-0.6	-	B=2.4m B=1.2m H_B=1.2m	Windows & doors	-
Lukkunaprasit et al.(2009)	Vertical release	0.04-0.08	1.4-2.6	B=0.15m H_B=0.15m	0, 25, 50	6.67
Santo and Robertson (2010)	Solitary wave	0.12-1.28	2.6-6.8	Wall W=2.3m Perforated wall - 3 × B = 0.05m - 3 × B = 0.15m - 3 × B = 0.30m	100 93 79 58	1.00 14.22 4.74 2.37
Triatmadja and Nurhasanah (2012)	Dam-break	0.15-0.19	2.6-3.5	B=0.20m H_B=0.20m	0, 7.5, 20 40, 60, 81	7.25
Hartana and Murakami (2015)	Dam-break	0.11	2.7	B=0.20m H_B=0.26m	40, 50, 60	2
Present study	Vertical release	0.13-0.25	1.93.6	B=0.30m H_B=0.3m B=0.9m H_B=0.3m	0, 17, 31, 34, 42, 60	4.67 1.56

Table 2.4 – Literature review of selected studies involving force measurements on buildings with openings

Santo and Robertson (2010) performed some tests on perforated walls with multiple columns of the same size, located side-by-side across the width of the entire channel. The purpose of this study was to simulate some typical ground floor configurations of tsunami-inundated buildings. These columns had dimensions of 0.05, 0.15 and 0.30m, leading to blockage ratios of 14.22, 4.74 and 2.37 (Table 2.4). The results in terms of horizontal forces were not always consistent and firm conclusions difficult to draw. Nevertheless, Santo and Robertson (2010) recommended that the effect of multiple columns be considered to increase the peak force by 25% for the case with closure percentage greater than 40%.

Thusyanthan and Madabhushi (2008) tested a "*tsunami-resistant house*" designed by the Harvard Design School in collaboration with MIT and compared it with a typical house in Sri Lanka (scale 1:25). The timber buildings had a porous structure with openings facing

the ocean and corner walls made of reinforced concrete (Figure 2.12a). As the wave could flow through the building, less splashes were observed and measurements showed reduced pressure values. This proved that a specific design can reduce the impact force and that the allowance of such flow through the building resulted into an overall better performance of the structure.

Lukkunaprasit et al. (2009a) and Chinnarasri et al. (2013) were the first to investigated the effect of openings on the resulting hydrodynamic force. They tested one-store buildings located on a 5 % sloped beach at a scale of 1:100 with porosities of 25 and 50% (Figure 2.12c). Results showed that the influence of openings on the peak pressure is negligible, however the force was reduced by 15 to 30 %. The pressure peaks occurred not simultaneously and the design using the spectrum would lead to an overestimation of the force. Both studies concluded that the reduction in the resulting force clearly demonstrates the benefits of openings in mitigating the effect of tsunamis on such buildings.
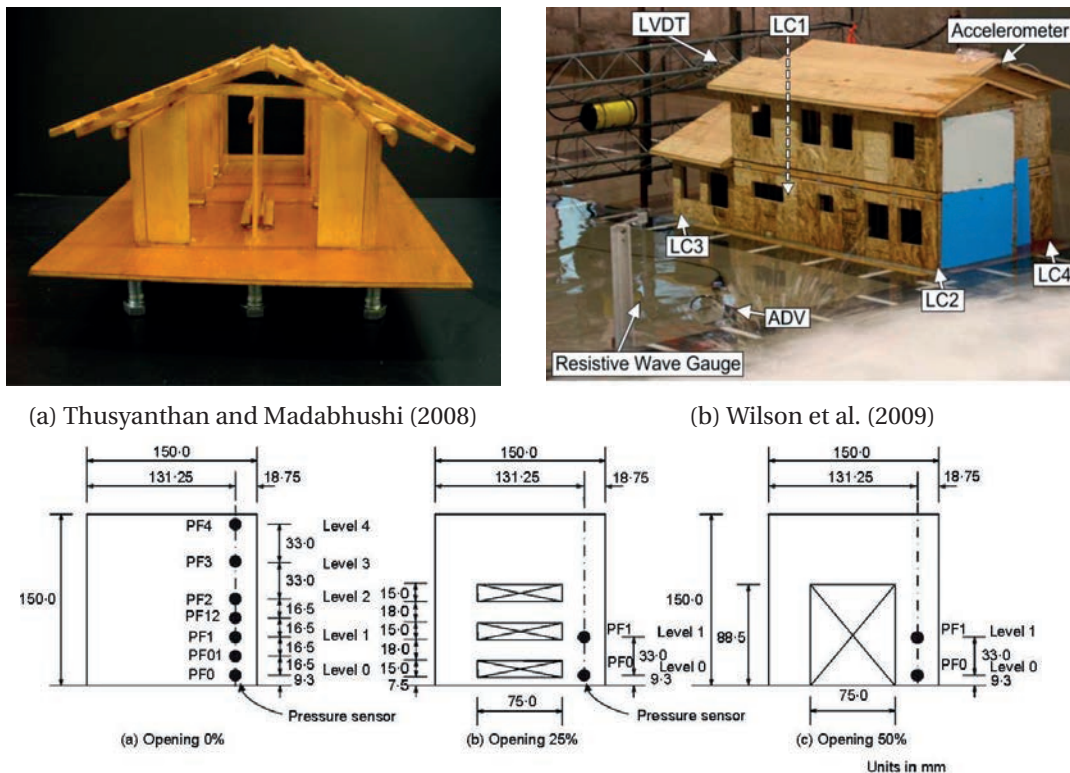
(a) Thusyanthan and Madabhushi (2008)   (b) Wilson et al. (2009)

(c) Lukkunaprasit et al. (2009a) and Chinnarasri et al. (2013)

Figure 2.12 – Porous configurations previously investigated

Wilson et al. (2009) and Van de Lindt et al. (2009) tested 1/6th scaled wooden residential houses in the USA with both windows open and closed (Figure 2.12b). Results showed that the configuration with windows closed had values 2.5 times higher, which meant that by simply opening the windows the charge was reduced by 60 %. They also showed that for structures with openings, the uplift (buoyancy) became important.

Nistor et al. (2009) also provided an example of force calculation for a 3D structure in the case of breakaway walls and non-breakaway walls using the different design codes. The results showed that the first case (breakaway structure) is more convenient. The force is also proportional to the length of the structure, therefore it is recommended to orient the building such that the shorter side faces the possible tsunami.

(a)

(b)
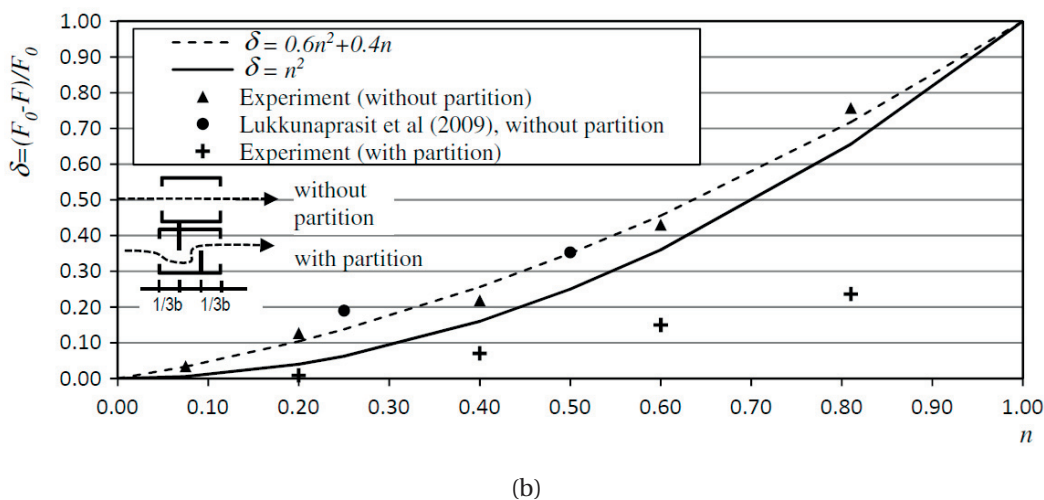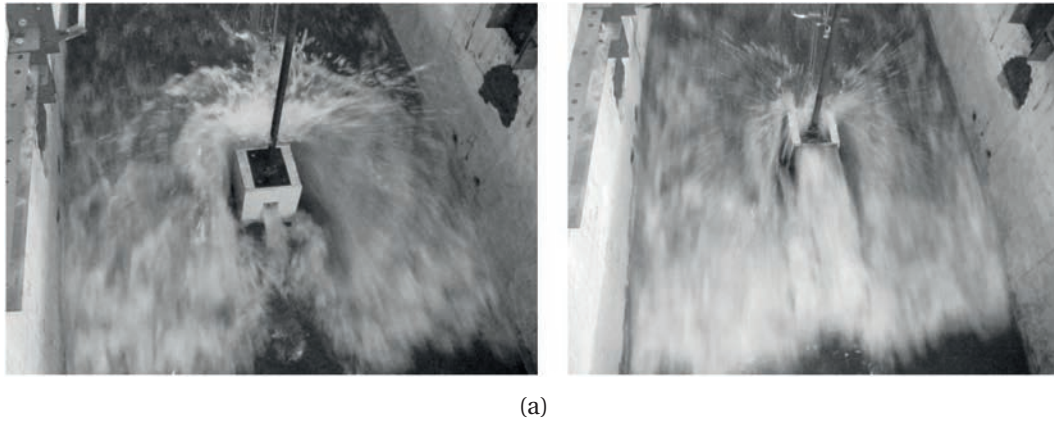
Figure 2.13 – Details of the experiments carried out by Triatmadja and Nurhasanah (2012): (a) experimental set-up and configuration studied; (b) results in terms of forces obtained for buildings with openings.

Triatmadja and Nurhasanah (2012) tested some, symmetrical and concentric openings of variable sizes as shown in Figure 2.13a. Porosities values ranged from 0 to 81 % and both configurations with and without internal partitions were systematically tested under hydrodynamic load conditions. For such structures, a non-linear relationship between porosity P and the resulting horizontal force was found. Porosity was defined as the ratio between the area of the openings and the front area of the structure. This relationship is graphically presented in Figure 2.13b.

$$F_{x,D} = 1 - \left[0.6 \cdot (P)^2 + 0.4 \cdot P \right] \tag{2.46}$$

Lastly, Hartana and Murakami (2015) compared some experimental tests to OpenFOAM numerical simulations for porosity values of 40, 50 and 60 % (Figure 2.14). This study showed that the flow through the structure changed the dynamics of the impact, with larger opening ratios resulting into lower inundation depths. In addition, some initial uplift forces were observed both experimentally and numerically. These were provoked by the change in flow direction because of the vertical elements in the front side, generating a jet-like flow in the vertical direction.
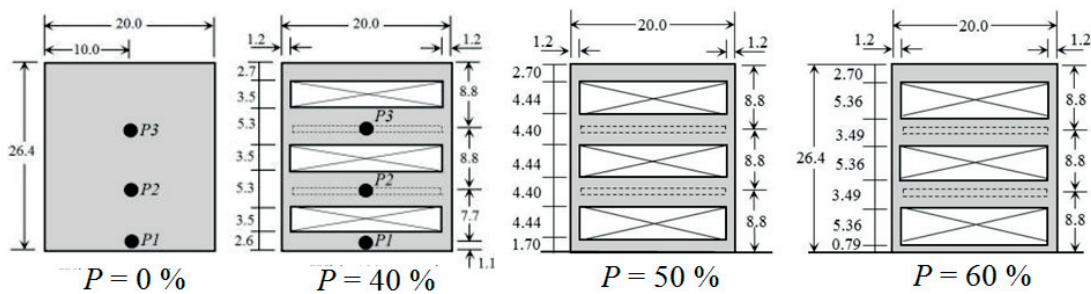
Figure 2.14 – Configurations of buildings with openings tested by Hartana and Murakami (2015)

2.6 Need of research

This *State of the Art* focused on the work previously conducted in the domain of wave generation and their impact on buildings with and without openings. Although some important contributions were provided by previous studies, this Chapter also pointed out some gaps in knowledge and thus an important need for further research.

1. The diversity of wave transformation and subsequent inland propagation has led researchers to develop several techniques to generate these tsunami-like flows in laboratories, such as dam-break waves, piston-types generators or vertical releases, among others. The use of a vertical release technique was rarely addressed in the past and a characterization of the generated wet bed bores and dry bed surges in terms of their hydrodynamic behaviour is thus necessary. Furthermore, uncertainties still exist on the velocity profiles behind the wave front for surges and bores generated with this technique.
2. Similar unsteady flows were used to investigate both vertical walls and free standing structures, leading to an excessive amount of formulae and theories to evaluate the resulting hydrodynamic impact force. Nevertheless, no agreement still exists in litera-

ture and the prediction of impact forces remains covered by high uncertainties. More specificity, a direct relationship between the measured forces and the hydrodynamic properties of the generated bores and surges is missing.

3. Previous studies dedicated little attention to the influence of building overflow on the loading process, as this did not represent a critical scenario. Nevertheless, the large amount of low-rise residential houses built on the coastline pointed out that this issue should no longer be neglected.

4. Literature review also revealed the lack of a comprehensive experimental study on the effect of openings on the resulting hydrodynamic force. As a consequence, its estimation remains difficult to assess and far from practical application.

Thus, this literature review highlighted a clear lack of knowledge and the need for more specific investigations, leading to the identification of the research objectives previously presented in Section 1.3.

3 Experimental Set-up

All experiments were conducted at the Laboratory of Hydraulic Constructions (LCH) at Ecole Polytechnique Fédérale de Lausanne (EPFL) in Switzerland, where a vertical release technique was used to produce surges and bores. The experimental facility represents a modification of the set-up previously used by Meile (2007) and Meile et al. (2008, 2011). Compared to these previous studies, a higher release discharge was needed to better reproduce tsunami-like inland flows. Subsequently, a new downstream channel was build. In order to conceive the optimal experimental facility, a focused literature review on the wave heigh h commonly used in literature is presented and discussed. This is followed by a discussion on the main parameters involved in the physical phenomenon, leading to the conception of the experimental set-up presented in the second part of the chapter. This showed that the generated waves were similar to tsunami-like flows.

3.1 Introduction

Through a detailed literature study presented in the previous chapter, the magnitude of the wave height was investigated. As presented in Chapter 1 and 2, wave heights up to 10-12 m were commonly observed during major events. Considering a downscaling Froude factor of $\Lambda \approx 30$, these values corresponded to wave heights $h \approx 0.3$ m, which are consistent with previous research, as shown in figure 3.1. These results were used to determine the wave height for the present study and to design the experimental set-up. A height of 9 m corresponds to buildings with 3 floors, that are commonly found on coastal areas where major events might occur.

3.1.1 Dimensional analysis

The main parameters involved in the process were identified: force (F), water density (ρ), wave velocity (v), wave height (h), building side (B), surface of the openings (A_{o}), gravitational acceleration (g) and dynamic viscosity (μ) . Since it is a 3-dimensional system (time, mass,

	Ramsden 1993	Thusyanthan & Madabhushi 2008	Wilson et al. 2009	Lukkunaprasit & al. 2009	Fujima et al. 2009	Arneson et al. 2009	Fuchs et al. 2010	Shafiei et al. 2010	Al-Faesly et al. 2011
Min [cm]	10.6	10	10	4	10	5	11.6	5	32
Max [cm]	12.69	10	60	8	20	10.3	18.5	10	83
● Average [cm]	11.645	10	35	6	15	7.65	15.05	7.5	57.5
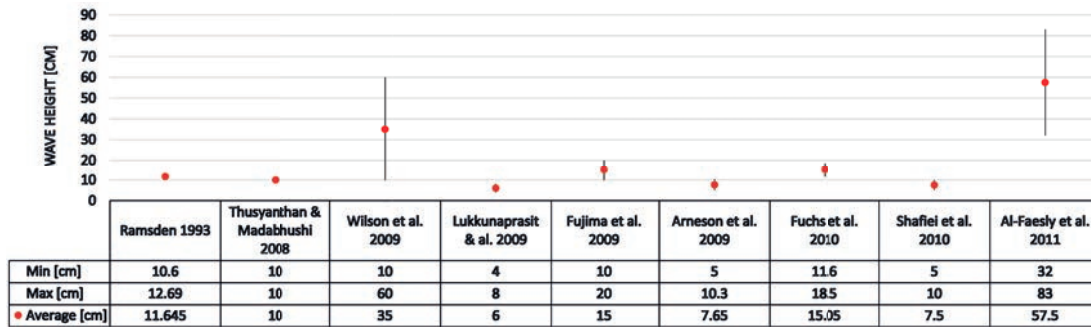
Figure 3.1 – Wave heights in previous research projects

length) according to the Buckingham theorem, there exist 8 - 3 = 5 dimensionless numbers to describe the system:

$$F, \rho, v, h, B, A, g, \mu = f\left(\mathrm{Fr} = \frac{v}{\sqrt{gh}}, \mathrm{Re} = \frac{vh}{v}, C_{\mathrm{D}} = \frac{2F}{\rho v^2 h^2}, \frac{A_{\mathrm{o}}}{B^2}, \frac{h}{B}\right) \qquad (3.1)$$

One can recognise some of the main π groups obtained through the application of the Buckingham theorem, including the Froude number (Fr) representing the ratio between inertial and gravitational forces, the Raynolds number (Re) representing the ratio between inertial and viscous forces and the drag coefficient (C_{D}) . The opening of the buildings and its main geometric features are shown to be some relevant parameters in the loading process.

3.2 Experimental facility

3.2.1 Vertical-release generation technique

The experimental set-up for the generation of surges and bores through the vertical release technique is presented in Figure 3.2. A 2.1×3.0×1 m upper reservoir with a storage volume of ∀ = 7.08 m³ was linked to a water-filled lower reservoir through three, newly installed, identical and independent PVC pipes with an internal diameter of 315 mm. These were symmetrical to the central axis of the channel, with a transversal distance of 0.45 m between adjacent pipes (Figure 3.3a). Each pipe was independently fitted with a PVC valve designed at LCH (Figure 3.4).

The sudden water release was obtained through a system of pulleys and Vectran-fibres ropes with a diameter of 0.01 m and an extension less than 1%. All ropes were linked to the same handle, ensuring the synchronised opening of all gates (Figure 3.3b). Pictures of the release mechanism are presented in Figure 3.3. The total difference in head between the upstream and the downstream reservoir was H_{R}= 2.1 m.
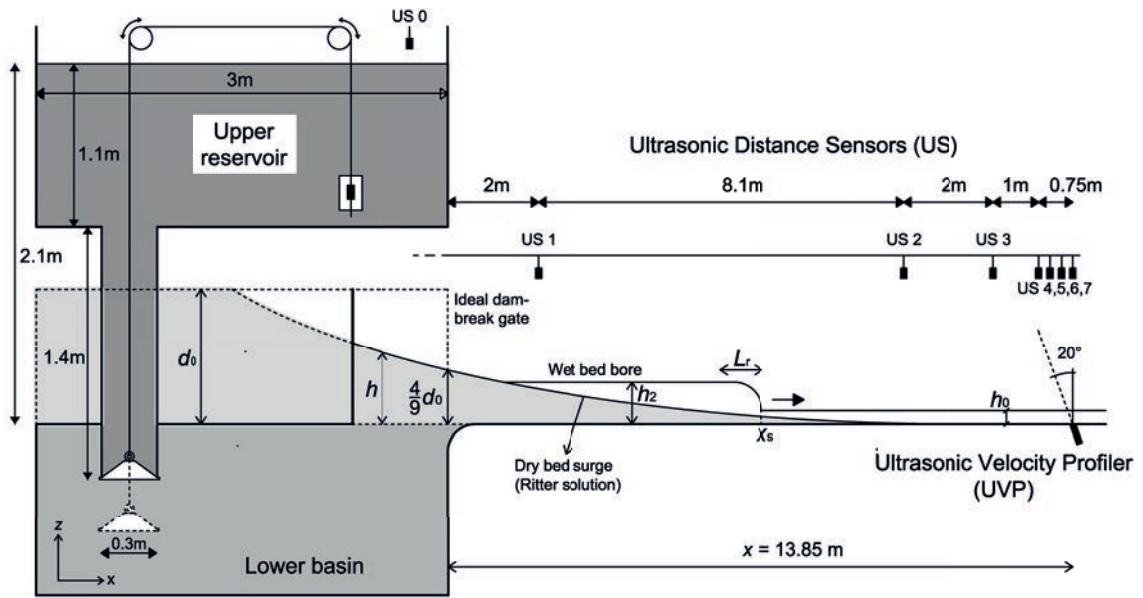
Figure 3.2 – Experimental set-up used in the present study to generate bores and surges through a vertical release technique.

(a) Upper reservoir   (b) Release mechanism   (c) Propagating channel
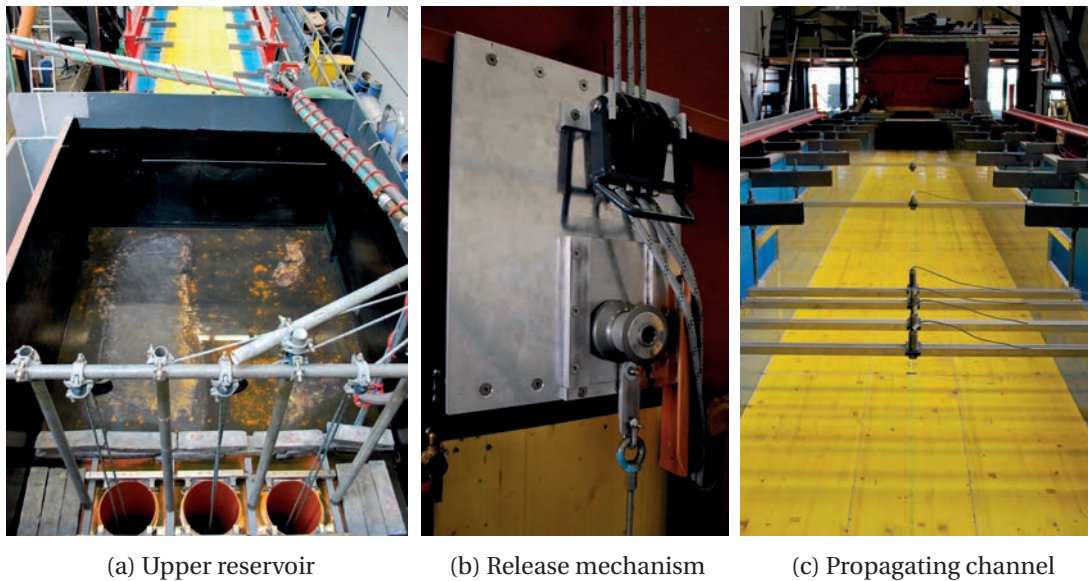
Figure 3.3 – Details of the release mechanism used to produce surges and bores.

When the system was activated, *i.e.* the ropes released, a difference in head between the upper and lower reservoir was established, resulting into a gravitational flow through the pipes. Being the lower basin completely filled with water, the incoming discharge resulted into an upward flow at channel inlet, with consequent, free surface overflow in the downstream flume. A schematic visualization of release mechanism and the resulting flow in the lower reservoir is presented in Figure 3.5.
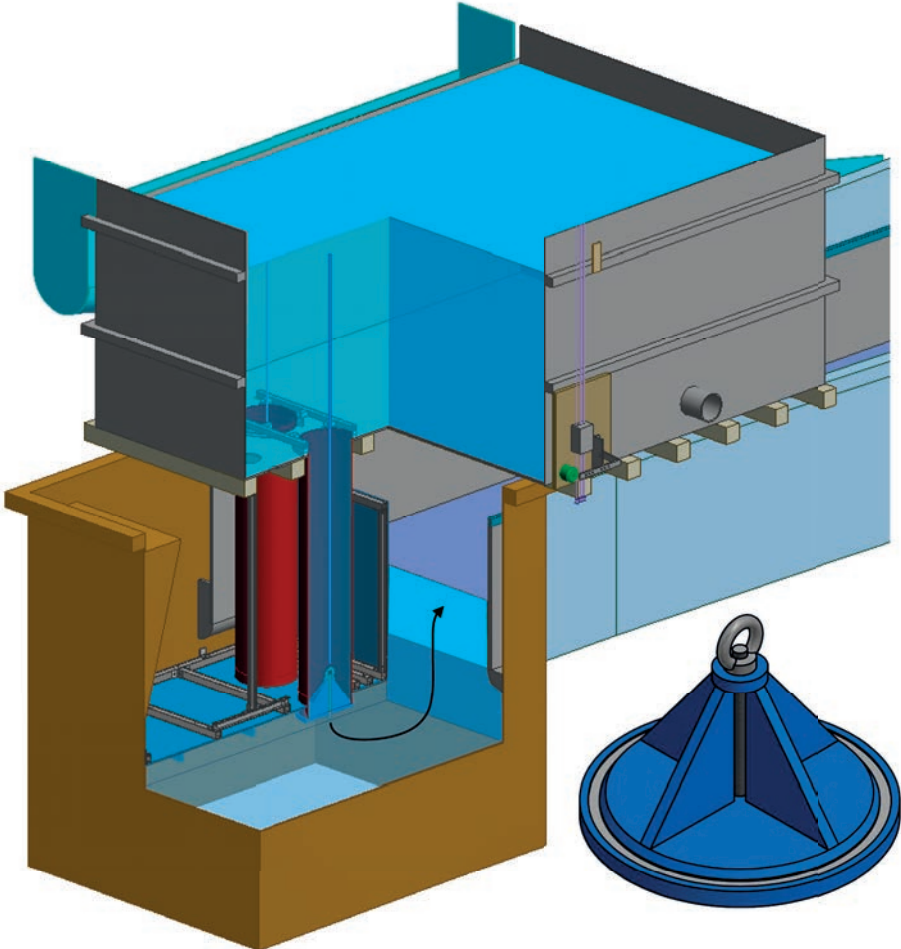
Figure 3.4 – Details of the release mechanism in *Autodesk Inventor*®.
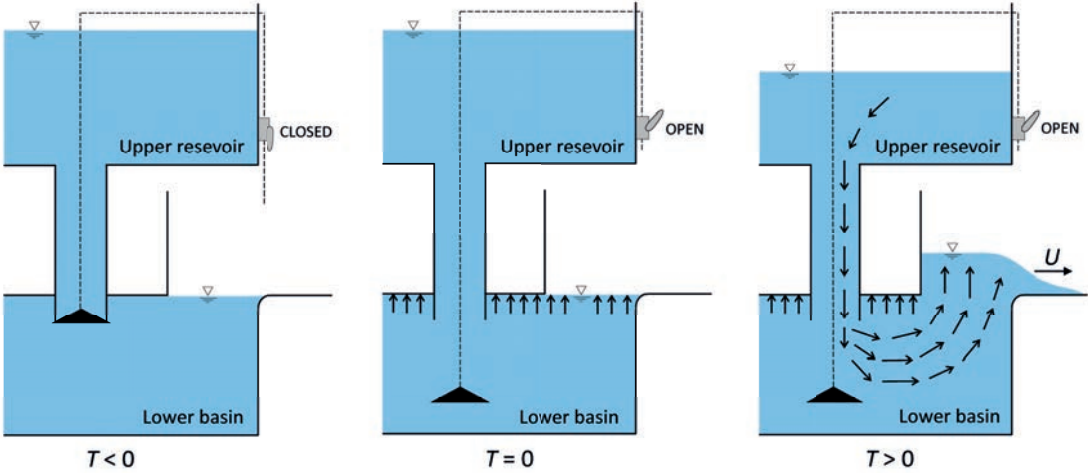
Figure 3.5 – Schematical representation of the release mechanism and its evolution in time.

A mathematical model similar to that developed by Meile (2007) was used during the design phase to simulate the wave formation process and to predict the main characteristics of the bore. The conception of the experimental set-up was carried out using a 3-dimensional program, *Autodesk Inventor*, allowing a better interpretation of volumes and existing constraints. A picture of the model is presented in Figure 3.6
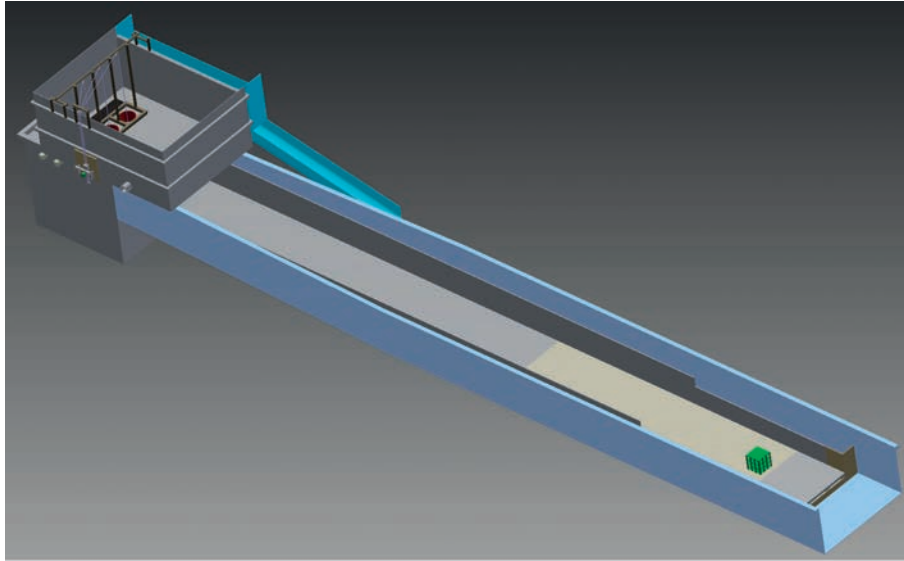
Figure 3.6 – Experimental set-up designed in *Autodesk Inventor* (building in green)

3.2.2 Propagating channel

Once the wave is generated, its propagation takes place in the *Canal Vevey*. The latter is an existing channel with a total length of 40 m and a width of 2 m. A secondary horizontal channel with a wooden floor and a length of 15.5 m and a width of 1.40 m was installed inside the existing facility (Figure 3.3c). For the generation of wet bed bores, an initial still water depth (h_0) on the flume ("wet bed" condition) was ensured using a vertical sill located at the downstream end of the channel. The water was evacuated at the downstream end of the flume, avoiding thus any backwater effect. A drainage pipe was installed below the channel to evacuate water before each test, preventing the channel from getting wet during test on dry bed.

On average, the Darcy-Weisbach friction factor of the channel was measured to be $f_{DW} = 0.021$ using steady-state experiments under various flow conditions. This corresponded to an average roughness $k_s = 0.66$ mm, which is consistent with the values suggested by Henderson (1966).

3.3 Instrumentations

The following instruments were used:

- **Ultrasonic distance Sensors (US)** - used to measure water depths
- **Ultrasonic Velocity Profilers (UVP)** - used to measure the velocity profiles
- **Force Plate** - used to measure forces and moments in all 3 main directions
- **Flow-meter** - to measure the inlet discharge (Steady-state tests only, Appendix C)

3.3.1 Ultrasonic distance Sensors (US)

The flow depth of the propagating waves were measured using seven ultrasonic distance sensors (US), type *Baumer, UNAM 30I6103*, shown in Figure 3.7a. These had a measuring range of the water level between 100 to 1000 mm. The US sensors were located along the channel at x = 2, 10.10, 12.10, 13.10, 13.35, 13.60 and 13.85 m from the flume inlet, *i.e.* the end of the lower basin, as shown in Figure 3.2. This also represented the origin of the system of coordinates. The location of the US sensors was chosen in order to carefully follow the evolution of the propagating surges and bores in time at multiple locations. The US sensors were sampled at an acquisition frequency of 12.5 Hz, with an accuracy of 0.5 mm and a response time of less than 80 ms. For all scenarios, the minimal required distance between two adjacent sensors to avoid any interference was conservatively respected.

An additional sensor (US0) with an extended measuring range (UNAM 50, 250-4000 mm, Figure 3.7b) was installed in the upper reservoir to ensure the accurate recording of the opening time of the system ($t = 0$ s). For all tests, the opening time was set when a decrease of 0.01 m was observed in the upper reservoir. A shifted time based on the surge/bore arrival time was defined as $T = t - t_0$. The specifics of each US sensors are presented in Table 3.1

(a)   (b)
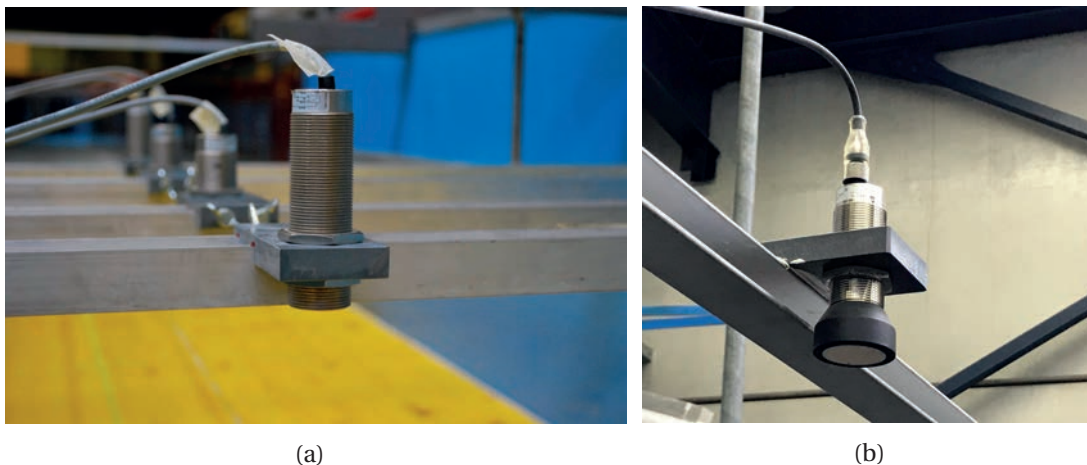
Figure 3.7 – Ultrasonic distance Sensors (US) used in the present study: (a) UNAM 30I6103 100-1000 mm; (b) UNAM 50 250-4000 mm

The calibration of all US sensors was achieved by measuring the output voltage signal for a minimum of 4 known depths within the foreseen measuring range. From these values a regression line was extrapolated, in the form $h = a' \cdot V + b'$. The calibration coefficients for all sensors are presented in Table 3.1 and the regression lines in Figure 3.8.

	Type	**Range** [mm]	**Location**	a'	b'	R^2
US 0	UNAM 50	250-4000	Upper reservoir	-0.266	1.667	0.999
US 1	UNAM 30I6103	100-1000	$x = 1.00$ m	-0.072	0.691	0.999
US 2	UNAM 30I6103	100-1000	$x = 10.10$ m	-0.073	0.636	0.999
US 3	UNAM 30I6103	100-1000	$x = 12.10$ m	-0.065	0.593	0.999
US 4	UNAM 30I6103	100-1000	$x = 13.10$ m	-0.116	0.570	0.999
US 5	UNAM 30I6103	100-1000	$x = 13.35$ m	-0.090	0.504	0.999
US 6	UNAM 30I6103	100-1000	$x = 13.60$ m	-0.092	0.510	0.999
US 7	UNAM 30I6103	100-1000	$x = 13.85$ m	-0.111	0.548	0.999

Table 3.1 – Technical specifications of the US sensors used in the present study
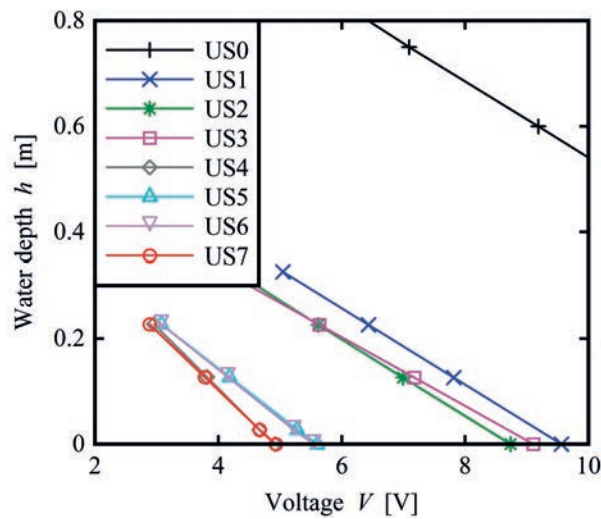
Figure 3.8 – Regression lines obtained during the calibration of the US sensors

3.3.2 Ultrasonic Velocity Profiler (UVP)

Flow velocity was investigated using an Ultrasonic Velocity Profile (UVP), type *DUO-MX SN* produced by the Met-Flow (Switzerland). This instrument provided instantaneous velocity profiles along the transducer axis by detecting the Doppler shift frequency of echoed ultrasound as a function of time. Both an emitter and a transducer are installed inside the ultrasonic sensor, allowing measurements of the projection of the velocity vector. For the present study, an emitting frequency of 2 MHz was chosen (Figure 3.10a). The transducer had a diameter of 8 mm and it was located 5 mm below the channel bottom with an angle of 20° in the upstream

direction. The empty space between the probe and the channel was filled with gel and sealed with plastic tape to assure the transmission of the emitting signal. A section of the installed UVP can be seen in Figure 3.9. The transducer was located at a distance of $x = 13.85$ m from the channel inlet, where the bore had reached a fully developed condition. One UVP per cross section was used and measurements were taken in the transducer axis direction, then projected in the main flow direction (x-axis). Velocity components in the vertical and transversal directions were not considered.
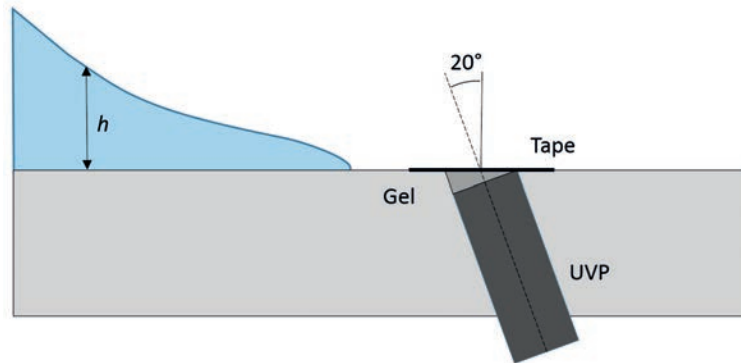
Figure 3.9 – Sketch of the UVP installed in the channel bottom

No calibration was needed for this instrument. A sensitivity analysis of the main parameters involved in UVP acquisition system was performed and more information are presented in Appendix A of this report. As a result, a number of 128 repetition per profile (within the same measure) was selected, leading to acquisition frequencies ranging from 12.5 to 55 Hz, corresponding to measurements durations of 80 to 18 ms, and an accuracy of ± 10 mm/s.

The acoustic scattering was increased using hydrogen bubbles produced through electrolysis induced in the flow, similarly to Blanckaert and Lemmin (2006) and Meile et al. (2008). For this, an anode and a cathode are installed in the upstream part of the channel, at $x = 1.5$ m from the channel inlet (Figure 3.2). This allowed sufficient mixing time for the hydrogen bubbles and guaranteed a uniform distribution in the vertical direction at measurement location. The spacing of the stems was 0.05 m in the longitudinal direction and 0.45 m in the transversal direction. These had a diameter of 0.008 m and a thin stainless steel wire ($\varnothing = 0.0001$ m) was wrapped around with a spacing of 0.05 m. The vertical bars were covered with waterproof paint to avoid their participation in the reaction. A potential difference of 30 V was applied between the two bars, producing hydrogen bubbles with diameter proportional to $\varnothing$.

3.3.3 Force Plate

An *AMTI MC6-1000* force plate is used to measure forces and moments in the three main directions. The force plate is squared (150 mm) with a thickness of 79.2 mm and it is presented in Figure 3.11. The force plate was installed on the channel at a distance $x = 14$ m from the channel inlet. It was assembled on a rigid holding structure composed or two C-shaped beams

(a) UVP transducer (2 MHz)

(b) Installation for production of hydrogen bubbles
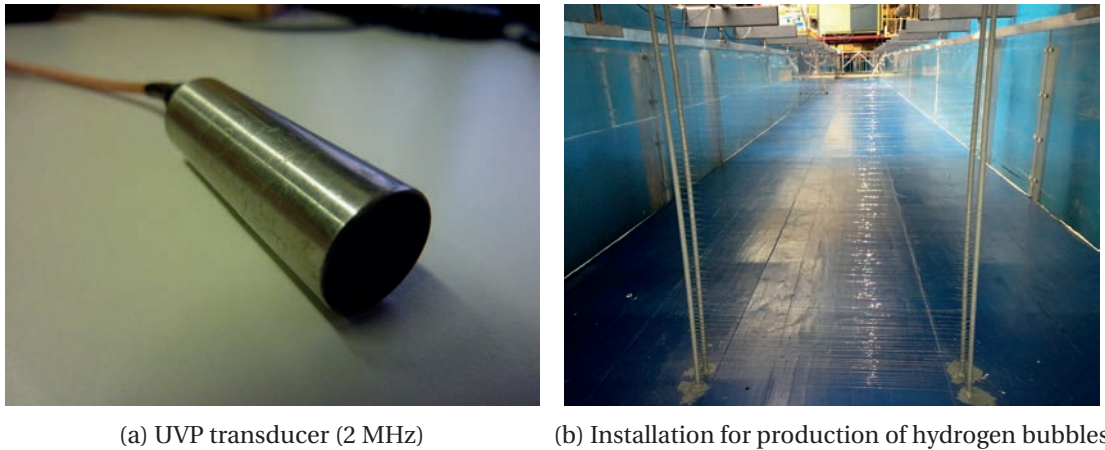
Figure 3.10 – Details of the UVP set-up used to measure velocity profiles

welded to channel bottom, as shown in Figure 3.11b. A 30 mm aluminium plate was installed between the force plate and the holding structure to rise the upper surface to the same channel level. The Force Plate was covered with an aluminium structure (Cover Plate) preventing any direct contact with water. The complete installation set-up for the force plate is presented in Figure 3.11b. The buildings are then screwed on top of the Cover plate. The water infiltrating below the channel was evacuated using a dedicated drain.

The Force Plate was connected to an Amplifier (*AMTI, Gen 5*) which directly provided the signal exported to the LabView® code, synchronised with the other instruments. The main specifications for the *MC6-1000* force plate are presented in Table 3.2. The force plate used metal foil strain gages to measure forces and moments in all directions. The measurement is carried out by placing the gauges in wheatstone bridges; the excitation is applied at the input of the bridge and the voltage measurement is carried out at the output. The output of the gauges is low and the signal needs to be amplified; the amplifier gains can range from 500 to 4000. The basic output of the gages is represented by the sensitivity terms (*s*) whose values are presented in Table 3.2.

	x-axis	y-axis	z-axis
Capacity (Force) [N]	2250	2250	4500
Capacity (Moment) [Nm]	340	340	170
Sensitivity s (Force) [μ V/(V· N)]	0.66626	0.65868	0.17201
Sensitivity s (Moment) [μ V/(V· Nm)]	6.18593	6.16098	16.32809
Stiffness [N/m]	$2.1 \cdot 10^7$	$2.1 \cdot 10^7$	$14 \cdot 10^7$
Resonant frequency [Hz]	550	550	620

Table 3.2 – Technical specifications of the *AMTI* force plate *MC6-1000*. [Data provided by *Prophysics SA* for *AMTI*]
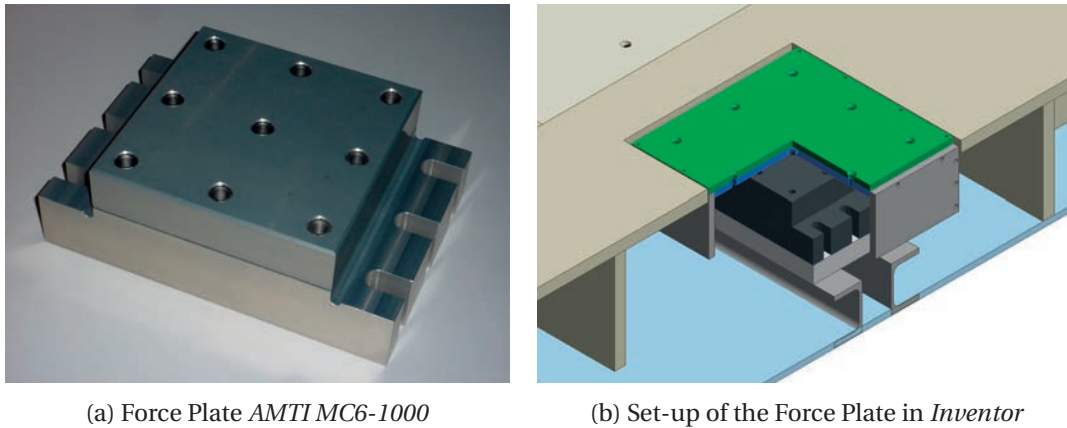
(a) Force Plate *AMTI MC6-1000*   (b) Set-up of the Force Plate in *Inventor*

Figure 3.11 – *AMTI* force plate *MC6-1000* and installation in the channel

The governing equations for acquisition of forces and moments through the *Gen5* Amplifier are the following:

$$F = \frac{V}{V_{\text{exc}} \cdot s \cdot G \cdot 10^{-6}} \qquad\qquad M = \frac{V}{V_{\text{exc}} \cdot s \cdot G \cdot 10^{-6}} \qquad (3.2)$$

where F is measured force (N), M the measured moment (Nm), V is the measured, amplified signal (V), V_{exc} is the excitation voltage (typically $V = 10$ V), s is the sensitivity term provided by the furnisher (Table 3.2) and G is the amplifier gain (500, 1000, 2000 or 4000).

3.3.4 Flow-meter

For the tests carried out under steady state conditions (Appendix C), an electromagnetic flow-meter (type *ABB FXE4000*) installed in the laboratory circuit was used to register the discharge in the channel. A validation of the calibration of the flow-meter was carried out, showing an error less than 1.5% for all tested discharges. For the verification a certain volume of water was diverted on a balance and weighted after a certain time. The same procedure was repeated for a wide range of discharges, as shown in Figure 3.12.
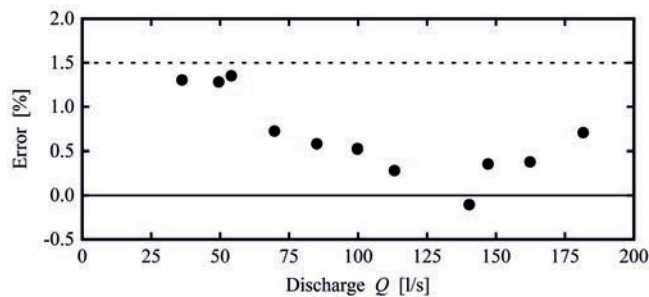
Figure 3.12 – Error obtained for the tested discharges during the calibration of the Flow-meter

3.3.5 Acquisition system and post-processing

Data was acquired by means of a LabView® data acquisition system developed at LCH. All 8 US sensors and the six channels of the Force Plate were directly connected to a *Main* master program, as shown in Figure 3.13. The synchronisation with the UVP-DUO unit was achieved through a Transistor-Transistor Logic (TTL)-Level (+5V, min) trigger signal, sent when the measure was launched from the *Main* panel. This synchronisation time was estimated to be less than 3 ms, which is small compared to the measurement duration of both instruments.This method allowed to initially set the same time reference for all instruments, ensuring that every velocity profile was associated to the corresponding flow depth and load condition.
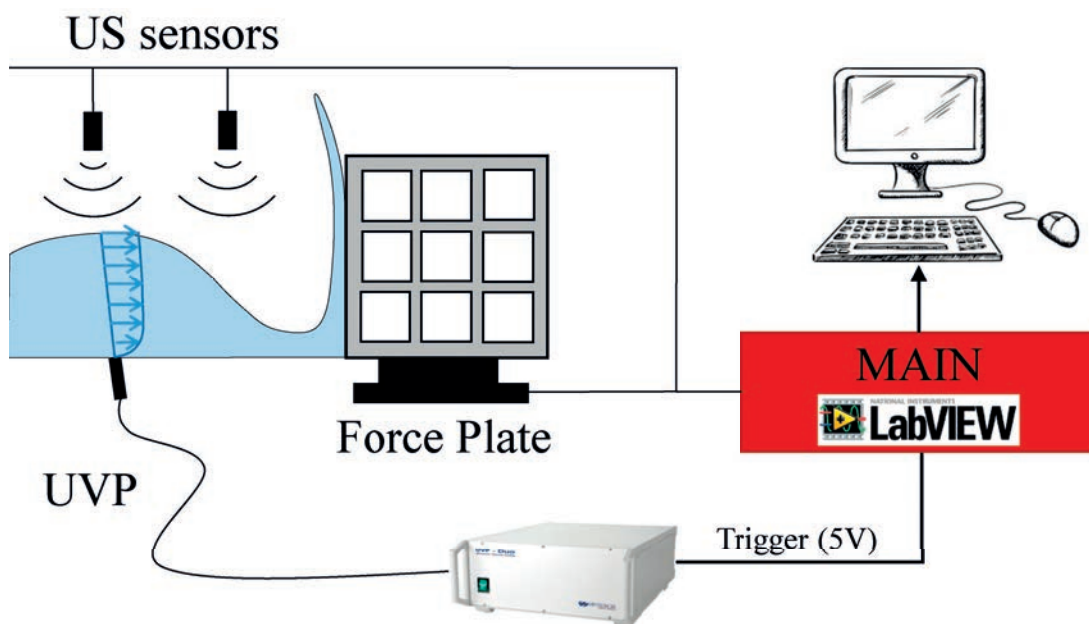
Figure 3.13 – Sketch of the used acquisition system

3.4 Building model

The tested buildings were located at a distance $x = 14.00$ m from the channel inlet to ensure the full development of the bores/surges. The building used in the present study is shown in Figure 3.14, with a side length of $B = 0.3$ m, resulting in a blockage ratio $\beta = W/B = 4.67$; this value was sufficiently large to limit side wall effects and was consistent with previous studies (Table 2.3). The impermeable building had a cubic shape and it was made of aluminium plates with a uniform thickness of 0.01 m. This was designed to be completely rigid, ensuring that the structure's dynamic response could be neglected. These buildings corresponded to prototype structures of 9 m if a geometrical scale of 1:30 is assumed. Such dimensions would be typical of residential buildings commonly observed in coastal zones exposed to tsunami hazard. The building height $H_B = 0.6$ m (Figure 6.1) was representative of a vertical shelter belonging to the Tsunami Risk Category II, as defined by the ASCE-7 Chapter 6 (Section 2.4.5).

(a)	(b)
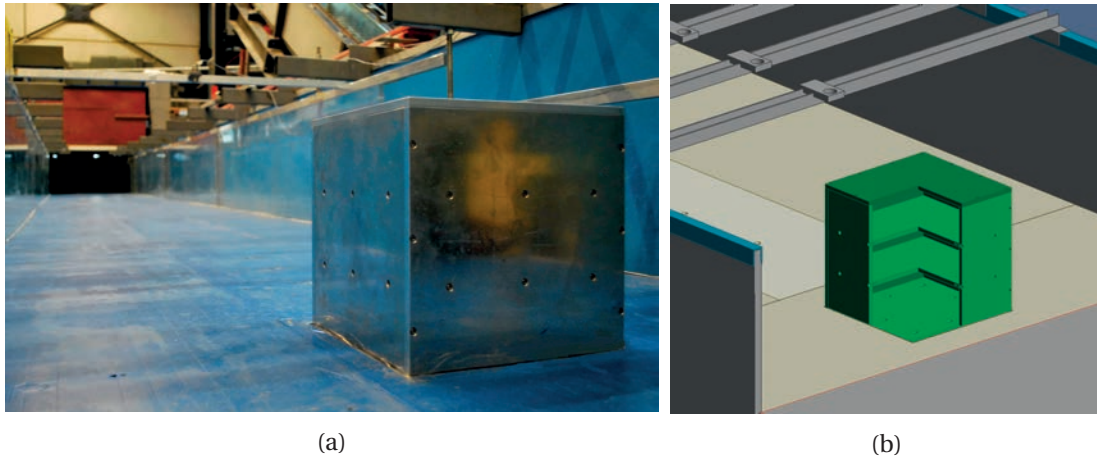
Figure 3.14 – Impervious structure ($P_{tot} = 0\%$, $H_B = 0.3$m) tested in the present study

As shown in Figure 3.11, the buildings were installed on a force plate (AMTI MC6-1000) which recorded the time histories of the forces and moments in all three dimensions. The coordinate system is shown in Figure 3.2 and Figure 3.15. The following sign convention is used throughout the research project:

- F_x is positive in the flow direction (frontal impact)
- F_y is positive to the left if surfing the wave downstream the flume
- F_z is positive in upward direction
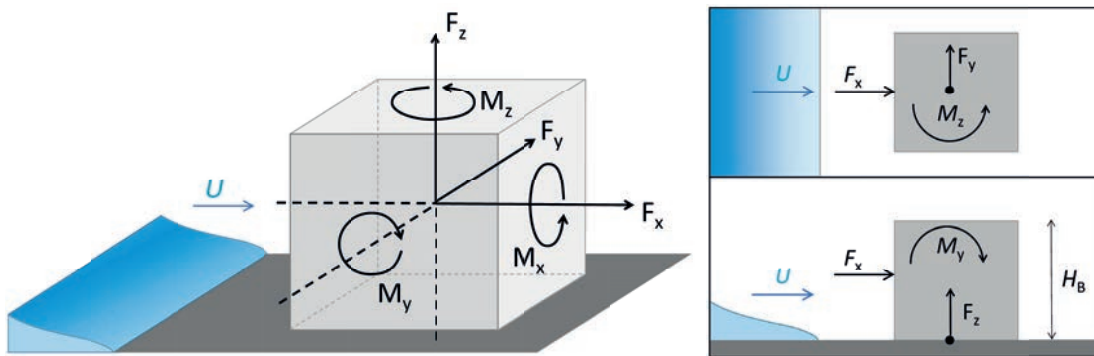
Figure 3.15 – Axis orientation and reference system used to define forces and moments

Building surface porosities

Different buildings with various opening values are tested in order to investigate the effect of surface porosity on the resulting impact load. Building surface porosity was defined as $P = A_o/B^2$, where A_o is the surface of the openings and B the building side. A total of six porosity configurations were chosen and their geometry is shown in Figure 3.16. All structures are realistic and accurately represent possible three-storey buildings commonly observed in coastal areas subject to tsunami hazard.

(a) P_{tot} = 17 % (b) P_{tot} = 34 % (c) P_{tot} = 60 %

(d) P_{tot} = 31.34 % (e) P_{tot} = 42.24 % (f) P_{tot} = 84 %
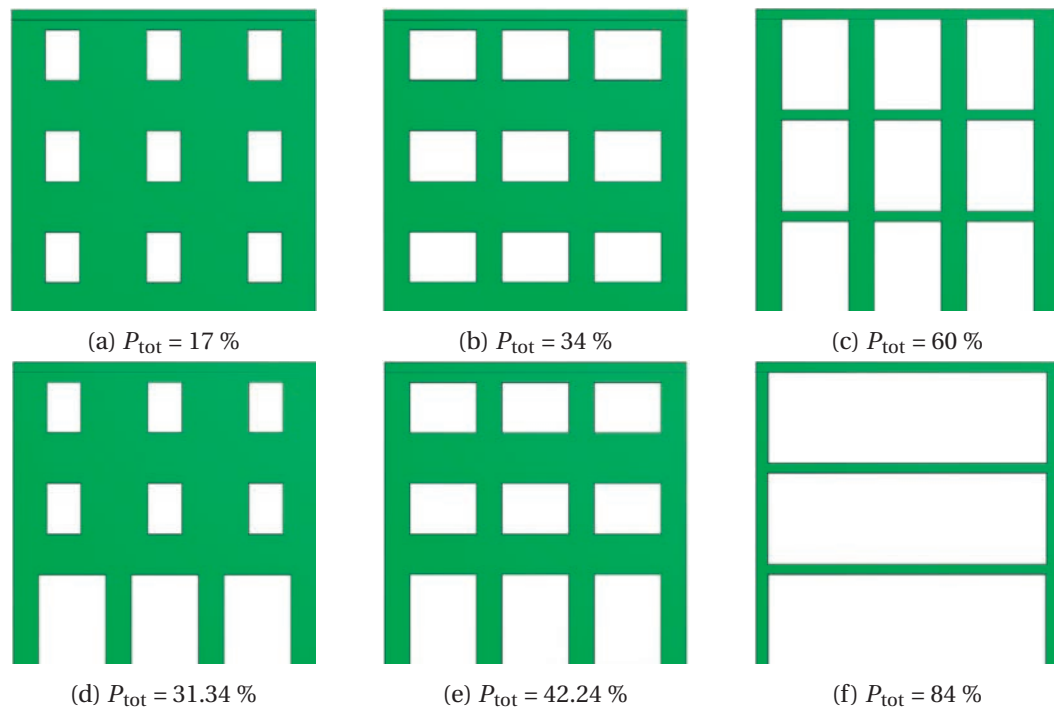
Figure 3.16 – Investigated building structures and porosities P_{tot}

All configurations have different values of total porosity, ranging from $P_{tot} = 0$ (impervious, reference) to 84%. Configuration (a) and (b) simulate single and double windows with prototype size 1×1.5 m and 2×1.5 m, respectively. Configuration (c) represents the bare structure of the building with pillars of 0.75 m. Configurations (d) and (e) simulate bottom openings due to the presence of shops; the upper part is equal to to (a) and (b). Lastly, configuration (f) represents a fully opened building. All structures are constructed assembling aluminium plates with a thickness of 10 mm. The total porosity of the structure (P_{tot}) is constant, whereas the equivalent porosity $P_{h,max}$ is defined as the cumulative porosity at $h = h_{max}$ and thus depends on the maximum wave height. The building front porosity is presented in Figure 3.17 as a function of height. At $h = H_B = 0.3$ m, than $P_{h,max} = P_{tot}$.

Configurations tested

Four main configurations were tested in the research project. These are presented in Figure 3.18 and summarized in Table 3.3.

1. **All porous sides** (0) - openings on all four sides
2. **Impervious lateral walls** (F) - openings on front and back, impervious lateral sides
3. **Impervious back** (B) - openings on the front and on both sides, impervious back
4. **With building sides** (S) - openings on the front and on the back, impervious on the sides (same as config. F). Additional sides were added next to the building, increasing the blockage ratio and simulating the effect of next-door buildings. These were independent and not connected to the central building.
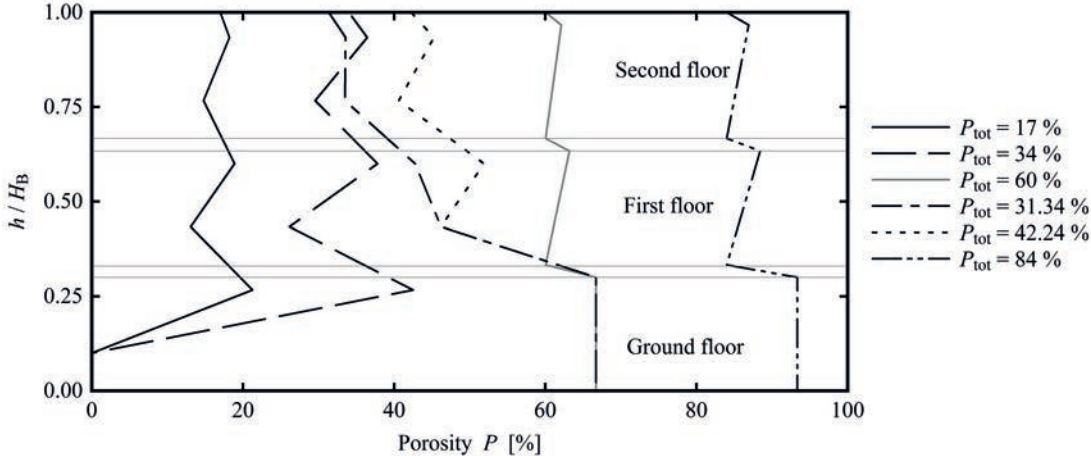
Figure 3.17 – Vertical distribution of building porosity

(a) All porous sides (0)

(b) Impervious sides (F)

(c) Impervious back (B)

(d) With sides (S)
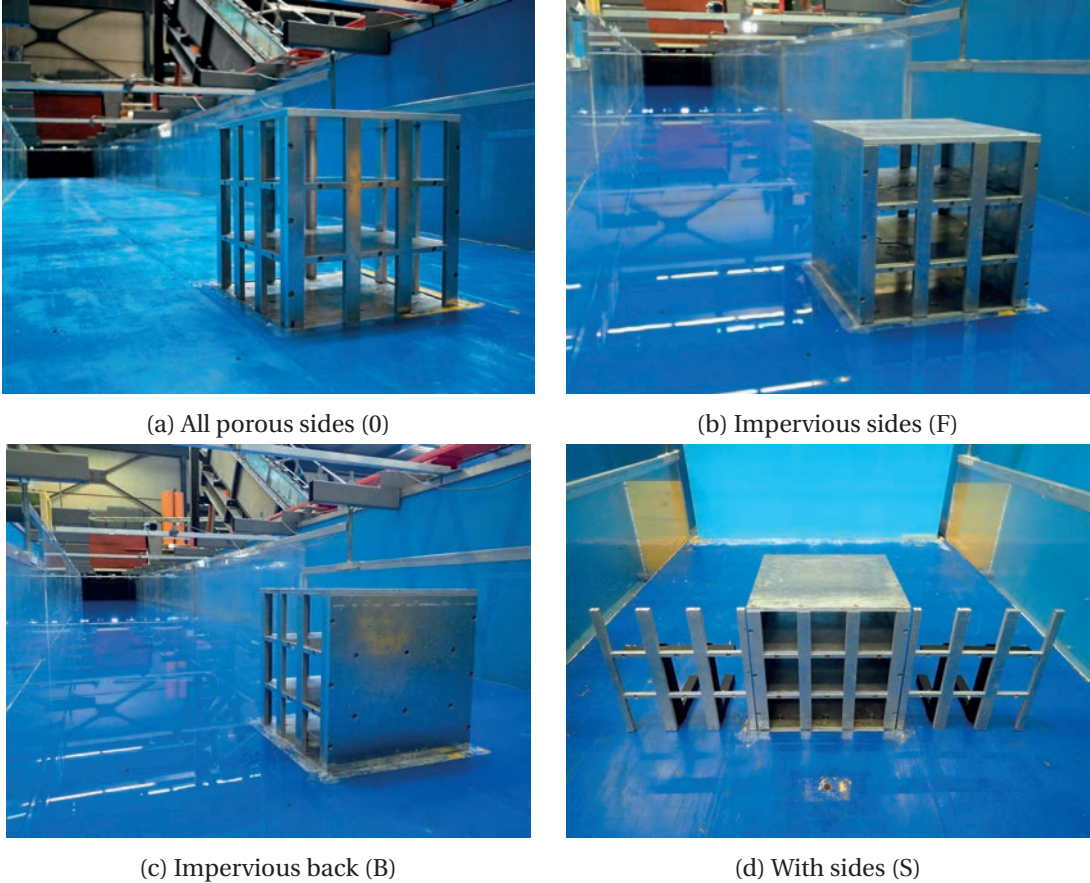
Figure 3.18 – Tested building configurations

All buildings had a squared section and were made of aluminium plates with a thickness of 10 mm. These were designed to be completely rigid, ensuring that the structures' dynamic response could be neglected. All pieces were assembled using M4 screws with a length of
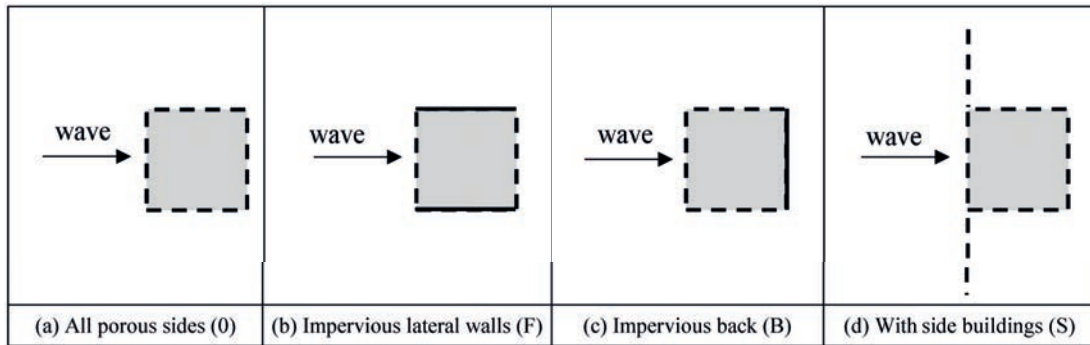
Figure 3.19 – Sketch of the tested configurations

14mm. The base was fixed to the cover plate using 8 × M8 screws with a length of 16 mm. The mass of the structures was calculated piece by piece using a high resolution analytical balance (*Mettler Toledo*) with a ±1 g precision. The volume was calculated analytically. Numerical values for both mass and volume are presented in Table 3.3 and Figure 3.20. For these calculations, the weight and volume of the screws are neglected. The relationship between mass and volume was linear (homogeneous material), with a density of $\rho = 2700$ kg/m^3, corresponding to aluminium.

Porosity [%]	Configuration	Front	Sides	Back	Volume [m^3]	Mass [kg]
0	0	Porous	Porous	Porous	$6.70 \cdot 10^{-3}$	18.00
17	0	Porous	Porous	Porous	$6.09 \cdot 10^{-3}$	16.35
31.34	0	Porous	Porous	Porous	$5.57 \cdot 10^{-3}$	14.98
34	0	Porous	Porous	Porous	$5.50 \cdot 10^{-3}$	14.77
42.24	0	Porous	Porous	Porous	$5.18 \cdot 10^{-3}$	13.91
60	0	Porous	Porous	Porous	$4.54 \cdot 10^{-3}$	12.18
17	F	Porous	Impervious	Porous	$6.39 \cdot 10^{-3}$	17.18
31.34	F	Porous	Impervious	Porous	$6.13 \cdot 10^{-3}$	16.48
34	F	Porous	Impervious	Porous	$6.10 \cdot 10^{-3}$	16.38
42.24	F	Porous	Impervious	Porous	$5.94 \cdot 10^{-3}$	15.95
60	F	Porous	Impervious	Porous	$5.62 \cdot 10^{-3}$	15.09
84	F	Porous	Impervious	Porous	$4.91 \cdot 10^{-3}$	12.36
17	B	Porous	Porous	Impervious	$6.24 \cdot 10^{-3}$	16.77
34	B	Porous	Porous	Impervious	$5.80 \cdot 10^{-3}$	15.58
42.24	B	Porous	Porous	Impervious	$5.56 \cdot 10^{-3}$	14.40
60	B	Porous	Porous	Impervious	$5.08 \cdot 10^{-3}$	13.64

Table 3.3 – Main properties of the tested buildings (model scale)
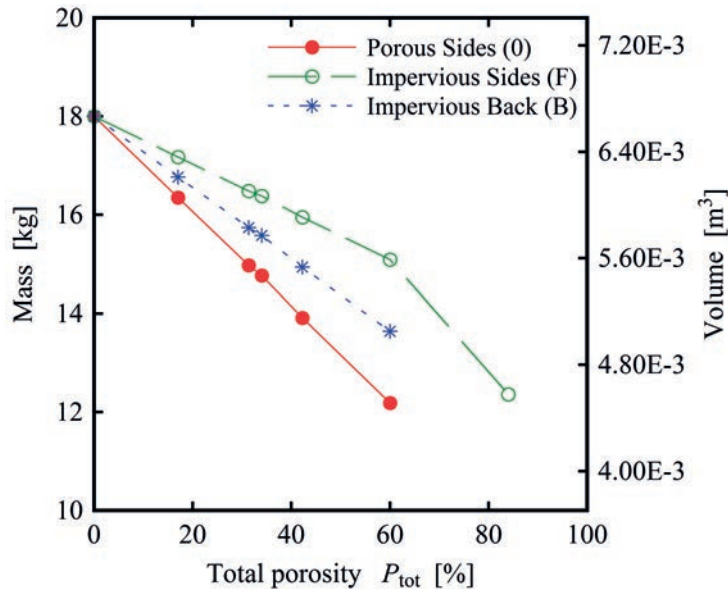
Figure 3.20 – Graphical representation of the main building properties

Eigen-frequency

In order to avoid any resonance between the tested buildings and the flow, the determination of the Eigen-frequency values for all tested configurations was necessary. All values were obtained through specific tests. For these, each configurations was hit with a hammer at a height $z = H_B$ and the Eigen-frequency obtained through a Fourier Fast Transform (FFT) of the resulting force measured in both x and y directions under dry bed condition. For consistency, this process was repeated at least twice in both negative and positive directions. An example of the measured signal in the x direction for $P_{tot} = 0$ % is presented in Figure 3.21a. The frequency distribution obtained from the FFT is presented in Figure 3.21b for the same configuration in both x and y directions. The results obtained for all configurations are presented in Table 3.4 and Figure 3.22. The magnitude of the results obtained is in agreement with the values obtained by Arnason et al. (2009) and Nouri et al. (2010) for similar buildings.

Finally, it is important to point out that the Eigen-frequencies of the impervious buildings were sufficiently high to avoid any interference with the flow frequency estimated to $f = 1.5$Hz for a Strouhal number St $= f \cdot B / U = 0.13$.

Stiffness

In addition to the Eigen-frequencies, the stiffness k of the tested buildings is an important parameter that should be provided to practical engineers. To do so, some Finite Elements Methods (FEM) numerical simulations of push-over tests were performed using the software Autodesk Inventor Professional 2015 (Figure 3.23). Four forces with various intensity (100, 500, 700 and 1000 N) were applied and the deflection δ recorded. The stiffness was then obtained
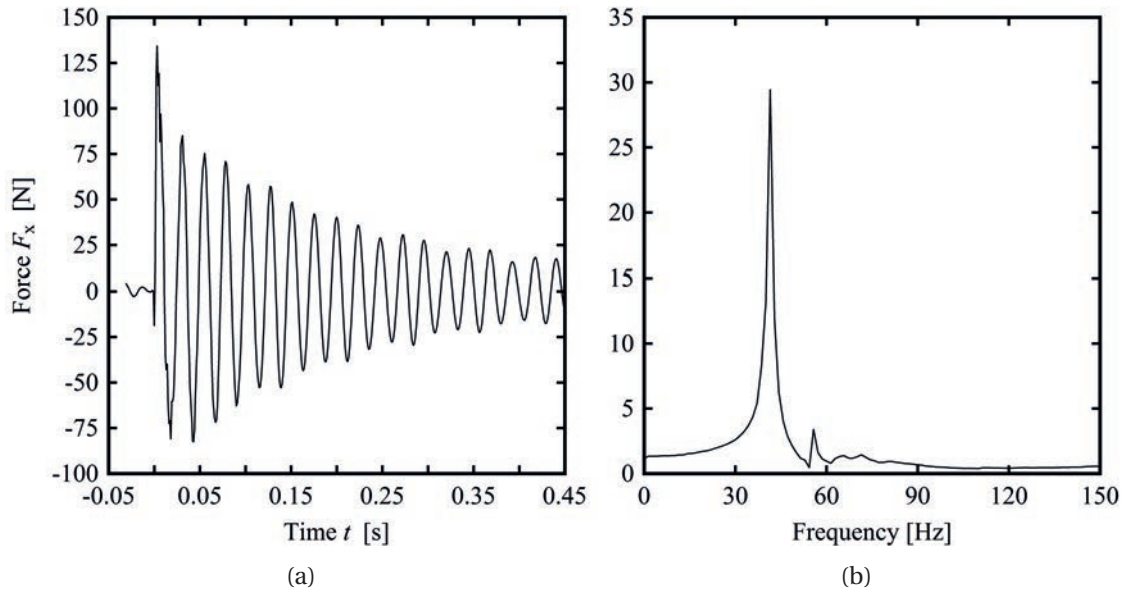
Figure 3.21 – Example of results obtained for the computation of the Eigen-frequency of the tested building configurations: (a) Measured force signal in the x direction (F_x); (b) FFT of the force measured in the x direction (F_x).
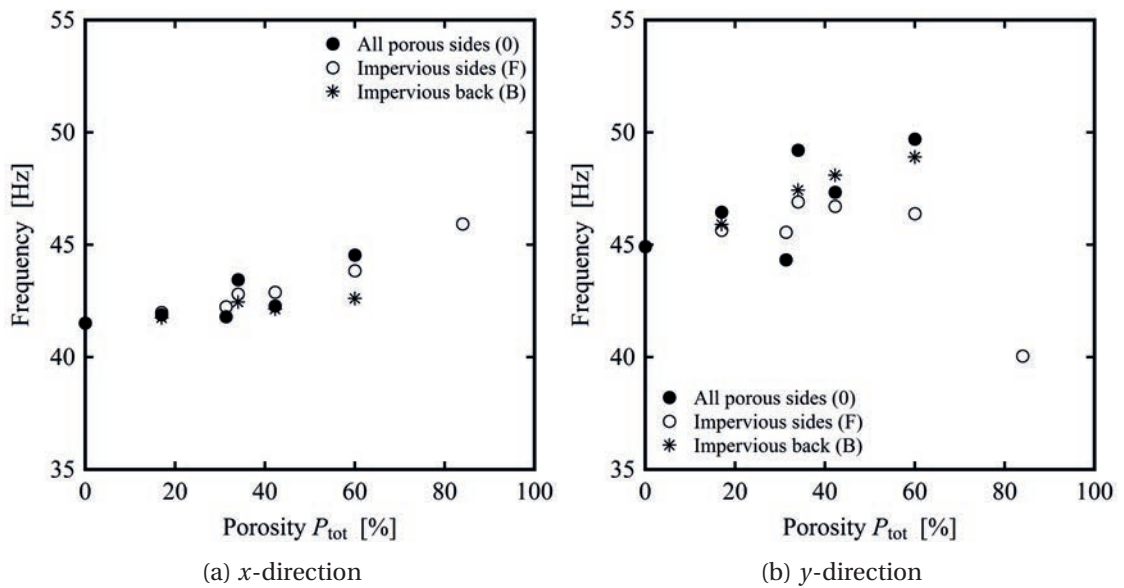
Figure 3.22 – Eigen-frequencies obtained for all tested configurations

as the ratio between the applied force and the maximum deflection:

$$k = \frac{F}{\delta} \qquad\qquad \delta \approx \frac{F \cdot H_B^3}{EI_y} \qquad\qquad k \approx \frac{EI_y}{H_B^3} \qquad\qquad (3.3)$$

where E is the elastic modulus and I_y the inertia moment. Values around $2 \cdot 10^7$ N/m were obtained for all buildings, as detailed in Table 3.4. These values, at model scale, were sufficiently high such that the building's dynamic response could be neglected.
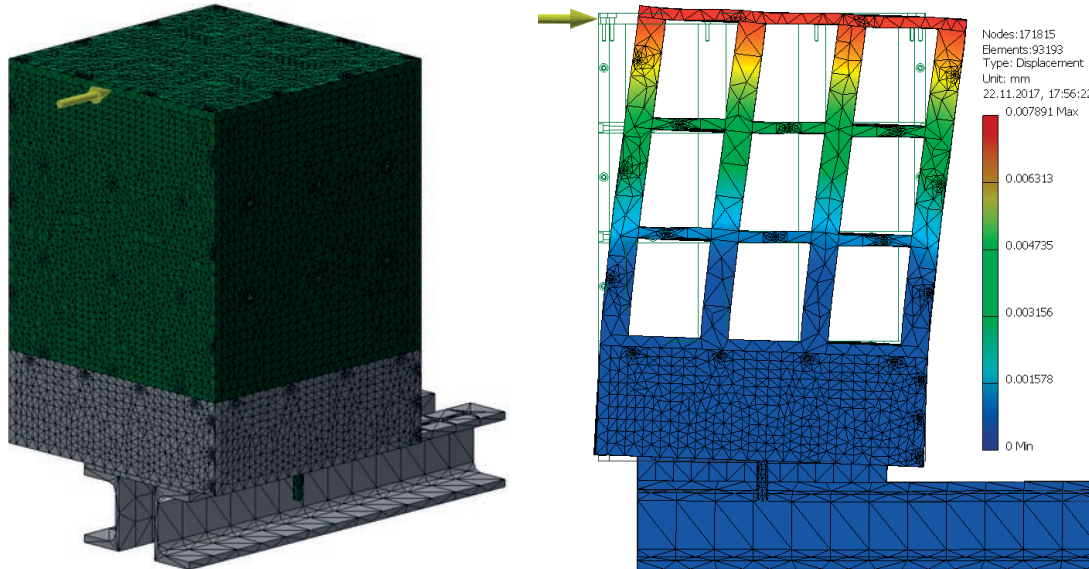
Figure 3.23 – Model and typical results of FEM numerical simulations used to obtain the stiffness values.

Porosity P_{tot} [%]	Configuration	Eigen-frequency x-direction [Hz]	Eigen-frequency y-direction [Hz]	Stiffness x-direction [N/m]
0	0	41.52	44.92	$1.69 \cdot 10^7$
0	H	30.60	33.85	$5.27 \cdot 10^6$
17	0	41.89	46.45	$1.61 \cdot 10^7$
31.34	0	41.80	44.33	$1.28 \cdot 10^7$
34	0	43.45	49.21	$1.33 \cdot 10^7$
42.24	0	42.28	47.34	$1.15 \cdot 10^7$
60	0	44.55	49.71	$6.34 \cdot 10^6$
17	F	41.99	45.65	$1.69 \cdot 10^7$
31.34	F	42.24	45.56	$1.62 \cdot 10^7$
34	F	42.81	46.91	$1.64 \cdot 10^7$
42.24	F	42.89	46.71	$1.60 \cdot 10^7$
60	F	43.85	46.39	$1.55 \cdot 10^7$
84	F	45.93	40.05	$1.42 \cdot 10^7$
17	B	41.75	45.91	$1.63 \cdot 10^7$
34	B	42.46	47.43	$1.36 \cdot 10^7$
42.24	B	42.14	48.10	$1.18 \cdot 10^7$
60	B	42.61	48.91	$6.68 \cdot 10^6$

Table 3.4 – Eigen-frequency and stiffness k values obtained for the tested configurations.

3.5 Scale effects

For all experimental studies, similarity between the model and prototype has to be guaranteed. In free-surface, gravitational-driven flows a Froude similitude is commonly used. This is based on the Froude number Fr, that for a rectangular sections is defined as

$$\text{Fr} = \frac{v}{\sqrt{gh}} \tag{3.4}$$

where v is a characteristic velocity and h a reference length, in this case, assumed equal to the flow depth. A conservation of the Froude number between prototype and model scales, leads to an unaltered ratio between gravitational and inertial forces.

If the same fluid (*i.e.* water) is used, in the downscaling process not all ratios can be kept constant, namely Froude and Reynolds numbers. The Reynolds number Re represents the ratio between inertial and viscous forces and it is defined as

$$\text{Re} = \frac{v \cdot h}{\nu} \tag{3.5}$$

where v is a characteristic velocity and h a reference length, commonly assumed equal to the the hydraulic diameter D_H for open channel flows (Chanson, 2004). During wave impact, the building is subject to both skin friction and wave drag. The first depends on the Reynolds number, whereas the second (wave drag) depends on the flow velocity and therefore on the Froude number. The skin-friction is considered to be negligible compared to the wave drag, implying that a Froude similitude is therefore reasonable (Thusyanthan and Madabhushi, 2008).

For fully aerated, compressible and pressure-dominated flows, a similitude based on the Cauchy number could be used.

$$\text{Ca} = \frac{\rho v^2}{K} \tag{3.6}$$

where K is a modulus representing the elasticity of the fluid. Such a similitude implies a conservation of the ratio between inertial and elastic forces between model and prototype. However, Bullock et al. (2001) showed that during a wave impact, the variation of the pressure can lead to an underestimation of maximum pressures and to an the overestimation of rise times. The same authors concluded that a Cauchy law scaling is therefore not recommended and that the use of Froude similitude did not lead to an overestimation of impact pressures compared to field measurements. Thus, if a geometrical scale Λ is assumed, the most common relationships between model and prototype are presented in Table 3.5.

Nevertheless, to minimize scale effects, the Reynolds number must be sufficiently large to guarantee a sufficient level of turbulence in the flow. For the present study Reynolds numbers between 10^5 to 10^6 were obtained for both surges and bores. These values were sufficiently

Physical parameter	Scaling factor
Length [m]	$(h)_p/(h)_m = \Lambda$
Velocity [m/s]	$(v)_p/(v)_m = \Lambda^{1/2}$
Time [s]	$(t)_p/(t)_m = \Lambda^{1/2}$
Discharge [m^3/s]	$(Q)_p/(Q)_m = \Lambda^{5/2}$
Force [N]	$(F)_p/(F)_m = \Lambda^3$
Frequency [Hz]	$(f)_p/(f)_m = \Lambda^{-1/2}$
Stiffness [N/m]	$(k)_p/(k)_m = \Lambda^2$

Table 3.5 – Scaling factors for a Froude similitude with geometrical ratio Λ

high to produce an adequate representation of the physical phenomenon in both aerated and non-aerated regions (Heller, 2011; Pfister and Chanson, 2012; Fuchs, 2013).

The effect of surface tension is relevant only for shallow flows and for broken bores, where air entrainment occurs. These effects are taken into account in the Weber number We, defined as the ratio between inertial forces and surface tension:

$$\text{We} = \frac{v^2 \rho h}{\sigma_T} \tag{3.7}$$

where σ_T is the surface tension (herein $\sigma_T = 0.07$ kg/s^2). For the generated waves, values of We ≈ 30 were computed, which is consistent with similar studies (Fuchs, 2013) and higher than the critical value We = 10 defined by Schüttrumpf and Oumeraci (2005) to avoid scale effects in case of wave overtopping and wave run-up.

3.6   Model effects

Tests carried out in experimental facilities are also subject to model effects. Some of these effects were identified during the design process and are briefly discussed hereafter along with the solutions to limit them.

- **Wave development** - For waves generated with the vertical release technique, some additional surface oscillations were observed in the upstream section of the channel. This was a result of the gravitational flow from the upper to the lower reservoir. A sufficient length was left between the generation tank and the measurement location (x = 14 m) in order for the wave to fully develop (Chanson et al., 2003; Meile, 2007).
- **Blockage ratio** - Buildings with sides $B = 0.3$ m, installed in a channel width $W = 1.4$ m, resulted into a blockage ratio $\beta = W/B = 4.67$ (Section 3.4). Side effects are thus not expected as the channel width is more than 4 times the building side. Furthermore, as shown in Table 2.3, this value is consistent with similar previous studies.

- **Sea-water properties** - Fresh water was used in the present study. This represents a conservative approach, since salt-water (more representative of tsunami events) leads to lower impact pressures (Bullock et al., 2001), as discussed in Section 2.4.3.
- **Building stiffness** - From a structural points of view, a similarity between the tested buildings and those observed on coastal areas must also be guaranteed. As shown in Table 3.5 the scaling factor for the stiffness k (defined as ratio between force F_x and deflection δ) is Λ^2. If we assume $\Lambda = 30$, this leads to values of $(k)_p \approx 1.8 \cdot 10^{11}$ N/m, which is high for existing, concrete structures. This confirmed that the structure's dynamic response can be neglected, leading to a conservative approach in the measurement of the resulting force.

3.7 Model validation

Once the construction of the experimental set-up was completed, preliminary tests were conducted to validate the facility and the applicability of the results to reality. The following issues were assessed:

- Profile repeatability for both dry bed surges and wet bed bores
- Bi-dimensionality in the lateral direction for both dry bed surges and wet bed bores
- Validation of the measurements carried out with the Force Plate
- Repeatability of force measurements

3.7.1 Wave profile repeatability

Preliminary tests were conducted to validate the results of the experimental model. Repeatability for both the dry bed surges and the wet bed bores, along with a verification of the uniformity of the wave profile in the transversal direction of the flume were investigated. As such, representative results of the wave height are presented in Figure 3.24 for dry bed surge (8 repetitions) and in Figure 3.25 for wet bed bore (5 repetitions). Details of the generated waves are presented in Table 4.1. For both scenarios, the wave height was measured at US 7, which was located 13.85 m from the channel inlet. Wave profiles were normalised using the impoundment depth (d_0) and the dimensionless time $(g/d_0)^{0.5}$. Results showed similar profiles for all tests with values of normalised standard deviation (σ/d_0) of less than 5 % for wet bed bores and less than 3 % for dry bed surges (Figure 3.26). These results are similar to those of Shafiei et al. (2016) for bores. Some differences were observed in terms of surface turbulence, however oscillations remained within the same range and the spectral distribution of oscillating frequency was similar for all tests (Appendix B).
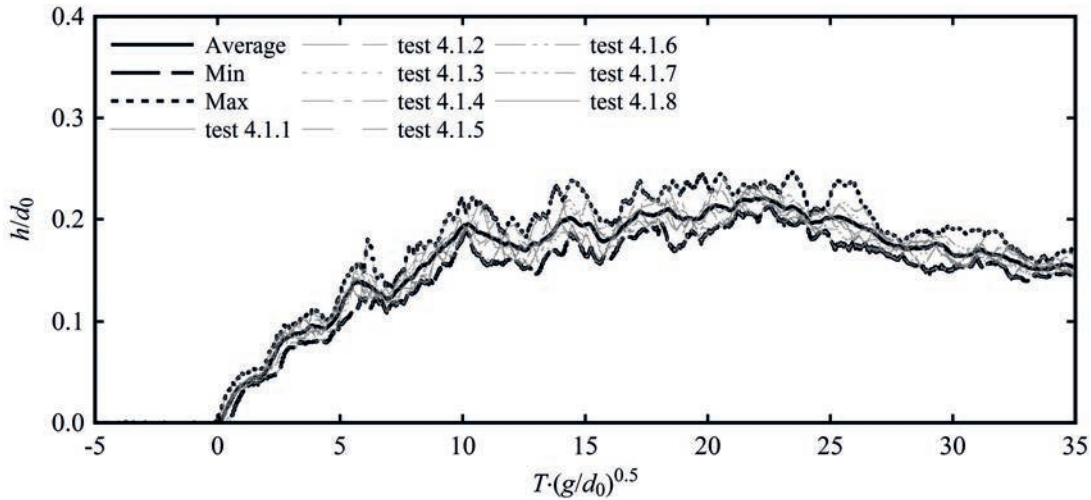
Figure 3.24 – Repeatability of a dry bed surge (d_0 = 0.82m) measured at US7 (x = 13.85 m)
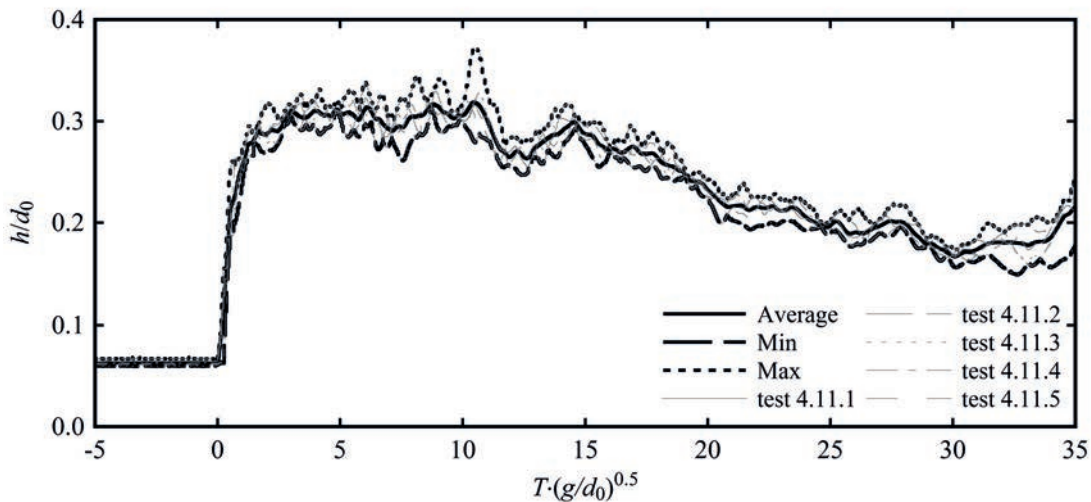
Figure 3.25 – Repeatability of a wet bed bore (h_0 = 0.05 m, d_0 = 0.82, test 4.11) measured at US7 (x = 13.85 m)

3.7.2 Wave longitudinal uniformity

The bi-dimensionality, or longitudinal uniformity, of the wave was verified by measuring the wave profiles at two locations in the transversal direction of the channel, *i.e.* at y/B = 0.5 and 0.25; both sensors were located at a distance of x = 13.35 m from the channel inlet. The comparison between the two sensors is presented in 3.27, where a good agreement between both profiles can be observed. An identical arrival time indicated that the front celerity of the dry bed surge was uniform in the transversal direction. Similarly to Figure 3.24 and 3.25, some minor differences were observed in terms of surface turbulence. Visually, the uniformity of both the dry bed surged and the wet bed bore is shown in Figures 4.3 and 4.7, respectively.
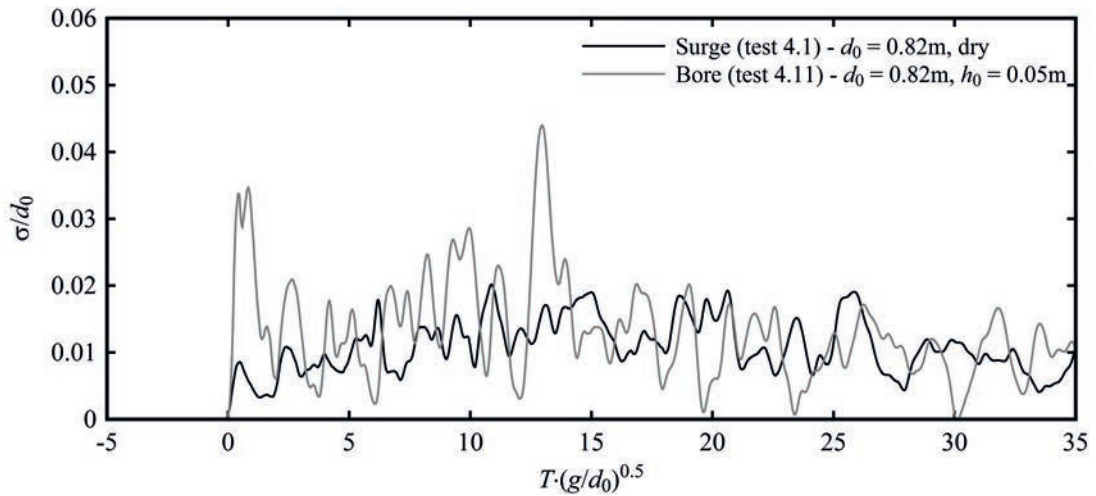
Figure 3.26 – Standard deviation σ obtained for multiple waves on both dry (8 tests) and wet bed (5 tests) with identical releasing conditions
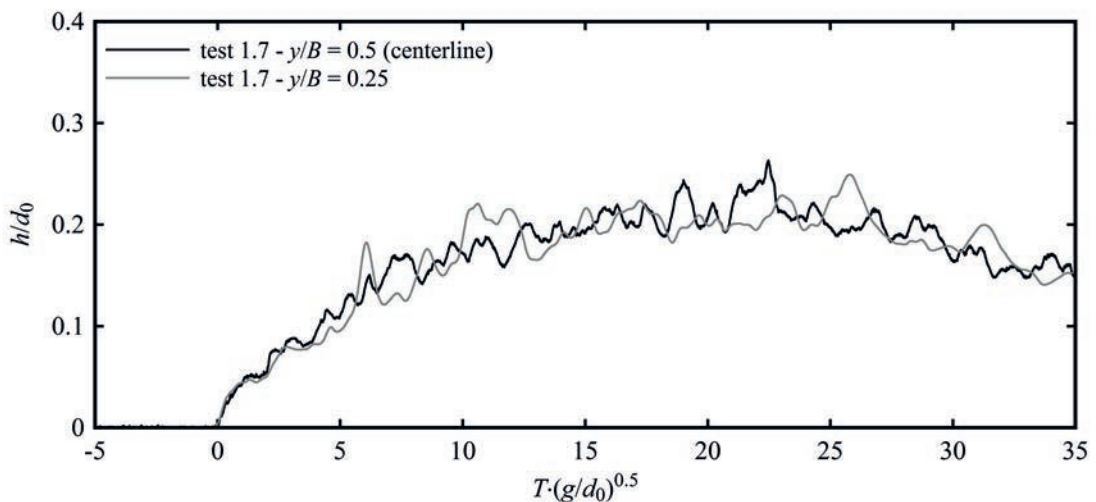
Figure 3.27 – Lateral uniformity for dry bed surges ($d_0 = 0.82$ m, dry, $x = 13.35$ m)

3.7.3 Opening time

The time origin was set as the opening time of the pipes, identified when a reduction in water elevation in the upper reservoir was measured. The wave arrival time at a specific location was set when a local wave height $h > 0.01$ m was recorded.

3.7.4 Force measurements

Although no calibration was needed for the AMTI MC6-1000 Force Plate, the recorded values were compared to some known forces in order to validate the measurements. In both x- and

y- directions, force measurements were successfully compared to those provided by a HCB Hanging Scale Device (KERN, Germany) with a precision of ±0.1 N.

Vertical forces F_z

Some preliminary tests were carried out for a wave without the building. The measured vertical forces are presented in Figure 3.28 and Figure 3.29, for a dry bed surge and a wet bed bore, respectively. The vertical forces F_z along the *z*-axis were later compared to the weight of the water depth with the corresponding wave height, calculated using Eq. 3.8.

$$F_z = h \cdot B^2 \cdot g \cdot \rho \tag{3.8}$$

Good agreement was observed for both the dry bed surge (Figure 3.28) and the wet bed bore (Figure 3.29). The latter presented some differences in the wave front, attributed to the highly aerated flow in this region. These differences can be observed in Figure 3.29, where the value predicted by the formula using the measured height overestimated the real value.
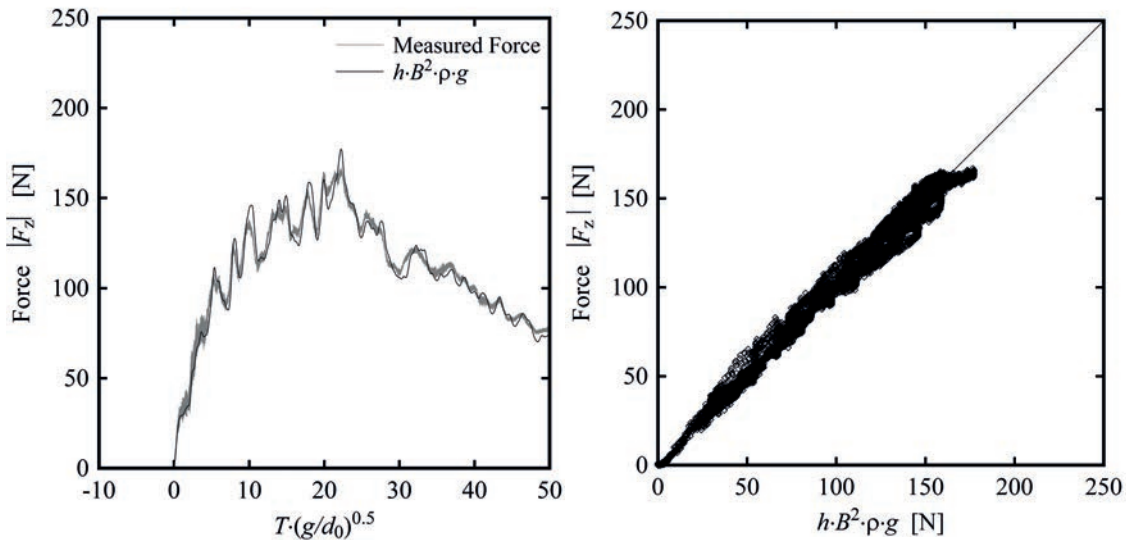
Figure 3.28 – Validation of force measurements F_z in the vertical direction for a dry bed surge ($d_0 = 0.82$ m, test 4.1)

Force repeatability

The repeatability of the force measurements in the horizontal direction was also tested. For this, the horizontal forces F_x were recorded during the impact of the same wave on both an impervious structure and a porous structure. The results obtained for a dry bed surge ($d_0 = 0.82$ m) on a porous structure ($P_{tot} = 42.24$ %) are presented in Figure 3.30, and those for a wet bed bore ($d_0 = 0.82$ m, $h_0 = 0.03$ m) on an impervious structure in Figure 3.31. Good repeatability of
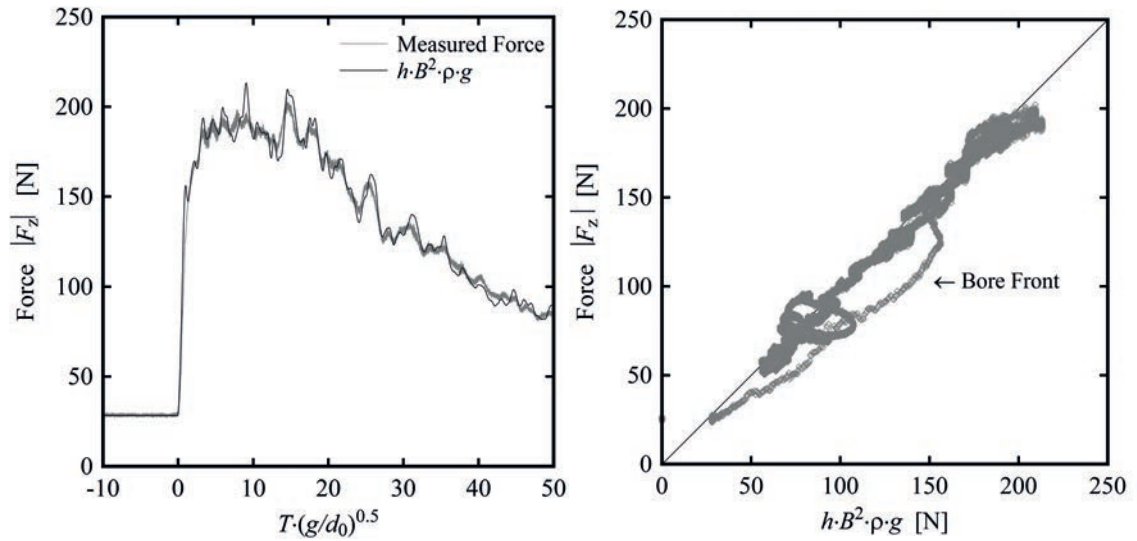
Figure 3.29 – Validation of force measurements F_z in the vertical direction for a wet bed bore ($d_0 = 0.82$ m, $h_0 = 0.03$ m, test 4.11)

the force measurements was observed for both scenarios, with standard deviation (σ) values around 13% for both surges and bores.
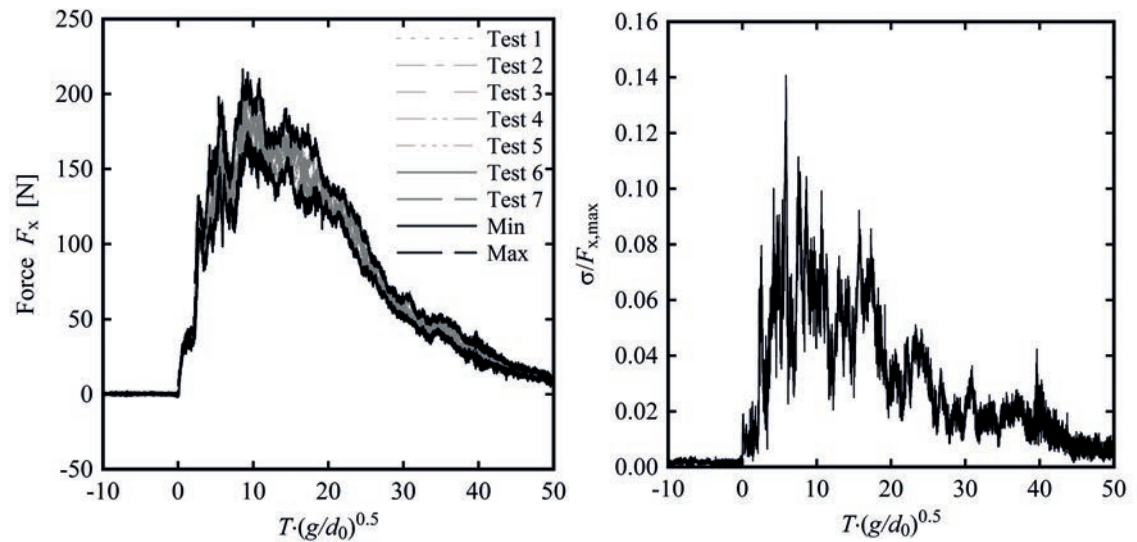
Figure 3.30 – Repeatability and standard deviation values (σ) of force measurements F_x for 7 dry bed surges ($d_0 = 0.82$ m) impacting against a porous structure ($P_{tot} = 42.24$ %)
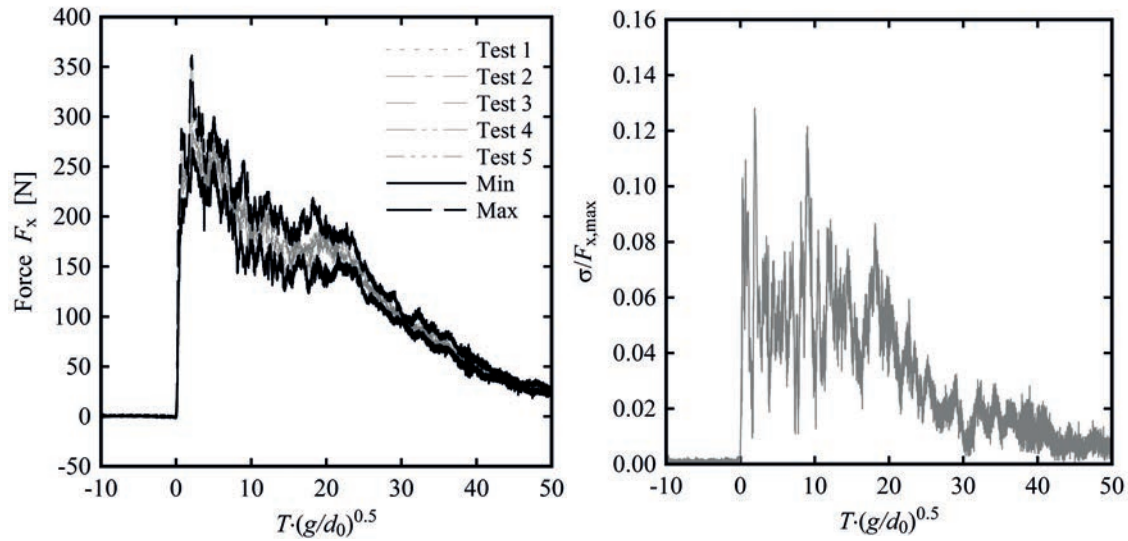
Figure 3.31 – Repeatability and standard deviation values (σ) of force measurements F_x for 5 wet bed bores ($d_0 = 0.82$ m, $h_0 = 0.03$ m, test 5.5) impacting against an impervious structure ($P_{tot} = 0$ %)

3.8 Parameters and test procedure

To obtain a full understanding of the processes the main parameters identified were varied, namely:

- Channel configuration (dry bed surges vs. wet bed bores)
- Wave hydrodynamic properties (h, U)
- Building height (H_B)
- Building surface porosity (P)
- Blockage ratio ($\beta = W/B$)

These parameters are summarized in Table 3.6 with the corresponding tested values and sections of the report where the findings are presented and discussed.

Parameter			Tested values	Section
Initial still water depth	h_0	[m]	0 (dry), 0.01, 0.03, 0.05 (wet)	Chapter 4 & 5
Building height	H_B	[m]	0.3, 0.6	Chapter 6
Building porosity	P_{tot}	[%]	0, 17, 31.34, 34, 42.24, 60, 84	Chapter 7
Blockage ratio	β	[-]	4.67, 1.56	Chapter 7

Table 3.6 – Range of the tested parameters

For each test the following procedure was strictly followed:

1. Release gates are securely locked.
2. The upstream tank is filled.
3. The water level in the lower reservoir is controlled through the drainage pipe to evacuate potential leaks coming from the upper reservoir. For tests over wet bed, the initial still water depth h_0 is imposed through the regulation of the downstream sill.
4. The settings of the Force Plate are verified and adjusted to the expected measuring range, if necessary.
5. The good performance of the US sensors is verified.
6. The UVP settings are set and the measure is launched (system starts acquiring data, but not registering).
7. Difference in potential between the wires is imposed in the hydrogen bubble generator.
8. Video recording devices are activated.
9. Force Plate signal is set to zero.
10. Measurements is launched; the trigger signal (5V) automatically activates the UVP recording.
11. Wave is generated manually.

For the tests focusing on wave hydrodynamics (Chapter 4), the same procedure was followed, without the force measurements. After the test, measurements are stopped and the facility prepared for the following test. In case of dry bed scenarios, water is evacuated and the channel is left drying.

4 | Wave hydrodynamics

4.1   Overview

This chapter investigates and validates a new generation system for dry bed surges and wet bed bores. There exist multiple techniques to experimentally generate such waves and the present study focuses on the generation of tsunami-like inundation conditions through the vertical release of a water volume. A detailed methodology to hydraulically characterize the generated waves in terms of their wave heights and flow velocities is presented and good agreement with the classical dam-break case for both dry surges and wet bed bores is demonstrated. Due to the importance of estimating the impact forces induced by such waves, particular attention is given to the wave front celerity and the velocity profiles measured behind the wave front. These were found in agreement with Prandtl's power law for open channel flows and in-depth measurements allowed to define an expression to estimate flow deceleration behind the wave front. Along with considerations on the Froude number and momentum, this chapter provides relevant information on the wave hydrodynamic properties to assist engineers to design safer infrastructures in areas prone to such extreme loading.

The main objectives of this chapter are the following:

1. To present and discuss the hydraulic behaviour of dry bed surges and wet bed bores generated using the vertical release technique.
2. To compare the generated surges and bores with existing theories developed for classical dam-break waves.
3. To provide an insights of the hydrodynamic behaviour of surges and bores in terms of front celerity, velocity profiles and deceleration behind the wave front.
4. To present and discuss the temporal behaviour of the Froude number and the momentum flux per unit width for both surges and bores.

	Initial water depth, h_0	Number of pipes	Impoundment depth d_0	h_0/d_0	Repetitions	
Dry	0.000	3	0.82	-	8	test 4.1
		2	0.63	-	2	test 4.2
		1	0.40	-	2	test 4.3
Wet	0.001	3	0.82	0.0012	1	test 4.4
	0.010	3	0.82	0.0122	3	test 4.5
		2	0.63	0.0159	2	test 4.6
		1	0.40	0.0250	2	test 4.7
	0.030	3	0.82	0.0366	4	test 4.8
		2	0.63	0.0476	2	test 4.9
		1	0.40	0.0750	2	test 4.10
	0.050	3	0.82	0.0610	5	test 4.11
		2	0.63	0.0794	2	test 4.12
		1	0.40	0.1250	2	test 4.13
	0.100	3	0.82	0.1219	1	test 4.14
Max	0.100	3	0.82	0.1219	8	-
Min	0.000	1	0.40	0.0012	1	-

Table 4.1 – Experimental program for the characterization of wave properties

For this, 38 tests were conducted, as detailed in Table 4.1. For the bores, all tests were performed for $h_0/d_0 < 0.13$, for which the influence of the initial still water depth h_0 was minimal.

4.2 Analogy with dam-break theory

Preliminary tests showed the key-role of the initial discharge Q_0 released into the channel for the definition of the main hydrodynamic properties of the produced wave. The use of 1, 2 or 3 pipes for the sudden release of the water allowed to control the initial discharge Q_0, producing surges and bores with different wave height h and front celerity U. A comparison with the theoretical solution proposed by Ritter (1892) for dam-break waves was conducted. Similarly to what was discussed by Chanson et al. (2002), through the initial discharge Q_0, an equivalent impoundment depth d_0 was obtained as:

$$d_0 = \frac{9}{4} \left(\frac{Q_0^2}{gB^2} \right)^{\frac{1}{3}} \tag{4.1}$$

where g is the gravity constant, B is the channel width and Q_0 is the initial discharge released into the channel. This was calculated as the outflow discharge from the upper reservoir, obtained as a function of dH_R/dt, where H_R is the water depth measured by the US0 (Figure 3.2). The graphs obtained for all 3 scenarios (1, 2 and 3 pipes) are shown in Figure 4.1 and the computed values of Q_0 presented in Table 4.2. Given the non-linear behaviour of the reservoir emptying process, the chosen values showed good agreement during the initial time, leading to some error in the latest phases of the test. T^* was defined as the dimensionless time after which the hypothesis of a constant released discharge was no longer satisfied ($H_R/H_{R,0} = 0.2$).
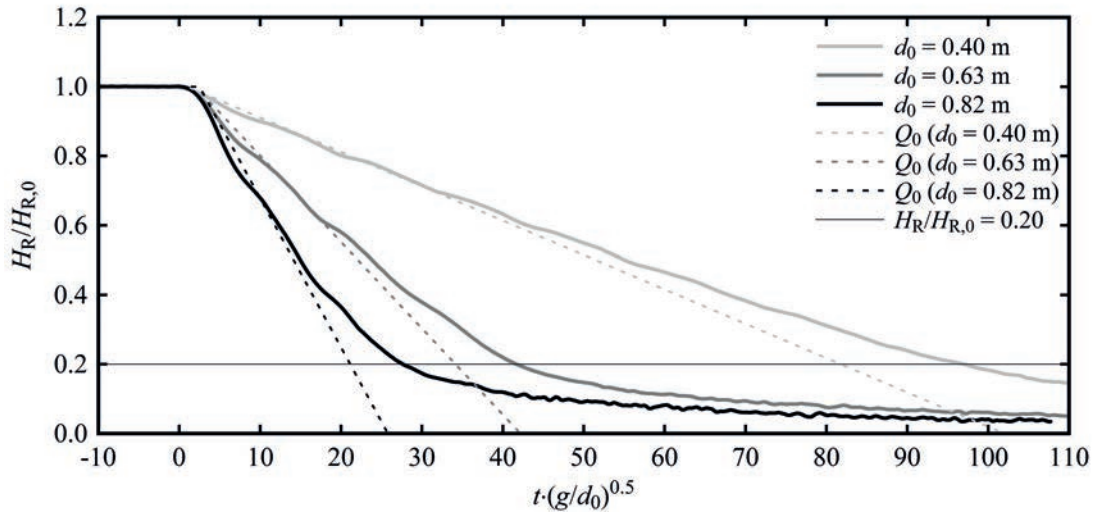
Figure 4.1 – Measurements of the water depth in the upper reservoir for the opening of 1, 2 and 3 pipes ($d_0 = 0.40$, 0.63 and 0.82 m respectively).

These initial discharges were also successfully compared with the theoretical values using the continuity equation:

$$Q_0 = A_P \cdot V_P \tag{4.2}$$

where A_P is the pipe surface and V_P is the velocity through the pipes, calculated as:

$$V_P = \sqrt{2g\left(\Delta H_R - \xi \Delta H_R\right)} \tag{4.3}$$

The head loss at the inlet of the pipes was assumed to be $\xi = 0.5$. If the friction losses through the PVC pipes and those in the trajectory between the pipes and the channel inlet are neglected, then the initial discharge can be obtained as

$$Q_0 = A_P \cdot \sqrt{2g\Delta H_R} \tag{4.4}$$

and the computed values are presented in Table 4.2.

N. of pipes	Pipe surface A_P [m^2]	Head [m]	Initial discharge Q_0 [m^3/s]	Equivalent impoundment depth d_0 [m]	T^*
1	0.073	2.1	0.34	0.40	97.1
2	0.146	2.1	0.68	0.63	41.8
3	0.219	2.1	1.03	0.82	27.8

Table 4.2 – Equivalent impoundment depths obtained for the vertical release technique through the progressive use of 1, 2 and 3 pipes

For a constant volume in the upper reservoir, a smaller released discharge allowed a longer time before the sudden reduction took place, resulting into waves with a longer duration. Higher discharges were associated with shorter durations, and the generated waves were characterised by an impulse behaviour.

Measurements of the water depth at the channel inlet ($x = 0$ m) were conducted to validate the comparison with the theory of Ritter (1892). The use of an additional US sensor at $x = 0$ m allowed to capture an oscillating behaviour of the flow around $h/d_0 = 4/9$, as shown in Figure 4.2, for the scenarios with 1, 2 and 3 pipes. These water depths are similar to those predicted by Ritter (1892) at the inlet of an infinite reservoir, thus implying close similarity between surges/bores produced with the classical dam-break and the vertical release techniques. Figure 4.2 shows that, after a certain time, the measured flow depth in the channel suddenly decreased as a consequence of the emptying of the upstream reservoir (Figure 4.1).
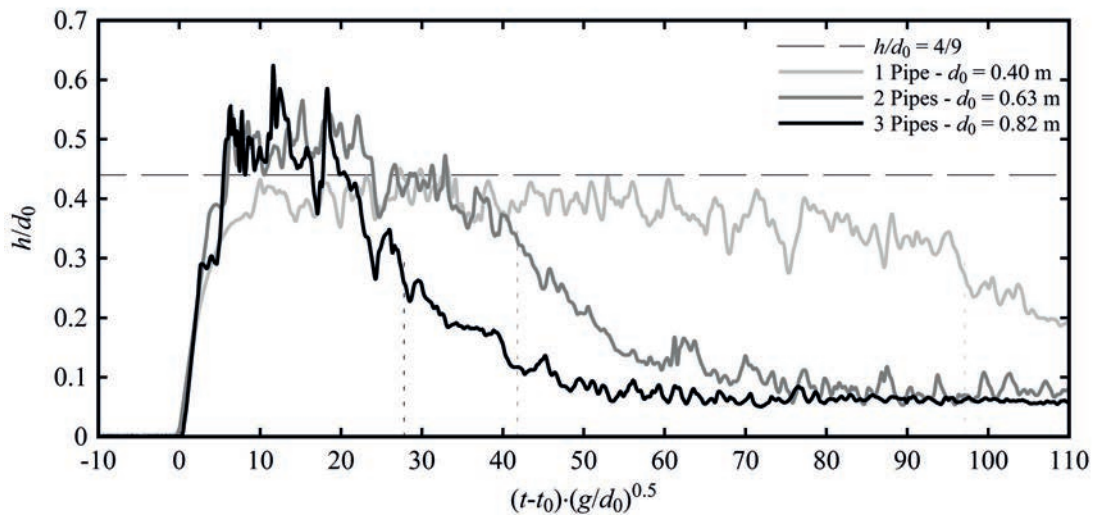
Figure 4.2 – Measurements of the water depth h at the channel inlet ($x = 0$ m) for three dry bed surges generated with the vertical release technique using 1, 2 and 3 pipes. The values of the released discharges are presented in Table 4.2.

4.3 Water surface profiles

The main characteristics of dry bed surges and wet bed bores produced with the vertical release technique are discussed herein. The difference in behaviour between dry bed surges and wet bed bores was previously presented in Section 2.3. For both types, water surface profiles were measured using seven US sensors located along the longitudinal axis of the channel (Figure 3.2). The synchronisation of the acquisition system allowed to combine all data and obtain a spatio-temporal evolution of the depth profile. In the following sections, the surges and the bore produced herein are also compared to the dam-break wave propagating on dry and wed bed, in the light of some relevant literature in the domain.

4.3.1 Dry bed surges

The propagation of the surge on the dry smooth channel visually appeared as a thin water layer followed by a constant rise in water depth until a maximum value was reached. Subsequently, the water level started to decrease. The surge front propagated uniformly and, visually, little to no aeration was observed, as shown in Figure 4.3.
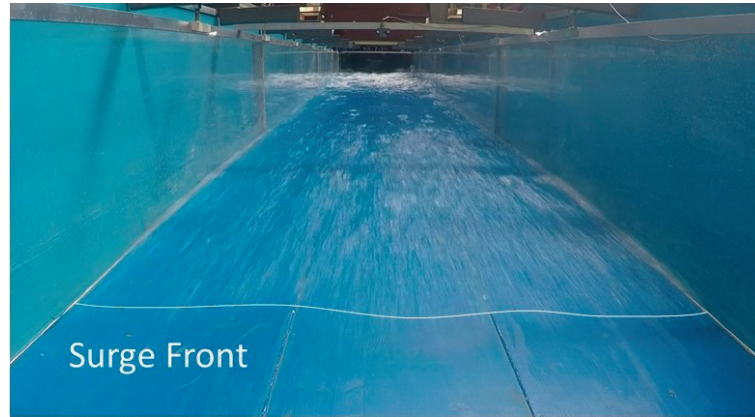
Figure 4.3 – Dry bed surge resulting from an impoundment depth $d_0 = 0.82$ m

The temporal development of the height of a specific surge ($d_0 = 0.82$, test 4.1) propagating over a dry bed with a flat smooth surface is presented in non-dimensional form in Figure 4.4. Each curve corresponds to a measurement location, with US 7 being located furthest downstream. A decrease of the maximum depth was observed as the surge propagated along the channel. This was attributed to the viscous and diffusive behaviour of the flow. The similarity of the profiles further downstream the channel ($x > 10$m) indicated that the surge was fully developed and that a quasi-uniform condition was reached. The observed surface fluctuations were secondary waves attributed to the turbulence of the flow. More informations concerning the surface fluctuating behaviour can be found in Appendix B.3. Some oscillations of the free surface due to the releasing mechanism were observed in the upstream section of the channel at $0 < x < 2$ m. However, they disappeared after the wave travelled a few meters further downstream from the channel inlet.

The longitudinal water surface profiles observed when the surge reached locations $x = 13.60$ m (US6) and $x = 13.85$ m (US7) were obtained for multiple dry bed surges with identical initial release conditions. The seven (7) water depth measurement locations along the channel (Figure 3.2) allowed to obtain multiple data sets that were compared with the theoretical parabolic profile of Ritter (1892) in Eq. 4.5. The experimental points are presented in Figure 4.5 using the non-dimensional stream-wise displacement defined as $x/[t \cdot (g d_0)^{0.5}]$.

$$\frac{h}{d_0} = \frac{1}{9} \cdot \left(2 - \frac{x}{t \cdot \sqrt{g d_0}} \right)^2 \tag{4.5}$$

Although some minor scattering was found in the upstream part of the surge due to water
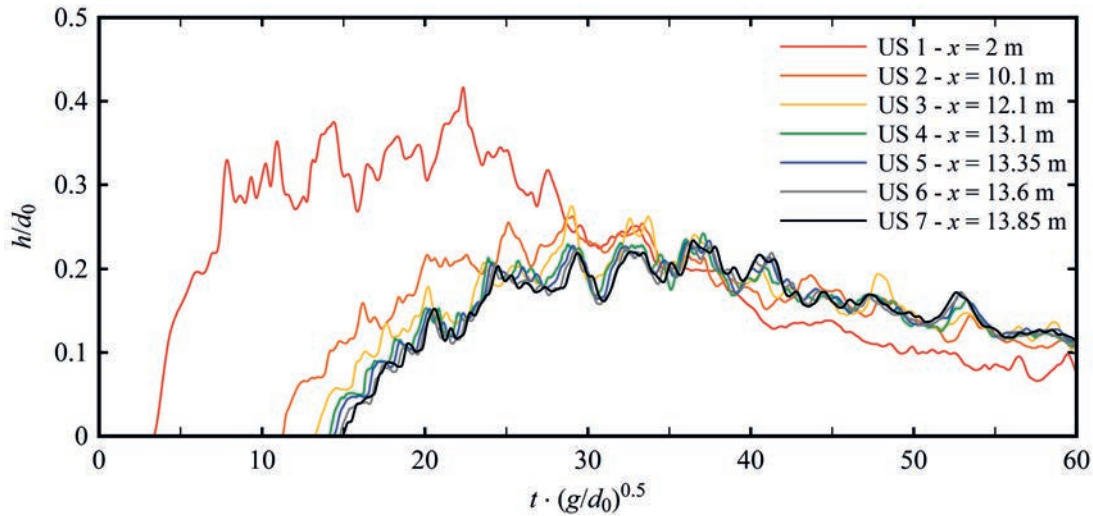
Figure 4.4 – Evolution of a dry bed surge with impoundment depth d_0 = 0.82 m (test 4.1).

surface fluctuations, good agreement between all tests was observed. A marginal variation occurred in the tip region for scenarios with different d_0 which is due to different propagating velocities.
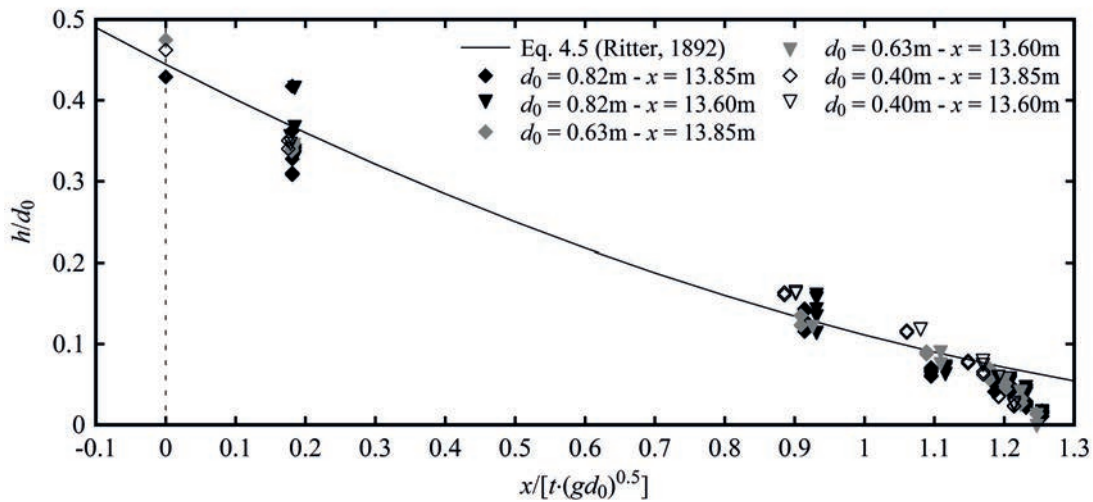
Figure 4.5 – Longitudinal dimensionless water surface profiles when the wave reached two measurement locations (US6: x = 13.60 m and US7: x = 13.85 m). Comparison of all generated surges (d_0 = 0.82 m, 0.63 m and 0.40 m) with the theoretical solution of Ritter (1892).

Figure 4.6 focuses on the wave tip region, where the higher density of US sensors allowed for a more precise investigation of its shape. The experimental points obtained for multiple surges with different impoundment depths (d_0) measured at various channel locations were compared with the theoretical solutions of Whitham (1955) presented in Eq. 2.12 with a friction

factor $f = 0.021$, a front celerity of $U = 3.56$ m/s, for $d_0 = 0.82$ m and a deceleration $\partial U / \partial t = 0.15$ m/s^2. The latter was calculated from the linear interpolation of the average velocity profiles obtained from the UVP measurements. Good agreement was also found with the theoretical solution of Chanson (2009) in Eq. 2.14 for the same friction factor. The results are presented in Figure 4.6, where good agreement between all data and curves can be observed, indicating consistency with literature. Furthermore, the experimental points were also compared to prototype points derived from a propagating tsunami-induced inundation advancing inland during the 2004 Indian Ocean Tsunami (Chanson, 2006). The good agreement observed in Figure 4.6 indicates that the dry bed surges generated with the vertical release technique are therefore representative of real tsunamis overland flow observed during such actual events.
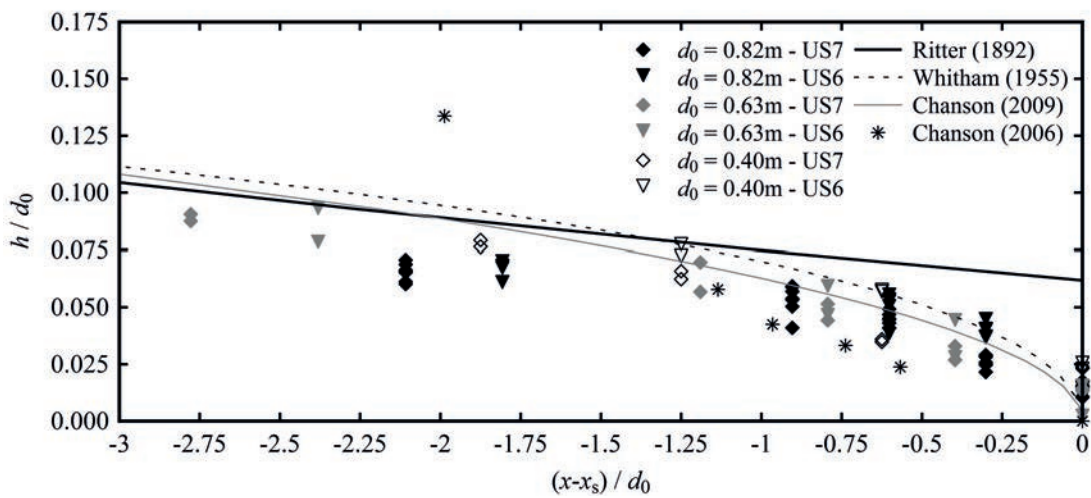
Figure 4.6 – Comparison of the measured longitudinal wave profiles with the theoretical solution of Ritter (1892), Whitham (1955), Chanson (2009) and prototype data Chanson (2006) in the wave tip region (US7: $x = 13.85$ m, US6: $x = 13.60$ m).

4.3.2 Wet bed bores

The difference between the dry bed surges and wet bed bores was pointed out in Figure 1.4b. Visually, the propagating bore was similar to a turbulent and highly aerated hydraulic jump (Figure 4.7) with periodic surface fluctuations in the form of lumps being ejected and with significant air entrainment observed in the front region. Similar observations were presented by Leng and Chanson (2015) for positive surges and tidal bores. According to Yeh and Mok (1990), the front roller is formed by the flow separation initiated at the front toe resulting from the streamline divergence caused by the sudden raise in water depth. Furthermore, the same authors observed a "*generation-advection cycle*", suggesting that eddies formed inside the roller were later advected in the flow, where a turbulence stretching in the slanting vertical direction was detected (Yeh and Mok, 1990). Air was entrained behind the bore front for a length L_r, where air bubbles could be observed, whereas further behind mainly clear water appeared.

Figure 4.7 – Wet bed bore with d_0 = 0.82 m and initial still water depth h_0 = 0.03 m (test 4.8)

The development of a wet bed bore propagating over a still water depth (h_0) was investigated at different locations along the longitudinal axis of the channel and its surface-time history is presented in Figure 4.8 for a specific case (d_0 = 0.82 m, h_0 = 0.05 m, test 4.11). A substantial difference in behaviour when compared with the dry bed surges was observed as bores were characterized by a sudden rise in water height at the front. For all wet bed bores, a temporal conservation of maximum depth was observed during the propagation along the channel. This resulted in a uniform translation of the bore shape.
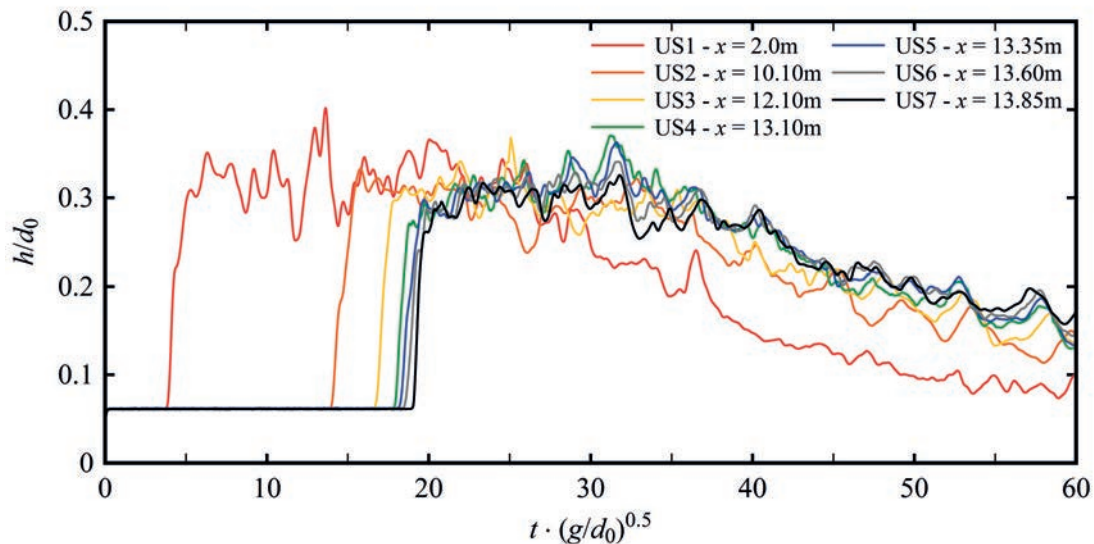
Figure 4.8 – Time evolution of a bore on wet bed (d_0 = 0.82 m, h_0 = 0.05 m, test 4.11) at different locations along the longitudinal axis of the channel.

The influence of the initial still water depth h_0 on the propagating bore was investigated by testing different values ranging from h_0 = 0.001 to 0.1 m, where the lower value represented a bore propagating over a thin water layer remaining from a previous test. Multiple impoundment

depths d_0 were tested, resulting into ratios of $0.0012 < h_0/d_0 < 0.1219$ (Table 4.1). Similarly to Chanson et al. (2003) and Nouri et al. (2010), results showed that, even for a thin still water layer, the properties of the propagating bore were different from those propagating over a dry bed surge. For still water depths larger than 0.03 m, similar profiles were measured, suggesting that beyond this value h_0 had a lesser influence. For decreasing initial still water depths ($h_0 < 0.03$ m), a transitional bore, whose behaviour became more similar to that of a dry bed surge with milder front steepness, was observed (Figure 4.9). The shift in arrival time revealed different bore front celerity magnitudes, depending on the initial still water depths h_0.
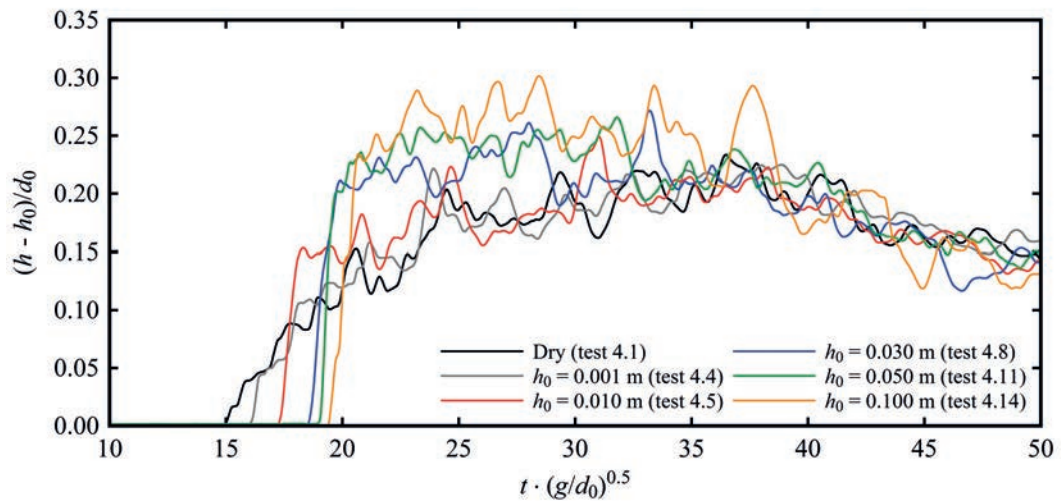
Figure 4.9 – Bore profiles for waves with different initial still water depths at $x = 13.85$ m (US7) for $d_0 = 0.82$ m, all profiles brought down to $h - h_0$ (test 4.1, 4.4, 4.5, 4.8, 4.11 and 4.14).

As previously discussed by Stoker (1957) the temporal evolution of a dam-break bore propagating over a wet bed can be divided into 5 main regions (downstream to up-stream): (0) the initial still water depth h_0; (1) the turbulent bore front; (2) a "*plateau*", *i.e.* a region with almost constant water height h_2; (3) a far-back region where the Ritter (1892) theory for a surge propagating on dry bed can be applied, and (4) the upstream reservoir where $h = d_0$. Figure 4.10 provides, for all experimental tests, the longitudinal profiles of the water surface (arrival time is defined when a threshold of $h = h_0 + 0.01$ m was registered at US7, $x = 13.85$). These are also successfully compared with Ritter (1892) in the far-back region and with Stoker (1957) for dam-break waves propagating over wet bed with zero initial velocities in both the upstream and downstream reservoirs. The good agreement observed in Figure 4.10 proves that, similarly to what was previously shown for surges, the vertical release technique produces bores which are comparable to the classical dam-break scenario. The height of the *plateau* region (h_2, horizontal lines in Figure 4.10) was predicted using the numerical approximation deduced from the continuity and momentum equations by Chanson et al. (2000) presented in Eq. 2.16 and compared to the experimental points in Figure 4.11. From the same figure, one can notice that, for all performed tests the ratio h_0/d_0 was lower than the critical value $h_0/d_0 = 0.138$, implying that the initial discharge Q_0 was in-dependent of the initial water depth, h_0.
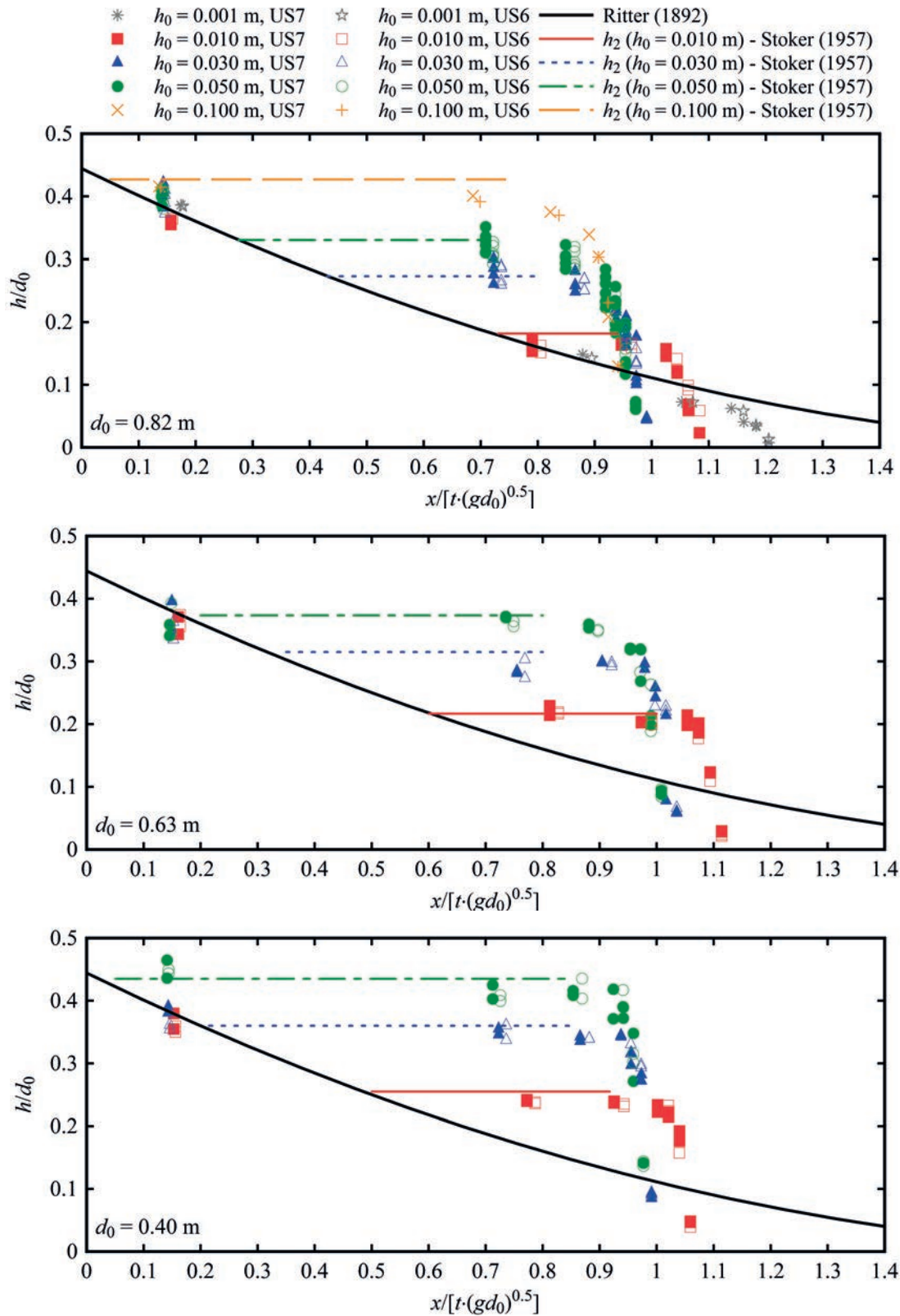
Figure 4.10 – Longitudinal free surface profile for bores with different values of h_0 and d_0; comparison with Ritter (1892) and h_2 obtained with Eq. [5] (Chanson et al., 2000); measurements at US 7 and US 6: (top) $d_0 = 0.82$ m, (middle) $d_0 = 0.63$ m, (bottom) $d_0 = 0.40$ m
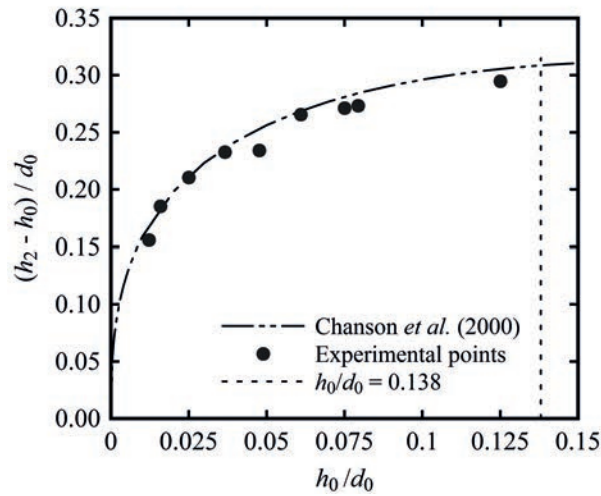
Figure 4.11 – Comparison of the experimental points of the plateau height (h_2) with the approximation proposed by Chanson et al. (2000) in Eq. 2.16.

In Figure 4.12 , for all tests performed on wet bed and for all values of h_0 and d_0, the shape of the bore front was normalised using h_2 and the roller length L_r and good agreement between all curves was observed. Given the differences in front celerity and flow depth, the length of the roller L_r was identified for every profile, using the time taken by the bore to reach the plateau height h_2. The roller length L_r was then derived using the bore celerity as $L_r = U \cdot t$. The experimental results were successfully compared to formulae found in literature and the longitudinal free-surface elevations showed a self-similar profile in the form of Eq. 2.18. For the present study the best fit was found with an exponent $N = 0.482$, which is located between the value $N = 0.441$ proposed by Chanson (2011) for hydraulic jumps, and $N = 0.540$, suggested by Wang and Chanson (2015).
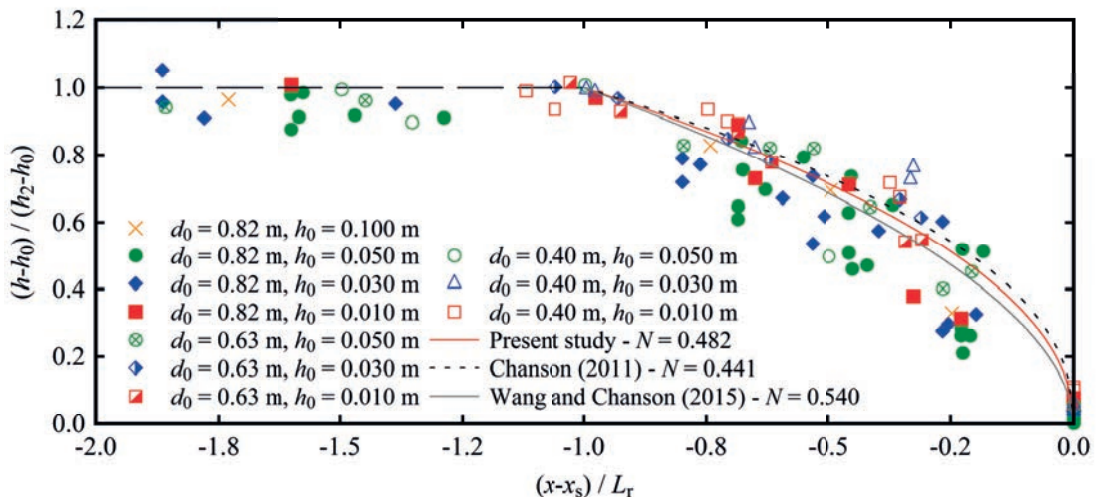
Figure 4.12 – Normalised bore front profiles for various values of d_0 and h_0. Comparison between experimental data for the proposed vertical release technique and the empirical formulas from Eq. 2.18 by Chanson (2011) and Wang and Chanson (2015) for hydraulic jumps.

4.4 Velocities

Two velocities were analysed in the present study:

1. The surge/bore front celerity U derived from the spatio-temporal advancement of the wave front as detected by the Ultrasonic distance Sensors (US) in Section 4.4.1
2. The velocity profiles within the wave, measured using the Ultrasonic Velocity Profilers (UVP) in Section 4.4.2

4.4.1 Front celerity

The average front celerity of the propagating wave was estimated using the measurements of the depth profiles over time:

$$U = \frac{\Delta x}{\Delta t} \tag{4.6}$$

where Δx is the distance between two US sensors and Δt is the difference in the wave front arrival time. The measurement locations corresponded to the location of the US sensors shown in Figure 3.2. The average front celerity is considered for each sensor (US2 to US7) relative to US1, which is located at $x = 2$ m from the channel inlet. The average front celerities obtained for **dry bed surges** were compared to formulae commonly used in design codes and practice (Figure 4.13). These formulae were mostly derived from physical models at laboratory scale and are presented in the form of Eq. 2.19, where α is a coefficient, whose values are presented in Table 2.2. This comparison proved that the waves generated with the proposed vertical release technique had celerity values consistent with other generation mechanisms described in literature. Their range is confined by values obtained from FEMA55 (2000) (upper bound) and CCH (2000) (lower bound). The experimental results obtained for the present study showed the best agreement with $\alpha = 1.25$.
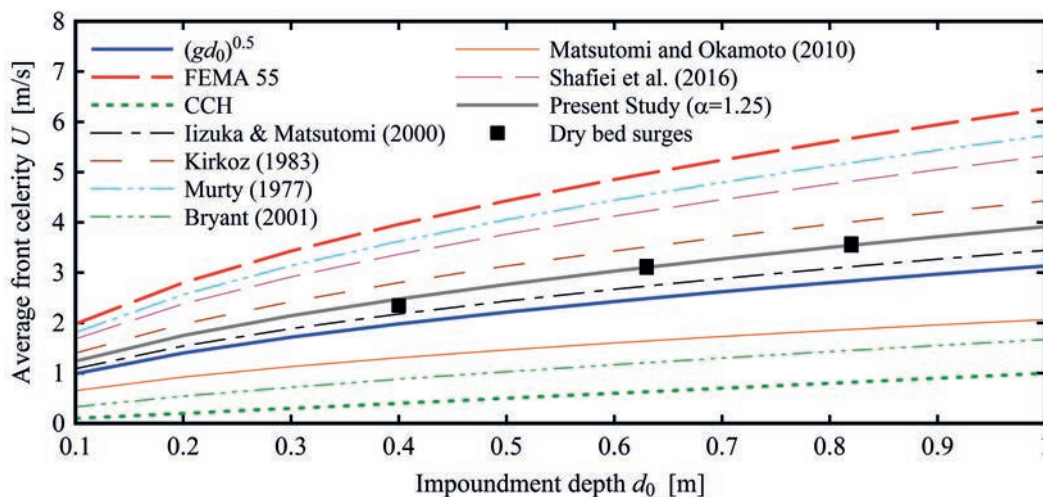
Figure 4.13 – Comparison of the measured average front celerity U with formulae from literature for dry bed surges (all values at model scale).

For the same release conditions, **wet bed bores** propagated with a slower front celerity when compared to that of the dry bed surges. This difference in behaviour can clearly be observed in Figure 1.4b for the case of a tidal bore, where the portion of the wave on dry bed propagated faster than the portion propagating over wet bed. The front celerity U of a bore moving over wet bed was a function of the initial still water depth (h_0) and small values of h_0 corresponded to velocities close to those observed for the dry bed condition, which represented its upper limit. The experimental wave front celerity U obtained for the wet bed bores with various values of h_0 and d_0 was compared with a theoretical solution derived from the momentum equation in Eq. 2.20 presented by Stoker (1957) and with the empirical approximation of Montes (1998), presented by Chanson (2004) in Eq.2.21 as a function of the initial equivalent impoundment depth d_0, the initial still water depth h_0 and the plateau height h_2 obtained from Eq. 2.16. Very good agreement between all formulae can be observed in Figure 4.14. Contrary to dry bed surges, this implies that, for wet bed bores, a precise prediction of the front celerity can be achieved through Eq. 2.20 and 2.21.
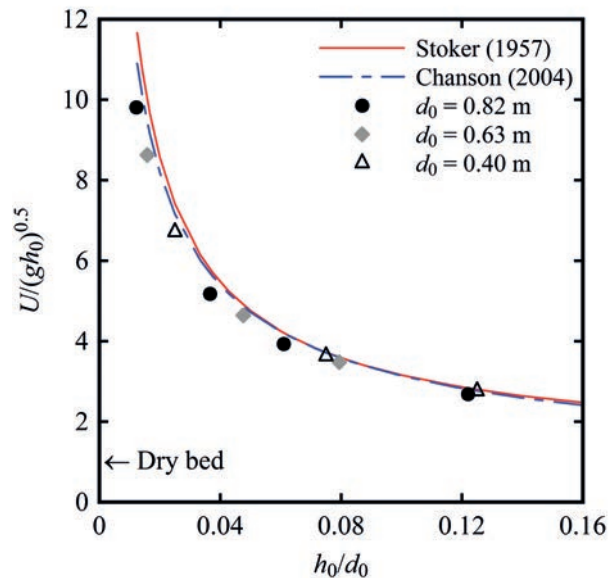
Figure 4.14 – Average bore front celerity (U) as a function of the initial still water depth (h_0). Experimental results are compared to the momentum equation (Eq. 2.20) and the approximation by Chanson (2004) in Eq. 2.21 for impoundment depths $d_0 = 0.82$ m (tests 4.4, 4.5, 4.8, 4.11 and 4.14), $d_0 = 0.63$ m (tests 6, 9 and 12), $d_0 = 0.40$ m (tests 4.7, 4.10 and 4.13).

4.4.2 Velocity profiles

Beside the recent contribution of Leng and Chanson (2017b,a), only few studies of the in-wave velocity profiles are available. For this reason a constant vertical velocity profile is commonly assumed (Whitham, 1955). Similarly to Meile et al. (2008, 2011), a UVP probe installed in the channel bottom measured the internal instantaneous velocity profile of the propagating surge/bore. Some representative velocity profiles are shown in Figure 4.15, indicating typical profiles associated with turbulent open channel flows.
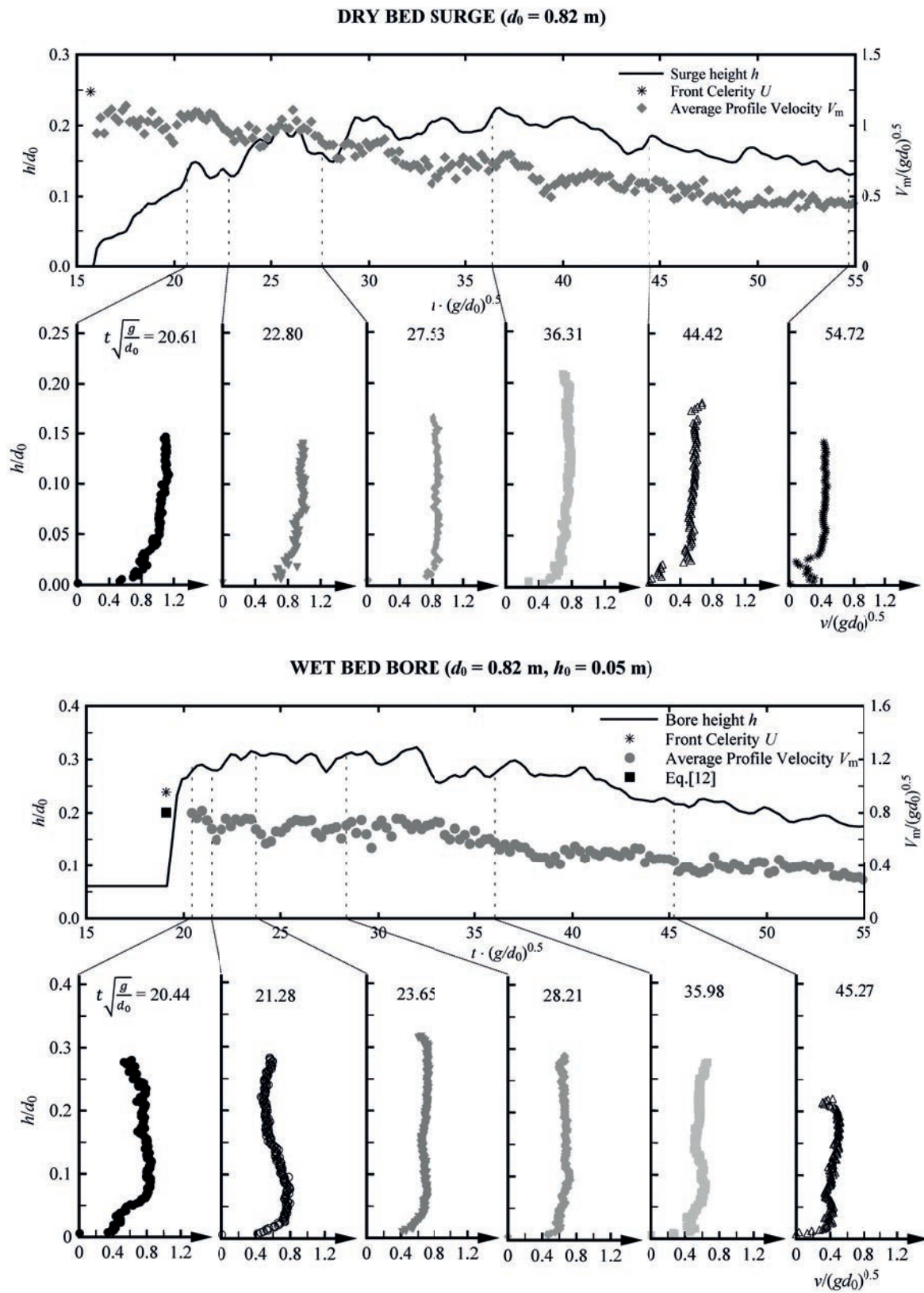
Figure 4.15 – Wave height (h), depth-averaged velocity (V_m) and velocity profiles at specific times for: (top) test 4.1: dry bed surge $d_0 = 0.82$ m and (bottom) test 4.11: wet bed bore $d_0 = 0.82$ m, $h_0 = 0.050$ m, both measured at US7, $x = 13.85$ m from channel inlet.

A well-defined boundary layer, followed by an upper sector where almost constant velocities were observed are also included. These results confirmed that surges travelled faster than bores.

For all profiles, the depth-averaged velocity (V_m) was computed as:

$$V_m = \frac{1}{h} \int_0^h v \, dh \tag{4.7}$$

where v is the local velocity at depth h. The time-history of V_m in Figure 4.15 is compared to the wave front celerity U measured with the US sensors. Looking at the depth-averaged velocity profiles, one can notice that the largest velocities occurred at the wave front, which is consistent with other reports in literature (Lauber and Hager, 1998). A constant deceleration occurred behind the wave front for all configurations, until a quasi-steady state was reached: this was previously reported by Al-Faesly et al. (2012) and Goseberg et al. (2013). Although the observed deceleration behind the wave front is predicted by continuity equation given the increase in water depth, the last part of the curve was influenced by the reduction of the water volume and, implicitly, of the hydraulic head in the upper basin. For this reason, all data for $T > T^*$ were not considered. The lower velocities observed after the passing of the wave front is in agreement with the findings of Lauber and Hager (1998) and those of Leng and Chanson (2017b,a). In Figure 4.15, for bores, the experimental data was also compared with the velocity V_2 behind the bore front predicted by the momentum equation presented in Eq. 2.22 as a function of h_0 and h_2 (Henderson, 1966; Chanson, 2004).

All individual velocity profiles were normalized using the measured depth-averaged velocity (V_m) and the wave height of every profile (h_i). Although the profiles show some scattering, probably attributed to random air bubbles or impurities occurring in the flow, good agreement between all measured profiles for a dry bed surge and a bet bed bore can be observed in Figure 4.16. The velocity profiles were successfully compared to Prandtl's power law with $N = 8$, obtained with a flow resistance value of $f = 0.02$ (Chanson, 2004).

$$\frac{h}{h_i} = \left(\frac{v}{V_m} \right)^N \tag{4.8}$$

Although a logarithmic profile, which takes into account that the velocity reduction close to the bottom due to the presence of the boundary layer is theoretically more appropriate, Figure 4.16 suggests that the assumption of a uniform constant velocity profile is a priori feasible for both dry bed surges and wet bed bores. This can be explained by the significant vertical exchange of momentum across the wave depth due to turbulence. The estimation of the average velocity works well in the fully developed region, where the height of the flow is sufficient to neglect the effect of the boundary layer. In the tip region, the thickness of the boundary layer is important and V_m is hence slightly under-estimated. The existence of a thin boundary layer was previously observed by Lauber and Hager (1998) through PIV tests, however this was small given the range of Reynolds numbers (Re $\approx 10^5 - 10^6$). The same

findings were confirmed by Leng and Chanson (2017b) for surges and bores in both steady and unsteady flows. Some scattering in velocity measurements is visible in the upper part of the profiles (Figure 4.16) probably probably attributed to the fluctuations observed on the flow surface (Wüthrich et al., 2016b). To gain a better insight of the turbulent behaviour of the surges and bores, the fluctuations were separated from the mean value and analysed per horizontal flow layer. This resulted in a turbulence intensity value Tu per layer, defined as:

$$Tu = \frac{\sqrt{\overline{(v - \overline{v})^2}}}{\overline{x}} \tag{4.9}$$

The derived Tu distribution is also presented in Figure 4.16, showing a constant behaviour with values $Tu < 0.11$ for dry bed surges and $Tu < 0.13$ for wet bed bores. Similar results were obtained for other surges and bores with different impoundment depths (d_0) and initial still water depths (h_0), presented in Appendix D.
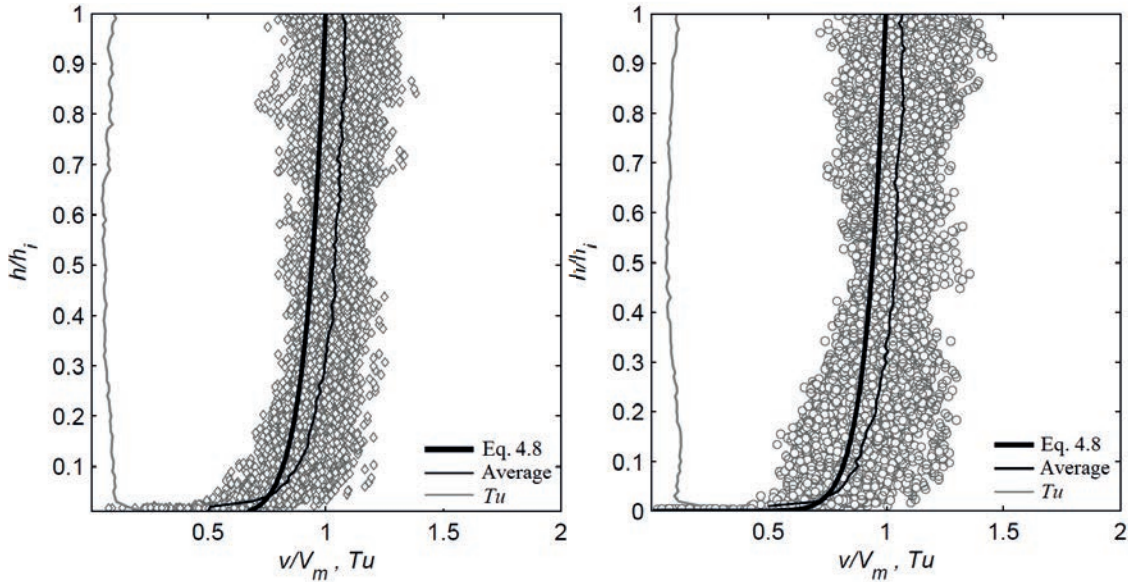
Figure 4.16 – Normalised velocity profiles for $T \cdot (g/d_0)^{0.5} < 42$: (a) dry bed surge (160 profiles, test 4.1) and (b) wet bed bore, $d_0 = 0.82$ m, $h_0 = 0.05$ m (104 profiles, test 4.11).

The depth-averaged velocities (V_m) for 12 dry bed surges and 19 wet bed bores at two measurements locations along the channel ($x = 10.20$ m and 13.85 m) are presented in dimensionless form in Figures 4.17 and 4.18, where $T = t - t_0$ is the shifted time, such that $T = 0$ coincides with the wave arrival time. The profile plotting was stopped at $T = T^*$, when the assumption of a constant water discharge Q_0 was no longer valid (Figure 4.1). Despite some scattering, good superposition was observed for all experimental points, for both dry bed surges and wet bed bores. For dry bed surges, the match between the front celerity and depth-averaged velocities was good, whereas for bores on wet bed, an under-estimation of the velocity magnitude was consistently observed in the wave front region [$T \cdot (g/d_0)^{0.5} < 15$, in Figure 4.18]. In this

region, V_m was equal to the velocity V_2, derived from the momentum equation (Eq. 2.22) as a function of h_0/d_0. For both surges and bores the decrease in V_m behind the front was best approximated by Eq. 4.10, imposing the boundary condition $V_m = U$ at $T \cdot (g/d_0)^{0.5} = 0$.

$$\frac{V_m}{U} = 1 - c \cdot \tanh\left[b \cdot T \sqrt{\frac{g}{d_0}} \right] \qquad (4.10)$$

where V_m is the depth-average profile velocity, U is the wave front celerity, T is the shifted time ($T = t-t_0$), g the gravity constant and d_0 is the initial impoundment depth.
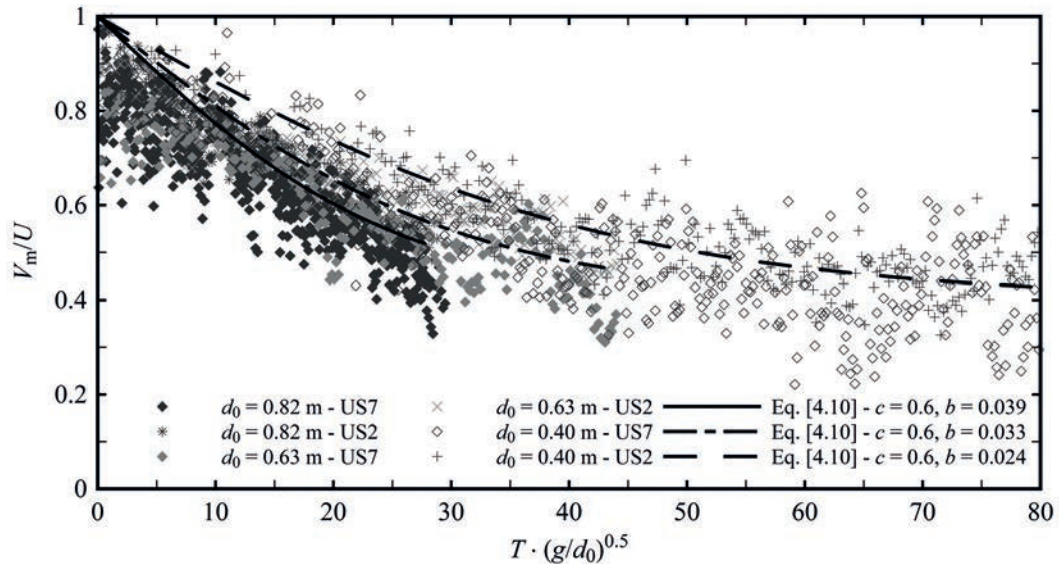
Figure 4.17 – Dimensionless depth-averaged velocities (V_m/U) for 12 dry bed surges with different impoundment depths at two different locations: US7 ($x = 13.85$ m) and US2 ($x = 10.20$ m);

Parameters b and c were derived empirically. For large values of $T \cdot (g/d_0)^{0.5}$, an asymptotic behaviour toward uniform flow conditions was observed. While the value of $c = 0.6$ was constant for both bores and surges (empirical best fit), b was influenced by the equivalent impoundment depth d_0, and the wave height h, as shown in Figure 4.19.

$$b = 0.0124 \cdot \left(\frac{d_0}{h_{max}} - 1 \right) \qquad (4.11a)$$

$$b = 0.0124 \cdot \left(\frac{d_0}{h_2 - h_0} - 1 \right) \qquad (4.11b)$$

The considered height h_{max} is the maximum wave height for a dry bed surge (Eq. 4.11a) and the plateau height h_2 for wet bed bores (Eq. 4.11b). For the latter, the value of b is implicitly influenced by the initial still water depth h_0 through the plateau height h_2, which is a function of the ratio h_0/d_0 (Eq. 2.16, Figure 4.11). However, Figure 4.19 does not reflect that this dependence is minimal, meaning that the main parameter controlling b is the impoundment
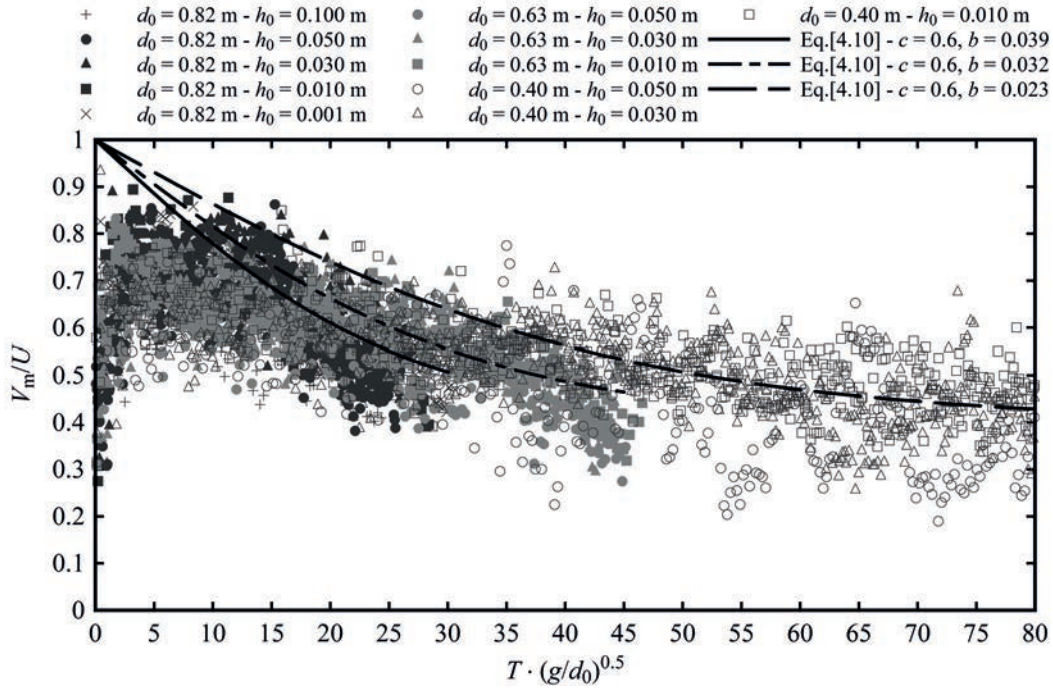
Figure 4.18 – Dimensionless depth-averaged velocities (V_m/U) for 19 wet bed bores with different impoundment depths and initial still water depths at a fixed location ($x = 13.85$ m)

depth d_0 (horizontal trend in Figure 4.19a). These findings showed that, within the tested range, the main influence of the initial still water depth depth h_0 was observed in the reduction of the wave front celerity U (Section 4.4.1), compared to a dry bed surge with the same release conditions.

The derivative of Eq. 4.10 with respect to the dimensionless time $T \cdot (g/d_0)^{0.5}$ represents the evolution of the velocity gradient ($\dot{V}$) over time. The latter is also the expression of the tangent line to Eq. 4.10 at a specific dimensionless time. As such, it can be expressed analytically as:

$$\dot{V} = \frac{d\left(\frac{V_m}{U}\right)}{d\left(T\sqrt{\frac{g}{d_0}}\right)} = -c \cdot b \cdot \left[1 - \tanh^2\left(b \cdot T\sqrt{\frac{g}{d_0}}\right)\right] \tag{4.12}$$

The behaviour of the velocity gradient $\dot{V}$ is shown in Figure 4.20 for different impoundment depths d_0, using the average values of b presented in Figure 4.19. One can notice that its variation is not constant in time and that a greater deceleration is observed in the vicinity of the wave front, whereas milder values are found in the far-field zone. This implied that the reduction of V_m is more significant right behind the wave front. The value $\dot{V}$ computed at a certain time T, represents the local deceleration of the flow behind the wave front. Its graphic representation is shown in Figure 4.20, and mathematically it is the tangent to the continuous line defined by Eq. 4.10 in Figures 4.17 and 4.18. The steeper the tangent the higher the deceleration of the flow. If one compare Eq. 4.10 to the cinematic expression $V_m = U - a \cdot t$ in dimensional form, one can derive Eq. 4.13, which allows to calculate the deceleration value

(a)   (b)
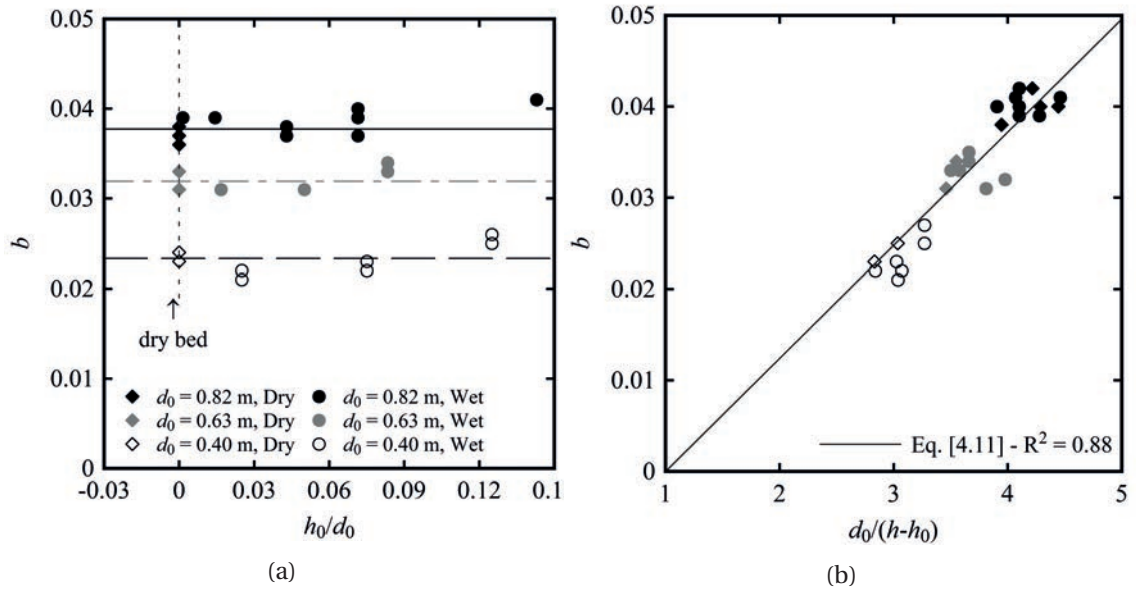
Figure 4.19 – Definition of parameter b in Eqs. 4.11: (a) as a function of h_0/d_0 and (b) $d_0/(h-h_0)$ where $h = h_{max}$ for surges and $h = h_2$ for bores. Same legend applies to both figures.
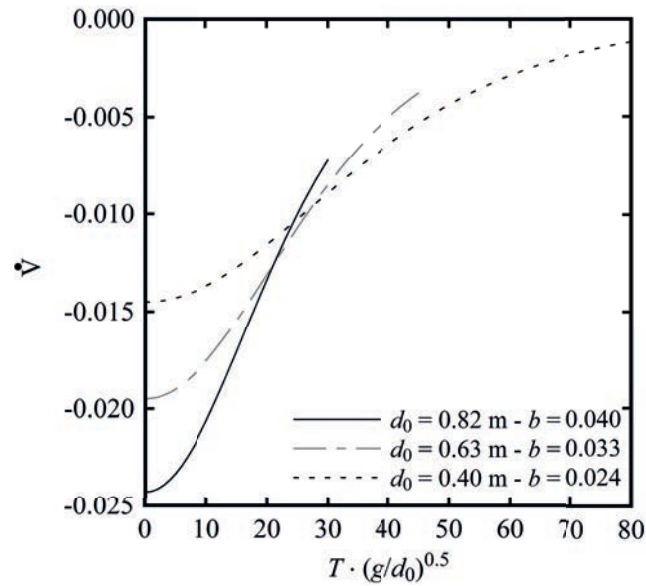
Figure 4.20 – Time-variation of the velocity gradient $\dot{V}$ for three impoundment depths. Average values of b are used in the computation.

a for a specific wave, knowing its wave front celerity U and the impoundment depth d_0

$$\dot{V} = \frac{a}{U}\sqrt{\frac{d_0}{g}} \tag{4.13}$$

4.5 Froude number

The time-development of the Froude number for both dry bed surges and wet bed bores was calculated using Eq. 4.14:

$$\text{Fr} = \frac{V_{m,i}}{\sqrt{g h_i}} \tag{4.14}$$

where V_m is the individual depth-averaged profile velocity, g is the gravity constant and h_i is the wave height of every profile. The values obtained are presented in Figure 4.21, where a clear difference between bores and surges is shown. The dry bed surge was highly supercritical in the first part of the propagating wave, followed by an asymptotic decrease toward $\text{Fr} \approx 1$. For wet bed bores, a more constant flow-pattern was observed at all times. This difference was more important as h_0 increased. The behaviour of wet bed bores with smaller initial still water depths h_0 became similar to that of the dry bed surges, proving, once again, the transition pattern between dry and wet bed. These findings are consistent with the video analysis of Fritz et al. (2012) who estimated Froude number values close to 1 in Kesennuma, during the 2011 Japan Tohoku Tsunami.

(a) Dry bed surge   (b) Wet bed bore
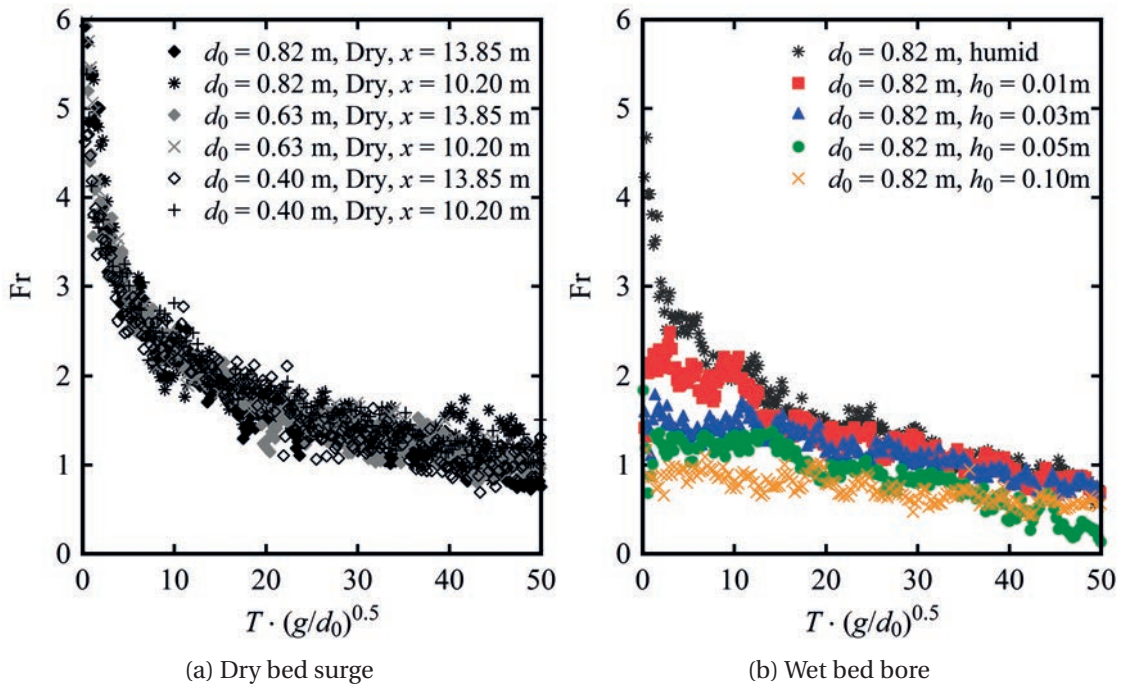
Figure 4.21 – Flow Froude number (Fr) computed for: (a) dry bed surges and (b) wet bed bores.

4.6   Momentum

The momentum associated with the moving wave is an important parameter, as it directly controls loading produced during the impact against a free-standing structure. The momentum (M) per unit width was calculated as the product of water density (ρ), unit discharge (q) and the average profile velocity (V_{m}), resulting into:

$$M = \rho \cdot q \cdot V_{\mathrm{m}} = \rho \cdot h \cdot V_{\mathrm{m}}^{2} \tag{4.15}$$

The results obtained from all tests are shown in Figure 4.22, where a similar pattern between surges and bores can be observed, including an initial section characterised by an increase in momentum, followed by a subsequent decrease. Although some scattering is present, results showed a peak for all configurations around $T \cdot (g/d_0)^{0.5} \approx 10$, for which values of $M/\rho g d_0^{2} \approx 0.20$ to 0.25 were obtained. It is important to notice that, herein, the maximum of the momentum per unit width does not occur either when the velocity is maximal, nor when the wave height is maximal, as previously indicated by Yeh (2007) and Chock et al. (2012). For all tested scenarios, the maximum momentum was reached before the maximum flow depth was observed.

◆ $d_0 = 0.82$ m, Dry, US7	✕ $d_0 = 0.82$ m, $h_0 = 0.10$ m	▲ $d_0 = 0.63$ m, $h_0 = 0.03$ m
◆ $d_0 = 0.63$ m, Dry, US7	● $d_0 = 0.82$ m, $h_0 = 0.05$ m	■ $d_0 = 0.63$ m, $h_0 = 0.01$ m
◇ $d_0 = 0.40$ m, Dry, US7	▲ $d_0 = 0.82$ m, $h_0 = 0.03$ m	○ $d_0 = 0.40$ m, $h_0 = 0.05$ m
✳ $d_0 = 0.82$ m, Dry, US2	■ $d_0 = 0.82$ m, $h_0 = 0.01$ m	△ $d_0 = 0.40$ m, $h_0 = 0.03$ m
✕ $d_0 = 0.63$ m, Dry, US2	✦ $d_0 = 0.82$ m, Humid	□ $d_0 = 0.4$m, $h_0 = 0.01$ m
+ $d_0 = 0.40$ m, Dry, US2	● $d_0 = 0.63$ m, $h_0 = 0.05$ m	

(a) Dry bed surge   (b) Wet bed bore
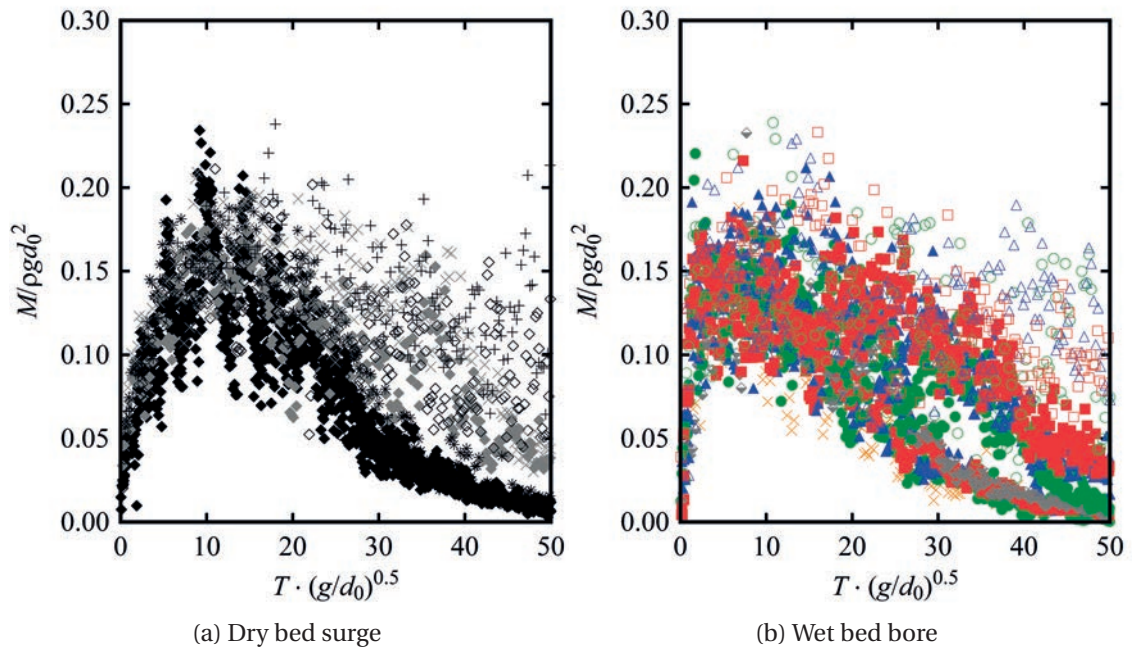
Figure 4.22 – Momentum ($M = \rho \cdot h \cdot V_{\mathrm{m}}^{2}$) computed for: (a) dry bed surges and (b) wet bed bores for various impoundment depths d_0 and initial still water depths h_0.

A variable h_M is introduced as the ratio between the height at which the maximum momentum occurs, $h(M_{max})$, and the maximum wave height h_{max}

$$h_M = \frac{h(M_{max})}{h_{max}} \tag{4.16}$$

The results for both surges and bores are shown in Figure 4.23 . These are compared to Chock (2015), who showed that the maximum momentum occurs when the water level has reached 67 % of the maximum wave height recorded on the rising limb of the inundating wave. This approach is, on average, supported by the results for dry bed surges ($h_0/d_0 = 0$). However, discrepancies are observed for the case of wet bed bores. For these, given the sudden water raise of the water depth, the maximum momentum is observed when the water depth is approximately 90 % of the maximum wave height. Thus, the chosen value of 67 % may not be conservative for some cases, as the maximum momentum might occur for higher water depths.
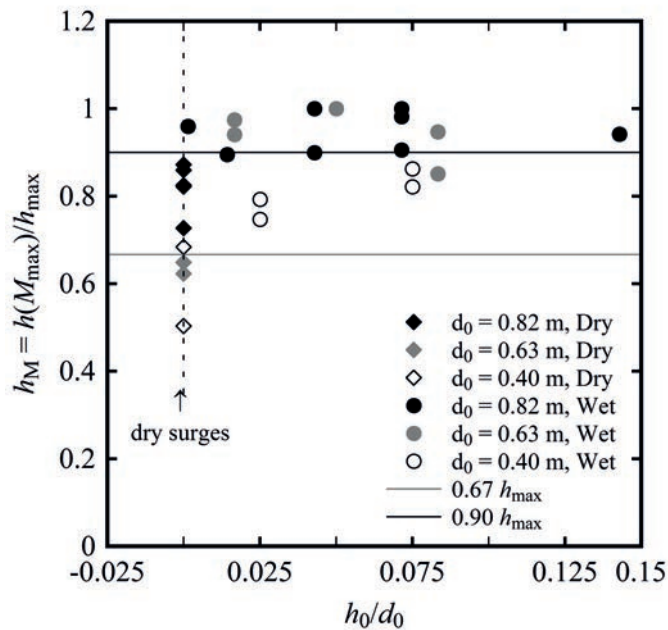
Figure 4.23 – Dimensionless surge and bore heights when maximum momentum occurs and with comparison with existing guidelines (Chock, 2015)

.

4.7 Discussion

The present study introduces a novel technique to generate dry bed surges and wet bed bores in a laboratory environment. If a 1:30 Froude scaling ratio is assumed, surge/bore depths ranged from 3.9 to 7.8 m (prototype scale), with front celerities between 10.59 and 19.5 m/s. These values were consistent with field data obtained through post-tsunami field surveys and observations, in which flow depths of 4 to 7 m were measured in the southern part of Khao Lak, Thailand, during the 2004 Indian Ocean Tsunami (Dias et al., 2006) and velocities of up to 10 to 13 m/s near the Sendai Airport during the 2011 Japan Tohoku Tsunami (Jaffe et al., 2012). The generated surges and bores were similar to those produced with the classical dam-break technique (Ritter, 1892; Whitham, 1955; Stoker, 1957), a method which is widely used at present to reproduce inland tsunami flows. Similarities between experimental and prototype data were also pointed out in the terms of shape at the surge front tip. Furthermore, similar Froude numbers between prototype and real tsunami events were presented. Thus, the authors conclude that the vertical released technique generates surges and bores which are consistent with other methods presented in literature and that this mechanism is well suited to simulate tsunami-like waves in laboratories.

4.8 Summary

The diversity of wave transformation and subsequent inland propagation has led researchers to develop several techniques to generate such tsunami-like flows in laboratories. This Chapter focused on the generation of long-waves (surges and bores) through the vertical release of a stored water volume. Both surges and bores produced with this vertical release technique were then analysed in terms of their hydrodynamic behaviour and characteristics, drawing the following conclusions:

1. A comparison with existing literature for the classical dam-break generation mechanisms showed good agreement between the dry bed surges generated by this vertical release method and the analytical solution of Ritter (1892) and Whitham (1955). For wet bed bores, the generated water surface profiles agreed well with the theory of Stoker (1957).

2. The values of the wave front celerity were successfully compared to those found in the existing literature and the current design guidelines and codes. To compute surge front celerity, a coefficient $\alpha = 1.25$ was suggested, leading to

$$U = 1.25 \cdot \sqrt{g d_0} \qquad (4.17)$$

For wet bed bores, very good agreement was found with the momentum equation (Eq. 2.20) and the numerical approximation of Chanson (2004). The influence of the initial impoundment depth h_0 was mostly observed in the wave front celerity U, whereas for bores propagating over smaller initial still water depths, h_0 had a behaviour similar to dry bed surges.

3. The use of UVP probes allowed to measure velocity profiles of the propagating wave behind the wave front, showing velocity profiles close to those observed in open channel flows. Although the normalised profiles indicated good agreement with Prandtl's exponential law, experimental results proved that the common assumption of a constant velocity profile over depth is acceptable. Flow deceleration was observed behind the front for all scenarios and an expression to predict the depth-averaged velocity at a certain time behind the front was proposed in Eq. 4.10. The latter did not directly depend on the initial still water depth h_0, but rather on the equivalent impoundment depth d_0.

4. Dry bed surges exhibited higher Froude numbers in the wave tip region, followed by their rapid decrease, whereas wet bed bores showed more constant Froude numbers over time. All tests had a similar shape for the momentum profiles with maxima occurring around $T \cdot (g/d_0)^{0.5} \approx 10$, which did not correspond to the maximum wave height, nor to the maximum flow velocity. The maximum momentum occurred at 65-70% of the maximum wave height for dry bed surges and 90% for wet bed bores, something consistent with the latest standard recommendations (Chock, 2015).

5 Impact on impervious buildings

5.1 Overview

Tsunamis, landslide-generated waves and floods due to dam failures are rare, but highly destructive phenomena, associated with extreme loading on infrastructure. Recent events showed that specific measures must be taken to guarantee safety of both people and the built environment. This chapter focuses on the forces and moments exerted on free-standing building-like structures which are induced by both surges and bores. The hydrodynamic impact was characterised by high splashes for both surges and bores, subsequently followed by a quasi-steady flow around the structure. For dry bed surges, the time-history of the horizontal force was shown to be proportional to the momentum flux per unit width. For wet bed bores, an attenuation of the peak force due to the presence of an aerated front was consistently observed and the introduction of a force reduction coefficient was necessary to achieve a realistic force estimation. Additional force analysis in terms of peak time, wave height at maximum force and impulse also pointed out some key differences between forces exerted by dry bed surges and wet bed bores. The occurrence of the maximum tilting moment on the building was shown to coincide with the maximum horizontal force and an evaluation of the cantilever arm was therefore possible.

The main objectives of this chapter are the following:

1. To apply the results presented in Chapter 4, characterizing wave velocity and momentum to determine the load conditions.
2. To provide a set of equations to define the magnitude of the horizontal force induced by the wave on the building.
3. To determine the tilting moment generated by the force and its application point.
4. To present a detailed analysis for horizontal forces, including the impulse transferred from the wave to the building and the wave height at which the peak force occurs.

This Chapter is based on the scientific article "Experimental study on the hydrodynamic impact of tsunami-like waves against impervious free-standing buildings" by D. Wüthrich, M. Pfister, I. Nistor and A.J. Schleiss under revision in *Coastal Engineering Journal*. The experimental work and the analysis presented hereafter is original and was performed by the author.

For this, 45 tests were carried out considering multiple waves with different hydrodynamic properties (Chapter 4). The experimental program is presented in Table 5.1. The maximum recorded wave height h_{max} was 0.181 m for the dry bed surge and 0.259 m for the wet bed bore, with a front celerity U ranging from 1.93 to 3.55 m/s. All parameters concerning the wave without the presence of the buildings were obtained as average values of minimum 3 tests (Appendix D). For a scaling of 1:30, these values corresponded to a prototype wave height of 5.5 to 8 m and a prototype celerity of 10.7 to 19.4 m/s, values which are consistent with reported field observations (Chock et al., 2012; Fritz et al., 2012; Jaffe et al., 2012).

	Impoundment depth d_0 [m]	Initial water depth h_0 [m]	Celerity U [m/s]	h_{max} [m]	h_0/h_{max}	Rep.	
Dry	0.82	0.00	3.556	0.181	0	4	test 5.1
	0.63	0.00	3.114	0.162	0	3	test 5.2
	0.40	0.00	2.347	0.132	0	4	test 5.3
Wet	0.82	0.01	3.074	0.191	0.052	4	test 5.4
		0.03	2.810	0.231	0.129	4	test 5.5
		0.05	2.755	0.259	0.193	4	test 5.6
	0.63	0.01	2.702	0.167	0.058	3	test 5.7
		0.03	2.518	0.201	0.146	3	test 5.8
		0.05	2.437	0.224	0.223	3	test 5.9
	0.40	0.01	2.104	0.135	0.072	5	test 5.10
		0.03	1.971	0.159	0.185	4	test 5.11
		0.05	1.933	0.177	0.280	4	test 5.12
Max	0.100	0.05	3.556	0.259	0.280	5	-
Min	0.000	0.01	1.933	0.132	0	3	-

Table 5.1 – Experimental program summarizing the hydrodynamic properties of the standard waves used in this chapter.

5.2 Visual observations

Visual observations proved that the difference between surges and bores discussed in Section 4.3 resulted into different behaviours during the wave impact with an impervious free-standing building. Nevertheless, for both cases, two main phases were observed:

1. an **initial impact** of the wave front, followed by
2. a **quasi-steady hydrodynamic** phase, during which the main body of the wave flowed around the building.

	DRY BED SURGE $d_0 = 0.82$m	WET BED BORE $d_0 = 0.82$m, $h_0 = 0.05$m
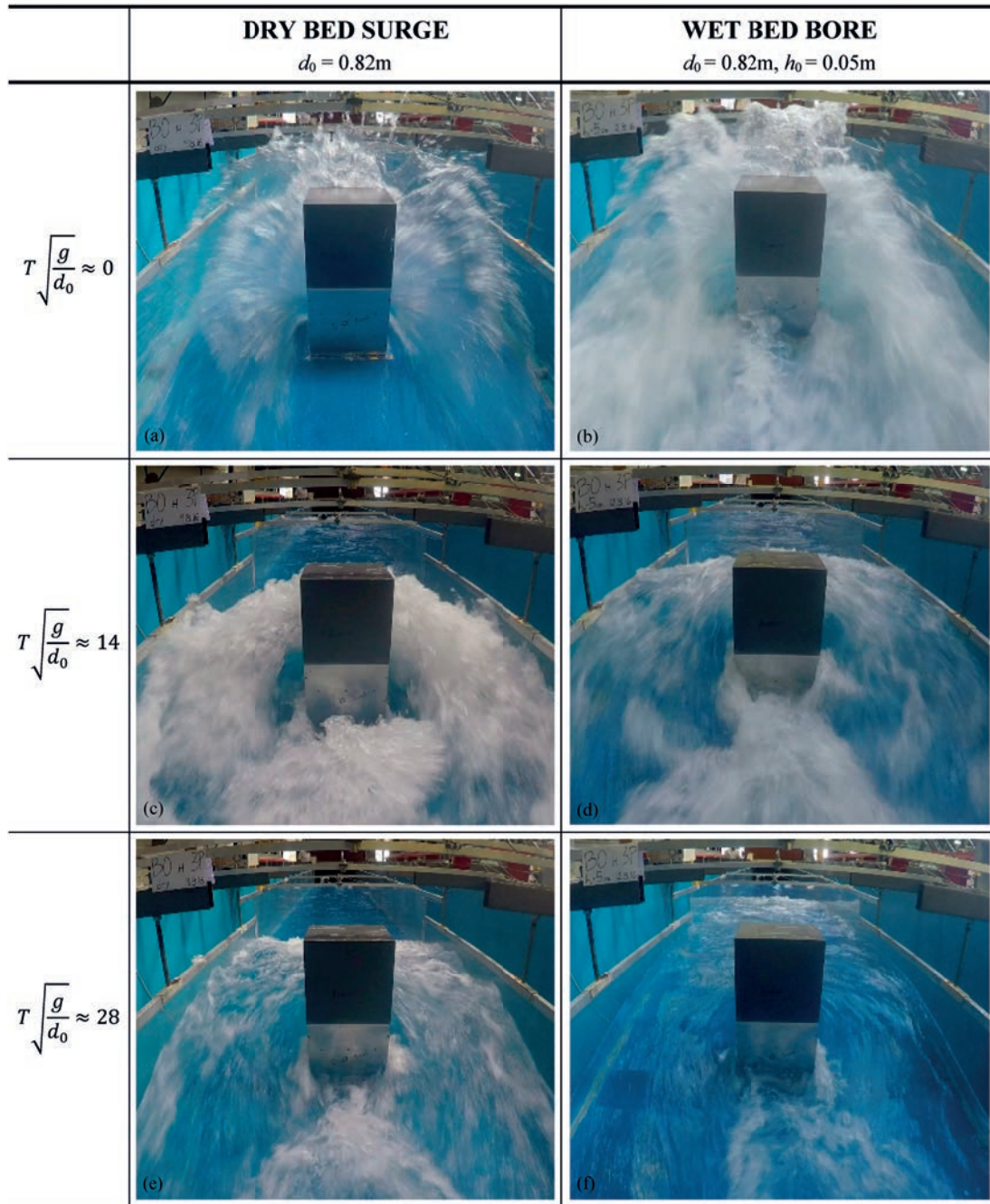
Figure 5.1 – Wave impact against an impervious buildings without overflow for a dry bed surge ($d_0 = 0.82$ m, test 5.1) and a wet bed bore ($d_0 = 0.82$ m, $h_0 = 0.05$ m, test 5.6)

These two phases are shown in Figure 5.1, where the time evolution of the impact is presented through pictures taken at $T \cdot (g/d_0)^{0.5} \approx 0$ s (impact phase, with highest run-up) and $T \cdot (g/d_0)^{0.5} \approx 14$ and 28 (post-impact hydrodynamic phase) for both surges and bores. Similar qualitative results were previously presented by Wüthrich et al. (2016c) for the case of buildings toppled by overflow.

During the initial impact phase, the wave front hit the building's upstream side and a vertical run-up height H was observed. As shown in Figure 5.1a-d, for both the case of bores and surges, the impact phase was characterized by significant splashes and turbulent air entrainment at the upstream side of the building. Due to the presence of the building, the run-up and splashes fell onto the incoming wave, producing a quasi-steady roller on the upstream side. This roller is characterized by high turbulence and substantial air entrainment. The formation of a roller in the upstream side is shown in Figure 5.1e-f and it marked the transition between the impact phase and the quasi-steady hydrodynamic one. As shown in Figure 5.1e-g and f-h, a visual assessment indicated that dry bed surges presented higher air entrainment compared to wet bed bores. Dry bed surges were also characterized by a pulsating flow behaviour which is attributed to the interaction between the high speed incoming wave and the return motion of the vertical run-up. For all test cases, no overflow of the building was seen. For all configurations, intense Von Kármán vortices in the downstream side of the building were observed (Figure 5.1).

The Ultrasonic Sensor US7, located 0.15 m upstream of the building (Figure 3.2), measured the time history of the vertical run up heights H, providing a more quantitative description of the previously discussed visual observations. The results are shown in Figure 5.2 for both a dry bed surge and a wet bed bore. These are compared with the wave profile h measured without the building. Results showed similar maximum values H_{max} corresponding to approximately 4 times the maximum wave height without the building h_{max}. If compared to bores, the measurements for the dry bed surge showed a more fluctuating behaviour and a constant decrease. On the contrary, wet bed bores showed a sudden reduction in water depth immediately following the run-up splash provoked by the initial impact.

(a) Dry bed surge   (b) Wet bed bore
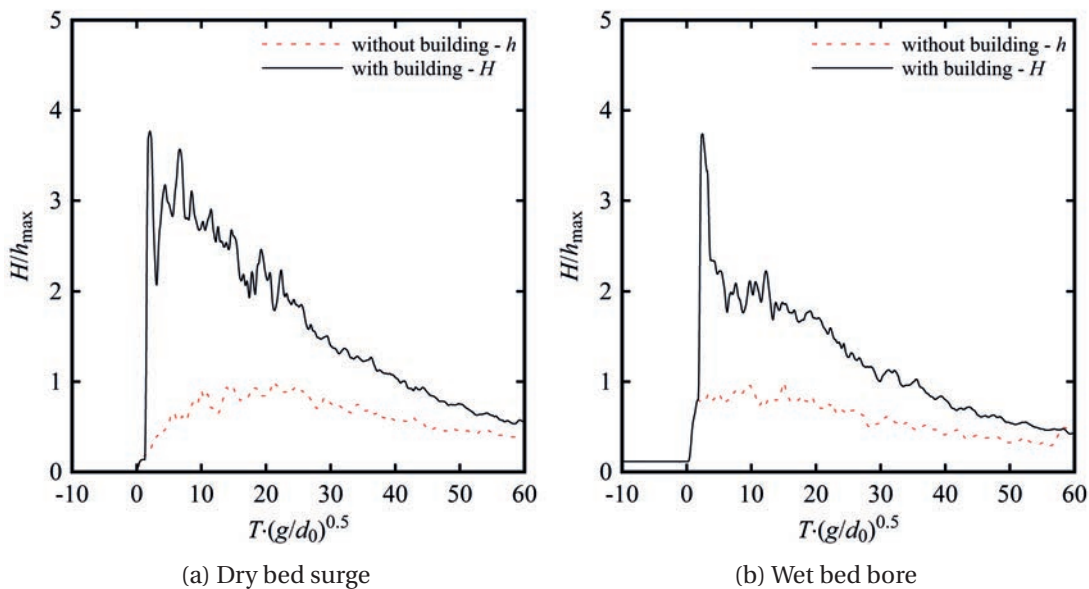
Figure 5.2 – Vertical run-up heights H (measured at US 7) for: (a) dry bed surge, $d_0 = 0.82$ m, $h_{max} = 0.181$ m, test 5.1; (b) wet bed bore, $d_0 = 0.82$ m, $h_0 = 0.03$ m, $h_{max} = 0.232$ m, test 5.5.

5.3 Impact forces

The buildings were simulated using 0.30×0.30 m aluminium plates, assembled on the force plate to record all forces and moments induced by the propagating wave along the three axis of coordinates. The time histories of forces and moments were sampled with an acquisition frequency of 1 kHz. An example of the raw data recorded for forces and moments induced by a dry bed surge as well as a wet bed bore are presented in Figure 5.3, pointing out some key differences between the two waves. Similar behaviour was previously observed by Ramsden (1996) and Nouri et al. (2010).

(a) Dry bed surge   (b) Wet bed bore
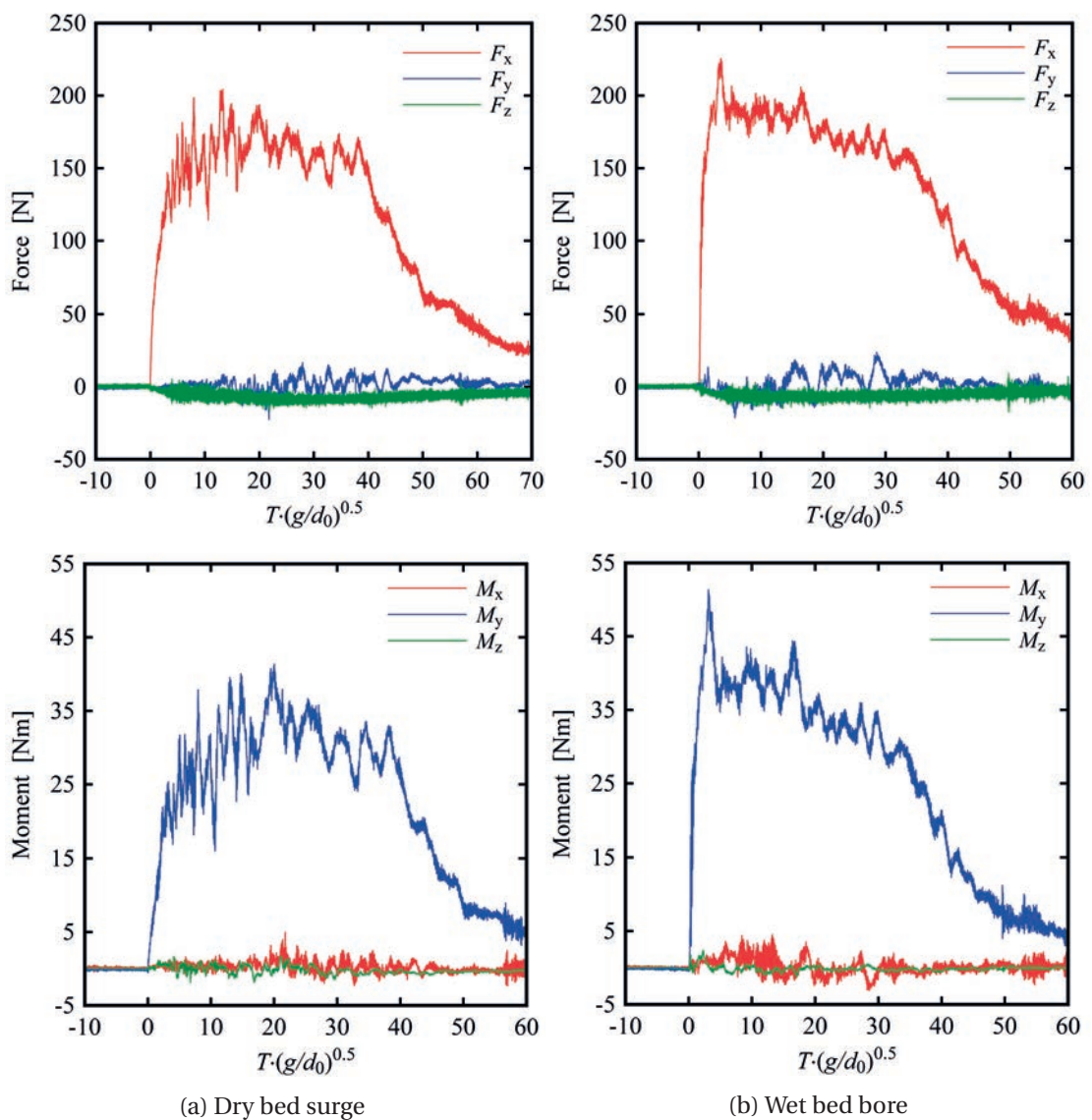
Figure 5.3 – Time histories of forces and moments measured with the Force Plate, for: (a) dry bed surge ($d_0 = 0.63$ m, test 5.2) and (b) wet bed bore ($d_0 = 0.63$ m, $h_0 = 0.03$ m, test 5.8).

In the present study, for the same release conditions ($d_0 = 0.63$ m), similar force maxima were observed for both the dry bed surge and the wet bed bore. Bores were characterized by a sudden rise in horizontal force F_x and moment M_y, whereas surges were associated with a more gradual rise in time. These findings are in agreement with those of Arnason et al. (2009) and Nouri et al. (2010). The magnitude of the forces and moments in the transversal (F_y, M_x) and vertical direction (F_z, M_z) was negligible compared to those recorded in the flow direction (F_x, M_y), proving the bi-dimensionality of the phenomenon. For this reason, the values of F_y, F_z, M_x and M_z are hereafter neglected and therefore not discussed herein. Given the differences between the force time-history, the two waves are hereafter considered separately: the dry bed surge is described in Section 5.3.1 while the wet bed bore is described in Section 5.3.2.

5.3.1 Dry bed surges

The estimation of the horizontal force produced by a flow moving against an obstacle can be calculated using the approach proposed by Morison et al. (1950). These equations take into account the hydrodynamic (or drag) force component and the inertia component. For tsunamis, due to their long periods, the inertia component becomes important only at the leading edge of the incoming wave, when the wave impacts the building: this is often termed surge force. The quasi-steady hydrodynamic component in the x-direction, $F_{x,D}$ can be computed as:

$$F_{x,D} = \frac{1}{2}\rho C_D B \cdot \left(h v^2\right) = \frac{1}{2}\rho C_D B \cdot M \tag{5.1}$$

where ρ is the water density ($\rho = 1000$ kg/m^3), B is the building width, h is the flow depth and v is the flow velocity. M is the wave momentum flux per unit width which is obtained through a combination of wave height and flow velocity ($M = h v^2$). The drag coefficient C_D depends on the obstacle geometry and on the flow conditions. More details regarding the drag coefficient can be found in Blevins (1984).

During these experimental tests, in agreement with what was visually observed after the initial impact, the flow became quasi-steady due to the surge's long period. Therefore, the estimation of the force could be obtained through Eq. 5.1. It is important to point out that the maximum force $F_{x,max}$ does not occur when both h and v are maximum, but when the momentum flux per unit width ($M = h v^2$) is maximum, i.e. $M_{max} = (h v^2)_{max} \neq h_{max} v_{max}^2$ (Yeh et al., 1996; Yeh, 2007).

Some diagrams for the dry bed surge are presented in Figure 5.3 and Figure 5.4, in which one can notice a constant increase of the force until a quasi-constant value is reached, corresponding to the quasi-steady hydrodynamic phase. Such behaviour is consistent with previous studies, including, among others, Ramsden (1996), Arnason et al. (2009), Lukkunaprasit et al. (2009b) and Nouri et al. (2010). In the present case, no force overshot due to surge component was observed during the initial impact, as discussed by Yeh (2007), Arnason et al. (2009) and

Foster et al. (2017). This is probably due to the mild slope of the incoming surge. It is therefore reasonable to conclude that, for a dry bed surge, the inertia component (surge force) can be neglected.

A combination of hydrostatic and hydrodynamic components was suggested by Cross (1967) to compute the total force resulting from wave impact (Section 5.3.4). Thus, this study confirms that the actual measured force F_x was less than the one computed using the run-up height H, assuming hydrostatic conditions ($F_x < F_{x,H}$), something which is in agreement findings by Ramsden (1996), Arnason et al. (2009) and Nouri et al. (2010). Furthermore, as shown in Figure 5.4, the measured values were also higher than the values computed using the wave height h in the absence of the building model ($F_x > F_{x,h}$).

In addition, for such rapidly varied flows, the hydrostatic and hydrodynamic components cannot be independently identified and any assumption of hydrostatic pressure repartition remains dubious. For these reasons, similarly to Arnason et al. (2009), a resistance coefficient C_R was used, instead of a *"classical"* drag coefficient, C_D. This approach allows to take into account the hydrostatic pressure difference between the back and the front sides of the building, which may contribute a portion of the measured impact force. As recommended by most design guidelines or by the new ASCE 7 Chapter 6, a value of $C_R = 2$ is initially chosen; however, more considerations are presented in Section 5.3.5 and in Appendix C.
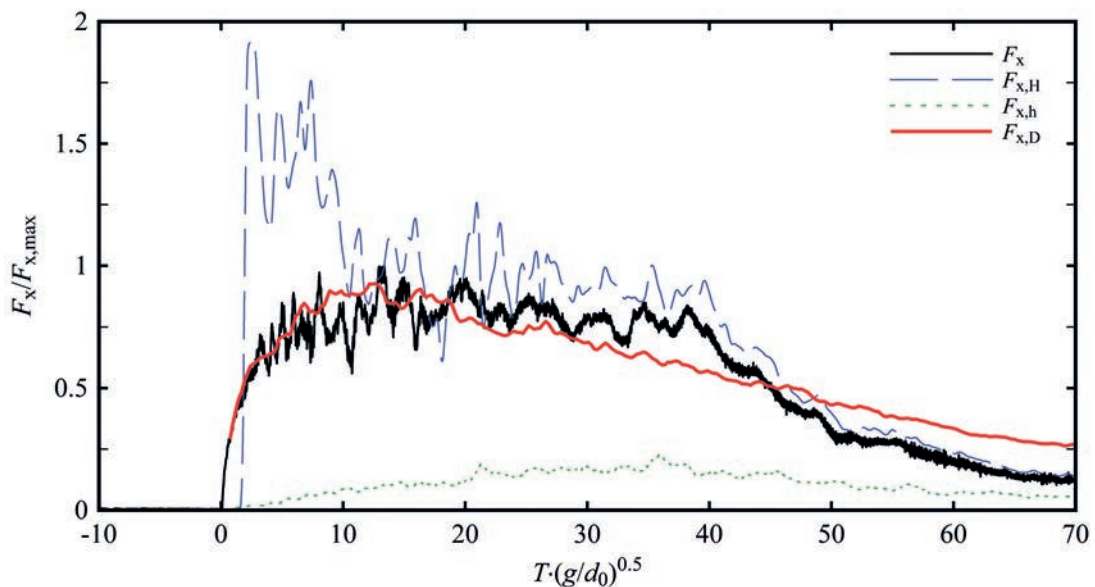
Figure 5.4 – Comparison of tests with hydrostatic and hydrodynamic approach for a dry bed surge with impoundment depth $d_0 = 0.63$ m (test 5.2). F_x is the measured horizontal force, $F_{x,H}$ is the hydrostatic force computed using the run-up height H (with the building), $F_{x,h}$ is the hydrostatic force computed using the measured wave height $h(t)$ without the building, and $F_{x,D}$ is the hydrodynamic force computed using Eq. 5.2.

The presence of the building reduced the wave velocity in the upstream reach of the channel, producing a backwater effect. Thus, the use of the wave front celerity U in the computation of wave momentum M, was not representative and such approach might lead to an overestimation of the resulting load. For this reason, Shafiei et al. (2016) suggested a reduction of the wave front velocity U, using the Bernoulli equation. Alternatively, the results presented in Chapter 4 allowed to quantify the decelerating behaviour of the wave velocity behind the wave front (V_m) and a more precise estimation of M in time was thus obtained. As such, a modified version of Eq. 5.1 is:

$$F_{x,D} = \frac{1}{2}\rho C_R B \cdot M = \frac{1}{2}\rho C_R B \cdot \left(h V_m^2\right) \tag{5.2}$$

where h is the wave height measured without the building, B the building width and V_m the depth-averaged wave velocity, calculated using Eq. 4.10. The good agreement (Figure 5.4) proved that the horizontal force F_x was proportional to the momentum flux per unit width ($M = h V_m^2$). Eq. 5.2 was tested for three dry bed surges with three different impoundment depths d_0, as shown in Figure 5.5.

Excellent agreement is observed for the configurations with shorter wave periods (impulsive type), whereas for waves with longer periods, a minor underestimation of the force is observed for larger times. This underestimation of the measured force F_x was particularly observed in the post-peak force region for $T \cdot (g/d_0)^{0.5} > 40$ (Figure 5.5). This is because all parameters in Eq. 4.10 refer to the wave properties measured without the building, whose flow conditions were associated with a shorter flow duration, given the absence of the building in the flume.

(a) $d_0 = 0.40$ m (test 5.3)   (b) $d_0 = 0.63$ m (test 5.2)   (c) $d_0 = 0.82$ m (test 5.1)
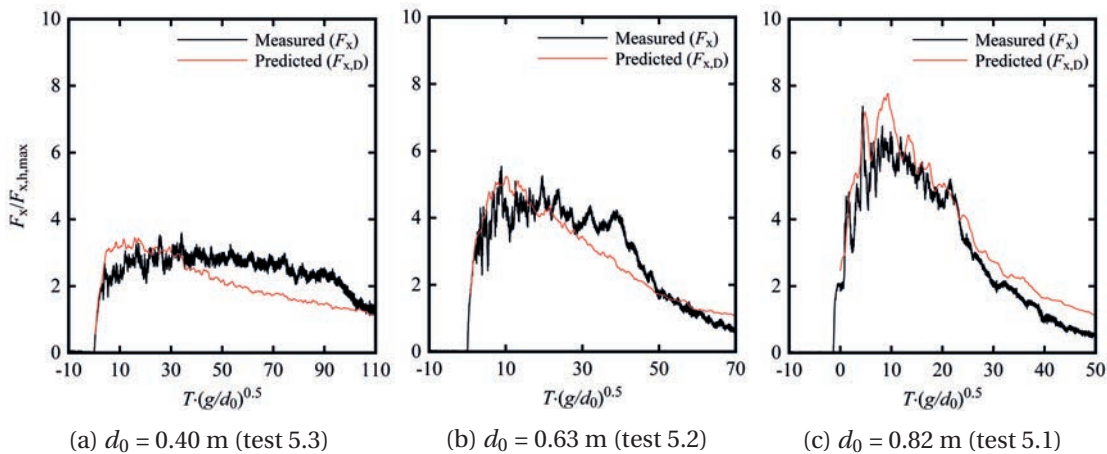
Figure 5.5 – Comparison of the measured force (F_x, black) with the values obtained using the momentum equation (Eq. 5.2) for three dry bed surges ($F_{x,D}$, red), (a) to (c). All forces are normalised using the hydrostatic force $F_{x,h,max}$ corresponding to the maximum wave height h_{max} without the building

5.3.2 Wet bed bores

A dam-break wave propagating on an initial still water depth h_0 is commonly called a bore. As discussed in Section 4.3, its hydrodynamic properties are different to those of surges. A bore has a steep turbulent aerated front, similar to a translating hydraulic jump (Figure 4.7). The general behaviour of the forces induced by wet bed bores is shown in Figure 5.3 and some key differences with the dry bed surges were pointed out at the beginning of Section 5.3. In the present research, an initial force overshot was not constantly recorded and, typical of wet bed bores, the increase in horizontal force F_x was proportional to the increase in water depth. This is in agreement with the observations made by Shafiei et al. (2016).

For the estimation of the force acting on the building, the procedure presented in Section 5.3.1 for the dry bed surge is here applied to wet bed bores. Nevertheless, it was noted that the estimation of the horizontal force F_x, through Eq. 5.2 constantly overestimated the measured value by some 20 to 50%, as shown in Figure 5.6b and Figure 5.8. Probably, this behaviour can be attributed to the complexity of the turbulent bore front and its aerated profile. Section 4.4.2 pointed out a discontinuity between the front celerity U and the depth-averaged velocities values V_m behind the wave front computed with Eq. 4.10 (Figure 5.6a). The authors initially attributed this to performances of the UVP probes in aerated flows. However, more recent developments have shown that such discontinuity in velocity values may be a consequence of the presence of the recirculating roller, associated with high energy losses. In addition, the presence of an aerated roller with pulsating and compressible behaviour might be partially responsible for the attenuation of the impact forces.
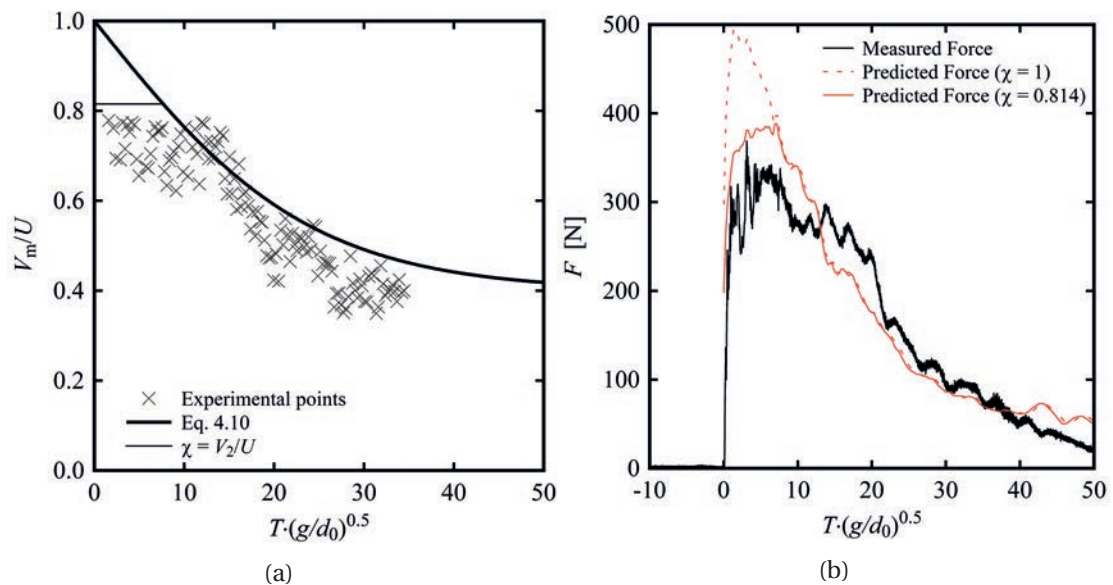
Figure 5.6 – Wet bed bore with impoundment depth $d_0 = 0.82$ m and initial still water depth $h_0 = 0.05$ m (test 5.6): (a) model suggested to take into account the wet bed reduction; (b) example of force estimation with and without the wet bed bore reduction coefficient χ.

For all these reasons, a wet bed force reduction coefficient χ was introduced (Figure 5.6) and a maximum value of $V_m/U = \chi$ was imposed, in agreement with the experimental measurements in Section 4.4.2. The values of the coefficient χ were extracted from experimental data for all bores at $T = \tau_{max}$ and presented in Figure 5.7. Two approaches are herein proposed:

1. In Figure 5.7a the values of χ are obtained as the best experimental fit, described by the empirical relationship in Eq. 5.3 with the coefficients 0.3 and 4.7 ($R^2 = 0.95$)

$$\chi = 1 - 0.3 \cdot \tanh\left(4.7 \cdot \frac{h_0}{h_{max}}\right)$$ (5.3)

2. In Figure 5.7b, the values of χ are obtained through the velocity V_2 behind the bore front predicted by the momentum equation presented in Eq. 2.22 as a function of h_0 and h_2

$$\chi = \frac{V_2}{U} = 1 - \frac{h_0}{h_2} = 1 - 1.073\left(\frac{h_0}{d_0}\right)^{0.629}$$ (5.4)

Regardless of the approach chosen, similar values of the reduction coefficient χ are obtained.
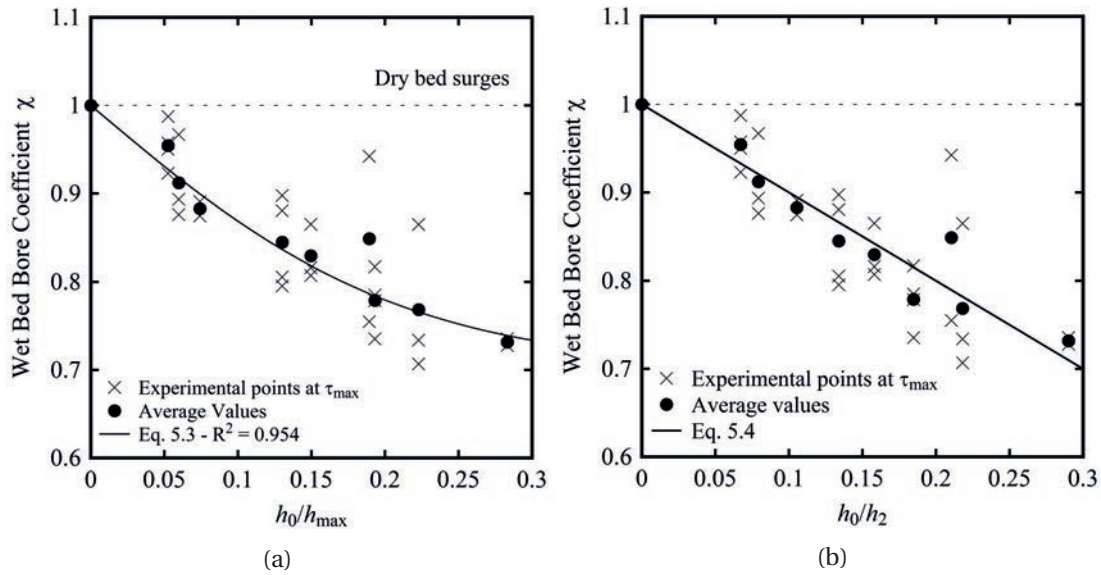
Figure 5.7 – Wet bed bore coefficient χ for all tested scenarios: (a) experimental approach, (b) semi-theoretical approach

Thus, the modified momentum flux per unit width, M^*, taking into account force reduction coefficient, was computed using:

$$M^*(t) = h(t) \cdot \left\{\min\left[\chi U; V_m(t)\right]\right\}^2$$ (5.5)

where $h(t)$ is the time-development of the wave profile without the building, χ the reduction coefficient, U the bore front celerity and V_m the depth-averaged profile velocity, defined through the expression presented in Eq. 4.10. For dry bed surges a coefficient $\chi = 1$ can be assumed.

In the computation of the total horizontal force if the wet bed force reduction coefficient χ and the modified momentum M^* are introduced, then Eq. 5.2 leads to:

$$F_{x,D} = \frac{1}{2}\rho C_R B \cdot M^* = \frac{1}{2}\rho C_R B h \cdot \left\{ \min\left[\chi U; V_m(t)\right] \right\}^2 \tag{5.6}$$

and the prediction of the horizontal force $F_{x,D}$ using Eq. 5.6 is presented in Figure 5.8 for three bores with different initial still water depth.

(a) $h_0 = 0.01$ m (test 5.4)   (b) $h_0 = 0.03$ m (test 5.5)   (c) $h_0 = 0.05$ m (test 5.6)
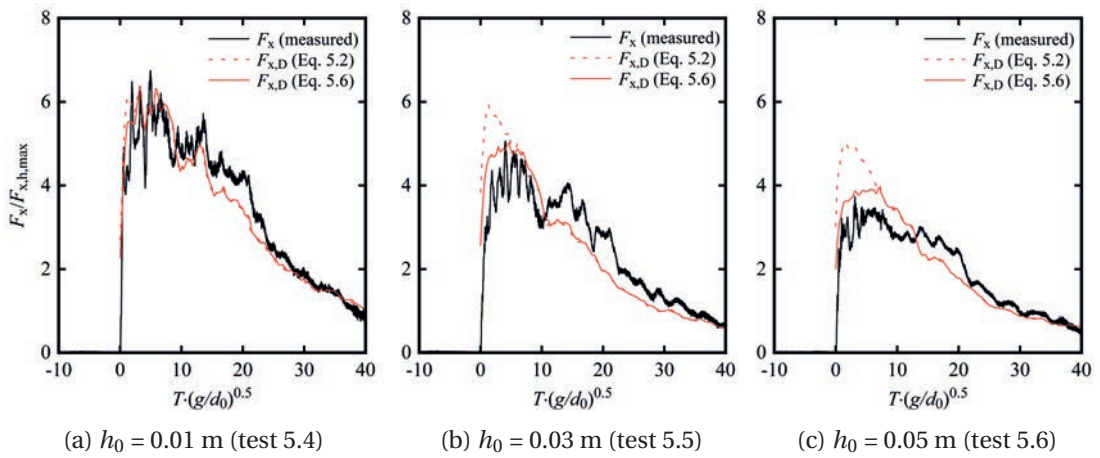
Figure 5.8 – Comparison of the measured horizontal force with the values obtained from the momentum equation for three wet bed bores with impoundment depth $d_0 = 0.82$m and various initial still water depths h_0. (black: measured value; red: predicted with Eq. 5.6; dotted: predicted with $\chi = 1$, Eq. 5.2)

5.3.3 Maximum forces

For all considered configurations (bores + surges), the experimental force maxima $F_{x,max}$ were extracted and compared to the values predicted using Eq. 5.6, $F_{x,D,max}$. These were shown to be proportional to the maximum momentum flux per unit width M^*_{max}, resulting in Eq. 5.7. Results showed a good agreement for all scenarios. Accordingly, for the present case, Eq. 5.6 and Eq. 5.7 provide a good estimation of the maximum impact load for both surges and bores on impervious buildings.

$$F_{x,D,max} = \frac{1}{2}\rho C_R B \cdot M^*_{max} \tag{5.7}$$
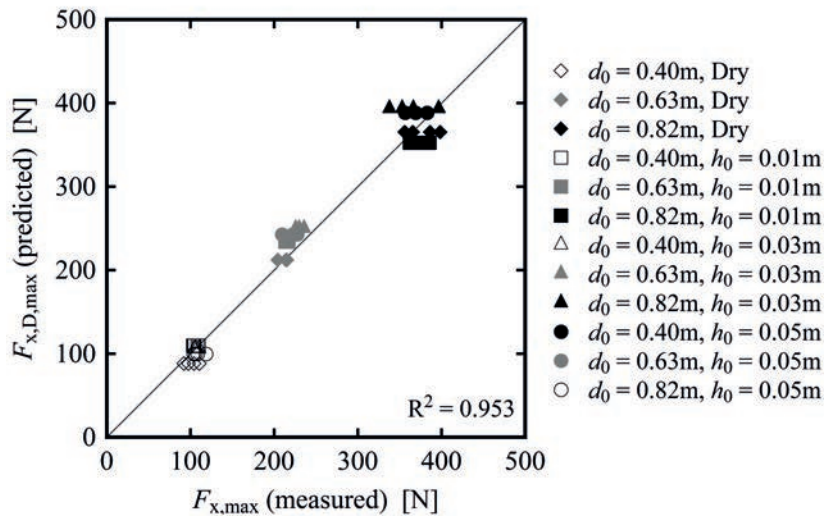
Figure 5.9 – Comparison of maximum measured forces ($F_{x,max}$) and predicted values ($F_{x,D,max}$) obtained with 5.7 ($R^2 = 0.953$).

5.3.4 Comparison with previous studies

The experimental values obtained in the present study were also compared with formulae and methodologies found in literature (Table 2.3). Results are plotted in Figure 5.10.

1. Cross (1967) suggests that the horizontal force is the sum of both hydrostatic and hydrodynamic components, as shown in Eq. 2.26.

2. The *Japanese design guideline* (SMBTR), based on the work of Asakura et al. (2000) and Okada et al. (2005) suggests to use 2.31, resulting into a force magnitude equal to nine times the hydrostatic force magnitude. Yeh et al. (2005) commented on the validity of this equation, indicating that this leads *"excessively overestimated values"*.

3. Fujima et al. (2009) propose an expression similar to Asakura et al. (2000), but based on the maximum inundation depth, leading to Eq. 2.37.

4. OCADI (2009) of the Ports and Harbors Bureau of Japan, proposes a triangular pressure distribution above the still water level with height $3h$ and base pressure given by $2.2\rho g h$. This base pressure is maintained constant throughout the depth of still water h_0. The resulting force on the wall is given by Eq. 2.38.

5. ASCE 7 Chapter 6 (Hydrodynamic formula 6.10-1) represents a conservative alternative to more detailed tsunami loading analysis. The maximum hydrodynamic loads are assumed to occur for the Load Case 2, when $h = 2/3 h_{max}$ (Section 5.4.2), assuming a conservative Froude number of $\sqrt{2}$. The suggested equations were previously presented in Eqs. 2.43 and 2.45

6. ASCE 7 Chapter 6 suggests to use the expression by Robertson et al. (2013) in Eq. 2.39, whose validity was proved during the 2011 Japan tsunami by Chock et al. (2012).

7. Foster et al. (2017) suggested to use Eq. 2.40 to predict the force, as a function of a parameter λ_F, defined in Eq. 2.41, taking into account the effect the blockage ratio.

All results are plotted in Figure 5.10a for dry bed surges and in Figure 5.10b for wet bed bores. One can observe that most existing formulae over-predict the herein measured forces. For dry bed surges, relatively good agreement was found using Eq. 2.38 (OCADI, 2009) and Foster et al. (2017), whereas for wet bed bores, the best agreement is provided by ASCE 7 (C6.10.1.4).

It is important to point out that most studies, including Ramsden (1996), Santo and Robertson (2010) and Robertson et al. (2013), were carried out for walls with blockage ratios $\beta = W/B = 1$. The difference in resulting forces shown in Figure 5.10 suggests that in reality this is a 3D phenomenon and that blockage ratio plays an important role in the computation of the total force. Nevertheless, neglecting the effect of the blockage ratio in the computation of the horizontal load is a conservative approach in the design process.
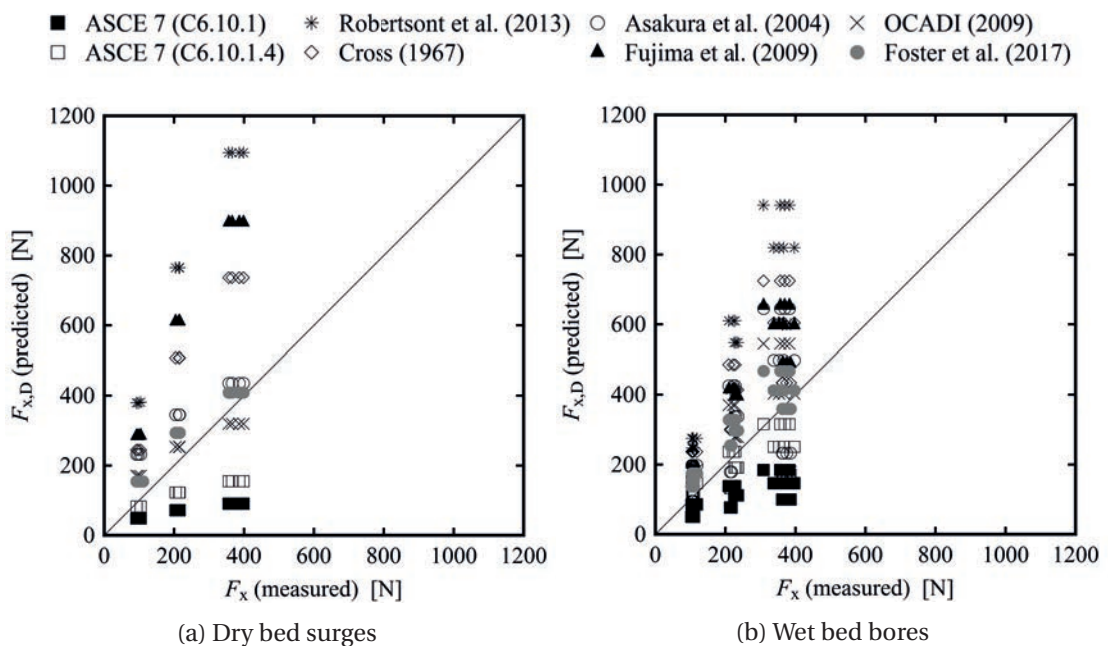
Figure 5.10 – Comparison of measured experimental horizontal force values (F_x) with those calculated using existing formulas in literature ($F_{x,D}$).

5.3.5 Resistance coefficient

As discussed in Section 5.3, during the impact phase, various components of the total force can be identified, including an initial surge force, hydrodynamic (or drag) and hydrostatic components. Since the process is highly unsteady and rapidly varied, these components are difficult to isolate and estimate. Thus, similarly to Gupta and Goyal (1975) and Arnason et al. (2009), a resistance coefficient parameter C_R, taking into account the surge, hydrostatic and hydrodynamic components was used. It is defined as:

$$C_R = \frac{2 \cdot F_x}{\rho B h V_m^2} = \frac{2 \cdot F_x}{\rho B M^*} \tag{5.8}$$

where ρ is the fluid density (herein $\rho = 1000$ kg/m^3), B is the building width, F_x is the measured horizontal force and h and V_m are the wave height and depth-averaged flow velocity, respectively, measured for the free flow condition without the presence of the building. As mentioned in Section 5.3.1, the definition presented in Eq. 5.8 is similar to the drag coefficient C_D for the computation of the hydrostatic component; however, the resistance coefficient C_R is a function of time rather than a constant value. C_R represents the value that would be required to obtain the exact measured value F_x, given the height h and velocity V_m of the wave without the presence of the building. If $C_R > 2$, then the force is underestimated, whereas for $C_R < 2$ the force is overestimated. For longer times, an increase in the value of C_R is observed especially for dry bed surges, suggesting an underestimation of the horizontal force in the quasi-steady hydrodynamic phase when using the conventional value of $C_R = 2$ (Figure 5.5a). This is due to the different wave periods between the wave without the building and the loading process. In Figure 5.11 the chosen normalisation T/τ_{max} allows to express the value of C_R at the moment of the force peak ($T/\tau_{max} = 1$). Good agreement is observed for all scenarios and a constant value of $C_R = 2$, suggested by numerous design codes including FEMA55 (2000), CCH (2000) and ASCE7-Chapter 6, seems appropriate. These findings are confirmed in Figure 5.12, where values of C_R at $T/\tau_{max} = 1$ are presented for various surges and bores tested. For wet bed bores, the independence of the resistance coefficient from the initial still water depth h_0 is shown.
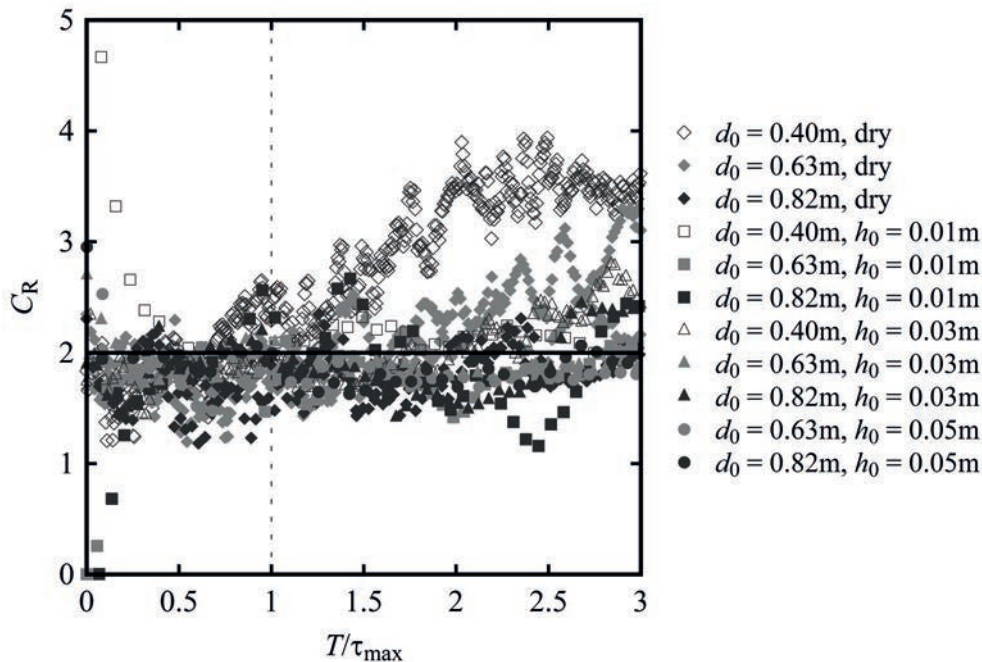
Figure 5.11 – Time history of the resistance coefficient C_R during the wave impact ($T = \tau_{max}$) for dry bed surges and wet bed bores
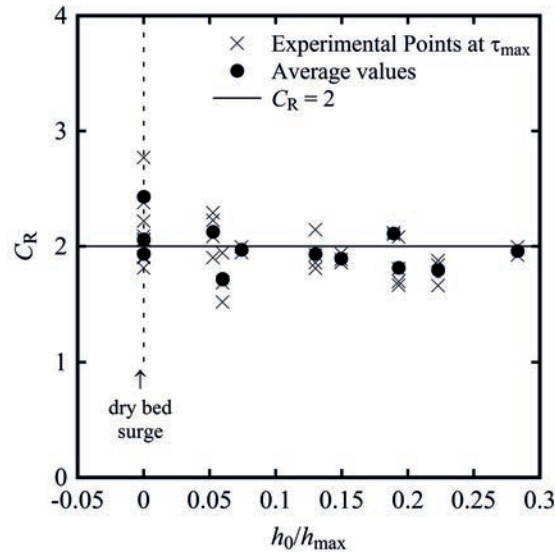
Figure 5.12 – Resistance coefficient C_R determined at τ_{max} for both bores and surges

5.4 Horizontal force analysis

An in-depth analysis of the measured horizontal force in the x-direction was conducted. The main parameters discussed are: (Figure 5.13)

- Time to peak, τ_{max}, corresponding to the time from wave arrival (t_0) to the force peak.
- Wave height at maximum force, h_{M}, at which the maximum horizontal force is measured
- Impulse, I, transferred from the wave to the building.
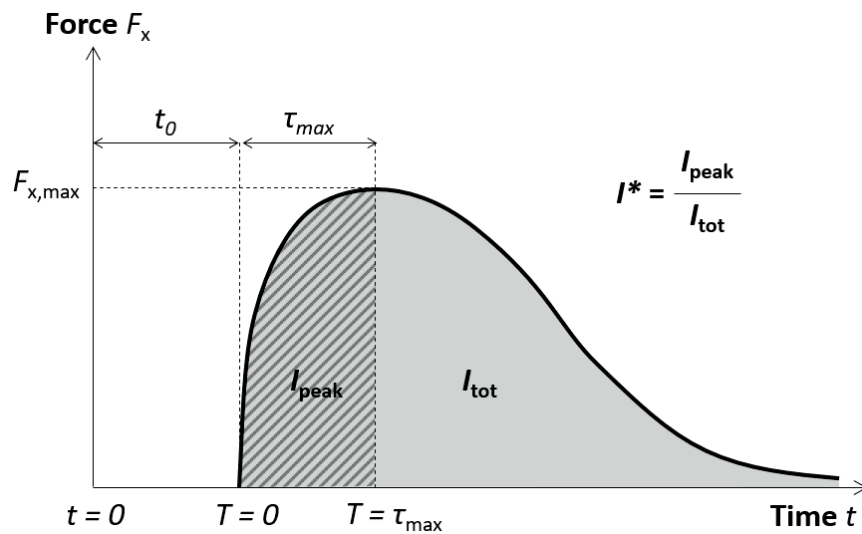
Figure 5.13 – Definition sketch of parameters used in the force analysis

5.4.1 Time to peak

The *"time to peak"*, τ_{max}, represents the time interval between the initial impact ($T = t - t_0 = 0$) and the maximum horizontal force $F_{x,max}$ measured by the Force Plate. The values of τ_{max} obtained for all tests are presented in Figure 5.14 as a function of h_0/h_{max}, where h_0/h_{max} = 0 represents the dry bed surges and $h_0/h_{max} > 0$ the wet bed bores. Results showed larger normalised values of τ_{max} for dry bed surges (h_0/h_{max}), ranging from $5 < \tau_{max} \cdot (g/d_0)^{0.5} < 35$, whereas for wet bed bores ($h_0/h_{max} > 0$), almost all maxima occurred instantaneously for $0 < \tau_{max} < 5$. These observations clearly confirmed a substantial difference between surges and bores, proving thus that maximum force on wet bed values occur before those recorded in the dry bed scenario. This therefore resulted into steeper average gradients $\mathrm{d}F/\mathrm{d}t$ and into a more severe loading condition.
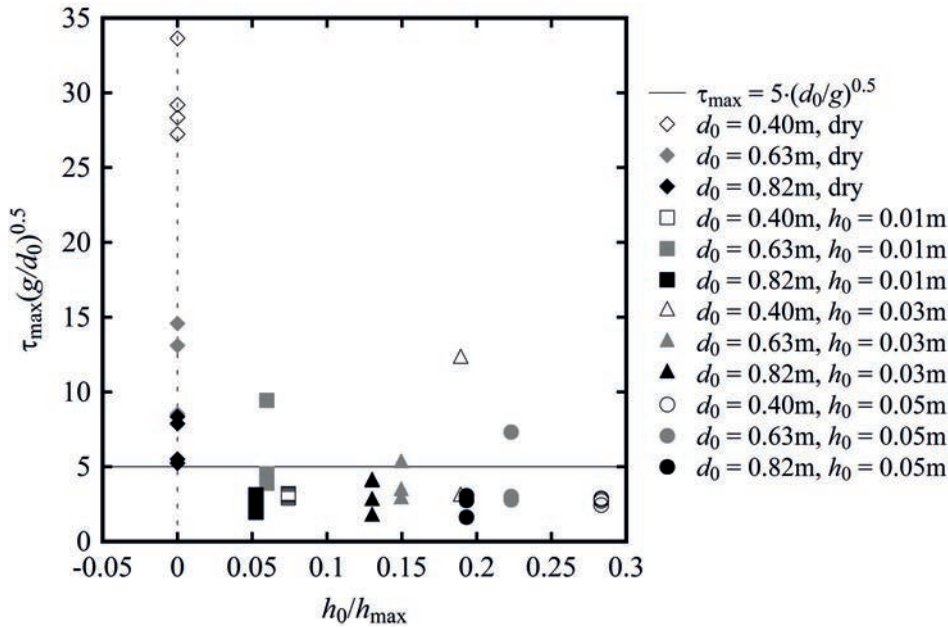
Figure 5.14 – Experimental values of the time to peak (τ_{max}) for both dry bed surges (h_0/h_{max} = 0) and wet bed bores ($h_0/h_{max} > 0$) with various impoundment depths and initial still water depths.

5.4.2 Wave height at maximum force

An important parameter in the design of resilient buildings is the wave height h at which the maximum force $F_{x,max}$ occurs ($T = \tau_{max}$), normalised with the maximum wave height h_{max} without the building.

$$h_M = \frac{h(T = \tau_{max})}{h_{max}} \tag{5.9}$$

The results obtained from the tests are presented in Figure 5.15. These are also compared to the design guidelines of the ASCE 7 Chapter 6, according to which the maximum hydrodynamic load occurs at the moment when the 2/3 of the maximum inundation depth is reached, *i.e.* when $h = h_M = 2/3 h_{max}$.

Results showed relatively good agreement with ASCE 7 guidelines for dry bed surges (h_0/h_{max} = 0) with an average value of $h_M = 0.71$ m. However, for wet bed bores with increasing values of h_0/h_{max}, the maximum forces occurs at a higher depth, due to the steeper front profiles previously shown in Section 4.3.2. Thus, for bores, the choice of $h_M = 2/3$ becomes less conservative. Since the maximum force is proportional to the maximum momentum, as shown in Eq. 5.1, these results are consistent with the findings presented in Section 4.6 for the maximum momentum flux per unit width M.
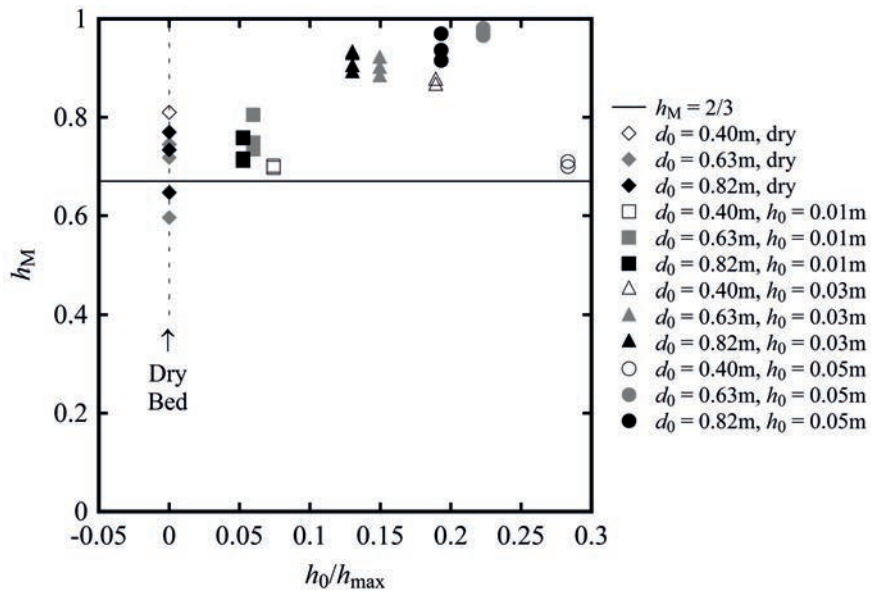
Figure 5.15 – Wave height at maximum force h_M at which the maximum force $F_{x,max}$ occurs. Experimental data and comparison with design guidelines of the ASCE7 - Chapter 6.

5.4.3 Impulse

The product of force F and time t is known as Impulse I. For the present case, the total impulse I_{tot} is the integral of the force F_x over time, until the upper limit $T = 100 \cdot (d_0/g)^{0.5}$ is reached. This value was chosen by the author as it represented the minimum time that allowed to include all loading processes for all waves. This is expressed as:

$$I_{tot} = \int_0^{100\sqrt{\frac{d_0}{g}}} F_x(T) \mathrm{d}T \qquad (5.10)$$

This quantity also represents the area of the surface below the curve, as shown in Figure 5.13. Given Newton's 2nd Law ($F = m \cdot a = m \cdot \Delta V / \Delta t$), the impulse can be expressed as $I = F \cdot \Delta t = m \cdot \Delta V$, corresponding to the change in momentum. The impulse experienced by the building I_{tot} equals therefore the exchange in momentum with the incoming wave. To better define the amount of impulse that is transferred to the building before the peak force occurs, similarly to Bullock et al. (2007), a parameter, I_{peak}, is defined as the integral between $0 < T < \tau_{max}$. The latter represents the area of the surface below the curve up to the moment when $F_{x,max}$ is recorded (Figure 5.13).

$$I_{peak} = \int_0^{\tau_{max}} F_x(T) dT \tag{5.11}$$
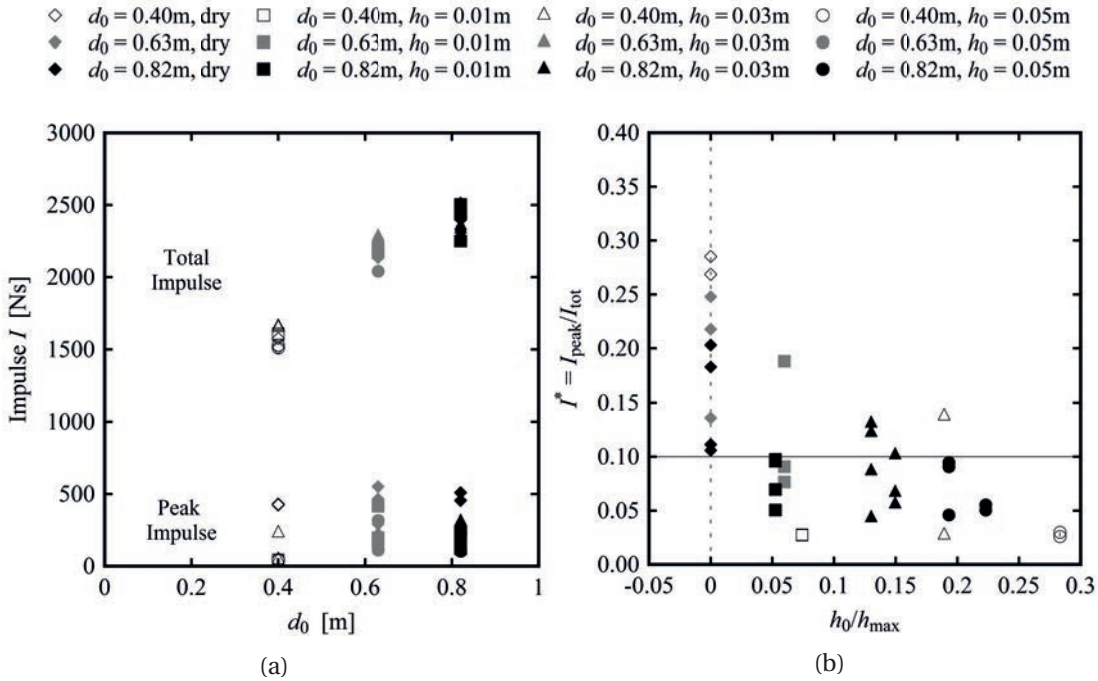
Figure 5.16 – Values of: (a) total and peak impuse; (b) $I^* = I_{peak}/I_{tot}$ computed for dry bed surges (h_0/h_{max}) and wet bed bores.

Both the total impulse and the peak impulse calculated for the tests are shown in Figure 5.16a. These results suggest that the Impulse transferred to the building before the occurrence of the force peak, is only a small portion of the total impulse. A parameter I^* is defined as the ratio between the peak impulse I_{peak} and the total impulse I_{tot}, corresponding the portion of impulse that is transferred to the building before the maximum force occurs.

$$I^* = \frac{I_{peak}}{I_{tot}} \tag{5.12}$$

Its values for the current experimental tests are presented in Figure 5.16b. A different behaviour can be observed between surges ($h_0/h_{max} = 0$) and bores ($h_0/h_{max} > 0$). In fact, for bores, less

than 10-15 % of the total impulse is transferred to the building before the peak. In contrast, for surges this can reach 30-35 %. This difference is also a consequence of the time to peak force values which were previously discussed in Section 5.4.1 and it is in agreement with Bullock et al. (2007), for whom $I_{peak} < 0.3\,I_{tot}$.

An estimation of the total impulse for all tested scenarios, employing Eq. 5.6, can be obtained through the following expression:

$$I_{tot,D} = \int_{0}^{100\sqrt{\frac{d_0}{g}}} F_{x,D}(T)\mathrm{d}T = \frac{1}{2}\rho C_R B \cdot \int_{0}^{100\sqrt{\frac{d_0}{g}}} M^* \mathrm{d}T \tag{5.13}$$

where ρ is the water density, C_R is the resistance coefficient assumed constant in time ($C_R = 2$), B is the building width and M^* is the modified momentum flux (Eq. 5.5). The results obtained are shown in Figure 5.17 , where a good agreement between measured and predicted values can be observed ($R^2 = 0.86$). This is in agreement with the findings of Bullock et al. (2007), according to which a linear relationship between total momentum flux and impulse were found.
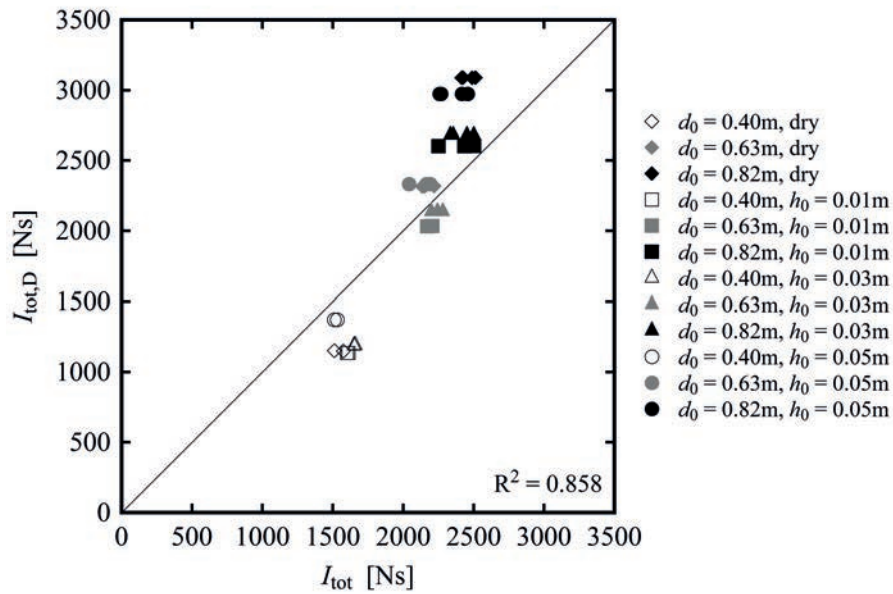
Figure 5.17 – Total impulse values measured (I_{tot}) and predicted values ($I_{tot,D}$) with Eq. 5.13.

5.5 Moment and cantilever arm

Any force applied outside of the centroid of an area produces a moment that is directly proportional to its application distance, called cantilever arm L_z. In this research, as pointed out in Section 5.3, only moments in the transversal direction (M_y) were considered. Since their magnitude was too low to be considered relevant, M_x and M_z were neglected, as previously

shown in Figure 5.3. The temporal evolution of the cantilever arm can be computed as:

$$L_z(t) = \frac{M_y(t)}{F_x(t)} \tag{5.14}$$

Despite some small scattering, results showed that overall the maximum moment $M_{y,max}$ occurred at the same time as the maximum horizontal force $F_{x,max}$, as shown in Figure 5.18a. The cantilever arm corresponds to the application point of the horizontal force, whose magnitude was identified in Section 5.3. As shown in Figure 3.2, the origin of the coordinates ($L_z = 0$) coincided with the channel bottom. Given the simultaneous occurrence of $F_{x,max}$ and $M_{y,max}$, as shown in Figure 5.18a, the value of L_z at $T = \tau_{max}$ can be obtained using Eq. 5.15. The values are normalised with the maximum wave height without the building h_{max}. The cantilever arm of all experimental points at $T = \tau_{max}$, for both dry bed surges and wet bed bore, is presented in Figure 5.18b.

$$(L_z)_{\tau_{max}} = \frac{M_{y,max}}{F_{x,max}} \tag{5.15}$$

These results showed that, for all tested scenarios, the cantilever arm had a fairly constant magnitude, ranging between 0.90 and 1.35 h_{max}, with an average value of 1.15 h_{max}, where h_{max} is the wave height for the case without building.

(a) Time to peak for forces and moments   (b) Cantilever arm
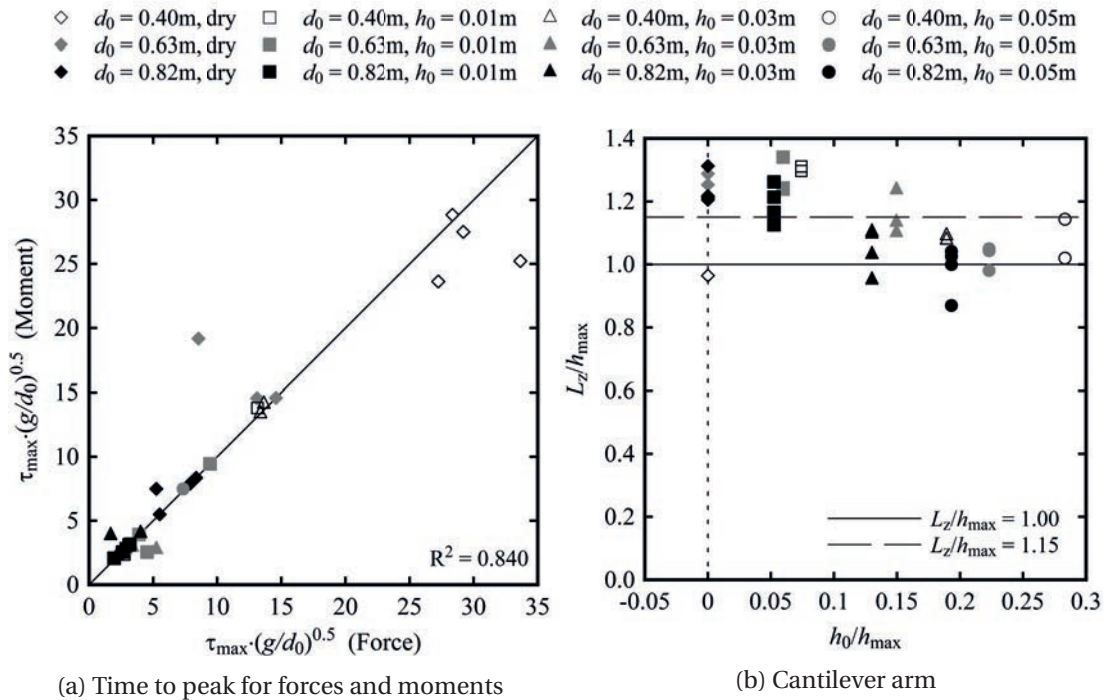
Figure 5.18 – (a) Time of occurrence of maximum horizontal force F_x and maximum moment M_y; (b) Cantilever arm L_z computed for both dry bed surges and wet bed bores for $T = \tau_{max}$

It could therefore be assumed that the maximum horizontal force defined in Section 5.3, was applied at a height that corresponded to 1.15 of the maximum wave height without the presence of the building, something which leads to Eq. 5.16:

$$M_{y,D,max} = F_{x,D,max} \cdot \mathbf{1.15} h_{max} \tag{5.16}$$

The prediction of the maximum moment $M_{y,D,max}$ through Eq. 5.16 is compared to the experimental data in Figure 5.19 : good agreement for all scenarios can be observed ($R^2 = 0.870$), thus proving its validity.
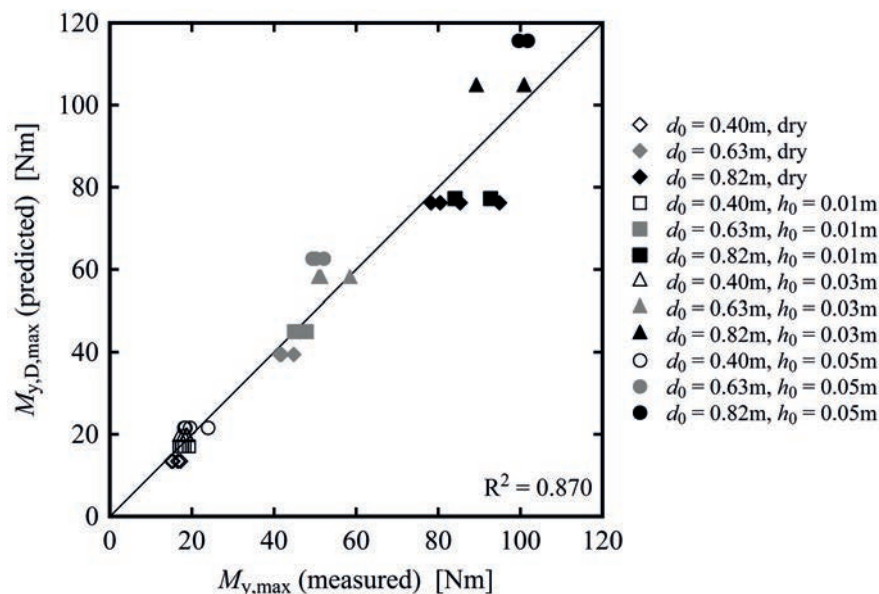
Figure 5.19 – Comparison of experimental moments $M_{y,max}$ with the values $M_{y,D,max}$ predicted through Eq. 5.16.

5.6 Summary

Post-tsunami forensic engineering field surveys have shown that specific building design can limit damages to vital infrastructures. In particular, the construction of vertical evacuation shelters can rescue numerous people. For this, an inner knowledge of the loading process is necessary and some experimental studies and few design guidelines are available to engineers. However, some disagreement with measured data and an overestimation of the forces still exists, especially for free-standing building-like structures.

This Chapter focuses on the impact loading process of bores and surges generated through the vertical release technique, on free-standing structures. For all scenarios, this impact was characterized by high splashes and significant turbulent air entrainment on the upstream side of the building. Following the initial impact, quasi-steady hydrodynamic flow conditions

115

around the building were observed. During the hydrodynamic loading process, only the forces and moments in the stream-wise direction (F_x, M_y) were considered, because the forces and moments in transversal and vertical directions were found to be too small to be relevant. The following conclusions can be drawn:

1. For **dry bed surges**, the horizontal force F_x was proportional to the momentum flux per unit width $M = hV_m^2$, where h and V_m are the height and velocity of the wave without the building. Eq. 5.2 describes well the horizontal forces for dry bed surges.

2. For **wet bed bores**, if Eq. 5.2 was applied, an overestimation of the maximum load was constantly observed. The aerated roller, similar to a translating hydraulic jump, suggested the presence of internal energy dissipation, responsible for a reduction in the subsequent flow velocities. For this, a wet bed force reduction coefficient χ (Eq. 5.3 and 5.4) was introduced and a modified momentum flux M^* defined. This approach gave a better agreement for all experiments (Eq. 5.6).

3. Since the wave impact process is highly unsteady and rapidly varied, the hydrostatic, hydrodynamic (or drag) and surge components were difficult to isolate and further estimate. For this reason, the drag coefficient, C_D, was herein replaced with a resistance coefficient C_R. The latter was a function of time and an average value $C_R = 2$ was shown to be appropriate at the occurrence of the maximum horizontal force, $F_{x,max}$.

4. The maximum horizontal force was shown to be proportional to the maximum modified momentum flux per unit width M_{max}^*. A good estimation for both surges and bores is represented by Eq. 5.7.

5. A comparison of the current experiments with previous studies and design guidelines showed a constant over prediction of the estimated horizontal force values. This pointed out the importance of the blockage ratio and the 3-dimensionality of the loading process.

6. Additional parameters were also introduced and discussed. The time to peak τ_{max}, defined as the time lap between the arrival of the wave t_0 and $F_{x,max}$, showed that the maximum force occurred before for wet bed bores than for dry bed surges. Especially for bores, the maximum force $F_{x,max}$ also occurred at a relative height h_M that was higher than the 2/3 value suggested by the ASCE 7-06. The impulse ($I = F \cdot t$) represented the exchange in momentum transferred from the wave to the building. Similar values were observed for surges and bores with the same initial conditions, however for bores only 10-15% of the total impulse were transferred to the building before the occurrence of the maximum horizontal force.

7. The maximum force $F_{x,max}$ and maximum moment $M_{y,max}$ were shown to occur at the same time.

8. The application point of the force (cantilever arm) was defined as $L_z = M_{y,max}/F_{x,max}$ and, for all scenarios an average value of 1.15 h_{max} was found. This allowed to predict the moment M_y using Eq. 5.16.

6 Impact on impervious buildings with overflow

6.1 Overview

As discussed in Chapter 1, some key buildings located in coastal areas are conceived as vertical shelters and therefore designed to withstand impact forces to guarantee safety to people. For such structures, the main loading features were discussed in Chapter 5. On the other hand, some of the non critical infrastructures, typically residential houses with lower elevation, are not conceived as vertical shelters and a submergence (or overflow) of the structure is therefore acceptable in case of natural disasters. An example of these structures were provided in Figures 1.6b and 1.8f. Most previous studies focused on free-standing structures that might act as possible vertical shelters and little interest was given to the loading process on smaller residential houses. As a result of the overflow, this experimental study pointed out flow depths that were lower on the upstream side of the building and higher on the downstream. This resulted into milder load conditions and, compared to a vertical shelter, a modified approach is therefore necessary to estimate the force and the moment.

The main objectives of this chapter are the following:

1. To provide an insight of the physical process for the overflow of a free-standing building.
2. To characterize the loading process for building with overflow in terms of horizontal forces, moments and impulse.
3. To conclude whether the results presented and discussed in Chapter 5 can also be applied to structures with overflow.

For this a 0.3×0.3×0.3 m aluminium cube representing the building was installed in the channel. Pictures of the configuration with and without submergence are presented in Figure 6.1. More information concerning the geometry and the structural properties of the buildings can be found in Section 3.4. The reference tests performed on the structure without overflow were presented and discussed in Chapter 5. The tests performed are presented in Table 6.1.

This Chapter is based on the article "Experimental study on effect of building overflow on the resulting hydrodynamic load" by D. Wüthrich, M. Pfister, I. Nistor and A.J. Schleiss under revision in *Journal of Hydraulic Research*. The experimental work and the analysis presented hereafter is original and performed by the author.

(a) $H_B = 0.6$m   (b) $H_B = 0.3$m
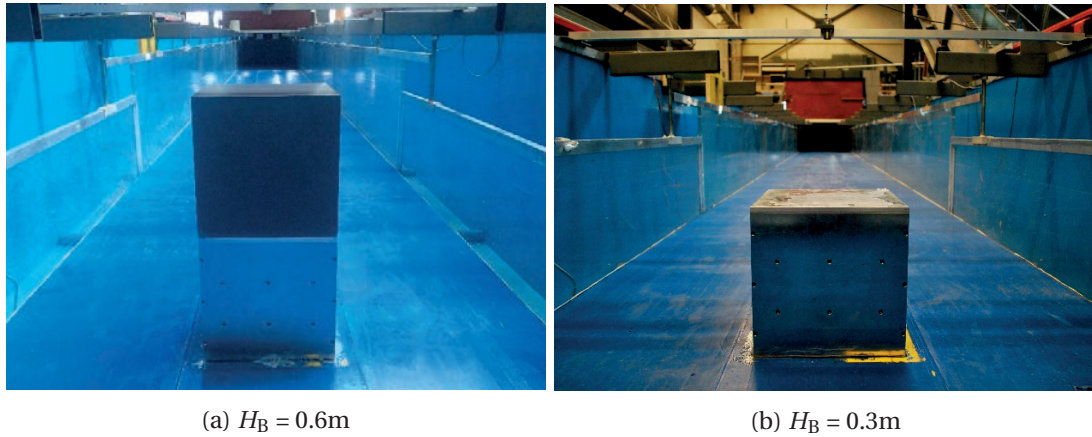
Figure 6.1 – Building heights H_B used in the present study, focusing on building overflow

H_B	Bed	d_0 [m]	h_0 [m]	U [m/s]	h_{max} [m]	h_0/h_{max}	Rep.	
0.3 m	dry	0.82	-	3.556	0.181	0	2	test 6.1
		0.63	-	3.114	0.162	0	2	test 6.2
		0.40	-	2.347	0.132	0	2	test 6.3
	wet	0.82	0.010	3.074	0.193	0.052	5	test 6.4
			0.030	2.810	0.232	0.129	4	test 6.5
			0.050	2.755	0.260	0.193	2	test 6.6
		0.63	0.010	2.702	0.172	0.058	2	test 6.7
			0.030	2.518	0.206	0.146	3	test 6.8
			0.050	2.437	0.224	0.223	2	test 6.9
		0.40	0.010	2.104	0.142	0.072	4	test 6.10
			0.030	1.971	0.162	0.185	2	test 6.11
			0.050	1.933	0.178	0.280	2	test 6.12

Table 6.1 – Experimental program of the tests performed with overflow ($H_B = 0.3$m).

6.2 Visual observations

As shown in Figure 6.1 two configurations with different building heights ($H_B = 0.3$ m and $H_B = 0.6$ m) were tested for both dry bed surges and wet bed bores. Similarly to what was observed in Section 5.2, for both cases with and without overflow, two main phases were recognised: (1) an initial impact of the wave front, followed by (2) a quasi-steady hydrodynamic phase during which the main body of the wave flowed around the structure. These two phases are visually presented in Figure 6.2, where the time evolution of the impact is presented through pictures taken at $T \cdot (g/d_0)^{0.5} \approx 0$ s (impact with highest run-up height) and $T \cdot (g/d_0)^{0.5} \approx$ 14 and 28 (post-impact hydrodynamic phase) for both surges and bores with and without overflow. Similar results were previously presented by Wüthrich et al. (2016c), pointing out some key differences between the impact of surges and bores.
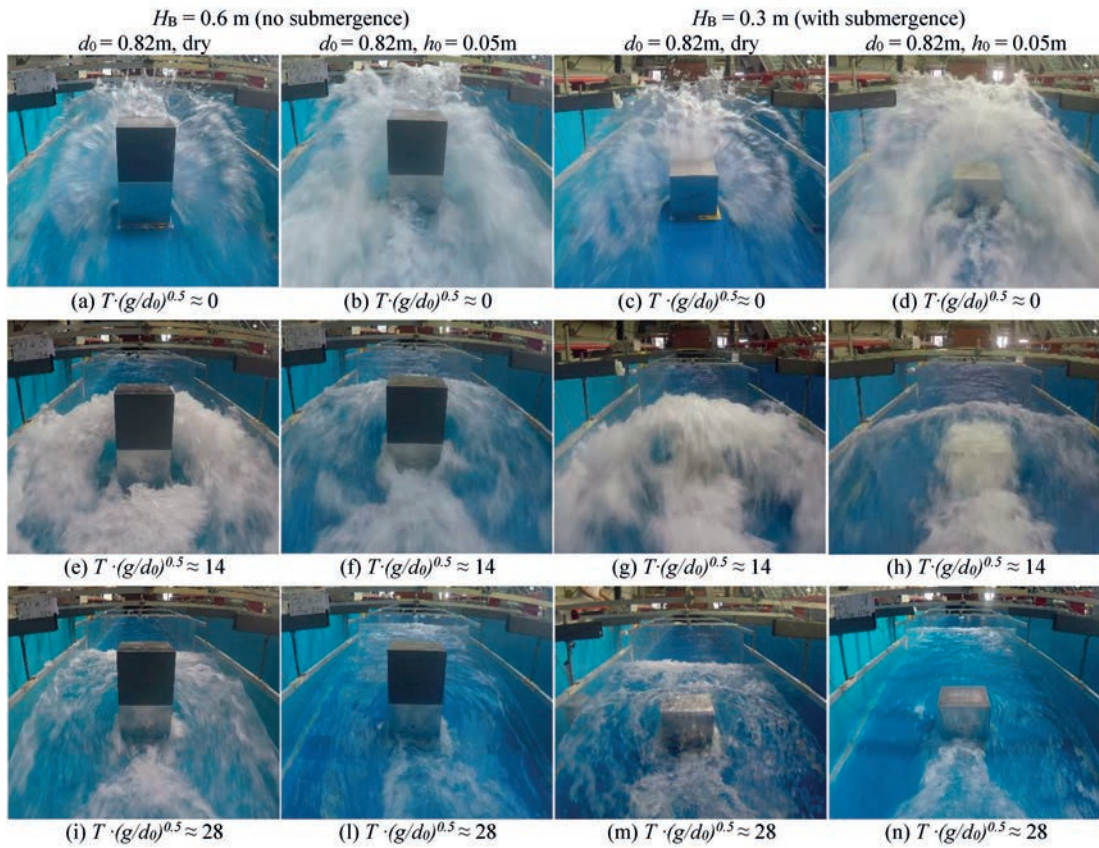
Figure 6.2 – Time evolution of the wave impact against an impervious building for a dry bed surge (h_{max} = 0.187m, d_0 = 0.82m, test 5.1 and 6.1) and a wet bed bore (h_{max} = 0.269m, d_0 = 0.82m, h_0 = 0.05m, test 5.6 and 6.6) with (c, d, g, h, m, n) and without (a, b, e, f, i, l) overflow.

During the initial impact phase no major differences were observed for the case with and without overflow, *i.e.* H_B = 0.3 m and H_B = 0.6 m, respectively. When the wave front hit the building upstream side, some vertical run-up heights H were observed. These were measured to be some 4 times the maximum wave height without the structure h_{max} (Figure 6.3). For both bores and surges the impact phase presented high splashes and some turbulent air entrainment in the upstream side of the building, as shown in Figure 6.2a-d. Due to the presence of the building, the run-up splashes fell on the incoming wave, producing a stationary roller on the upstream side of the building, associated with high level of turbulence and air entrainment. The formation of a roller in the upstream side is shown in Figure 6.2e-f and it marked the transition between the impact and the hydrodynamic phase. Overall dry bed surges presented higher air entrainment compared to wet bed bores, as shown in Figure 6.2e-g and f-h. This is probably due to the higher velocities and Froude numbers associated with the incoming surge (Section 4.5). Dry bed surges were also characterized by a pulsating behaviour, attributed to the interaction between the high speed incoming wave and the reflection of the vertical run-up. For the higher buildings (H_B = 0.6 m), no overflow was observed and the water flowed completely around the obstacle. For the lower buildings (H_B = 0.3 m) an overflow was

observed for the largest waves (d_0 = 0.63 and 0.82 m). The higher flow velocities associated with the dry bed surge produced an aerated jet overpassing the building (Figure 6.2g), whereas for the bore a non-aerated flow submerging the structure was observed (Figure 6.2h). Visually, the overflow seemed more important for bores, due to the higher constant wave height of the incoming wave (h_2). For all scenarios the presence of the building provoked a constriction, with a decrease in flow velocity and an increase in water level. The combination of these effects lead to a change in flow regime and to the propagation of a bore in the upstream direction. For all configurations intense vortices in the downstream side of the structure for both the surge and the bore were observed (Figure 6.2).

The Ultrasonic Sensor (US7) located 0.15 m upstream the building side (Figure 3.2) allowed to measure the vertical run up heights H providing a more quantitative description of the visual observations previously discussed. The results are shown in Figure 6.3 for both a dry bed surge and a wet bed bore, with and without overflow. These are also compared with the wave profile h measured without the structure. The shift in arrival time confirmed that the surge propagating on dry bed had higher propagating velocities than the bore on wet bed (Section 4.4). A difference in flow behaviour can be noticed and these measurements confirmed the visual observations that the surge had a more fluctuating behaviour with higher aeration. For the surge similar upstream level were observed, regardless of the building height H_B, whereas for bores, the higher discharge over the structure resulted into a reduction of the sustained water depth on the upstream side of the building.

(a) Dry bed surge   (b) Wet bed bore
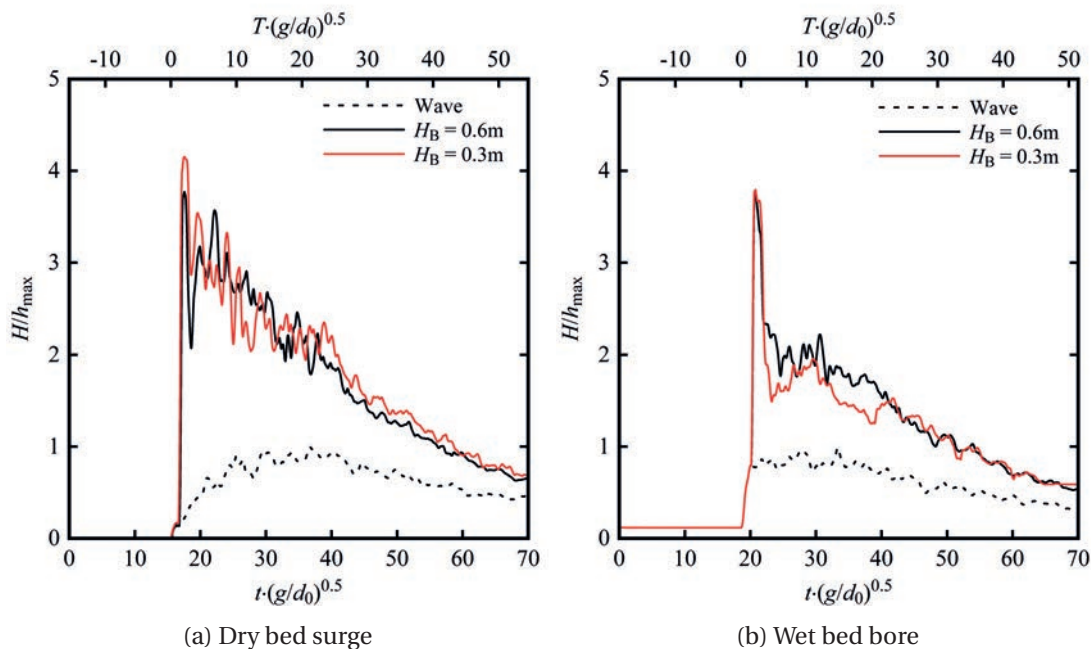
Figure 6.3 – Wave profiles (H) at US 7 for two building heights (H_B), normalised with the maximum wave height without the building (h_{max}): (a) dry bed surge (d_0 = 0.82m, h_{max} = 0.162m, test 5.1, 6.1); (b) wet bed bore (d_0 = 0.82m, h_0 = 0.03m, h_{max} = 0.162m, test 5.5, 6.5)

6.3 Horizontal forces

Both buildings were installed on a force place, allowing a detailed measurement of the forces and moments in all three directions during the wave impact. As discussed in Section 5.3 the magnitude of the forces and moments in the transversal (F_y, M_x) and vertical direction (F_z, M_z) was negligible compared to those observed in the flow direction (F_x, M_y). For this reason the values of F_y, F_z, M_x and M_z will be hereafter neglected. It was shown in Figure 5.3 that for the same release conditions, similar maximum values are obtained for both the dry bed surge and the wet bed bore. Thus, bores are characterized by a sudden rise in horizontal force F_x and moment M_y, whereas surges are associated with milder loading conditions (Section 5.3).

As presented in Table 6.1, two scenarios were herein compared: buildings with a height of H_B = 0.6 m, where no overflow was observed for any tested wave, and building with a height of H_B = 0.3 m, where some overflow was observed for larger waves ($d_0 \geq 0.63$ m). For the smaller waves ($d_0 = 0.40$ m), for both configurations no submergence was observed, showing good results with the findings presented in Chapter 5. Some minor overflow was noted for $d_0 = 0.63$m (2 pipes, medium wave) and major overflow for $d_0 = 0.82$ m (3 pipes, larges wave).

In this study, force measurements showed that for both dry bed surges and wet bed bores, the values recorded for a submerged structure were lower compared to the non-submerged scenario. Figure 6.4a shows the loading behaviour of two structures ($H_B = 0.6$ and 0.3 m) under the impact of the same incoming dry bed surge ($h_{\max} = 0.181$ m, $U = 3.556$ m/s, test 5.1 and 6.1). One can notice a similar behaviour for both buildings during the first seconds of the impact. Some differences in magnitude can be observed in the hydrodynamic phase of the impact, being the overflowed building less stressed. Analogous results are obtained for other dry bed surges (not shown). A similar case for a wet bed bore with an initial still water depth h_0 = 0.03 m ($h_{\max} = 0.254$ m, $U = 2.810$ m/s, test 5.5 and 6.5) is presented in 6.4b. Also for the wet bed bore, the magnitude of the recorded forces was lower than the scenario without overflow and compared to the dry bed surge in Figure 6.4, the difference between the two scenarios is more important for bores.

Figure 6.4 also shows the behaviour of the force F_z in the vertical direction for both a dry bed surge and a wet bed bore. This force represents the gravitational weight of the water over-flowing the building. One can observe that higher values of F_z were measured for the wet bed bore, confirming the visual observations suggesting a more important overflowing discharge (Figure 6.2h). For a dry bed surge, visual observations in Figure 6.2g showed an aerated jet overpassing the structure, which might be responsible for the lower values of F_z measured by the force plate. Additionally, higher water levels were observed on the downstream side of the building for the scenarios with overflow (Figure 6.2m,n), contributing to a lower hydrostatic component in the total horizontal force. This was also identified by Esteban et al. (2017).

The reduction in $F_{x,\max}$ can clearly be observed in Figure 6.5 where the use of Eq. 5.2 and 5.6 presented in Chapter 5 overestimated the forces predicted for the scenarios with overflow (red/orange symbols). The experimental points are also compared to those obtained for

(a) Dry bed surge
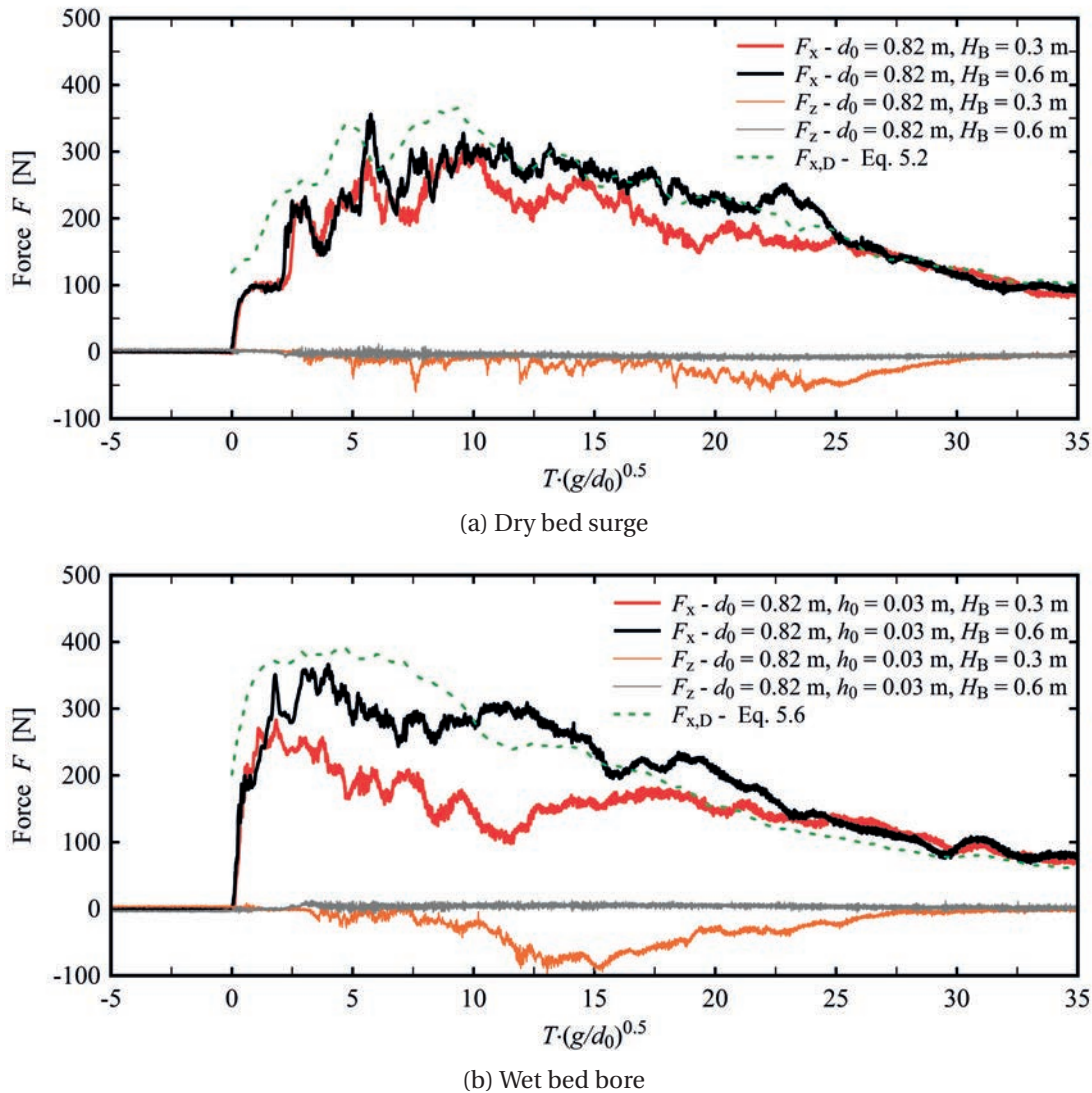
(b) Wet bed bore

Figure 6.4 – Horizontal (F_x) and vertical (F_z) forces measured for: (a) dry bed surge (h_{max} = 0.187 m, U = 3.556 m/s, test 5.1 and 6.1) and (b) wet bed bore (h_{max} = 0.232 m, h_0 = 0.03 m, U = 2.81 m/s, test 5.5 and 6.5) impacting against an impervious building with (H_B = 0.3 m) and without (H_B = 0.6 m) overflow.

the building without overflow, previously presented in Chapter 5. Results also showed that for minor overflow (d_0 = 0.63m) the difference was negligible, however this became more important for higher impoundment depths (d_0 = 0.82 m).

Thus, a combination of the reduced upstream run-up height (Figure 6.3) and an increased downstream water level are responsible for a lower horizontal force. In the computation, this translated into a reduced resistance coefficient C_R, as shown in Figure 6.6. Experimental data showed that, for the scenarios with overflow, a value $C_{R,S}$ = 1.5 was more appropriate, rather than the value C_R = 2.0 for buildings without overflow.
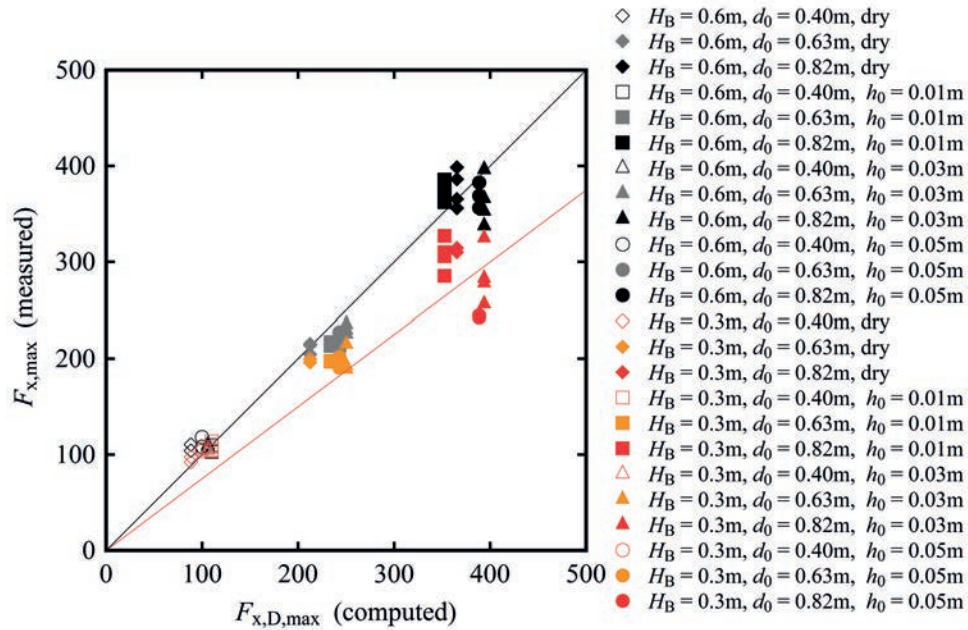
Figure 6.5 – Comparison of computed forces $F_{\mathrm{x,D,max}}$ using Eq. 5.2 and 5.6 with measured maximum horizontal forces $F_{\mathrm{x,max}}$ for both configurations with (H_{B}, red/orange symbols) and without overflow (H_{B}, black/gray symbols).
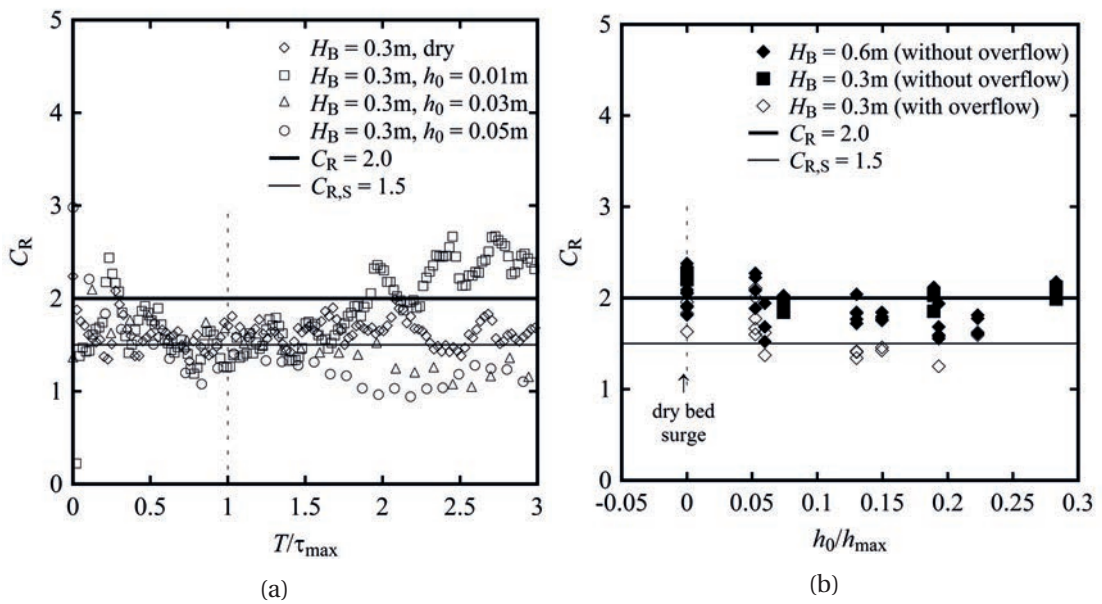
Figure 6.6 – Resistance coefficient C_{R} for buildings with ($H_{\mathrm{B}} = 0.3$m) and without ($H_{\mathrm{B}} = 0.6$m) overflow for both dry bed surges and wet bed bores: (a) time development before and after the occurrence of the maximum force ($T/\tau_{\max} = 1$) for waves with $d_0 = 0.82$m; (b) values of C_{R} at $T/\tau_{\max} = 1$, presented as a function of $h_0/h_{\max}$.

123

6.4 Force analysis

Similarly to Section 5.4, a deeper analysis of the horizontal forces is carried out in this section. The main parameters discussed are presented hereafter and visually described in Figure 5.13:

- Time from the wave arrival until the occurrence of the force peak, τ_{max} (Section 6.4.1)
- Wave height h_M at which the maximum horizontal force is measured (Section 6.4.2)
- Impulse I transferred from the wave to the building (Section 6.4.3)

6.4.1 Time to peak

The "*time to peak*" τ_{max} represents the time interval between the impact ($T = 0$) and the maximum measured horizontal force $F_{x,max}$ (Figure 5.13). The values of τ_{max} obtained for all tests are presented in dimensionless form in Figure 6.7 as a function of h_0/h_{max}, where $h_0/h_{max} = 0$ represents the dry bed surges and $h_0/h_{max} > 0$ the wet bed bores. In agreement with the findings presented in Section 5.4.1, these results showed larger values of τ_{max} up to $\tau_{max}(g/d_0)^{0.5} = 40$, for dry bed surges ($h_0/h_{max} = 0$), whereas for bores ($h_0/h_{max} > 0$) almost all maximum forces occurred for $\tau_{max} < 5 \cdot (d_0/g)^{0.5}$. The results presented in Figure 6.7 also showed that the force maximum took place a little earlier for buildings with overflow, compared to the previous scenario (Chapter 5) in Figure 5.14.
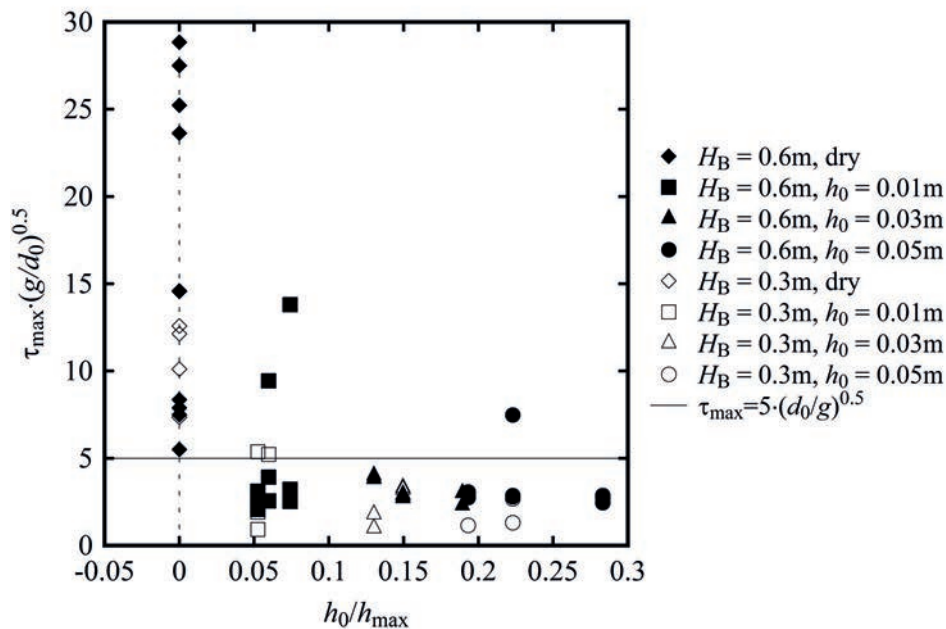
Figure 6.7 – Values of the time to peak (τ_{max}) for both dry bed surges ($h_0/h_{max} = 0$) and wet bed bores for scenarios with ($H_B = 0.3$m) and without ($H_B = 0.6$m) overflow.

6.4.2 Wave height at maximum force

An important parameter in the design of resiliant buildings is the wave height h at which the maximum force $F_{x,max}$ occurs. This relative height h_M is defined in Eq. 5.9 as the ratio between the wave height at which the maximum force occurs $h(T = \tau_{max})$ and the maximum wave height h_{max}. The results obtained from the experimental tests are presented in Figure 6.8 for both scenarios with and without overflow, where no major differences in behaviour are noted between the two cases.
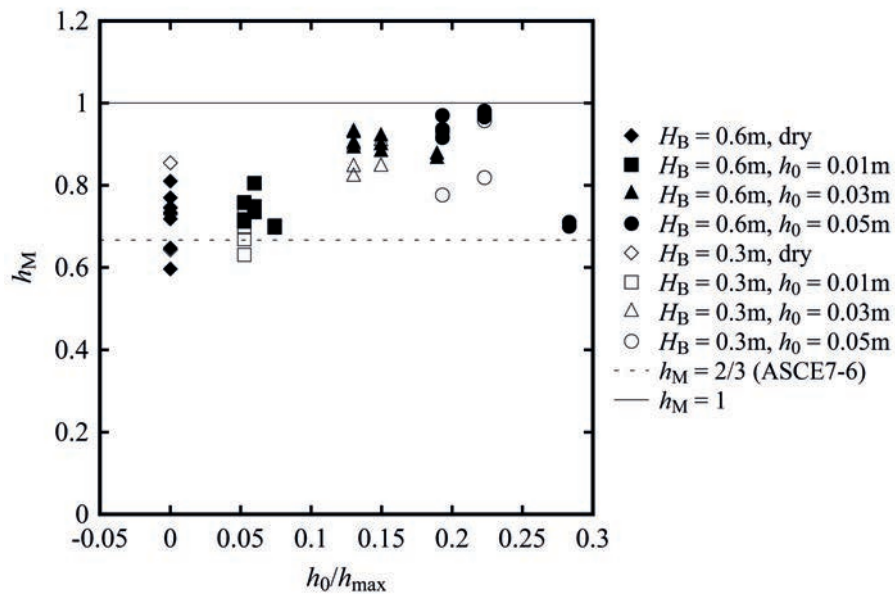
Figure 6.8 – Relative wave height h_M at which the maximum horizontal force $F_{x,max}$ occurs, and comparison with design standards presented in ASCE7 - Chapter 6 ($h_M = 2/3$).

Similairly to Figure 5.15 these experimental points are also compared to the newest design guidelines of the ASCE 7 Chapter 6, according to which the maximum hydrodynamic load should occur at 2/3 of the maximum inundation depth, *i.e.* when $h = 2/3 h_{max}$. Results showed, on average, relatively good agreement for dry bed surges ($h_0/h_{max} = 0$), however for increasing values of h_0/h_{max}, the maximum force occurs for higher water levels. For this cases, similarly to the findings presented in Chapter 5, the choice of $h_M = 2/3$ becomes less conservative. Being the maximum force proportional to the maximum momentum in Eq. 5.7, these results are consistent with the findings showed in Chapter 4 for the maximum momentum flux per unit width M.

6.4.3 Impulse

As previously discussed in Section 5.4.3, in physics the product of a force F and time t is commonly known as Impulse I. In our specific case, the total impulse I_{tot} can be identified as the integral of the force F_x over time, until $T = 100 \cdot (d_0/g)^{0.5}$ is reached (Eq. 5.10). This quantity

also represents the surface below the curve, as shown in Figure 5.13 and it corresponds to the exchange in momentum between the incoming wave and the free standing building. The values of the total impulse I_{tot} were computed for all experimental tests and the results are presented in Figure 6.9. These findings show that for the building subject to overflow ($H_B = 0.3$ m, $d_0 > 0.63$ m), lesser impulse will be transferred to the structure. This is a consequence of the smaller force magnitude discussed in Section 6.3 and observed in Figure 6.4b. From Figure 6.9, one can also notice that I_{tot} appears to stabilise around a constant value and no difference is observed between the two largest impoundment depths $d_0 = 0.63$m and 0.82m. To better define the amount of impulse that is transferred to the structure before the peak occurs, a new parameter I_{peak} is defined as the integral between $0 < T < \tau_{max}$. This parameters represents the surface below the curve until $F_{x,max}$ is reached (Eq. 5.11). The computed values are also presented in Figure 6.9 for both scenarios with and without overflow ($H_B = 0.3$ and 0.6m, respectively). Results showed some similar results with values below $I_{peak} = 500$ Ns for both configurations.

A parameter I^* can therefore be defined as the ratio between the peak impulse I_{peak} and the total impulse I_{tot}. This corresponds to the percentage of total impulse that is registered before the maximum force occurs. I^* was defined in Eq. 5.12 and sketched in Figure 5.13. The values obtained from the experimental tests are presented in Figure 6.9b, where the difference in behaviour between surges and bores is once again shown. For wet bed bores only 10 % of the impulse is transferred before the peak, whereas for dry bed surges, this percentage can reach up to 30%. These results are in agreement with what was previously observed in Chapter 5 and no major differences are observed with the impervious buildings without overflow.

(a)   (b)
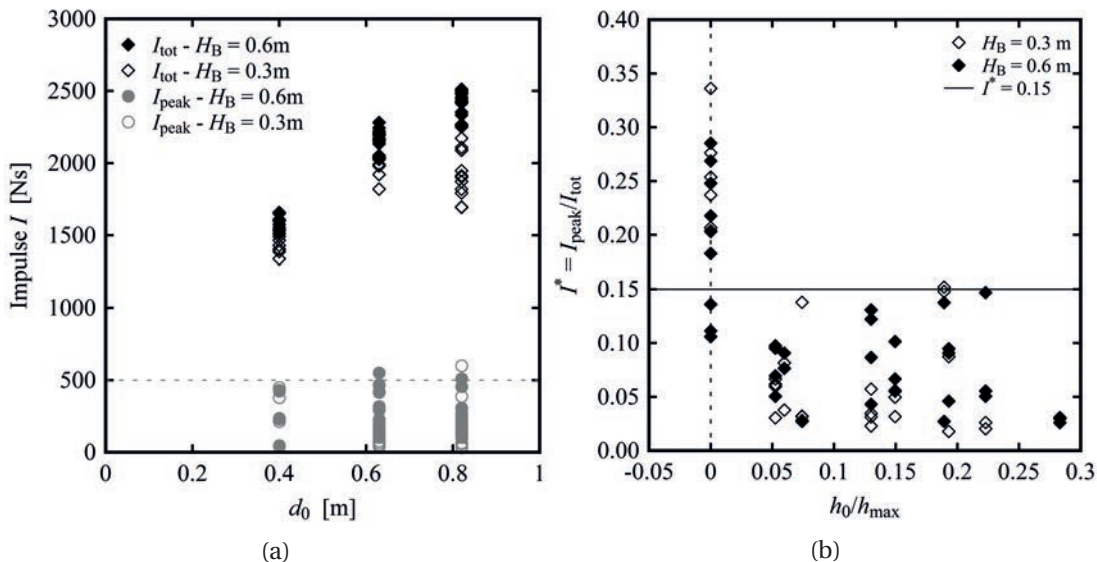
Figure 6.9 – (a) Total (I_{tot}) and peak impulse (I_{peak}); (b) $I^* = I_{peak}/I_{tot}$ for both dry bed surges ($h_0/h_{max} = 0$) and wet bed bores ($h_0/h_{max} > 0$), with ($H_B = 0.3$ m) and without overflow ($H_B = 0.6$ m).

6.5 Moment and cantilever arm

Any force applied outside of its reference point produces a moment that is directly proportional to the application distance, called cantilever arm L_z. These moments are important in the design of structures, because they can be responsible for its overturn, if the foundation is not designed accordingly. In this study only moments in the transversal direction (M_y) were considered. Since their magnitude was too low to be relevant, M_x and M_z were neglected, as shown in Figure 5.3. Despite some scattering, results showed that even for buildings with overflow, the maximum horizontal force F_x and the maximum moment M_y occurred at the same time, as shown in Figure 6.10.
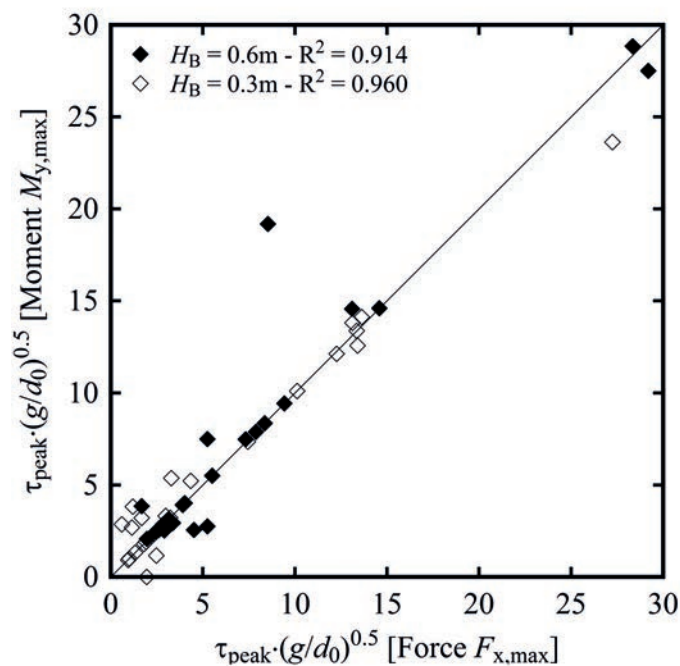
Figure 6.10 – Temporal occurrence (τ_{max}) of maximum horizontal force $F_{x,max}$ and maximum moment $M_{y,max}$, presented in normalised form.

Similarly to what was observed in Section 5.5, buildings with overflow constantly showed moments that were lower than the configuration without overflow. Once the maximum horizontal force is known (Section 6.3), the moment can be obtained through the cantilever arm (L_z). Experimentally, the behaviour of the cantilever arm (L_z) over time in the z direction can be calculated as the ratio between moment and force, as presented in Eq. 5.14. If both maximum force and moment occur at the same time, than the cantilever arm at $T = \tau_{max}$ can be obtained through Eq. 5.15. The values obtained from the experimental points are presented in Figure 6.11 as a function of h_0/h_{max} for dry bed surges and wet bed bores. These are also compared with the values previously obtained for the impervious structure without overflow ($H_B = 0.6$m). All values are normalised using the wave height h_{max} measured without the building.
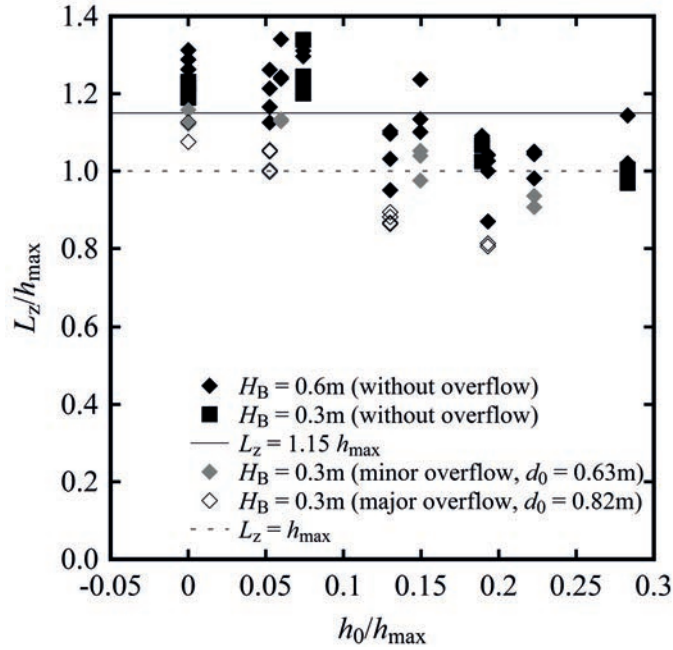
Figure 6.11 – Values of the lever arm L_z for both dry bed surges ($h_0/h_{max} = 0$) and wet bed bores ($h_0/h_{max} > 0$), normalised with the maximum wave height without the building h_{max}.

The results in Figure 6.11 show that for all tested scenarios, the cantilever arm had a fairly constant behaviour ranging around an average value of 1.00 h_{max}. It could therefore be assumed that, on average, the total horizontal force defined in Section 6.3, was applied at a height that corresponded to the maximum wave height h_{max} measured without the presence of the building. This allowed to obtain an expression to compute the maximum moment $M_{y,D,max}$ as a function of the hydrodynamic properties of the wave without the building:

$$M_{y,D,max} = F_{x,D,max} \cdot \mathbf{1.00} h_{max} = \frac{1}{2} \rho C_{R,S} B M_{max}^* \cdot h_{max} \tag{6.1}$$

where $F_{x,D,max}$ is the maximum horizontal force computed using Eq. 5.7 with a resistance coefficient $C_{R,S} = 1.5$ defined in Section 6.3 for the scenarios with overflow. The values predicted using Eq. 6.1 are compared to the experimental values in Figure 6.12.

6.6 Discussion

The previous sections showed that when the building is overflowed, then a reduction in force, impulse and moment occurs. From a structural points of view, a building that is overflowed, is therefore subject to milder load conditions. The comparison with the results obtained in the previous section showed that a modification of the resistance coefficient C_R and the cantilever arm L_z was necessary to obtain a better approximation of the forces and moments starting from the basic hydrodynamic properties of the wave measured without the building.
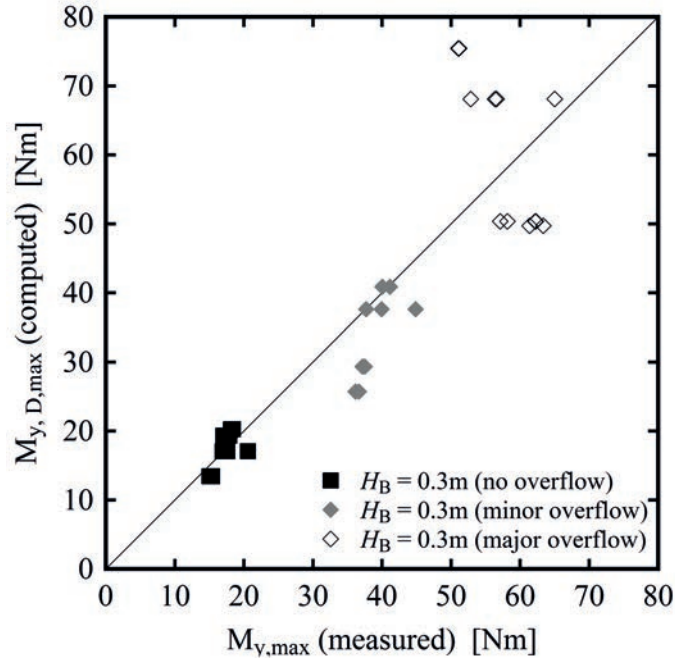
Figure 6.12 – Comparison of maximum measured values $M_{y,max}$ with $M_{y,D,max}$ computed through Eq. 6.1 ($R^2 = 0.764$).

Hereafter the reduction in total impulse ΔI_{tot} due to the overflow of the structure is addressed. For this a submergence coefficient S is defined in Eq. 6.2 as the ratio between the equivalent overflow depth H_{eq} and the building height H_B. The equivalent overflow depth H_{eq} was derived through Eq. 3.8 for the maximum vertical force F_z acting on the force plate. This option was chosen because the US measurement were affected by air entrainment and run-up splashes. A value of $H_{eq} = 0$ implies that no water passed over the building, whereas for $H_{eq} > 0$ the building was overflowed. Similarity, if $S > 0$, then some overflow is observed, otherwise if $S = 0$ no overflow is registered.

$$S = \frac{H_{eq}}{H_B} = \frac{F_z}{B^2 g \rho \cdot H_B} \tag{6.2}$$

Results obtained are presented in Figure 6.13a, where an increasing behaviour of $\Delta I_{tot} / I_{tot}$ can clearly be observed for all configurations. This proved that the reduction of impulse was a function of the submerge coefficient S ad therefore of the amount of water that is overflowed. Similarity, also the cantilever arm L_z is shown to be proportional to the submergence coefficient in Figure 6.13b. Higher values of S corresponded to lower horizontal forces, cantilever arms and therefore reduced moments. Nevertheless, the submergence of a structure is, generally, not known by practical engineers and it cannot be deduced from the basic hydrodynamic properties of the wave. For this reason, loading conditions computed using a resistance coefficient $C_{R,S} = 1.5$ and cantilever arm $L_z = h_{max}$ were shown to represent a good first approach.
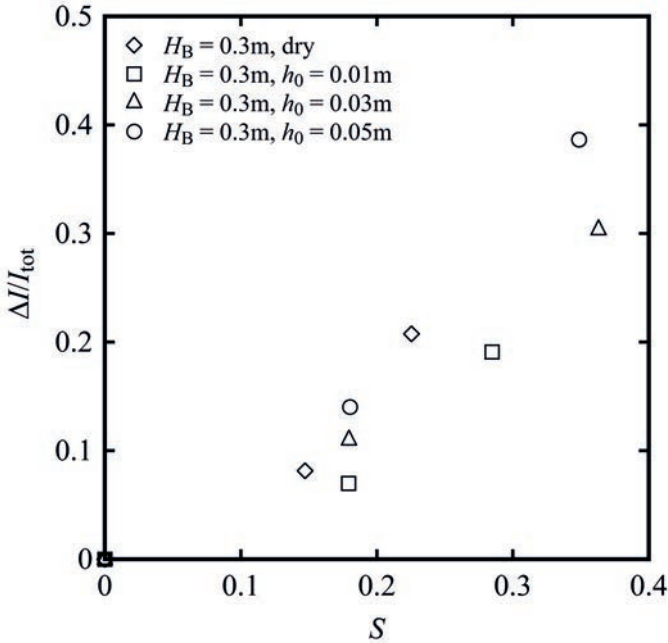
(a) Total impulse
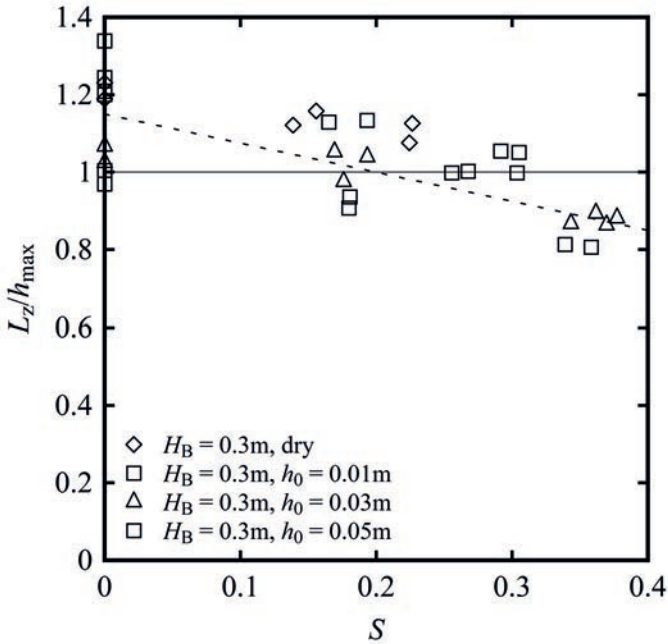
(b) Cantilever arm

Figure 6.13 – Dependence of: (a) relative variation of total impulse $\Delta I / I_{\text{tot}}$ and (b) normalised cantilever arm $L_{\text{z}} / h_{\text{max}}$ on the degree of overflow of the building, here described through the submergence coefficient S, defined in Eq. 6.2.

6.7 Summary

Some critical buildings in coastal areas are designed to become vertical shelters, whereas for others overflowing is accepted. This experimental work mainly focused on buildings potentially overflowed in case of extraordinary events. This issue was rarely addressed in the past. The results obtained for these lower buildings were then compared with the impervious free-standing buildings discussed in Chapter 5. The following conclusions can be drawn:

1. In case of overflow, visual observations showed lower water depths with less aeration on the upstream side of the building. As a result of the flow over the structure, higher water levels were observed on the downstream side of the building, compared to the configuration without overflow.

2. In terms of hydrodynamic loading, structures with overflow constantly presented lower horizontal forces and impulse values compared to the buildings that were not overflowed. This is probably a consequence of the lower difference in water depth between the upstream and downstream sides, resulting into a reduced hydrostatic component. Results also showed that, mostly for wet bed bores, the maximum force occurred slightly earlier for the structures with overflow. This modified dynamic of the buildings with overflow also resulted into reduced cantilever arms, and therefore lower tilting moments.

3. The results presented and discussed in Section 5 can conservatively be applied to structures potentially overflowed, however these overestimate the actual values. If a more precise estimation is desired, then a modified approach with a reduced submerged coefficient $C_{R,S} = 1.5$ can be used. In addition, the resulting force should be applied at a height equal to the maximum wave height h_{max} measured without the building.

4. Nevertheless, this reduction in terms of horizontal forces and moments remained limited for buildings subject to minor overflow ($d_0 = 0.63$m), whereas for major overflow ($d_0 = 0.82$m), these differences became more important. This showed a dependence of these values on the water depth over the structure, however this parameter is difficult to derive from the basic hydrodynamic properties of the wave. The methodology previously described therefore represents a good first approach in the design process of coastal buildings subject to potential overflow.

7 Impact on buildings with openings

7.1 Overview

Previous studies and field surveys showed that a specific design can decrease the load on free-standing buildings along the coast, providing safer vertical shelters. This experimental study investigates the effect of openings in buildings (windows, doors and foyers) on horizontal forces and tilting moments induced by both dry bed surges and wet bed bores. Four configurations were systematically tested with openings ranging from 0 (impervious) to 84% (highly permeable). Due to the presence of openings, the flow through the buildings reduced the upstream water depths. Openings were shown to produce a linear reduction of the maximum horizontal force, if compared to the corresponding impervious building. The configuration with an impervious back showed similar results to those measured for the impervious buildings. The occurrence of the maximum tilting moment was shown to coincide with the maximum horizontal force and an estimation of the cantilever arm was therefore possible. The latter was constant for all configurations, independently from the geometry of the openings. Finally, two equations to predict the maximum horizontal force and the tilting moment were proposed, taking into account the effect of openings within the resistance coefficient. These had a good agreement with experimental points and previous studies.

The main objectives of this chapter are the following:

1. To systematically investigate the effect of building openings, equally distributed on all four sides.
2. To detect potential influences of the impervious lateral and/or back walls.
3. To qualitatively investigate the effect of additional, adjacent side buildings.
4. To provide an estimation of horizontal forces, its application point and the resulting tilting moment.
5. To present preliminary results on the vertical forces acting on the building during inundation.

For this, 280 experimental tests were carried out for 12 standard waves (Chapter 4). The main hydrodynamic properties of the waves (without buildings) are detailed in Appendix D and the key features summarized in Table 7.1. These waves were used to investigate 6 building porosities and 4 configurations (Figure 3.16 and 3.18), as detailed in Table 7.2. The complete list of performed tests is presented in Appendix E.

Wave name	d_0 [m]	h_0 [m]	h_{max} [m]	h_0/h_{max} [-]	U [m/s]	$(hV_m^2)_{max}$ [m^3/s^2]	Fr $= U/(gh_{max})^{0.5}$ [-]	Rep.
WD1	0.40	0.00	0.132	0	2.347	0.294	2.06	3
WD2	0.63	0.00	0.162	0	3.114	0.711	2.47	3
WD3	0.82	0.00	0.181	0	3.556	1.218	2.67	6
WW1 - 1P	0.40	0.01	0.139	0.070	2.104	0.375	1.80	3
WW1 - 2P	0.63	0.01	0.172	0.059	2.702	0.681	2.08	3
WW1 - 3P	0.82	0.01	0.193	0.046	3.074	1.130	2.24	4
WW3 - 1P	0.40	0.03	0.162	0.184	1.971	0.332	1.56	3
WW3 - 2P	0.63	0.03	0.206	0.141	2.518	0.731	1.77	3
WW3 - 3P	0.82	0.03	0.232	0.118	2.810	1.227	1.86	5
WW5 - 1P	0.40	0.05	0.178	0.270	1.933	0.333	1.46	3
WW5 - 2P	0.63	0.05	0.224	0.216	2.437	0.682	1.64	3
WW5 - 3P	0.82	0.05	0.260	0.186	2.755	1.073	1.73	7

Table 7.1 – Hydrodynamic properties of the tested waves (without the structure).

Configuration	Total porosity [%]	Waves	Rep.
All porous sides (0)	17, 34, 60, 31.34, 42.24	WD1, WD2, WD3 WW1-1P, WW1-2P, WW1-3P WW3-1P, WW3-2P, WW3-3P WW5-1P, WW5-2P, WW5-3P	64
Impervious lateral walls (F)	17, 34, 60, 31.34, 42.24, 84	WD1, WD2, WD3 WW1-1P, WW1-2P, WW1-3P WW3-1P, WW3-2P, WW3-3P WW5-1P, WW5-2P, WW5-3P	114
Impervious back (B)	17, 34, 60, 42.24	WD1, WD2, WD3 WW1-1P, WW1-2P, WW1-3P WW3-1P, WW3-2P, WW3-3P	48
With building sides (S)	17, 34, 60, 31.34, 42.24	WD1, WD2, WD3 WW1-1P, WW1-2P, WW1-3P WW3-1P, WW3-2P, WW3-3P	54

Table 7.2 – Experimental program for the investigation of buildings with openings.

7.2 Visual observations

The impact of surges and bores on impervious free-standing buildings was visualized in Section 5.2. The effects of building overflow were addressed in Section 6.2. For the impervious scenario, after an initial impact characterised by high splashes and run-up heights of some 4 times the wave height measured without the structure, a quasi-steady hydrodynamic phase was observed. During this phase, the main body of the incoming surge/bore flowed around the structure and an aerated rolled on the upstream side of the building was observed. Finally, the level decreased as the wave passed by.

For structures with openings, the water was able to partially flow through the building, resulting into an interaction between the incoming surge/bore and the building. An example of the impact of a dry bed surge for all tested configurations is presented in Figure 7.1 at different times. Initially the water flowing through the building only affected the ground floor, however with the increase of the upstream water depth, also the first and second floors were eventually inundated (Figure 3.17). For all configurations, a fluctuating behaviour of the water surface was observed on the upstream side of the building, attributed to the presence of an aerated recirculating roller. The latter was less intense for the buildings with openings compared to corresponding impervious case. As a consequence of the openings, the discharge seeping through the reduced the upstream water depths, ensuring safer vertical shelters.

For the configuration with openings on all four directions (Configuration 0, Figure 3.18a), a portion of the water entering from the front went out through the lateral openings, resulting into an interaction with the flow around the structure (Figure 7.1b). On the contrary, for the configuration with impervious lateral walls (Configuration F, Figure 3.18b), this was not observed, resulting into a more linear flow, as shown in Figure 7.1c. For the configuration B (Figure 3.18c), when the wave front hit the impervious back, two lateral jets ejecting the water outside the building were clearly observed (Figure 7.1d). After this initial impact, the hydrodynamic phase was similar to that observed for the impervious structure. Lastly, for the configuration S (3.18d), with the additional lateral buildings, higher upstream water levels were constantly observed (Figure 7.1e).

Measurements carried out with US probes at different locations allowed to measure the run-up heights during the impact; these are presented in Figure 7.2 for US5 ($x = 13.35$ m) and US7 ($x = 13.85$ m). At US7 (Figure 7.2a), one can notice similar run-up heights H_{max} during the impact for all tests, nevertheless on the upstream side, lower water levels were recorded for larger porosity values. For all scenarios a fluctuating behaviour was observed, attributed to the presence of a recirculating roller. Figure 7.2b shows the water levels on the upstream side of the building, where the measurements are not affected by the recirculating roller. These values showed the effectiveness of the openings in reducing the water levels, thus generating safer vertical shelters. Some similar results in terms of visual observations of experimental tests and comparison with numerical simulations were carried out by Hartana and Murakami (2015) for structures with openings and internal slabs.
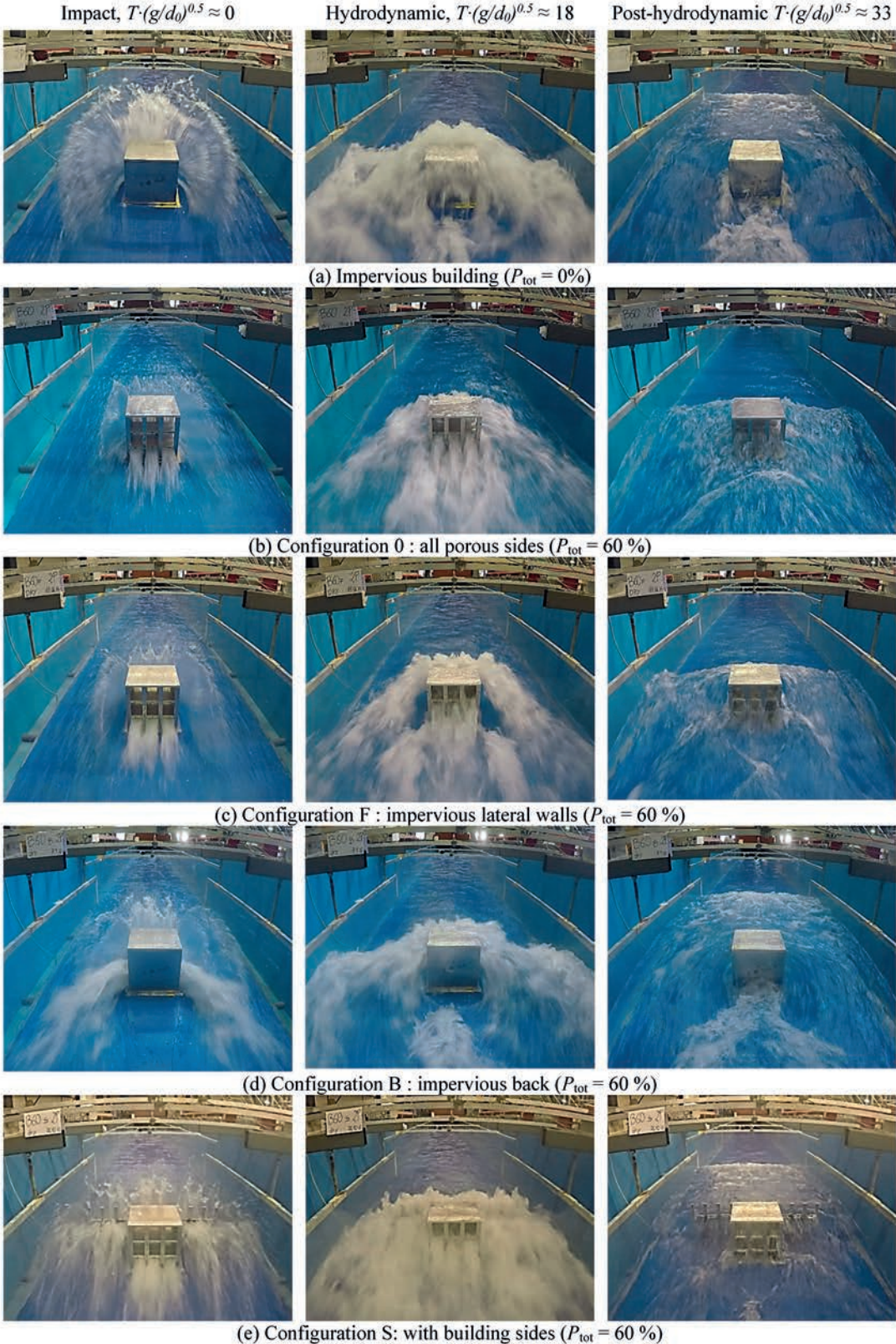
Figure 7.1 – Visual observation of wave impact for different configurations at various dimensionless times (dry bed surge WD2, $d_0 = 0.63$m, $h_{max} = 0.162$ m, $U = 3.11$ m/s).

(a) US7 (x = 13.85 m)
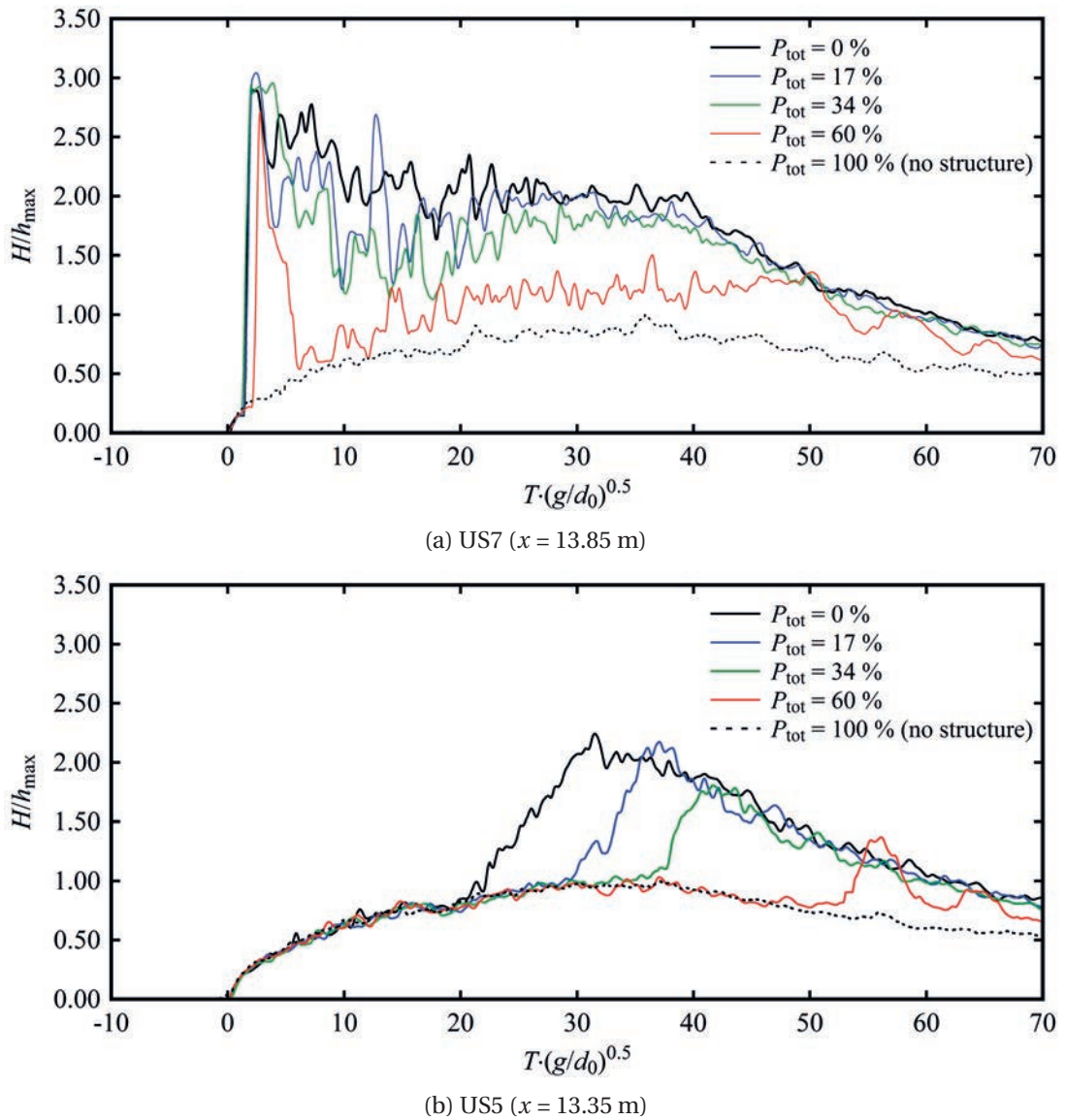
(b) US5 (x = 13.35 m)

Figure 7.2 – Ultrasonic distance sensors (US) measurements of run-up heights H for various porosity values (dry bed surge WD2, d_0 = 0.63m, h_{max} = 0.162 m, U = 3.11 m/s) at two measurement locations: (a) US7 (x = 13.85 m) and (b) US5 (x = 13.35 m).

7.3 Effect of building openings

The effect of openings was shown to be beneficial for the building, reducing the forces exerted by the incoming surge/bore. Four configurations are herein considered, as presented in Figure 3.18 and Figure 3.19. Results are presented and discussed hereafter.

- All porous sides (Configuration 0) - Section 7.3.1
- Impervious lateral walls (Configuration F) - Section 7.3.2
- Impervious back (Configuration B) - Section 7.3.3
- With additional building sides (Configuration S) - Section 7.3.5

7.3.1 All porous sides (Configuration 0)

Initially, the openings were equally distributed on all four building sides, with total porosity values ranging from $P_{tot} = 0$ to 60 %, (Figure 3.16 and Figure 3.18a). The time-histories of the horizontal forces F_x induced by the same dry bed surge and wet bed bore on four buildings with different opening values are plotted in Figure 7.3. One can notice that the overall behaviour was similar for all scenarios: after an initial increase of the force, the load stabilized around a constant value before decreasing once the bore/surge has passed. The observed behaviour is consistent with results presented in Section 5.3 and previous studies (Arnason et al., 2009; Nouri et al., 2010). However, major differences were observed in terms of the magnitude of the measured forces, with large porosities leading to lower values. This reduction is attributed to the presence of openings on the structure, partially reducing the inundation depth in front of the building, as previously observed by Hartana and Murakami (2015). Moreover, for dry bed surges, porous buildings had a less steep force increase resulting into a more gradual and milder loading condition. For wet bed bores, this difference was less pronounced.

(a) Dry bed surge (b) Wet bed bore
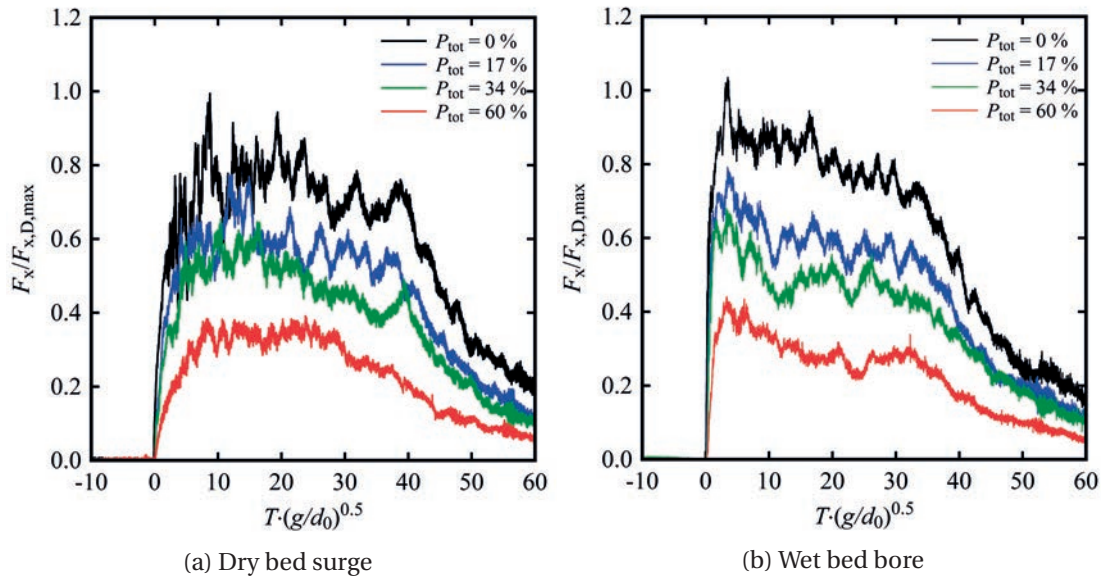
Figure 7.3 – Time-history of the horizontal force F_x for: (a) dry bed surge and (b) wet bed bore with $h_0 = 0.03$ m for the same initial release conditions ($d_0 = 0.63$ m).

For all tests, the maximum measured force $F_{x,max}$ was plotted as a function of the porosity $P_{h,max}$ defined in the interval $0 < z < h_{max}$ and normalized using the maximum horizontal force computed for the reference impervious building $(F_{x,D,max})_{P_{tot}=0}$. Results are presented in Figure 7.4 for both surges and bores with different approach conditions in terms of water height h and front celerity U. One can notice that an overall linear force decrease appears for increasing porosities. It is hypothesized that the horizontal force F_x is zero in the absence of the structure ($P_{tot} = 100$ %).

$$F_{x,max} = (F_{x,max})_{P=0} \cdot (1 - P_{h,max}) \tag{7.1}$$

This suggests that the reduction of the horizontal load is proportional to the surface that is exposed to the incoming wave. The preliminary conclusions drawn by Lukkunaprasit et al. (2009a), who suggested to use a linear approximation in lack of experimental tests, are thus supported. Nevertheless, further comparison with previous studies is carried out in Section 7.3.4. Good linear agreement was also found for the impulse *i.e.* the integration of the force over time (Section 7.4.3), as shown in Figure 7.13.
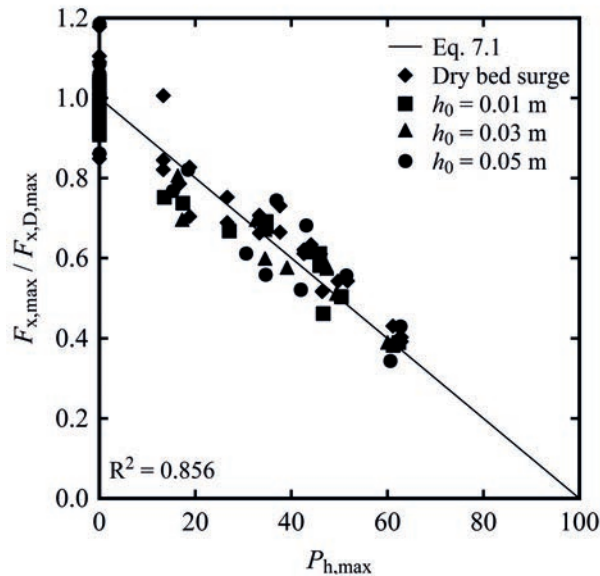
Figure 7.4 – Maximum horizontal force $F_{x,max}$ as a function of surface porosity at h_{max} ($P_{h,max}$) for both dry bed surges and wet bed bores with various initial release conditions.

7.3.2 Impervious lateral walls (Configuration F)

In this section, the configuration (F) with impervious lateral walls (Figure 3.18b) is discussed. Similarly to the previous case, six porosity values were tested for surges and bores with different wave properties. Results showed a similar behaviour to that shown in Figure 7.3, however slightly lower values were observed for the configuration with impervious lateral walls (F), as shown in Figure 7.5. This phenomenon is probably attributed to straight flow through the structure and the lack of interaction with the main flow across the lateral walls. Nevertheless this reduction remains small during the impact and its negligence represents a conservative approach during the design phase. In the quasi-steady hydrodynamic phase ($10 < T \cdot (g/d_0)^{0.5} < 30$) the difference in behaviour between the building with porous (0) and impervious (F) sides becomes more important, in agreement with the steady-state tests presented in Appendix C.5.2. For these, reductions up to 30% of total value of the force were found (Figure C.5).

The maximum horizontal force $F_{x,max}$ measured for all tests for Configuration F is compared in Figure 7.6 with the corresponding values obtained for the configuration 0 with all porous sides. Results show a good agreement between the two configurations, suggesting that the influence of the lateral walls had a negligible effect in the estimation of the maximum horizon-
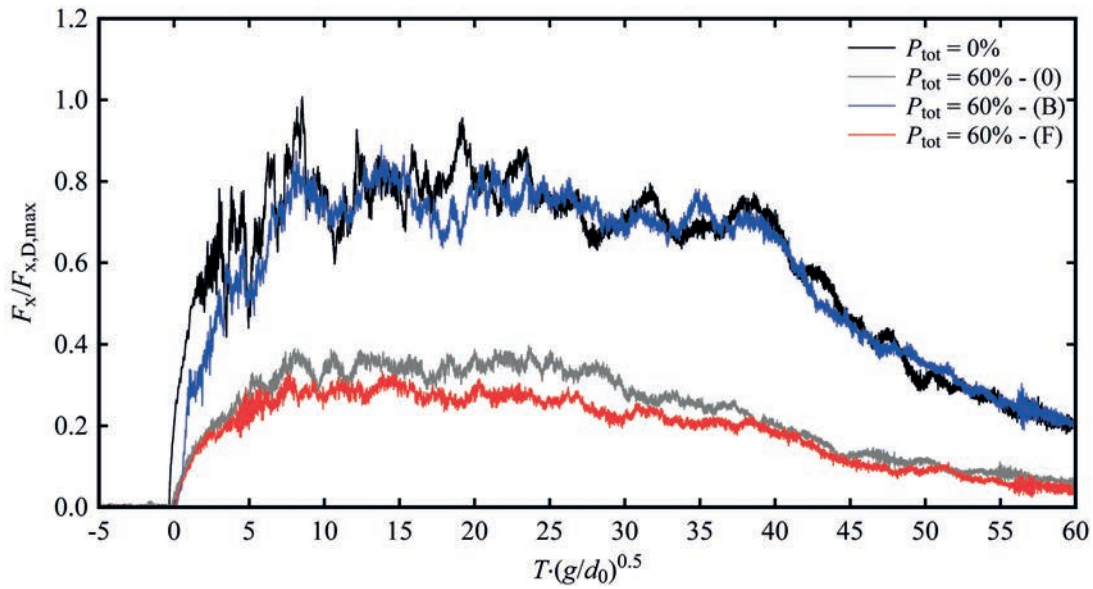
Figure 7.5 – Comparison of the measured forces ($F_x/F_{x,D,max}$) for the impervious structure ($P_{tot} = 0\%$) and the building with $P_{tot} = 60\%$ for the configuration 0 (with all porous sides, Figure 3.18a), configuration F (with impervious lateral walls, Figure 3.18b) and configuration B (with impervious back, Figure 3.18c, discussed in Section 7.3.3).

tal force $F_{x,D,max}$. This implies that the linear relationship in Eq. 7.1 can be extended to the configuration F with impervious lateral walls, as shown in Figure 7.7.
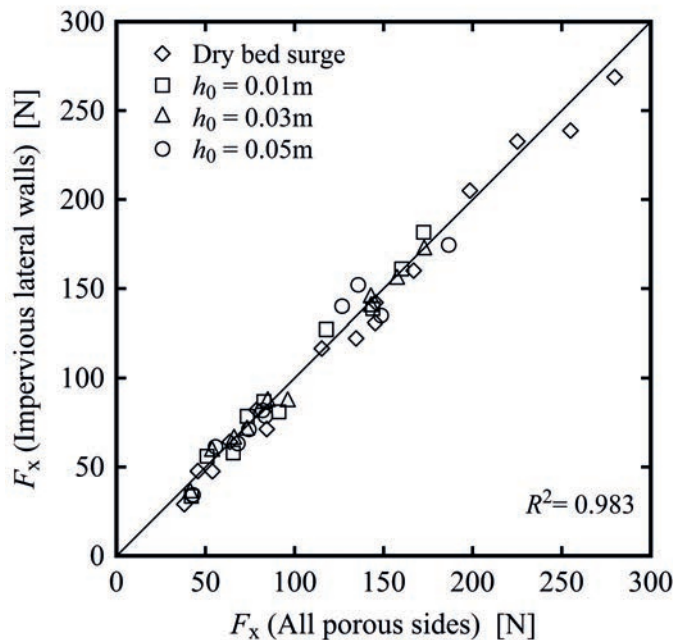
Figure 7.6 – Comparison of forces (F_x) for the configurations with all porous sides (Figure 3.18a) and with impervious lateral walls (Figure 3.18b).

7.3.3 Impervious back (Configuration B)

A configuration with openings on the front and lateral walls, but impervious back was tested (Figure 3.18c). As shown in Figure 7.5 the temporal development of the horizontal force for the configuration B without openings on the back side, was similar to that observed for the fully impervious building ($P_{tot} = 0\%$). This indicated that simply closing one of the sides orientated perpendicularly to the flow, has the same effect of bringing the whole building back to the impervious configuration. The experimental results in terms of the maximum measured horizontal force $F_{x,max}$ plotted in Figure 7.7 confirmed this, showing forces equal to those predicted for the impervious buildings for all porosities values.

7.3.4 Comparison with previous studies and design codes

Previous studies were carried out by Triatmadja and Nurhasanah (2012), who found a non-linear behaviour for structures with symmetrical and concentric openings of variable sizes without internal partitions. Their approach is presented in Eq. 2.46 and compared to the experimental results in Figure 7.7. These values obtained with Eq. 2.46 slightly overestimated the measured force, thus providing a conservative design. Nevertheless, its applicability remains limited due to the particular choice of opening geometries to represent residential buildings. To account for openings and failure/breakage of walls/windows, Fukuyama et al. (2011) introduced a de-amplifying coefficient, whose value should always be greater than 0.7 because of the existence of the interior walls. ASCE 7 (2016) – Chapter 6, embraces this approach, suggesting to use a minimum closure ratio of 70% of the pressure-exposed surface area of the exterior enclosure (Figure 7.7).

7.3.5 Discussion: force estimation

In the previous sections, the force was shown to be linearly proportional to the porosity of the building due to presence of openings. The ratio presented in Figure 7.7 between the measured force $F_{x,max}$ and the value $F_{x,D,max}$ (computed using Eq. 5.7 for impervious buildings $p_{tot} = 0\%$) for the same incoming wave, can be seen as the ratio between the resistance coefficients, with and without openings. For this reason we assume a linear reduction of the resistance coefficient C_R compared to the corresponding value computed for the impervious structure $C_{R,0}$. Therefore, for the computation of the resulting hydrodynamic force, the following model taking into account the presence of openings is proposed:

$$C_R = C_{R,0} \cdot \Pi \tag{7.2}$$

where $C_{R,0} = 2.0$ is the resistance coefficient defined for impervious structures (Section 5.3.5) and Π is the porosity coefficient, obtained as a combination of openings on both the front and
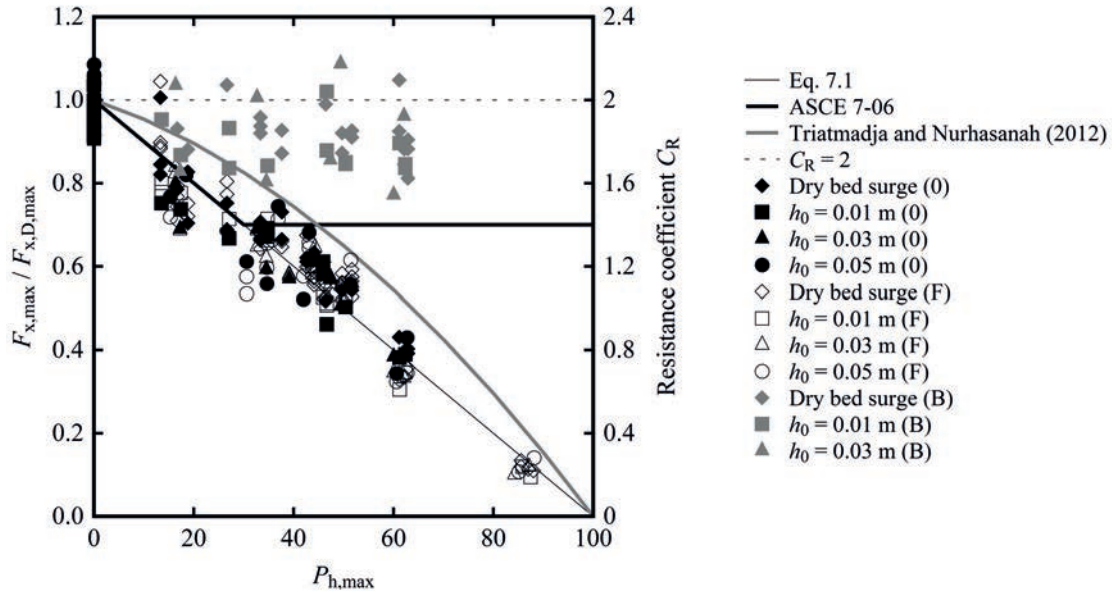
Figure 7.7 – Comparison of the configuration with all porous sides (configuration 0), with impervious lateral sides (configuration F) and with the impervious back (configuration B) in terms of maximum horizontal force. The experimental points are also compared with Eq. 7.1 and previous studies in literature.

back sides. Openings on side walls were neglected, as shown in Section 7.3.2.

$$\Pi = 1 - \min \left[(P_{h,max})_{front} ; (P_{h,max})_{back} \right] \tag{7.3}$$

where $(P_{h,max})_{front}$ is the porosity values in the front side of the building and $(P_{h,max})_{back}$ is the porosity values in the back side of the building. For impervious structures this model leads to $\Pi = 1$ and $C_R = 2.0$, which is consistent with literature. The definition of a porosity coefficient Π is related to the concept of *"projected surface"* previously discussed by Fukuyama et al. (2011). Note that, in the present study, internal vertical walls and partition were not considered.

The predicted force $F_{x,D}$ can therefore be obtained as:

$$F_{x,D} = \frac{1}{2} \rho \left(C_{R,0} \cdot \Pi \right) \cdot B \cdot M^* \tag{7.4}$$

and the predicted maximum horizontal force $F_{x,D,max}$ becomes:

$$F_{x,D,max} = \frac{1}{2} \rho \left(C_{R,0} \cdot \Pi \right) \cdot B \cdot M^*_{max} \tag{7.5}$$

The excellent agreement Eq. 7.5 with the experimental data is presented in Figure 7.8, with global coefficient of determination $R^2 = 0.968$ for all configurations.

142
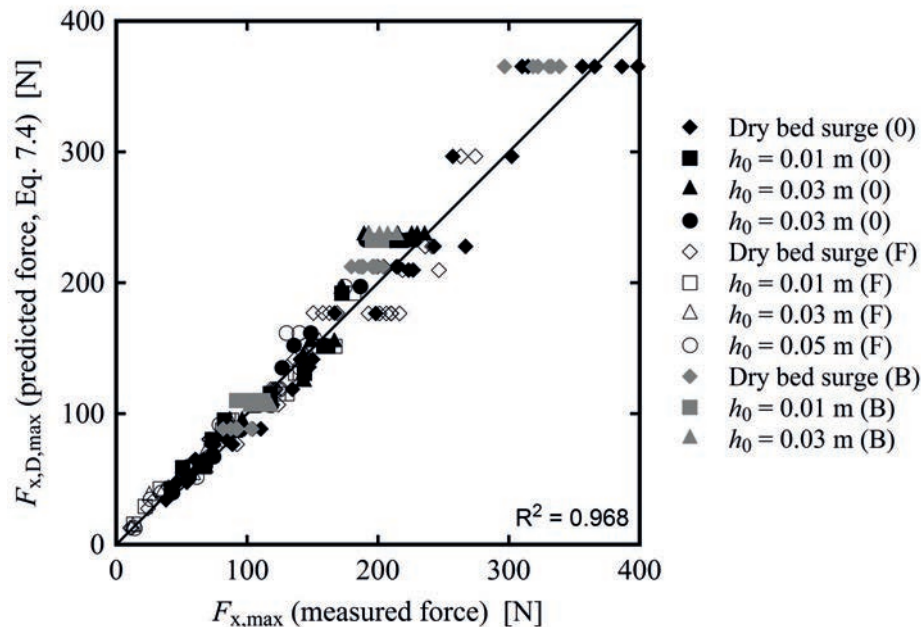
Figure 7.8 – Comparison of the measured forces ($F_{x,max}$) with those predicted using Eq. 7.5 ($F_{x,D,max}$).

Effect of additional side buildings (Configuration S)

On the base of configuration F (impervious lateral walls, Figure 3.18b), additional sides were installed next to existing building to simulate the effect of neighbouring building on the resulting total forces (Configuration S, Figure 3.18d). These additional sides were independent from the central structure and their forces therefore not recorded by the force plate. This configuration had a higher blockage ratio $\beta = W/3B = 1.56$ compared to the value $\beta = 4.57$ for the *"isolated"* building (configurations 0, F and B). Consequently, these tests allowed to qualitatively identify the influence of the blockage ratio on the resulting hydrodynamic force. Data presented in Figure 7.9 showed that, on average, the presence of side buildings provoked an increase in total force of about 20 %. This pointed out the importance of the blockage ratio in the computation of the resulting hydrodynamic load. These findings are in agreement Nouri et al. (2010) and ASCE 7 (2016) – Chapter 6.

7.4 Force analysis

As previously performed in Sections 5.4 and 6.4 for impervious buildings, some additional parameters are considered in the analysis. These are presented hereafter and visually described in Figure 5.13:

- Time to peak τ_{max}, corresponding to the time from wave arrival (t_0) to the force peak.
- Wave height at maximum horizontal force, h_M.
- Impulse I, transferred from the wave to the building.
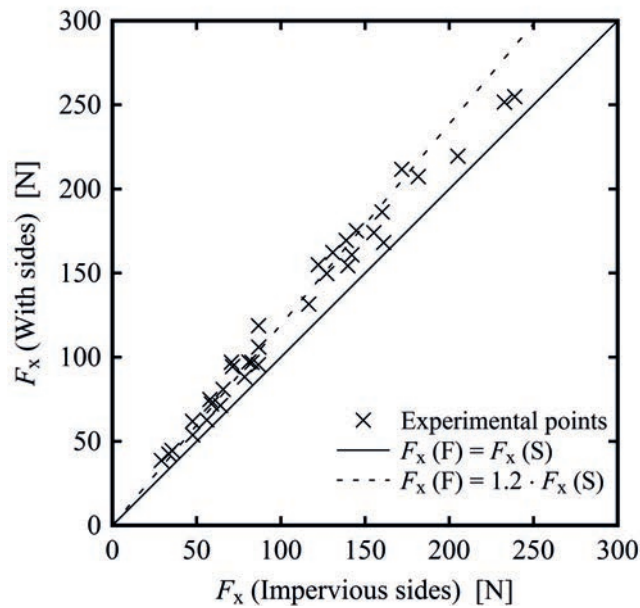
Figure 7.9 – Comparison of forces (F_x) for the configurations with impervious sides (Config. F, Figure 3.18b) and with additional sides to increase the blockage ratio (Config. S, Figure 3.18d).

7.4.1 Time to peak

The *"time to peak"*, τ_{max}, represents the time interval between the initial impact ($T = t - t_0 = 0$) and the occurrence of the maximum horizontal force $F_{x,max}$. The values of τ_{max} obtained for all tests (all porosities and configurations) are presented in Figure 7.10 as a function of h_0/h_{max}, where $h_0/h_{max} = 0$ represents the dry bed surges and $h_0/h_{max} > 0$ the wet bed bores. The results for porous structures showed a similar trend to that observed in Sections 5.4.1 and 6.4.1 for impervious structures with and without overflow. For bores, almost all maxima occurred instantaneously for $0 < \tau_{max} \cdot \sqrt{g/d_0} < $ 5-10, whereas for dry bed surges, these occurred mostly for $\tau_{max} \cdot \sqrt{g/d_0} > 10$. These observations clearly confirmed a well-known substantial difference between surges and bores in terms of their respective behaviour, proving that maximum force values for surges occur after those recorded for wet bed bores. Consequently, this resulted into steeper average gradients dF/dt for wet bed bores.

7.4.2 Wave height at maximum force

The parameter h_M is defined as the wave height at which the maximum force $F_{x,max}$ occurs ($T = \tau_{max}$), normalised with the maximum wave height h_{max} without the building (Eq. 5.9). The experimental data are shown in Figure 7.11 and compared to the design guidelines of the ASCE 7 (2016) - Chapter 6, according to which the maximum hydrodynamic load occurs when $h = h_M = 2/3 \cdot h_{max}$. The present data, in agreement with Sections 5.4.2 and 6.4.2 for impervious buildings with and without overflow, showed that although the choice of $h_M = 2/3$ is, on average, acceptable for surges. However, this is not conservative for bores as it would result into lower water depths in the design phase, for which $2/3 < h_M < 1$.
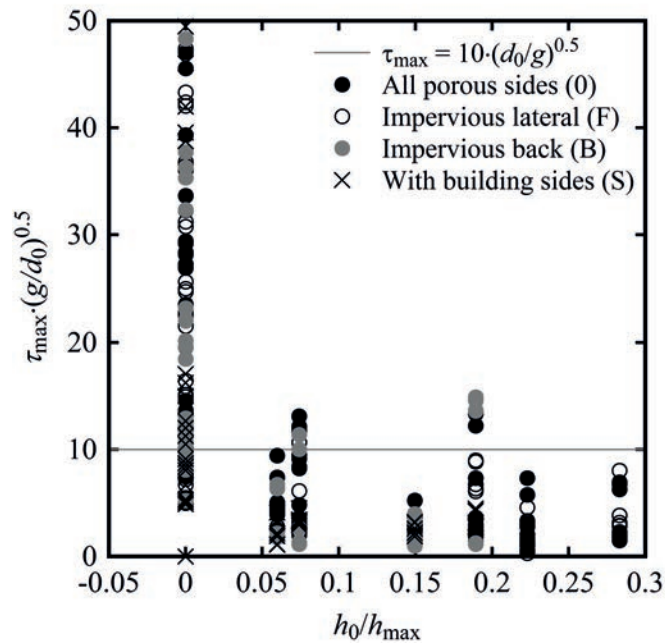
Figure 7.10 – Time to peak (τ_{max}): comparison between bores and surges for all 280 tests, where $h_0/h_{max} = 0$ represents dry bed surges and $h_0/h_{max} > 0$ the wet bed bores.
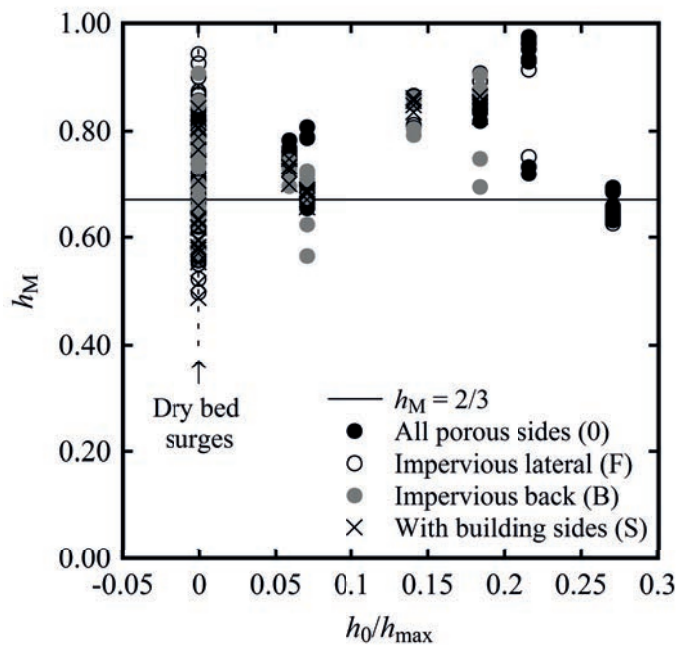
Figure 7.11 – Wave height at maximum force h_M for both wet bed bores and dry bed surges (280 tests). Results presented as a function of h_0/h_{max}, where $h_0/h_{max} = 0$ represents the dry bed surges and $h_0/h_{max} > 0$ the wet bed bores.

7.4.3 Impulse

The product of force F and time t is known as Impulse I. For the present case, the total impulse I_{tot} is the integral of the force F_x over time, until an upper limit $T = 100 \cdot (g d_0)^{0.5}$ is reached (Eq. 5.10). The impulse also represents the area of the surface below the time development of the horizontal force. Impulse has the advantage of being less variable if compared to peak forces (Bullock et al., 2007). Given Newton's 2nd Law ($F = m \cdot a = m \cdot \Delta V / \Delta t$), the impulse can be expressed as $I = F \cdot \Delta t = m \cdot \Delta V$, corresponding to the change in momentum. The impulse I_{tot} experienced by the building therefore equals the exchange in momentum with the incoming wave. Overall, the results in term of total impulse confirmed the previous findings obtained from the horizontal forces. Thus, Figure 7.12 shows that the total impulse computed for the configuration with impervious sides (F) is slightly lower than corresponding value for the configuration with all porous sides (0). This confirmed the previous statement that the presence of openings on the side walls had an influence mostly visible on the post-peak, quasi-steady hydrodynamic portion (Appendix C.5.2). Similarly the results for the configuration (S) with additional sides showed some impulse values 20% higher, as previously shown for the forces in Section 7.3.5.The values obtained for all experimental points are presented in Figure 7.13 as a function of $P_{h,max}$. These results confirm the previous findings obtained for horizontal force F_x, showing that a linear reduction is also applicable to the total impulse. Furthermore, as previously indicated, for the configuration with the impervious back (B), the total momentum equals that computed for fully impervious building.

(a) Configuration F   (b) Configuration S
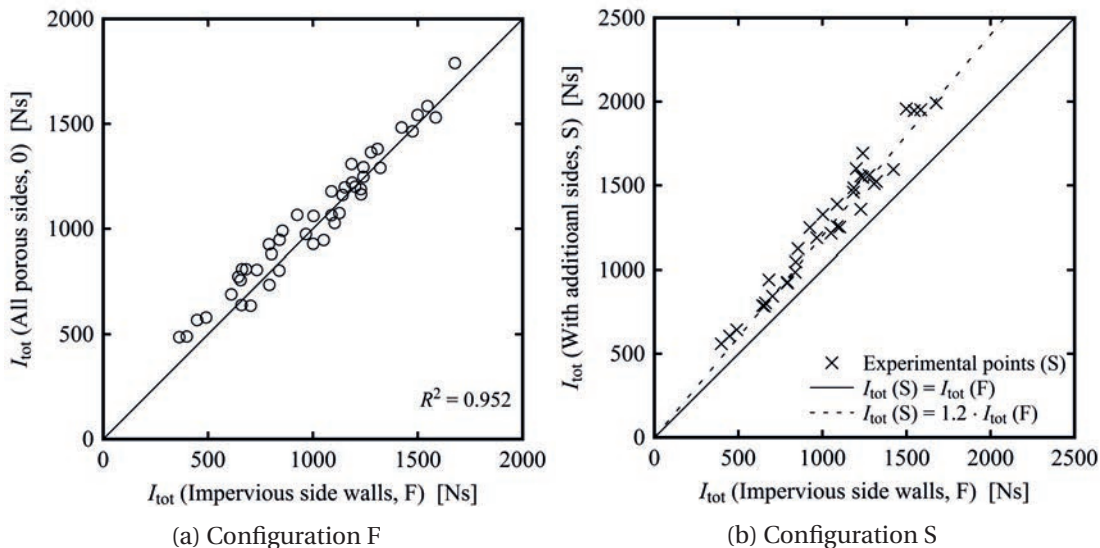
Figure 7.12 – Comparison of Total impulse I_{tot} for: (a) the configuration with impervious side walls (F) and (b) the configuration with additional building sides (S).

(a) Total impulse I_{tot} (b) $I^* = I_{peak}/I_{tot}$
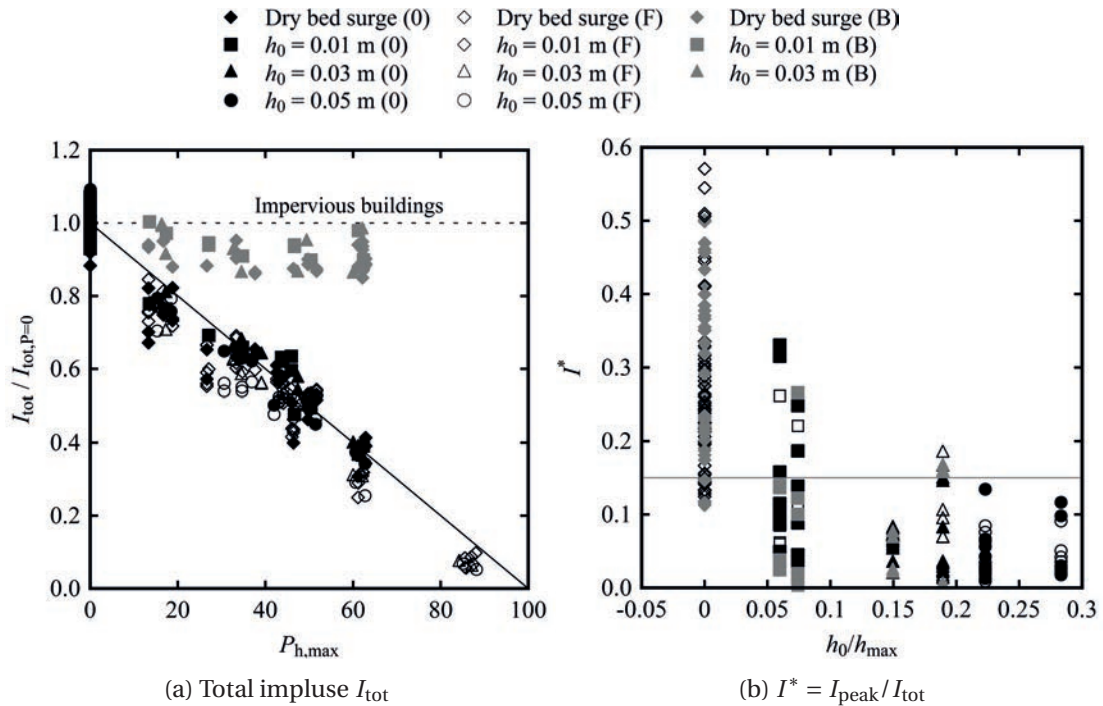
Figure 7.13 – Reduction of total impulse (I_{tot}) as a function of porosity $P_{h,max}$ and (b) values of $I^* = I_{peak}/I_{tot}$ computed for dry bed surges and wet bed bores (280 tests). Results presented as a function of h_0/h_{max}, where $h_0/h_{max} = 0$ represents the dry bed surges and $h_0/h_{max} > 0$ the wet bed bores.

To better quantify the impulse transferred to the building before the peak force occurs, similarly to Sections 5.4.3, 6.4.3 and Bullock et al. (2007), a parameter, I_{peak}, is defined as the integral between $0 < T < \tau_{max}$ in Eq. 5.11. The portion of total impulse that is transferred to the building before the maximum force occurs I^* is defined as the ratio between I_{peak} and I_{tot} (Eq. 5.12). The experimental results are presented in Figure 7.13b, where smaller values are found for wet bed bores with $I^* < 0.20$. These findings for buildings with openings are in agreement with those previously obtained for impervious buildings with and without overflow.

7.5 Moment and cantilever arm

All forces applied outside of the gravity centre of the building produce a moment. Consequently, horizontal forces produce a moment around the y-axis that might destabilise the structure and lead to the building tilting. The force-plate installed below the buildings also captured the behaviour of the moment M_y in time. A maximum moment value $M_{y,max}$ was identified for every test, along with its time of occurrence $\tau_{max,M}$. The results are compared to those obtained for the maximum horizontal force in Figure 7.14. The relatively good agreement between the two data sets validate for buildings with openings the approach presented in Section 5.5, implying that force and moment maxima occurred simultaneously.
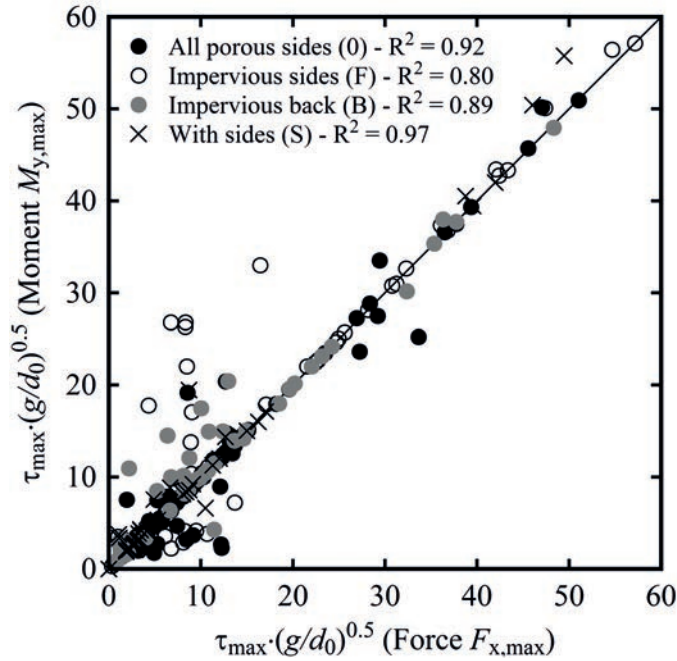
Figure 7.14 – Temporal occurrence (τ_{max}) of maximum horizontal force $F_{x,max}$ and moment $M_{y,max}$, presented in normalised form (280 tests).

For design purposes, once the magnitude of $F_{x,max}$ is defined through Eq. 7.5, the elevation at which this force acts and the resulting tilting moment are necessary. Given the simultaneous occurrence of $F_{x,max}$ and $M_{y,max}$ (Figure 7.14), the cantilever arm L_z arm at $T = \tau_{max}$ can be obtained through Eq. 5.15.

The values obtained from the experimental points are plotted in Figure 7.15a and normalized using the maximum wave height measured without the building (h_{max}). According to the results, the openings of the structure do not significantly influence the application point of the force F_x, which can be assumed constant for all configurations (Figure 7.15a). Although some scattering can be observed, the average value $L_z = 1.15 \cdot h_{max}$ introduced for impervious buildings in Section 5.5, can be extended to buildings with openings, independently of the geometry of the openings.

Consequently, similar to Eq. 5.16, the tilting moment results into:

$$M_{y,D,max} = F_{x,D,max} \cdot 1.15 h_{max} = \frac{1}{2}\rho \left(C_{R,0} \cdot \Pi\right) \cdot B \cdot M_{max}^* \cdot 1.15 h_{max} \qquad (7.6)$$

The comparisons of Eq. 7.6 with all experimental points is shown in Figure 7.15b, with good agreement for all configurations.
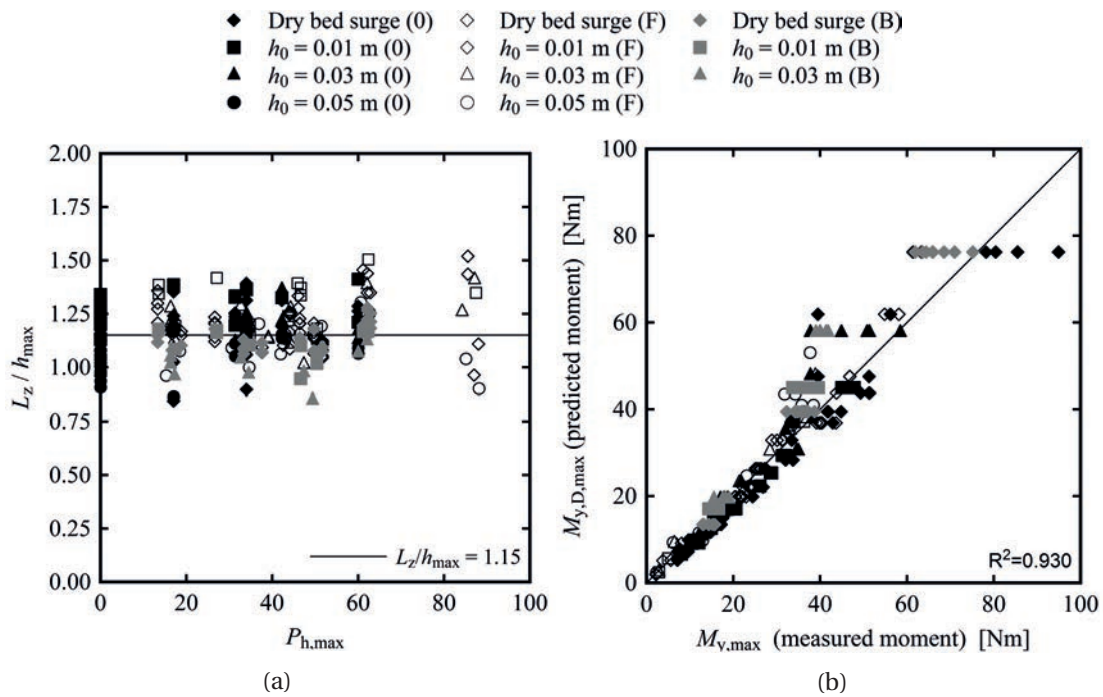
Figure 7.15 – Cantilever arm, L_z computed as the ratio $M_{y,max}/F_{x,max}$ for all porosity values and (b) comparison of measured maximum momentum $M_{y,max}$ with the value predicted using Eq. 7.6, $M_{y,D,max}$.

7.6 Vertical forces

In addition to horizontal forces, vertical forces F_z also act on the building. These can be distinguished into two main components: buoyancy ($F_{z,B}$) and the gravitational weight of water ($F_{z,g}$). In the chosen reference system, the $F_{z,B}$ has to be considered positive, and $F_{z,g}$ negative (Figure 3.15), being the total force at the foundation :

$$F_z = F_{z,B} + F_{z,g} \tag{7.7}$$

Being the process highly unsteady and the upstream water level continuously varied, the isolation of each component is hard to compute. The total force measured by the instrument is presented in Figure 7.16 for buildings with various porosities, along with the weight of water without the structure ($P_{tot} = 100\%$), corresponding to the weight of the propagating wave. For the impervious buildings, the absence of overflow above the structure resulted in vertical forces F_z close to zero, however for porous buildings the weight of the water flowing through the openings became predominant. One can notice that for porosities between $P_{tot} = 17$ and 34 %, similar behaviours were observed, reaching up to twice the gravitational weight of the wave, measured without the structure. For larger porosity values ($P_{tot} = 60\%$), smaller vertical forces were recorded (Figure 7.17). This is probably attributed to the *"accumulation"* of water upstream and inside the structure: in fact larger openings can facilitate the flow through the building and reduce the vertical load. The upper limit was represented by the scenario without building ($P_{tot} = 100$ %) showing lesser values if compared to the scenarios with the obstruction.

An initial uplift of the building was observed for P_{tot} = 17 and 34 %, attributed to the initial step encountered by the incoming wave, forcing the flow to deviate in the vertical direction and pushing the building upward (Figure 7.18). The uplift did not occur for P_{tot} = 60 % since the building bottom was located at the same level as the channel. Similar results were previously discussed by Hartana and Murakami (2015).
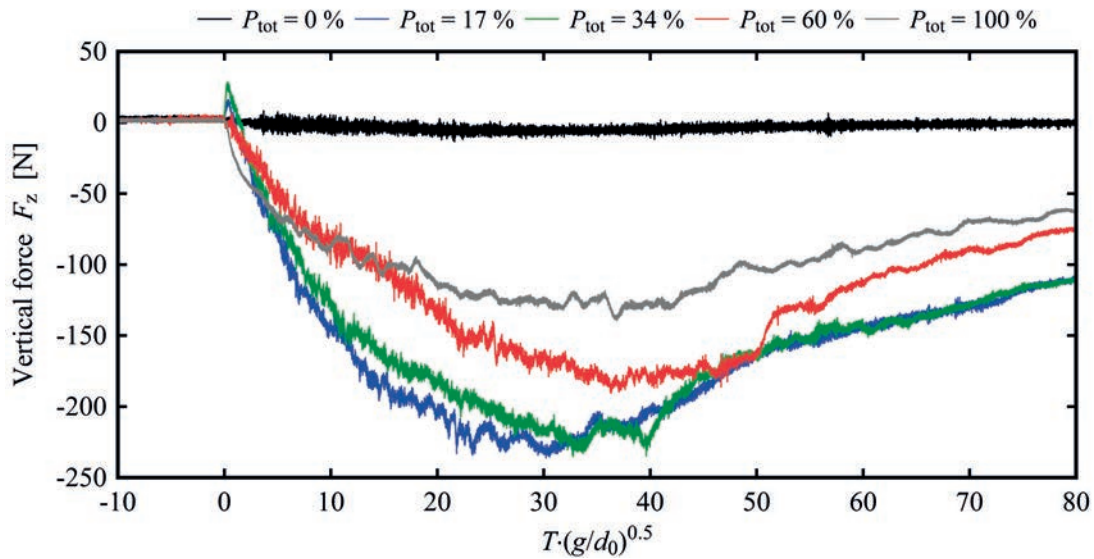
Figure 7.16 – Time history of the total vertical forces F_z, measured for various porosity configurations, for a dry bed surge (WD2, d_0 = 0.63 m).
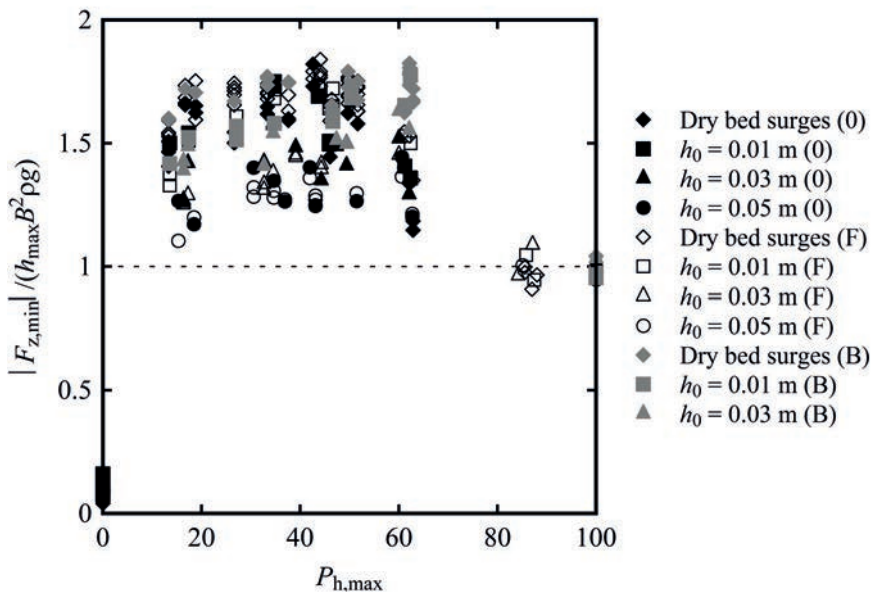
Figure 7.17 – Normalised vertical forces F_z as a function of building porosity $P_{h,max}$.
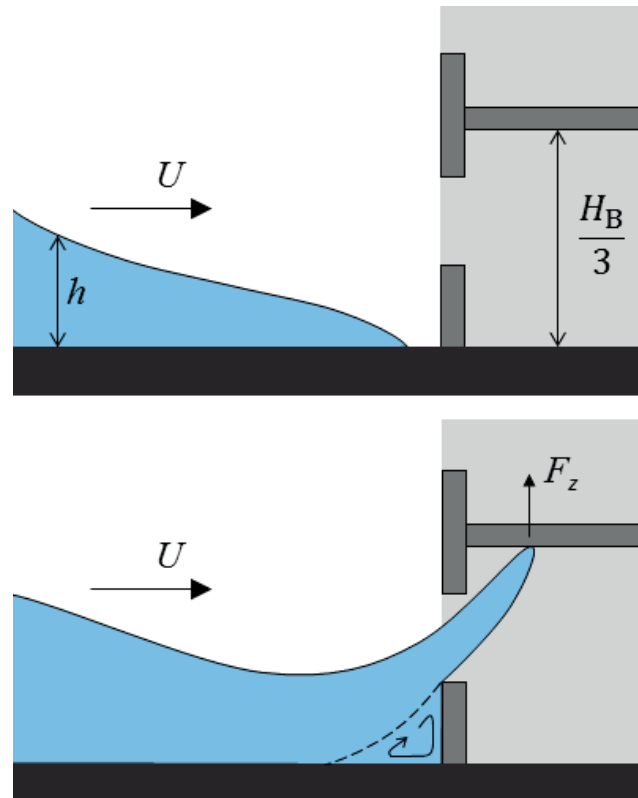
Figure 7.18 – Sketch of the positive vertical forces produced during the initial impact of the wave against the building.

7.7 Summary

Field surveys and visual observations showed that buildings with openings seem to perform better under hydrodynamic loading. This technique could therefore be used to design safer vertical shelters, thus reducing casualties and reconstruction costs. However, up to now, very few studies have addressed this issue and this research presents a comprehensive experimental study on the effect of openings on the resulting hydrodynamic force.

For this, four configurations with six openings ranging from 0 (impervious, reference) to 84% were experimentally tested for 12 standard waves with different approach conditions. The research lead to the following findings:

1. Visual observations pointed-out an interaction between the incoming wave and the buildings, resulting into a flow through the openings. This generated lower upstream inundation depths compared to impervious buildings, leading to safer vertical shelters.
2. The presence of openings produced a linear reduction of the maximum horizontal force, if compared to the corresponding impervious building. Configurations with and without openings on the lateral walls had a similar behaviour in terms of maximum horizontal force. The configuration with impervious back showed similar results to those measured

for the fully impervious case. The total impulse, computed as the integral of the force over time, had a behaviour similar to the force, confirming the linear relationship.

3. Also for buildings with openings, the occurrence of the maximum horizontal force was shown to take place earlier for wet bed bores than for dry bed surges. Similarly to the impervious case, the maximum force $F_{x,max}$ occurred at a wave height that was higher than 2/3 of the maximum wave height measured without the building (h_{max}), as suggested by the ASCE 7-06.

4. Experimental data suggested that the presence of additional side buildings, equal to a higher blockage ratio, increased the forces on the main structure by 20%, with higher upstream inundation depths.

5. Both maximum horizontal force and moment occurred simultaneously. The application point of the total horizontal force (cantilever arm) was constant for all configurations and for all porosities. In agreement with previous studies on impervious structures, this could be assumed equal to $1.15 \cdot h_{max}$.

6. New equations (Eq. 7.5 and 7.6) are proposed to predict the horizontal force F_x and the tilting moment M_y, taking into account the effect of building openings within the resistance coefficient C_R. These had a good agreement with experimental points and previous studies.

7. Because of the flow through the openings, vertical forces showed downward values up to twice the wave-weight, measured without the building. Highest values were found for middle porosities (17-34 %), as a consequence of the upstream accumulation.

8 | Conclusions

The generation of dry bed surges and wet bed bores was experimentally investigated through a vertical release technique. Subsequently, their impact on typical buildings, with and without openings, located on coastal areas subject to tsunami hazard, was assessed. The main results and limitations of this research are summarized herein, as well as some key points for future work.

8.1 Main results

8.1.1 Wave hydrodynamics

In the last decades the world suffered some major catastrophic events, characterized by significant damages and devastation. Dam-break waves, impulse waves, tsunamis, tidal bores and storm surges are very different physical phenomena, but all characterized by a sudden increase in water depth, often leading to flows with extreme hydrodynamic conditions. The rarity and diversity of these events make a comparison with visual observations difficult to assess, resulting into multiple generation technique used to reproduce such waves in laboratory environments. The vertical release of a known water volume from an upper reservoir into a downstream channel was used to generate tsunami-like waves. The variation of the released discharge allowed to generate waves with different hydrodynamic properties in terms of velocity and water depths. Visual observations confirmed a significant difference in behaviour between dry bed surges, characterised by a faster, non-aerated front followed by a constant increase in water depth, and wet bed bores, characterised by higher water levels with a turbulent aerated roller, similar to a translating hydraulic jump. All generated waves were compared to field data, existing guidelines and previous studies available in literature, thus proving that the vertical release technique can be used to generate tsunami-like flows propagating inland. Because of their key role in the estimation of hydrodynamic forces, importance was given to the velocities of the generated waves. This led to the definition of a new expression to predict the front propagating celerity of surges propagating on dry bed as a

function of the impoundment depth (d_0):

$$U = 1.25 \cdot \sqrt{g d_0} \tag{4.17}$$

For wet bed bores, excellent agreement was observed with existing literature. The velocity profiles of the propagating surges and bores behind the front were also analysed, showing some profiles typical of open channel flows. These were successfully compared to Prandtl's exponential law, thus proving that the common assumption of a constant velocity profile throughout the water depth is acceptable. An expression to estimate the deceleration of the average velocities behind the wave front as a function of the impoundment depth d_0 was provided:

$$\frac{V_\mathrm{m}}{U} = 1 - c \cdot \tanh \left[b \cdot T \sqrt{\frac{g}{d_0}} \right] \tag{4.10}$$

In addition, this equation allowed to obtain the time developments of the Froude number and the momentum flux per unit width.

8.1.2 Impervious buildings

The tragic nature of tsunamis, impulse waves and dam-break waves also showed that measures had to be taken to reduce reconstruction costs and limit casualties. For this, the design of resilient structures acting as vertical shelters is necessary, especially in areas where access to high elevation refuges is difficult or too far. The large amount of studies and formulae available in literature showed that disagreement still exists on the computation of hydrodynamic forces for such unsteady impacts. Thus, through an extensive experimental program, twelve standard waves were released against an impervious free-standing building. This was assembled on a force plate, providing the time-histories of the forces and moments in all three directions. Visually, all impacts presented high splashes for all configurations, followed by a quasi-steady hydrodynamic flow around the building. Forces were shown to be proportional to the hydrodynamic properties of the wave, measured <u>without</u> the building. In the computation of the force a resistance coefficient C_R was preferred to the classical drag coefficient, taking into account both hydrostatic and hydrodynamic components (herein $C_{\mathrm{R},0} = 2.0$). For dry bed surges a good agreement was directly found with the momentum flux per unit width (M), obtained as the product of water depth h and the decelerating velocity values V_m:

$$F_{\mathrm{x,D}} = \frac{1}{2}\rho C_\mathrm{R} B \cdot M = \frac{1}{2}\rho C_\mathrm{R} B \cdot \left(h V_\mathrm{m}^2 \right) \tag{5.2}$$

For wet bed bores, because of the presence of a discontinuity in the form of an aerated roller, an overestimation of the force was constantly observed. For this, the introduction of a wet bed bore reduction coefficient χ was necessary, resulting into a modified momentum flux (M^*):

$$F_{\mathrm{x,D}} = \frac{1}{2}\rho C_\mathrm{R} B \cdot M^* = \frac{1}{2}\rho C_\mathrm{R} B h \cdot \left\{ \min\left[\chi U; V_\mathrm{m}(t) \right] \right\}^2 \tag{5.6}$$

Some structures located on the shore are not designed as vertical shelters and for these overflow is accepted. Specific experimental tests showed that once the structure is submerged, higher water levels are observed in the downstream side, thus reducing the hydrostatic component of the total force. As a consequence, milder loading conditions were systematically registered, resulting into reduced values of the resistance coefficient ($C_{R,S} \approx 1.5$). This implied that from a structural point of view, the overflow does not represent a critical scenario.

8.1.3 Effect of building openings

Field surveys showed that structures with openings performed better under hydrodynamic load, however no systematic study of the effect of openings was available in literature. Experimental tests for six opening values arranged in four configurations indicated that a flow through the building could act as a mitigation measure, thus reducing the total load on the structure. Visually, the presence of openings resulted in a different impact dynamic, with lower upstream inundation depths and therefore safer vertical shelters.

A new model to predict the maximum force, taking into account the effect of building openings was proposed through the introduction of a porosity parameter Π within the resistance coefficient:

$$F_{x,D,max} = \frac{1}{2}\rho \left(C_{R,0} \cdot \Pi \right) \cdot B \cdot M_{max}^* \tag{7.5}$$

The presence of openings on both the front and the back sides of the building were taken into account. Openings on the side walls were shown to be non-influential in the computation of the maximum impact force. However, these became non-negligible in the quasi-steady post-peak hydrodynamic phase, where the absence of flow through the side walls was responsible for forces some 30% lower (Appendix C). The relationship between the maximum hydrodynamic force and the building openings was shown to be **linear**. In addition, for both buildings with and without opening, all experimental tests showed that the maximum horizontal force (F_x) and moment (M_y) occurred at the same time. This allowed to compute an expression of that cantilever arm equal to 1.15 times the maximum wave height measured without the structure (h_{max}). As a consequence, an estimation of the tilting moment was possible through the following equation:

$$M_{y,D,max} = F_{x,D,max} \cdot 1.15h_{max} = \frac{1}{2}\rho \left(C_{R,0} \cdot \Pi \right) \cdot B \cdot M_{max}^* \cdot 1.15h_{max} \tag{7.6}$$

and this model showed a good agreement with all experimental points and previous studies available literature.

In addition, these studies pointed out some key differences between the impact of dry bed surges and wet bed bores, for both buildings with and without openings. From the experimental tests, it emerged that the maximum force occurred before for wet bed bores and that it was associated with higher water depths, compared to dry bed surges. All results derived in terms

of forces were also confirmed for the impulse (*i.e.* the integral of the force over time), known for being a less variable parameter compared to peak forces. It is also important to point out that only 5 to 30 % of the total impulse was transferred to the structure before the occurrence of the maximum force, showing that the quasi-steady post-peak hydrodynamic phase should not be neglected.

This research was fully experimental and the current results could be used to validate or calibrate existing numerical models. Furthermore, the above findings will assist practical engineers and contribute to a safer and better design of resilient buildings.

8.2   Limitations

The results of this research have the following limitations:

1. The results obtained were derived from dry bed surges and bores propagating on a smooth horizontal bed. The beneficial effect of beach slopes in dissipating wave momentum are herein not considered, resulting into a more conservative approach. In addition, results are valid for waves within same Reynolds and Froude numbers as the tested scenarios (Fr $\approx$ 1-5, Re $\approx 10^5$).
2. The findings are only applicable to elastic structures, for which no plastic deformations are observed.
3. Results showed that the blockage ratio (channel width/ building width) influenced the magnitude of the measured force. Thus, these findings have to be applied to scenarios with similar blockage ratios.
4. The results only apply to flows in the absence of debris and transported material. In case of debris, openings are most likely to be blocked (*debris damming* effect) and the beneficial effect of openings may be reduced.
5. For this experimental set-up, buoyant forces were only partially recorded. Thus, solid conclusions on the vertical forces acting on the structure cannot be drawn.

8.3   Outlook

The present study provides a relevant contribution in the domain of wave impact against buildings with openings. Nevertheless the behaviour of fluid-structure interaction during highly unsteady hydrodynamic impacts is still not fully understood. In this context, the following points may require further investigations to expand the knowledge in both wave hydrodynamics and wave impact on buildings:

Wave hydrodynamics

- A specific and comprehensive study on the turbulent behaviour of the generated waves is recommended, including a larger number of repeats to isolate the fluctuations from

the ensemble-average. This would provide some relevant additional information in terms of Reynolds stresses and Turbulent intensity for tsunami-like flows propagating inland.

- Wet bed bores showed that presence of an aerated roller, which was shown to have an influence on the resulting loading process. For this, an empirical coefficient χ was introduced. Nevertheless the effect of air entrainment on the impact forces should be investigated through specific tests in terms of air-water flow properties.

Wave impact on buildings

- The exploitative studies revealed that the resulting load on free-standing structures was influenced by the blockage ratio. Tests varying the building width could be performed to isolate and quantify such effect.
- Focused experimental investigations on the effect of openings on the resulting drag coefficient C_D under choked, subcritical, steady-state flows are also recommended.
- Previous studies showed that the orientation of impervious free-standing structures along the coastline had a beneficial effect on the resulting forces. The combined effect of building orientation and openings would also be of interest.
- In coastal areas subject to tsunami hazard, water often carries a high amount of debris, including poles, logs, containers and vehicles. These result into a blockage of the building openings, generating the so-called *"Debris-damming"* phenomenon and thus limiting the beneficial effects of porous structures. Although some studies are already being carried out on perforated walls, it would be of interest to combine the effect of openings and debris motion for a better evaluation of the resulting forces.
- This research focused on the hydraulic aspects of the impact. An implementation of these results from a structural prospective, providing practical application guidelines is necessary. A combination of the wave-induced loads with the seismic and wind design could be implemented.

A UVP Sensitivity Analysis

Ultrasonic Velocity Profilers (UVP) type *DUO-MX SN* (produced by the Met-Flow - Switzerland) were used to detect the quasi-instantaneous velocity profiles of the moving waves. For this, a 2 MHz transducer was installed in the channel bottom with an inclination of 20° in the upstream direction. One UVP per cross section was used and measurements were taken in the transducer axis direction, then projected in the main flow direction (x-axis). Velocity components in the vertical and transversal directions were not considered. A complete description of the UVP used herein can be found in Section 3.3.2.

Bores are a highly unsteady phenomenon, meaning that its properties rapidly change in space and time, requiring a high frequency for all measurements. For most instruments the quality and the reliability of the measured data is proportional to the number of repetitions used, implying a longer duration and therefore a lower acquisition frequency. A compromise between high frequency and quality of the results was therefore necessary and a sensitivity analysis was carried out on three wet bed surges with initial still water depth $h_0 = 0.05$ m to investigate the influence of the main acquisition parameters. These are presented in Table A.1.

	Number of repetitions	Acquisition duration [ms]	Acquisition frequency [Hz]
Bore 1	32	18	55.6
Bore 2	64	38	26.3
Bore 3	128	74	13.5

Table A.1 – Variation of the acquisition parameters in the sensitivity analysis

(a) Bore 1 (32 repetitions)

(b) Bore 1 (32 repetitions)

(c) Bore 2 (64 repetitions)

(d) Bore 2 (64 repetitions)

(e) Bore 3 (128 repetitions)

(f) Bore 3 (128 repetitions)
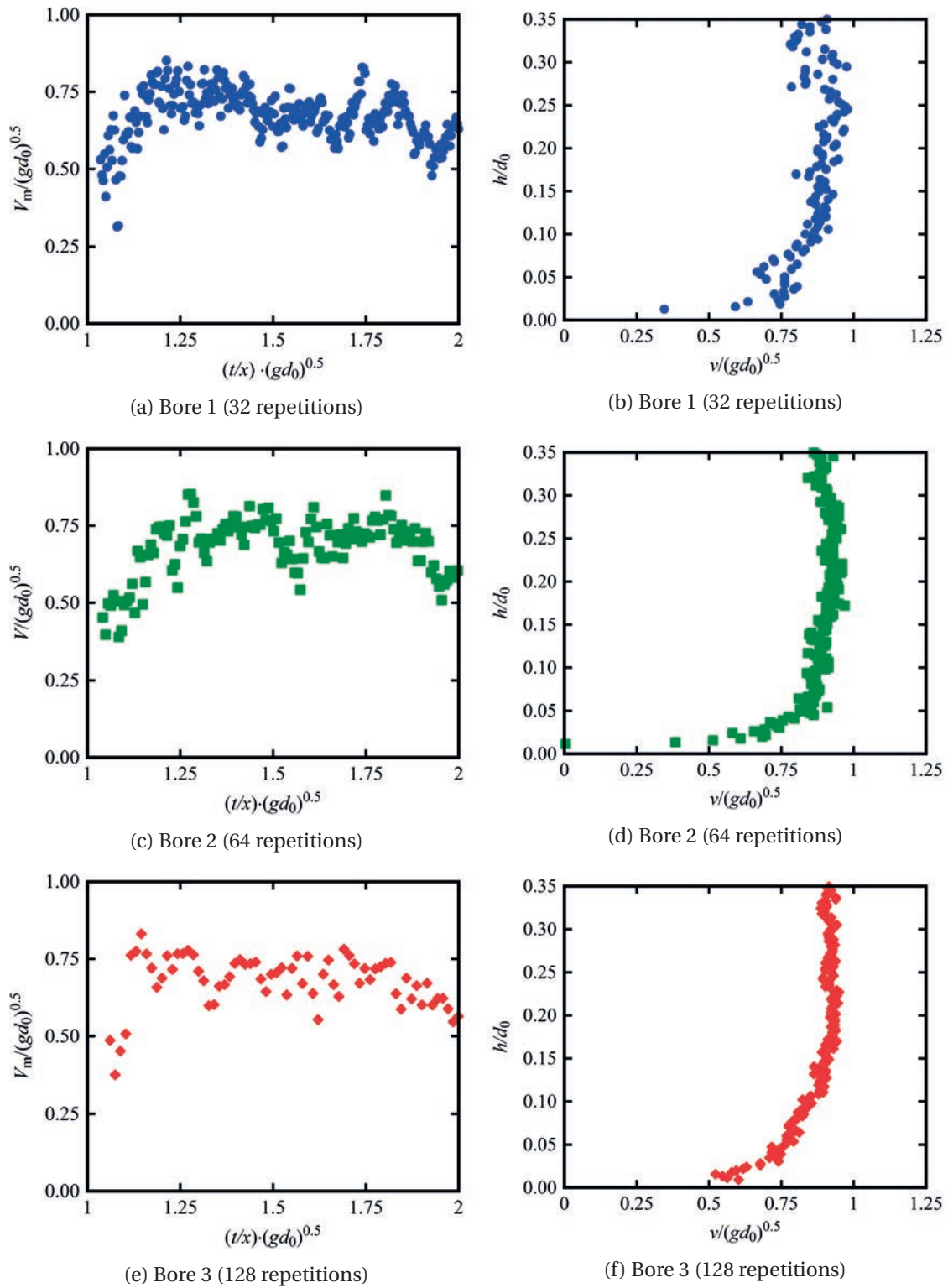
Figure A.1 – Sensitivity analysis for the use of UVPs: (left) time evolution of the Average Profile Velocity V_{m} and (right) examples of profiles obtained for $t = 6.5$ s, after the turbulent bore front.

As shown in Chapter 4, a depth-average profile velocity (V_m) was calculated for every profile obtained using Eq. A.1, in which i varied from 0 (channel bottom) to n (h_{max}).

$$V_m = \frac{1}{n} \sum_{i=0}^{i=n} v_i \qquad\qquad (A.1)$$

The results obtained for all three bores are presented in Figure A.1 as a function of time, where a similar behaviour is observed for all tested bores. One can notice that a higher frequency (Figure A.1a, 32 repetitions) corresponded to a greater number of points, but lower precision and higher scattering were found. With lower frequencies, the number of measurements was reduced, the overall profile behaviour remaining unchanged. It is important to point out that being the first part of the wave highly aerated and turbulent, the transmission of the echo was obstructed by the presence of air bubbles. This resulted into velocity profile measurements characterised by high scattering and low physical meaning. Results also showed some interesting logarithmic profiles typically associated with open channel flows for all scenarios. As an examples the profiles obtained at $t = 6.5$, behind the aerated bore front, are also presented in Figure A.1 . Similarly to the previous case, for higher acquisition times a smoother profile was observed, whereas for higher frequencies more scattering was found. For these reasons in the present study a resolution of 128 repetitions was chosen and applied to all tests (Wüthrich et al., 2016a).

B Bed roughness and water surface fluctuations

Secondary waves with various frequencies were observed behind the front for both surges and bores. For unbroken waves these phenomena might be classified as Favre secondary waves (Favre, 1935; Henderson, 1966). The behaviour of secondary oscillations was previously investigated for dam-break waves (Marche et al., 1995) and for open channel flows (Meile et al., 2013; Terrier et al., 2013). Their appearance is probably due to the non-hydrostatic pressure distribution around the wave front (Soares-Frazão and Zech, 2002). A theory implying the superposition of wavelets with different velocities was developed by Chow (1959). Some specific studies focusing on turbulence in bores were carried out by Yeh and Mok (1990) who compared their behaviour to hydraulic jumps. A "*generation-advection cycle*" was observed, in which eddies were formed in the roller and then advected behind the front. For large Froude numbers, the whole bore was saturated with turbulence.

The purpose of this appendix is to further investigate the fluctuating behaviour of wet bed bores and dry bed surges behind the front. Both smooth and rough beds were considered and data were analysed in frequency and time domains. The results yielded a characterisation of the free-surface oscillations according to the time evolution of the bore. Significant differences between the structure of the oscillations in the near-front region and in the region situated away from the front were observed. These differences were analysed in terms of their spectral energy distribution.

This Chapter is based on the papers "Surface Turbulence on Bores and Surges propagating on Smooth and Rough Beds" by D. Wüthrich, M. Pfister, P. Manso, G. Constantinescu and A.J. Schleiss, published in the proceedings of the 6th *International Conference on the Application of Physical Modelling in Coastal and Port Engineering and Science* (Coastlab16) in Ottawa, Canada (7-9 May 2016) and "Estimation of wave propagation velocity on a channel with smooth and rough bed" by D. Wüthrich, M. Pfister, I. Nistor and A.J. Schleiss, published in the proceedings of the 37th *IAHR World Congress* in Kuala Lumpur, Malaysia (13-18 August 2017). The experimental work and the analysis presented hereafter is original and was performed by the author.

B.1 Experimental set-up

The experimental set-up is described in details in Chapter 3. The tests with a smooth bed took place on painted wooden panels with a Darcy-Weisbach friction factor measured to $f_{DW} \approx 0.021$ (Figure 3.3c). To increase the roughness of the channel bed, an artificial green carpet was added (Figure B.1); the latter had a thickness of 7 mm and some detailed steady state experiments were carried out to measure the Darcy-Weisbach friction factor $f_{DW} \approx 0.04$, corresponding to an equivalent roughness $k_s = 2.8$ mm. This value is consistent with the findings of Choufi et al. (2014) for a similar material. The bore was characterised in terms of velocity and height using 7 Ultrasonic distance Sensors (US) installed along the channel (at $x = 2, 10.1, 12.1, 13.1, 13.35, 13.6$ and 13.85 m). These had a sampling frequency of 12.5 Hz and the analysis was carried out using a 6 Hz cut-off frequency, in accordance with Nyquist-Shannon theorem.
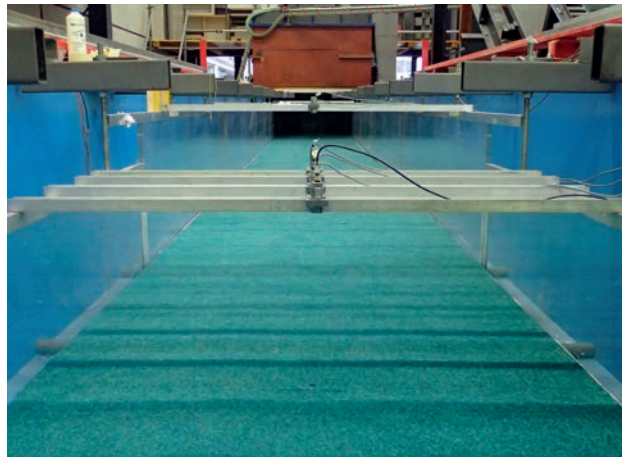
Figure B.1 – Rough configuration installed on the smooth channel.

B.2 Effect of bed roughness

Four tests were selected on both smooth and rough, dry and wet bed conditions. Details concerning the experiments can be found in Table B.1. As discussed in Chapter 4, dry bed surges and wet bed bores showed a different behaviour: dry bed surges presented a thin front followed by a constant increase in water depth following the front and no major aeration was observed, whereas wet bed bores presented a highly turbulent, recirculating roller propagating over an irrotational, initially still, water level. Wet bed bores showed a sudden increase in water height, followed by a relatively long and constant water height. For both wet bed bores and dry bed surges, less aeration was observed behind the front and some secondary waves with multiple time periods were recognised. The surface oscillation presented a 3-dimensional pattern and some movements were also observed in the transversal direction. Pictures of the propagating bores and surges are presented in Figure B.2.

	Bed surface	**Bed condition**	d_0 [m]	U [m/s]	h_{max} [m]	Re	Fr	Fr_B
Surge	Smooth ($f_{DW} \approx 0.21$)	dry	0.82	3.55	0.185	$2.52 \cdot 10^7$	2.63	-
	Rough ($f_{DW} \approx 0.40$)	dry	0.82	2.86	0.220	$2.10 \cdot 10^7$	1.94	-
Bore	Smooth ($f_{DW} \approx 0.21$)	wet (h_0=0.05m)	0.82	2.74	0.269	$2.12 \cdot 10^7$	1.68	3.91
	Rough ($f_{DW} \approx 0.40$)	wet (h_0=0.05m)	0.82	2.74	0.279	$2.15 \cdot 10^7$	1.66	3.92

Table B.1 – Experimental program of tests carried out for the present study

(a) Dry bed surge - smooth bed

(b) Wet bed bore - smooth bed

(c) Dry bed surge - rough bed

(d) Wet bed bore - rough bed
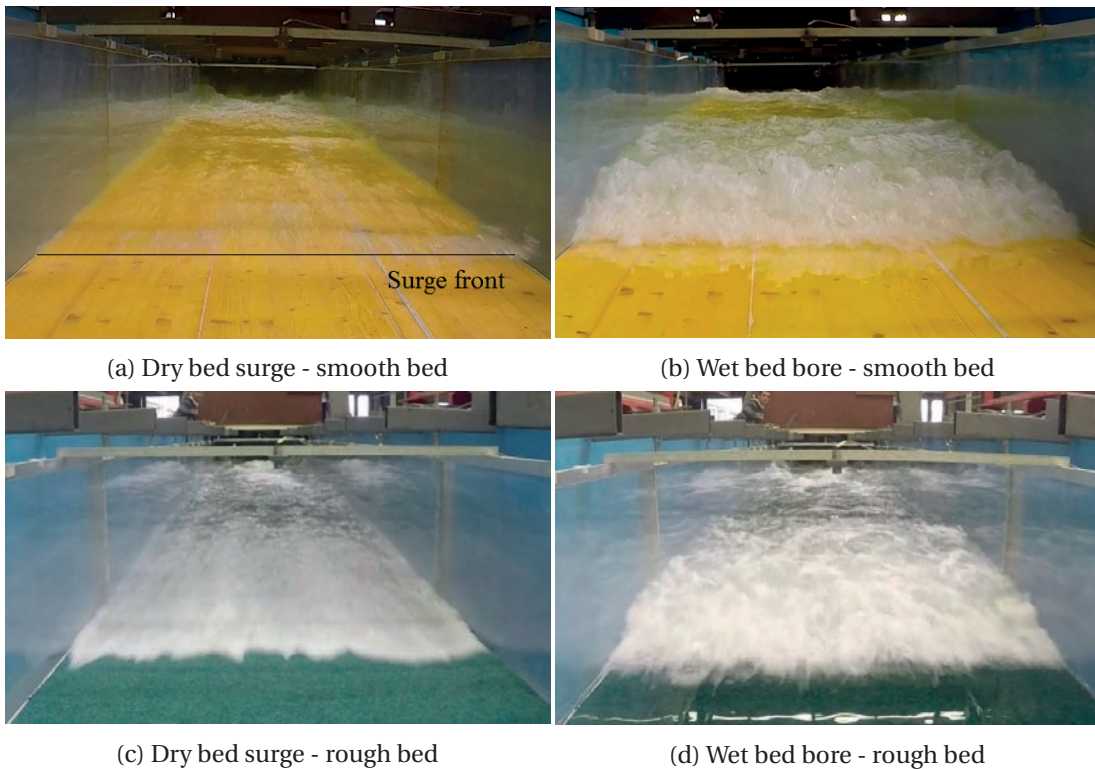
Figure B.2 – Propagating of dry bed surges and wet bed bores on both smooth ($f_{DW} \approx 0.02$) and rough ($f_{DW} \approx 0.04$) bed

The time evolutions of the wave profiles measured at US7 (x = 13.85 m) for both surges and bores are presented in Figure B.3. Results showed that the surge propagating on the rough bed had lower velocities than the surge propagating on the smooth bed. Furthermore the dry bed surge on rough bed had a more aerated front (Figure B.2c). Both measurements and visual observations showed that bores over a wet bed presented similar behaviours regardless of the bed roughness. The findings suggested that the still water level had more influence than the bed roughness. The profiles obtained for the dry bed surges showed a constantly increasing behaviour directly followed by the decreasing limb, whereas bores over wet bed presented a sudden raise followed by a relatively constant water level (plateau height, h_2) before decreasing. These behaviours are in agreement with the theory of Ritter (1892) and Stoker (1957) for dam break waves on dry and wet bed respectively (Chapter 4).

(a) Dry bed surge   (b) Wet bed bore
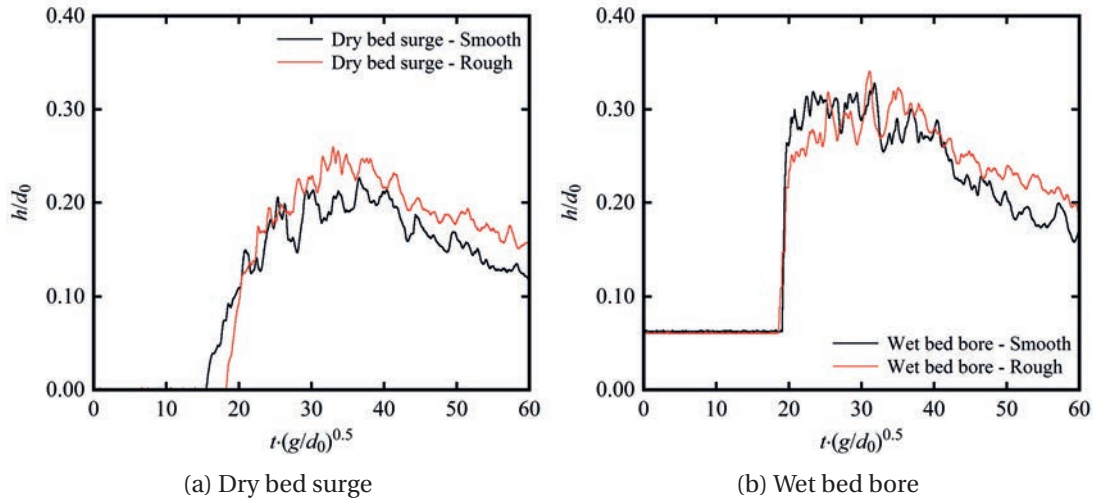
Figure B.3 – Comparison of wave profile h/d_0 on smooth and rough beds for: (a) dry bed surges, $d_0 = 0.82$ m; (b) wet bed bores, $d_0 = 0.82$ m and $h_0 = 0.05$ m.

For the smooth configuration, the longitudinal water depth profiles obtained when the dry bed surge reached $x = 13.85$ m and 13.60 (location of US 7 and US6, respectively) were compared to the theoretical solutions of Ritter (1892) and Chanson (2009) in Section 4.3.1. The influence of bed friction was implemented by Dressler (1952, 1954) and Whitham (1955). The profiles obtained for the experiments over rough bed are compared to these theoretical solutions in Figure B.4, where a good match can be observed with existing literature (Ritter, 1892; Chanson, 2009). For wet bed bores, no differences are observed between the smooth and the rough conditions in terms of wave profiles (herein not shown), showing that both scenarios were well described by the theory of Stoker (1957). These findings suggested that for the tested roughness values, the initial still water depth h_0 had a greater influence on the resulting wave than friction.

Knowing the spatial repartitions (Δx) of the US sensors, an estimation of the wave propagation celerity U was obtained through the ratio $\Delta x/\Delta t$. Based on these values, both the Reynolds (Re) and Froude (Fr) numbers of the flow were calculated using Eq. B.1:

$$\text{Re} = \frac{U \cdot D_H}{\nu} \qquad \text{Fr} = \frac{U}{\sqrt{g \cdot h_{\max}}} \qquad \text{Fr}_B = \frac{U}{\sqrt{g \cdot h_0}} \tag{B.1}$$

where D_H is the hydraulic diameter ($D_H = 4R_H$), ν is the kinematic viscosity of water, g the gravity constant and h the wave height. For the wet bed bore a bore Froude number (Fr_B) was also calculated. Results showed similar values of the Reynolds number for all configurations, with $\text{Re} \approx 2 \cdot 10^7$ during the wave peak. The relatively high values of the Reynolds number, computed using the front celerity U and the maximum wave height $h_{\max}$ (that might not occur at the same time) represented an upper value indicating a high level of turbulence inside the wave. The higher velocities of the dry-bed surges were compensated by the higher

166
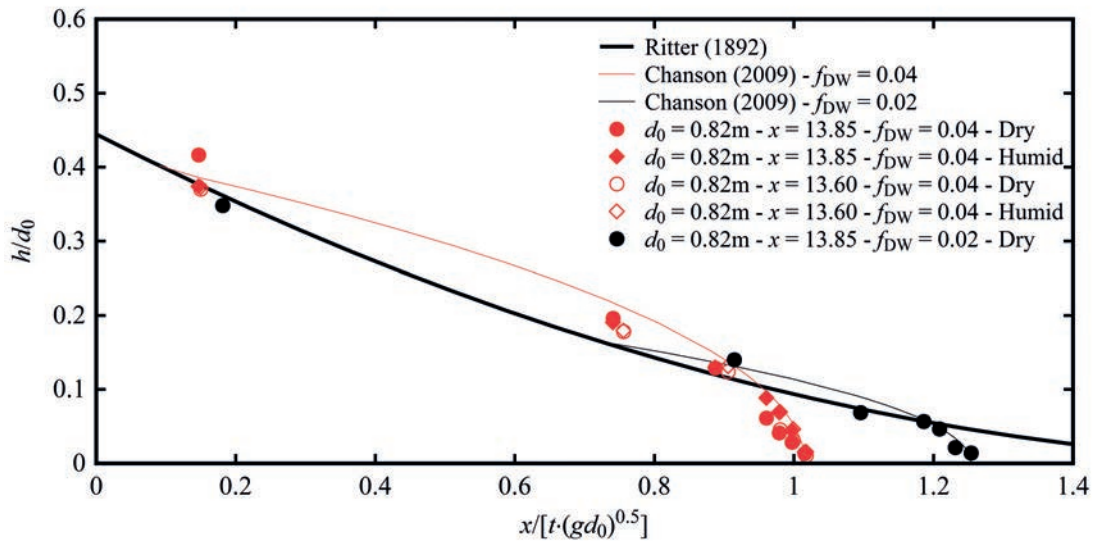
Figure B.4 – Comparison of longitudinal wave profiles for smooth and rough beds with theo-retical solutions of Ritter (1892) and Chanson (2009).

water elevation for the wet bed bores, explaining the similarity of the resulting values for all scenarios. Similarly to some previous studies, a bore Froude number was calculated based on the initial still water depth (h_0) (Yeh and Mok, 1990; Leng and Chanson, 2015), with values Fr_B > 2. This implied that the flow behind the bore front was saturated with advected eddies Yeh and Mok (1990).

The US sensors also captured secondary wave patterns behind the front and all tests presented multiple fluctuations of the water surface with frequencies varying from large to small scale. Some substantial differences were observed between the increasing and decreasing limbs of the wave, as the first seemed to have a higher density of secondary waves with greater ampli-tude and shorter periods. According to Yeh and Mok (1990) the fluctuations and the turbulent formations immediately behind the front are related to the behaviour of the propagating roller. Furthermore, a "*generation-advection cycle*" was observed, suggesting that the eddies formed inside the roller and were then advected in the flow, where a vertical stretch was detected. The secondary turbulence patches were related to the intermittent nature of the flow, as discussed by Longuet-Higgins and Turner (1974). A difference in water elevation between the smooth and the rough configurations was observed in the steady flow following the wave. The bores propagating over a rough bed were characterised by a lower level of surface turbulence with fewer fluctuations than those observed for the smooth bed cases. This might be attributed to the larger turbulence intensities of the flow generated over a rough bed, resulting in a more efficient dissipation of the eddies than on smooth bed, without interaction with the air-water interface. For the smooth-bed cases, the less efficient energy dissipation inside the flow would then result into enhanced surface turbulence with a repeating pattern to dissipate the remaining energy.

B.3 Water surface fluctuations

To get an insight in the surface fluctuations of the waves, an exploratory spectral analysis was carried out using the transient water level data presented in Figure B.3. First a Fourier Fast Transform (FFT) was applied to all raw height signals to identify the density of the frequencies observed on the water surface. The Fourier transform decomposes a signal into its frequency components. Results are presented in Figure B.5 for all tests. As expected, a predominance of the low frequencies was observed for all profiles. Furthermore, some typical turbulent profiles associated with open channel flows were observed for both bores and surges. The high-frequency part of the spectrum followed the $-5/3$ decay law predicted

(a) Dry bed surge	(b) Wet bed bore
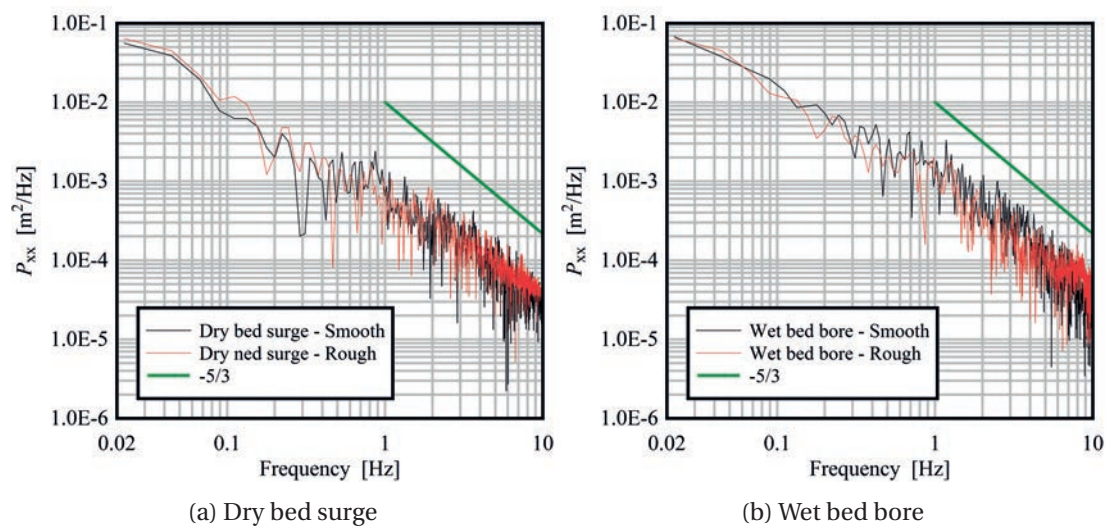
Figure B.5 – Spectral density functions for wave profile raw signals and comparison with Kolmogoroff decay law: (a) dry bed surges, $d_0 = 0.82$ m; (b) wet bed bores, $d_0 = 0.82$ m and $h_0 = 0.05$ m. (acquisition frequency 12.5 Hz, duration of the raw signal around 30s each, Figure B.3)

by the Kolmogoroff (1931) turbulent cascade theory, implying energy transfer from larger scales to lower scales all the way to viscous sub-layer. Although it is not supported by a solid theoretical explanation for bores and limited to the extent of the observed transient signals, is the author's impression that the oscillation of the wave surface can give an insight of the eddy size distribution inside the wave, and therefore on the energy content of the secondary waves. A second analysis was carried out to characterise the surface turbulence, where the oscillations of the secondary waves were isolated using a "*Reynolds-like*" decomposition, in which a time-dependent moving average was subtracted from the original signal:

$$h'(t) = h(t) - h_{\mathrm{m,av}}(t) \tag{B.2}$$

where $h'(t)$ is the fluctuation, $h(t)$ the measured profile and $h_{\mathrm{m.av}}(t)$ the moving average over a period of 3 seconds. This value was selected as it represented the shortest period that allowed to isolate the surface oscillations from the profile while keeping the fluctuating behaviour. The

decomposition and the obtained signals are presented in Figure B.6 for all scenarios. Given their substantial difference, the signal was then divided into two main parts: the **Head** and the **Tail** of the main wave, each portion lasting around 10 seconds. The front was visually characterised by the presence of higher frequencies with a greater amplitude, whereas the tail part was characterised by lower amplitude oscillations with better regularity. Visually, this difference in signal is clearly presented in Figure B.6. To improve the precision of the spectral analysis, several data sets from identical tests were summed up in order to obtain a longer signal for the FFT, hereafter called "*ensemble signal*". All the considered sub-sets had similar values in terms of their average and variance.

(a) Dry bed surge - smooth bed

(b) Wet bed bore - smooth bed

(c) Dry bed surge - rough bed

(d) Wet bed bore - rough bed
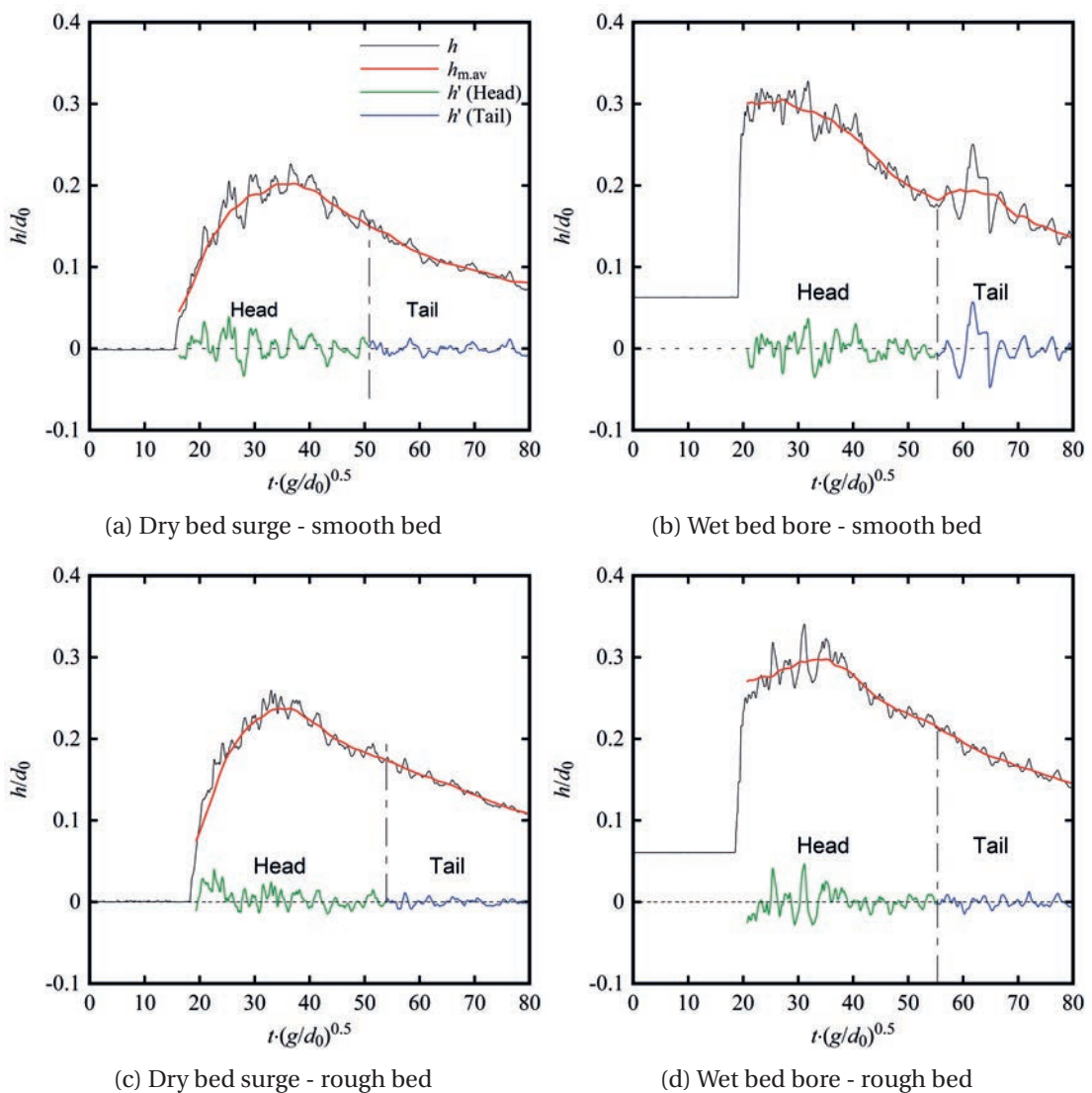
Figure B.6 – "*Reynolds-like*" decomposition of the original profile (h, black line) in moving average ($h_{m.av}$, red line) and fluctuations (h') for a single data-set: in green the values obtained for the head, in blue those for the tail.

169

A Fourier Fast Transform (FFT) was applied to the ensemble signals (head and tail, smooth and rough); the results are presented in Figure B.7 for all configurations. As observed for the raw signal (Figure B.5), the spectra for the ensemble signals for all scenarios and for each part of the wave presented a typical profile similar to the previous ones, including the $-5/3$ slope for the Kolmogorov inertial sub-range (not shown). For this analysis the remaining lower frequencies were not considered, as they represented a residual of the moving average decomposition. For both dry bed surges and wet bed bores the highest density of frequencies were observed for $0.5 < F < 2$ Hz, corresponding to wave periods of 0.5 to 2 seconds. The energy content of frequencies above 2 Hz was small compared to that of the lower frequencies. For all configurations a lower density was observed in the tail part of the signal and overall higher peaks were recorded for waves propagating over smooth bed. For the tail part a dominant frequency is clearly observed for $f = 0.6$ Hz in the rough bed cases, corresponding to a wave period of 1.4 s. If an average velocity of 2.5 m/s is assumed a wavelength of 3.5 m is obtained, which is consistent with visual observations.

Overall, the spectra confirmed the visual observations that the tail part of the signal contained waves with longer periods compared to the head part. Especially in the tail, less smaller-scale turbulence was observed for the rough bed cases. For the head part, a single dominant frequency could not be recognised, however the signal was composed of multiple repeating ones, proving the high level of turbulence in the approaching wave.

	Dry, smooth	Wet, smooth	Dry, rough	Wet, rough
σ^2 [0.5-6 Hz] - Head	0.0031	0.0031	0.0030	0.0045
σ^2 [0.5-6 Hz] - Tail	0.0012	0.0022	0.0010	0.0015

Table B.2 – Variance values for $0.5 < f < 6$ Hz for all tested configurations

The integral of the spectral density (σ) with frequencies between 0.5 and 6 Hz was computed for all configurations; the upper limit was chosen based on the Shannon-Nyquist Theorem. The integral corresponds to a fraction of the signal's variance or, in other words, to the energy associated with the mentioned frequency range; results are presented in Table B.2. It was noted that for all configurations the head part of the wave had a higher energy content associated with frequencies in the interval $0.5 < f < 6$ Hz. For the tail signal, a higher energy content was obtained for the wet configurations, confirming the visual observation of a higher turbulent intensity inside the bore wake for such configurations.

B.4   Front celerity

For engineers designing structures resistant to hydrodynamic loads, it is fundamental to determine the celerity U of the incoming wave. For wet bed bores velocities can be precisely predicted using the theory of Stoker (1957), as discussed in Section 2.3.3. On the contrary, incertitude still exists in the evaluation of the front celerity for dry bed surges (Nistor et al.,

(a) Dry bed surge - smooth bed

(b) Wet bed bore - smooth bed

(c) Dry bed surge - rough bed

(d) Wet bed bore - rough bed
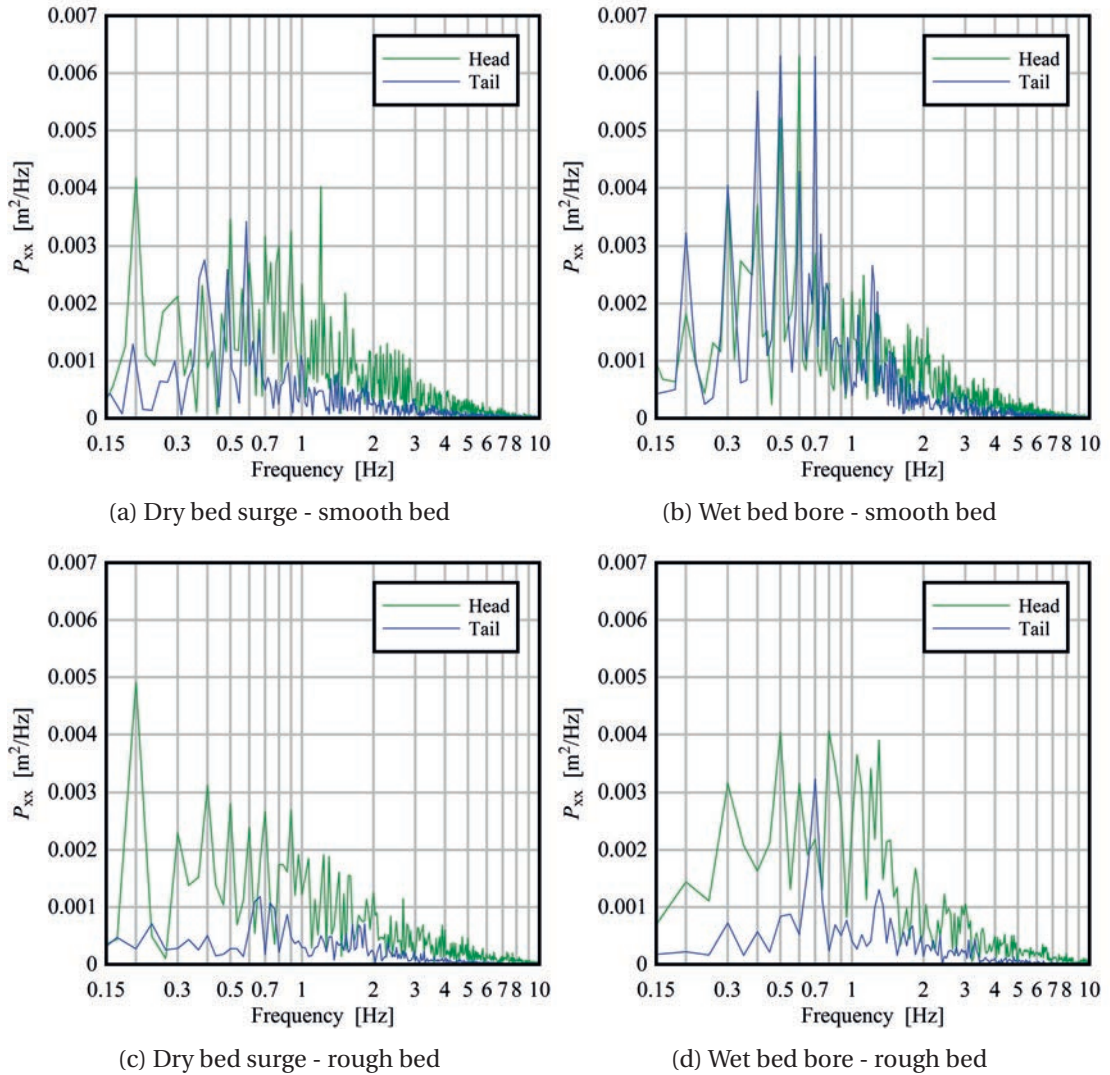
Figure B.7 – Spectra obtained for the ensemble signals of the wave height fluctuations for both parts of the wave (head and tail) for all configurations.

2009) as shown in Chapter 2. For these, it is commonly assumed that:

$$U = \alpha \cdot \sqrt{g \, d_0} \tag{B.3}$$

where U is the wave front celerity, d_0 the impoundment depth if a dam-break wave is considered, and α is a velocity coefficient whose value is covered by high uncertainties. Various values of α can be found in literature and the most relevant ones were presented in Table 2.2. As shown, for the the present study on the smooth channel, the best approximation was found with a coefficient $\alpha = 1.25$ (Figure 4.13). These were also compared to the experimental tests on rough bed. For these, a significant influence of roughness was observed and lower celerity values measured over rough bed, leading to an overestimation of the celerity values up to 25 % for a coefficient $\alpha = 1.25$.

Appendix B. Bed roughness and water surface fluctuations
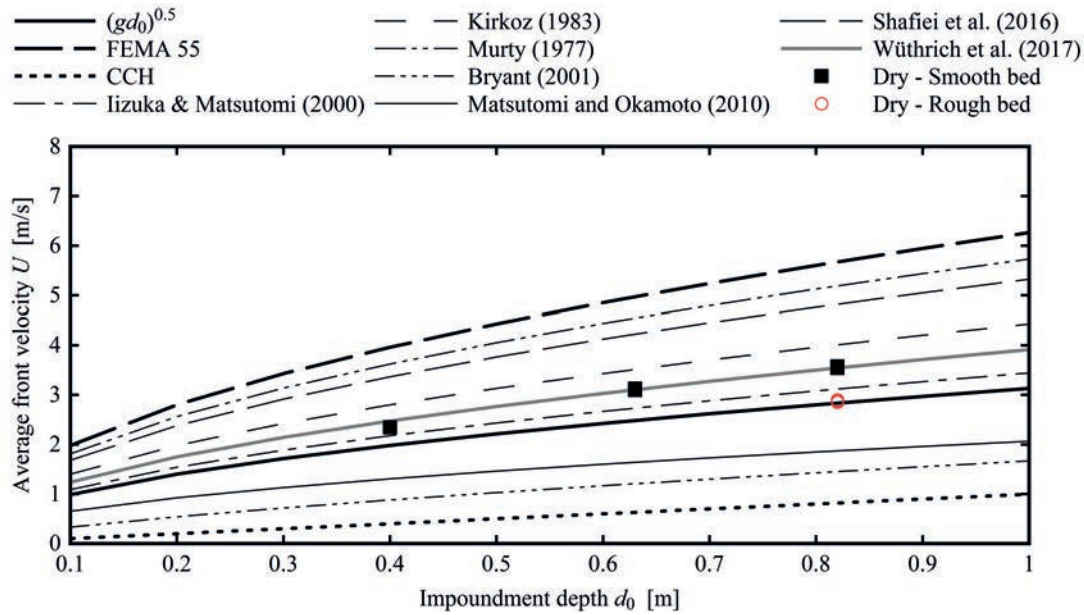
Figure B.8 – Comparison of experimental data with previous existing formulae

These findings clearly indicated a dependence of α on the friction factor f_{DW} that should be taken into account in the prediction of U. For wet bed bores the roughness was shown to have a less significant influence and the same celerity values were recorded for both smooth and rough scenarios. Both behaviours are presented in Figure B.9, in which the values of α were plotted as a function of the friction factor f_{DW}. The decreasing behaviour of α for larger values of f_{DW} confirms its dependence on the bed roughness for dry bed surges.

(a) Dry bed surge

(b) Wet bed bore ($h_0 = 0.05$ m)
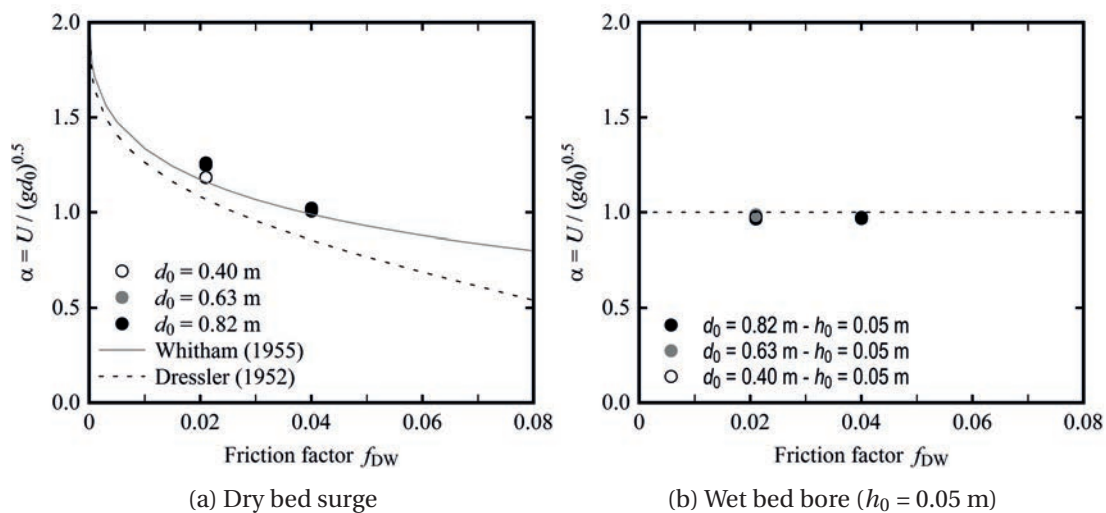
Figure B.9 – Velocity coefficient α as a function of friction factor f_{DW} for both dry bed surges and wet bed bores

The experimental points were also compared to some existing theories found in literature, mainly in Dressler (1952, 1954) and Whitham (1955). Dressler (1952) solved the Saint-Venant equations using a perturbation method assuming a constant friction factor, leading to the Eq. B.4 (readapted by Chanson (2004)).

$$\frac{U}{\sqrt{gd_0}} = \frac{2}{3}\left(1 + \frac{x}{t \cdot \sqrt{gd_0}}\right) + F_1 \cdot \frac{f_{DW}}{8}\sqrt{\frac{g}{d_0}} \cdot t \tag{B.4}$$

where F_1 is a first order correction factor for the flow resistance, whose value is expressed in Eq.B.5.

$$F_1 = -\frac{108}{7\left(2 - \frac{x}{t \cdot \sqrt{gd_0}}\right)^2} + \frac{12}{2 - \frac{x}{t \cdot \sqrt{gd_0}}} - \frac{8}{3} + \frac{8\sqrt{3}}{189} \cdot \left(2 - \frac{x}{t \cdot \sqrt{gd_0}}\right)^{\frac{3}{2}} \tag{B.5}$$

An analogous solution was proposed by Whitham (1955) solving the Saint-Venant equations using an adaptation of the Polhausen Method (Chanson, 2004), leading to Eq.B.6.

$$\frac{U}{\sqrt{gd_0}} = \frac{2}{1 + 2.90724\left[\left(\frac{f_{DW}}{8}\right)\sqrt{\frac{gt^2}{d_0}}\right]^{0.4255}} \tag{B.6}$$

For both theories, on a completely smooth surface ($f_{DW} = 0$), a celerity value equal to the propagation of the forward characteristic in the Ritter (1892) theory can be assumed, implying $\alpha = 2$. An asymptotic behaviour toward this value can be observed in Figure B.9a for $f_{DW} \to 0$ leading to a vertical tangent. For large roughness values ($f_{DW} \to \infty$) zero velocity should be expected, implying $\alpha = 0$, even if this scenario is physically impossible. This represents a limitation for both theories of Whitham (1955) and Dressler (1952, 1954) that are no longer valid for large tip regions, *i.e.* for large roughness values (Chanson, 2004). Figure B.9 showed a relative good match for low friction factors with both theories, however differences become more important for rougher surfaces and Whitham (1955) theory represented the experimental tests better.

B.5   Summary

A better understating of the effect of bed roughness and secondary waves observed behind wet bed bores and dry bed surges was obtained. The investigation of the surface oscillations allowed an insight of the internal turbulent behaviour and the eddy size distribution close to the top of the wave.

As expected, the surge propagating on a rough bed had lower velocities, whereas similar height profiles and velocities were observed for the bores propagating over an initial still water depth, suggesting that the bed roughness had less or almost no influence. All test cases were conducted with a high Reynolds number ($Re \approx 10^7$), implying a highly turbulent flow.

Appendix B. Bed roughness and water surface fluctuations

The regular and less oscillating pattern observed for the rough configurations suggested a higher level of internal smaller-scale turbulence, which was able to more efficiently dissipate larger eddies, whereas in the smooth configuration the residual energy was dissipated with repetitive surface fluctuations. A frequency domain analysis was carried out and through FFT power spectra of the wave height profiles were obtained for all configurations. A Reynolds-like decomposition was applied to the wave height signal, allowing to isolate the fluctuations of the surface turbulence. A difference in the shape of the spectra was observed between the increasing (head) and the decreasing (tail) parts of the wave from the wave profile. The head was characterised by higher frequencies compared to the tail, with larger amplitude. The computation of the integral of the spectrum showed higher energy associated to the tail for frequencies between 0.5 and 6 Hz.

The wave profiles were shown to be in agreement with existing theories in the domain of dam-break waves for both smooth and rough horizontal beds. While no influence of bed roughness was observed for wet bed bores, results clearly showed a dependence of the wave celerity on the friction factor for dry bed surges. For the two tested roughness values, lower celerity were observed for higher roughness, suggesting that friction should be considered when estimating the approaching velocity of a tsunami inland. The experimental points showed good agreement with previous theoretical solutions found in literature.

C Steady-state experiments

C.1 Introduction

Highly unsteady flow motions are potentially harmful for the inundated structures. Past examples showed that, while most buildings collapsed during initial impacts of incoming waves, major damages were also observed during the quasi-steady flow around the buildings. In both Chapters 5 and 7 it was shown that the portion of the total horizontal force observed before the peak is minimal and that the impulse transferred to the structure before the occurrence of the peak force corresponds to 30% for surges and 15% for bores. This means that the impact phase is followed by an important quasi-steady flow motion characterised by longer duration and responsible for more than 60% of the impulse transferred to the structure. For this reason an understanding of the quasi-steady flow condition is important and a more precise estimation of the drag coefficient for both impervious and porous structures is necessary.

The influence of obstacles in an open channel flow is well established and, among others, is worth mentioning the contributions of Nagler (1918), Yarnell (1934), Benjamin (1956) and Raju et al. (1983). According to Qi et al. (2014), the drag coefficient depends on the shape of the obstacle, the blockage ratio (*i.e.* B/W, where B is the building side and W the channel width), the ratio between flow depth and obstacle side (*i.e.* h/B) and the Froude number of the impinging flow (Fr, Eq. C.1). The dependence of C_D on the Reynolds number is commonly assumed to be weak because of the turbulent nature of most open-channel flows, both in the laboratory and in the field. The drag coefficient is typically defined for low Froude numbers (subcritical regimes) with similar upstream and downstream flow depth. Furthermore, most values of the drag coefficient were derived from the loss of momentum flux through flow depths measurements (Henderson, 1966). Qi et al. (2014) conclude that this technique is not suitable for 3-dimensional bodies because of the unsteady behaviour of the wave field.

As mentioned before, for highly subcritical flows, the same flow depths are observed on both the upstream and downstream sides of the obstacle. For increasing Froude numbers, the flow becomes **choked** and a difference in water depth is observed between the two sides, resulting into a non negligible hydrostatic component. In addition, for the choked flow a hydraulic

jump is observed downstream of the structure (Figure C.2a). Field studies have shown Froude numbers Fr ≈ 1 for tsunami flows propagating inland (Fritz et al., 2012). For this reason, in the present study, only the chocked case is considered, with Froude numbers included between 0.81 and 0.87 (Table C.1).

The computation of the drag component under subcritical steady conditions was widely investigated in the past and agreement on a common value of C_D = 2.0 for squared structures is found Blevins (1984). For wave impacts, the laboratory experiments by Arnason (2005) indicated a C_D = 2.0 for a square prism with orientation θ = 0°. This value is also adopted by FEMA (2012). Yeh (2006) noted that most C_D values were appropriate for steady flows conditions, but did not directly applied to tsunamis flows. If a long tsunami period is considered, then the assumption of a quasi-steady conditions can be made and the classical drag force equation (Eq. C.2) applied, provided that an appropriate C_D is chosen. Shafiei et al. (2016) isolated the hydrodynamic force component by subtracting the hydrostatic force component from the total force, leading to a values of C_D = 1.65. Section 5.3.5 suggested to combine both hydrostatic and hydrodynamic component into a Resistance coefficient, whose values C_R = 2.0 was shown to be applicable to unsteady wave impacts for porous structures.

This sections presents preliminary results on the computation of the drag coefficient for buildings with and without openings under laboratory controlled steady-state conditions.

C.2   Experimental set-up and methodology

The same facility described in Chapter 3 is used herein. The key features of the experimental set-up used for the steady-state experiments, as well as the main parameters involved in the process are presented in Figure C.1. All building configurations and porosities presented in
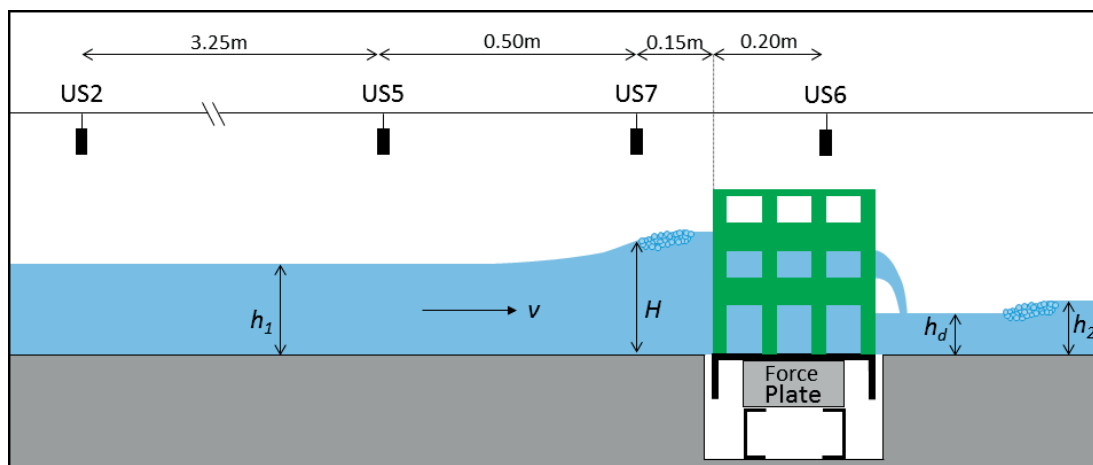
Figure C.1 – Experimental set-up used for the steady-state experiments, showing the position of the US sensors, the installation of the force plate and the definition of the key parameters involved in the study.

Figures 3.18 and 3.16 were also tested under steady-state conditions. The flow was investigated in terms of flow depths, horizontal forces and moments using US sensors and a dynamo-metric Force Plate, as detailed in Section 3.3. The discharged was imposed through the pumps installed in closed-circuit of the laboratory. The flow-meter was verified prior to the tests and its error was below 1%, as shown in Section 3.3.4. Both water depth and forces acting on the structures were acquired with a Labview controlled acquisition system with a frequency of 1 kHz for the force plate and 12.5 Hz for the US sensors. A minimum of 10 discharges for all measurements were performed over a duration of $\Delta t = 60$ seconds, as detailed in Table C.1.

Configuration	Porosity [%]	Discharge [l/s]	Fr_1	Re
All porous sides (0)	0, 17, 31.34, 34, 42.24, 60	23.1 - 170	$\approx 0.44\text{-}0.65$	$1.0\text{-}4.2 \cdot 10^5$
Impervious sides (F)	0, 17, 31.34, 34, 42.24, 60	23.1 - 170	$\approx 0.44\text{-}0.65$	$1.0\text{-}4.2 \cdot 10^5$
Impervious back (B)	0, 17, 34, 42.24, 60	23.1 - 170	$\approx 0.44\text{-}0.65$	$1.0\text{-}4.2 \cdot 10^5$

Table C.1 – Experimental program of tests carried out for the steady-state condition

The Froude number is herein defined as

$$\text{Fr}_1 = \frac{V_1}{\sqrt{gh_1}} = \frac{Q}{h_1 W \cdot \sqrt{gh_1}} \tag{C.1}$$

Some preliminary tests showed that for the smooth, horizontal channel, for all tested discharges, the flow was subcritical (Fr < 1). The presence of the building therefore had an influence on the upstream flow, resulting into modified water depth. Similar conclusions were obtained by Qi et al. (2014).

C.3 Theoretical model

Drag (or hydrodynamic) force is given by the sum of two components: a form drag and a hydrostatic force:

$$F_D = \frac{1}{2} C_D \rho B h V^2 + \frac{1}{2} C_H \rho g B (h_1^2 - h_d^2) \tag{C.2}$$

where C_D and C_H are empirical constants. For low Froude numbers ($Fr_1 \approx Fr_2$), the difference in flow depth between the upstream and downstream section is negligible and the hydrostatic component irrelevant. The drag coefficient C_D is defined for low Froude numbers (Fr $\rightarrow$ 0) and it is a function of the blockage ratio. If C_{D0} is the drag coefficient for an unbounded flow ($B/W \rightarrow 0$), C_D can be defined as:

$$C_D = C_{D0} \left(1 + \frac{C_{D0} B}{2W}\right)^2 \tag{C.3}$$

177

For higher Froude numbers the flow becomes choked and the difference in water depth becomes non negligible ($h_1 >> h_d$) and the drag force can be computed as

$$F_D = \frac{1}{2} C_K \rho B g (h_1^2 - h_2^2) \tag{C.4}$$

where C_K is an empirical coefficient $C_K \approx 1$. Qi et al. (2014) introduced a consistent model to describe the traditional behaviour by using a semi-empirical form of the drag force taking into account both form and hydrostatic component:

$$F_D = \lambda_F \cdot \rho B g^{1/3} V_1^{4/3} h_1^{4/3} \tag{C.5}$$

where λ_F is a function of the blockage ratio B/W and the upstream Froude number Fr_1.

$$\lambda_F = \frac{1}{2} C_D \text{Fr}_1^{2/3} + \frac{1}{2} C_H \left(\frac{1}{\text{Fr}_1^{4/3}} - \frac{1}{\text{Fr}_d^{4/3}} \right) \tag{C.6}$$

Qi et al. (2014) concluded that, even in choked regime, the majority of the drag is originated from form drag, whose intensity is weakly affected by the blockage ration B/W. The hydrostatic component becomes important only for high blockage ratios.

C.4   Visual observations

Previous experimental studies showed that a for highly subcritical flows, the upstream and downstream Froude numbers were similar ($\text{Fr}_1 \approx \text{Fr}_2$). When the upstream Froude number Fr_1 approaches a critical value Fr_{1c}, then the downstream Froude numbers increases drastically (Qi et al., 2014). The water depth around the sides of the building decreases and a hydraulic jump is generated just downstream, as shown in Figure C.2a. This sets the beginning of a choked regime.

The effect of the presence of the impervious structure on the flow can clearly be observed Figure C.2a. Some disturbances in the form of small surface oscillations are observed on the upstream side of the building, following the streamline around the structure. The water depth drastically reduced along the impervious lateral sides of the structure as the flow accelerates, resulting into the formation of a *V-shaped* hydraulic jump. On the downstream side, some low water depths are observed and the formation of the typical Von Kármán vortexes is somehow disturbed by the presence of the hydraulic jump.

The presence of openings establishes a seepage flow through the building, resulting into a modification of the flow dynamic around the structure, as shown in Figure C.2d. Similarly to the impervious scenario, some disturbances are observed on the upstream side, resulting into circular streamlines. Major differences attributed to the openings can be observed in the downstream side, where higher water levels are constantly observed. Because of the interaction between the discharge coming out of the building and the flow around the structure, a

(a) Fr$_1 \approx 0.44$, $P_{tot} = 0$ %

(b) Fr$_1 \approx 0.48$, $P_{tot} = 17$ %

(c) All porous sides ($P_{tot} = 17$ %)

(d) Impervious side walls ($P_{tot} = 17$ %)
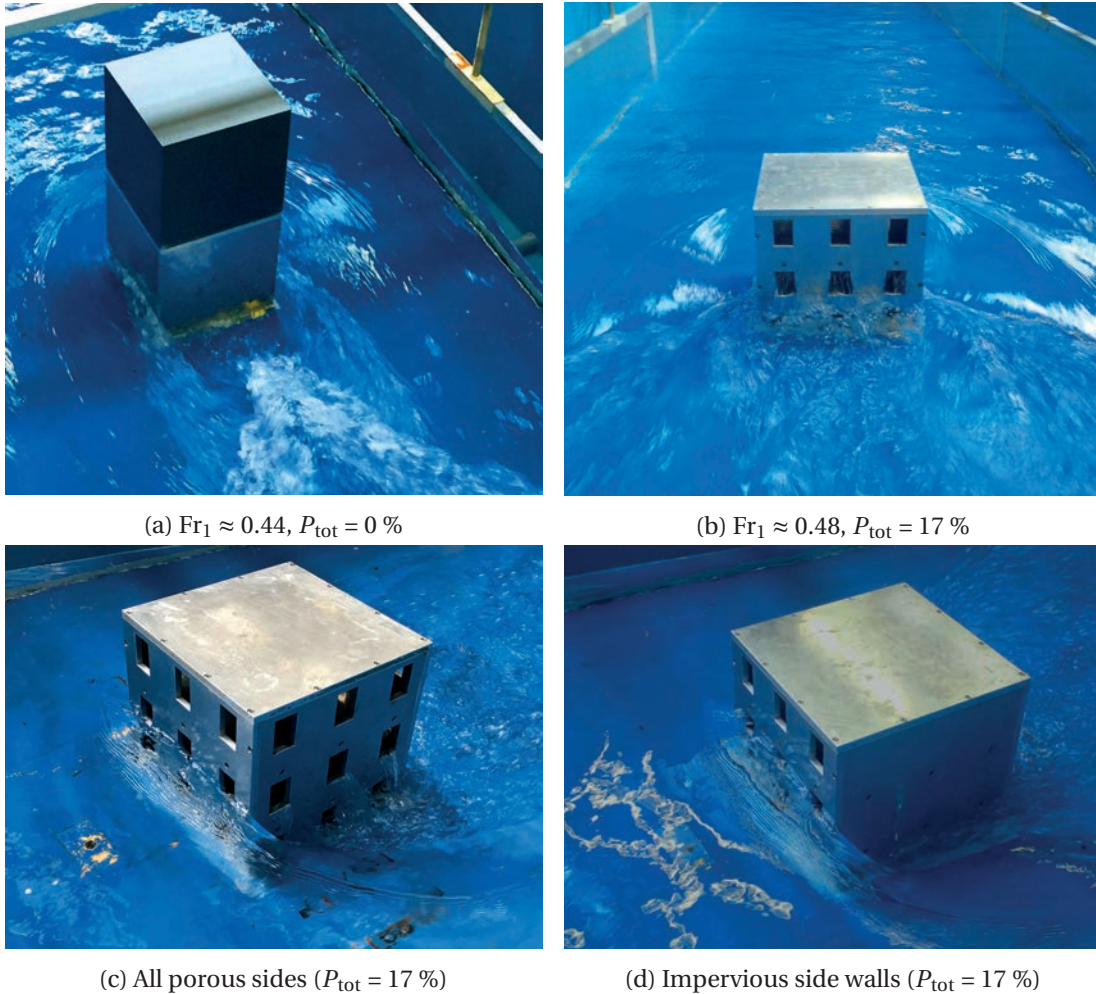
Figure C.2 – Visual observations for the steady-state flow around: (a) impervious, reference, building; (b) configurations with openings. The influence of the openings on the sides is shown in (c) for an all impervious structure and in (d) for the configuration with impervious side walls.

high level of turbulence with intense surface fluctuations are observed on the downstream side (Figure C.2d). Because of this interaction, a fully developed hydraulic jump is not observed and the formation of Von Kármán vortexes is disturbed.

The presence of openings on the side walls was shown to have an influence on the dynamics around the structure, as shown in Figures C.2c and C.2d. For the configuration with openings on the front and back sides and impervious side walls (configuration F), the water level on both lateral sides of the building decreases drastically, installing a flow behaving similarly to the fully impervious, reference structure (Figure C.2a) also observed by Qi et al. (2014). On the contrary, for the buildings with openings on all four sides (configuration 0) the continuous water exchange through the walls resulted into higher water levels and into a visually more intense turbulent flow.

C.5 Results

The average values of the horizontal force $\overline{F_x}$ and moment $\overline{M_y}$ were computed using Eq. C.7

$$\overline{F_x} = \frac{1}{\Delta t} \int_0^{\Delta t} F_x \mathrm{d}t \qquad\qquad \overline{M_y} = \frac{1}{\Delta t} \int_0^{\Delta t} M_y \mathrm{d}t \qquad\qquad\qquad (C.7)$$

For the experimental set-up presented in Section C.2, a blockage ratio $B/W = 0.2$ is considered, implying that the contribution of the hydrostatic fraction in the total drag force is less relevant compared to the drag form. For this, its contribution is included in a *Resistance Coefficient* C_R, defined in Eq. C.8. A similar approach was previously presented by Arnason et al. (2009), Wüthrich (2017) and Wüthrich et al. (2018a).

$$C_R = \frac{2\overline{F_x}}{\rho B h_1 V_1^2} \qquad\qquad\qquad (C.8)$$

where $\overline{F_x}$ is the average horizontal force (Eq. C.7), B the channel width, h_1 the flow depth and V_1 the flow velocity upstream of the structure. The velocity V was computed through the continuity equation as $V = Q/(hW)$.

C.5.1 Impervious buildings

The experimental points of the resistance coefficient C_R obtained from the present study are presented as a function of the upstream Froude number Fr_1 in Figure C.3. For similar blockage ratios ($B/W \approx 0.2$), a good agreement was observed with the experimental points of Qi et al. (2014). Values of $C_R \approx 5$ were observed herein for all tested discharges. Although these values are higher than those suggested by most the design codes and Blevins (1984) for highly subcritical flows, these are in agreement with those obtained by Qi et al. (2014) for similar obstacles subject to choked flow (Figure C.3). These values obtained for the impervious building are then used as a reference in the comparison with the buildings with openings (Wüthrich et al. (2018c)).

The AMTI Force Plate on which the buildings were installed provided measurements of both forces and moments in time. Thus an estimation of the application point of the resulting horizontal force F_x, *i.e.* the cantilever arm L_z can be obtained as:

$$L_z = \frac{\overline{F_x}}{\overline{M_y}} \qquad\qquad\qquad (C.9)$$

The experimental points showed an excellent agreement at $L_z = 0.5 \cdot h_1$, confirming the hypothesis of a rectangular repartition of the pressures on the upstream side of the building.
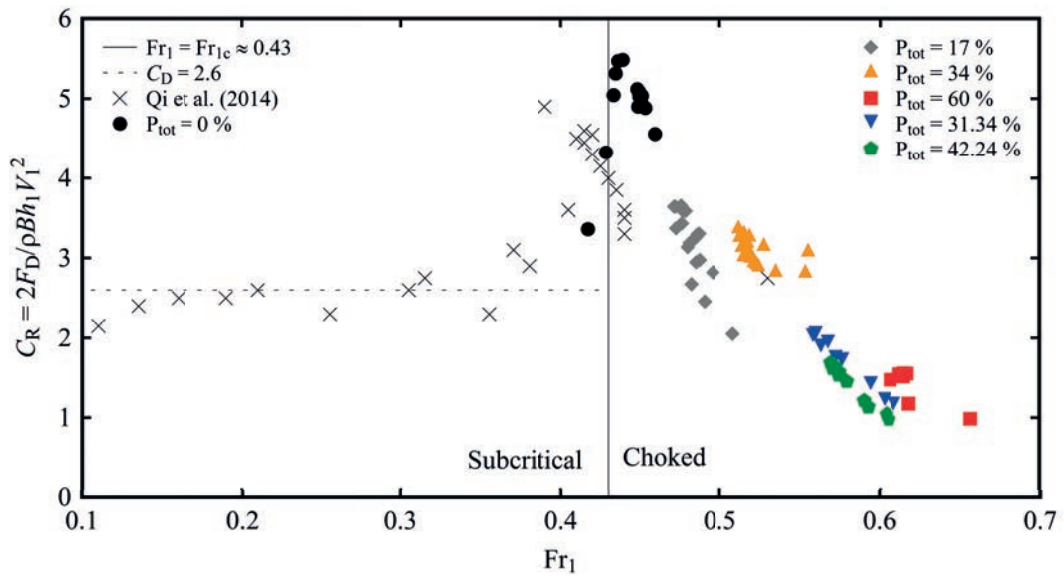
Figure C.3 – Values of the resistance coefficient C_R as a function of the upstream Froude number Fr_1 for buildings with and without openings. These were also compared with the experimental points of Qi et al. (2014).
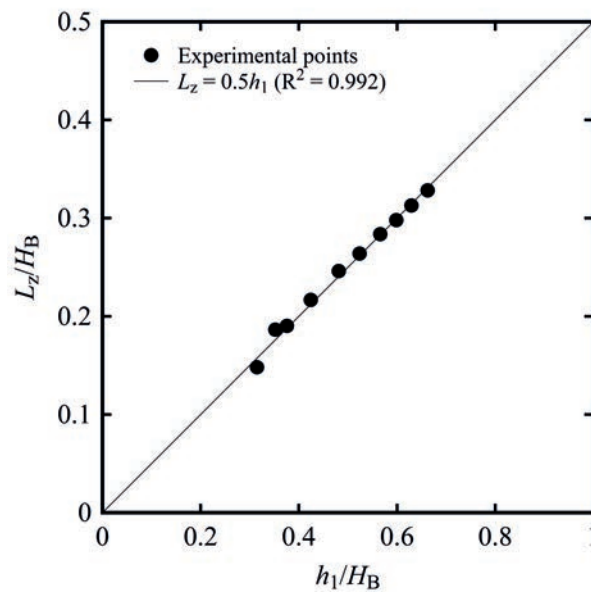
Figure C.4 – Values of the cantilever arm L_z compared to upstream flow depth h_1

C.5.2   Buildings with openings

For buildings with openings the seepage discharge through the building changed the dynamic of the flow, reducing the difference in water depth between the upstream and the downstream sides. This limited the importance of the hydrostatic component in Eq. C.2. Furthermore,

because of the turbulent nature of the flow downstream of the structure, a precise identification of the water level h_d is not possible and the definition of a global resistance coefficient C_R, including both drag and hydrostatic components, seems an appropriate approach.

Figure C.3 shows higher values of the critical Froude number (Fr_{1c}) for the configurations with openings. This is probably a consequence of the lower blockage ratio B/W resulting from the openings inside the building. In addition, the same figure also shows a reduction of the resistance coefficient C_R as a result of the openings on the building. This reduction is quantified a function of porosity in Figure C.5. For this, similarly to Section 7.3.1, the porosity value $P_{h,max}$ was identified at a building height $h = h_1$.
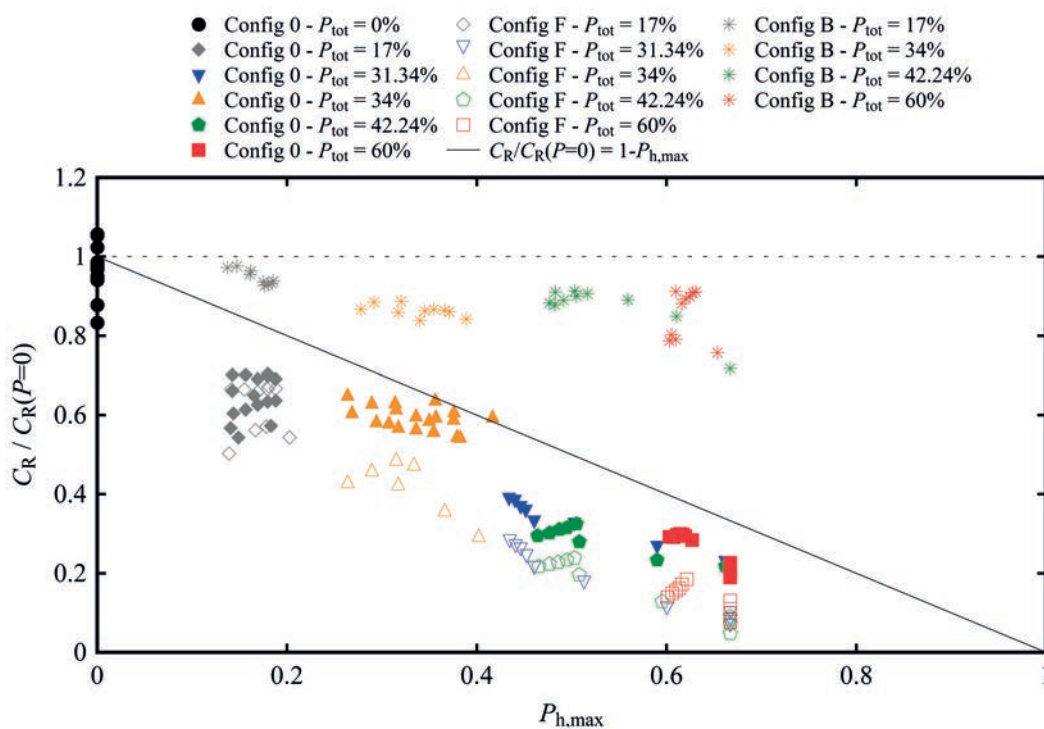
Figure C.5 – Values of the Resitance coefficient C_R as a function of porosity for the configuration 0 (all porous sides), configuration F (Impervious lateral walls) and configuration B (Impervious back side)

For the unsteady, initially supercritical, impact of bores and surges against porous structures, the resistance coefficient was shown to have a linear behaviour as a function of porosity. The same approach is presented in Figure C.5, where an overestimation of the measured values can be observed for all tested configurations. This suggested that the linear approximation is acceptable for unsteady, supercritical flows, however its applicability to the steady-state condition remains questionable.

Some configurations with openings on the front and back sides and impervious sides walls were also tested (Figure 3.18b). Visual observations presented in Section C.4 showed lesser interaction between the incoming flow and the seepage discharge, resulting into a more *linear*

behaviour (Wüthrich et al., 2018b). As a result, lower forces were constantly recorded for all tested discharges and porosity values, as shown in Figure C.5. In addition, the absence of openings on the side walls, and therefore surfaces on which the hydrodynamic force might be applied to, is partially responsible for this reduction in total force. The influence of openings on the side walls was shown not to have an influence on the resulting maximum force under unsteady flow conditions (Section 7.3.2). Nevertheless, this influence becomes non-negligible in the steady-state condition, where the reduction represents some 30% of total value.

Similarly to the results obtained for the unsteady flows in Section 7.3.3, tests under steady-state conditions revealed in Figure C.5 that the absence of openings on the back side of buildings reproduces the same loading conditions as the reference, impervious configuration.

C.6 Conclusions

Past tsunami events showed that most infrastructure collapsed during the impact phase of the incoming wave. Nevertheless, major damages were also observed during the post-peak quasi-steady flow conditions. This portion was shown in the previous sections to be responsible for more than 50-60% of the total impulse transferred to the structure (Section 5.4.3 and 7.4.3). In this section the effect of building openings on the resulting hydrodynamic force is experimentally addressed. For this, the same installation described in Chapter 3 was used and flow investigated in terms of flow depths, forces and moments acting on the buildings. Given the nature of tsunami waves propagating inland only choked subcritical flows (Fr > 0.45) were investigated herein. For impervious structures, this resulted into an important difference in flow depth between the upstream and the downstream sides. The experimental values of the drag coefficient ($C_D \approx 5.0$) obtained herein were in agreement with previous studies for similar geometries. It was also shown that the total horizontal force was applied at a height equal to 50% of the flow depth, confirming the hypothesis of a rectangular repartition of the pressures on the upstream side of the building. In case of openings, as a result of the seepage flow through the building, this difference in water level, and therefore the hydrostatic component, became negligible. Given the difficulty in isolating the hydrostatic and the drag forces, for the present study a global resistance coefficient C_R taking into account both components was chosen, in agreement with similar previous studies for unsteady flow conditions. Results showed a reduction of the resistance coefficient as a function of building porosity, however this was not linear, as previously shown for unsteady flows. Furthermore, the configuration with impervious sides (F) showed lower forces by some 30% due to the lack of water exchange through these walls, whereas the building with impervious back had similar load conditions to the impervious, reference scenario.

D Testsheets: wave hydrodynamics

This research characterised in terms of their hydrodynamic behaviour, dry beds surges and wet bed bores produced with the vertical release technique. A number of standard waves on both dry and wet bed was identified, whose the technical details are presented in Table D.1. The testsheets for all these tests are presented in the following pages.

Note:

- h_2 is the plateau height, obtained with Eq. 2.16 for wet bed bores.
- χ is the wet be bore coefficient, obtained with Eq. 5.4.
- M is the momentum flux per unit width, defined as $M = h \cdot V_m^2$.
- Fr is the Froude number, defined as $\text{Fr} = V_m / \sqrt{gh}$.

Test	Name	h_0 [m]	N. Pipes	d_0 [m]	Repetitions	Ref.
1	WD1	0	1	0.40	3	page 186
2	WD2	0	2	0.63	4	page 187
3	WD3	0	3	0.82	11	page 188
4	WDH	0.001	3	0.82	1	page 189
5	WW1-1P	0.01	1	0.40	3	page 190
6	WW1-2P	0.01	2	0.63	3	page 191
7	WW1-3P	0.01	3	0.82	5	page 192
8	WW3-1P	0.03	1	0.40	3	page 193
9	WW3-2P	0.03	2	0.63	3	page 194
10	WW3-3P	0.03	3	0.82	5	page 195
11	WW5-1P	0.05	1	0.40	3	page 196
12	WW5-2P	0.05	2	0.63	3	page 197
13	WW5-3P	0.05	3	0.82	7	page 198
14	WW10-3P	0.10	3	0.82	1	page 199

Table D.1 – Experimental program for the tests conducted on the waves without the buildings

WAVE PARAMETERS

Wave type		Dry bed surge	
Name		WD1	
Repetitions		3	
Impoundment depth	d_0	0.40	[m]
Initial still water depth	h_0	-	[m]
Maximum wave height	h_{max}	0.132	[m]
Plateau height	h_2	-	[m]
Front celerity	U	2.347	[m/s]
Maximum momentum flux	M_{max}	0.294	[m³/s²]
	χ	1	[-]
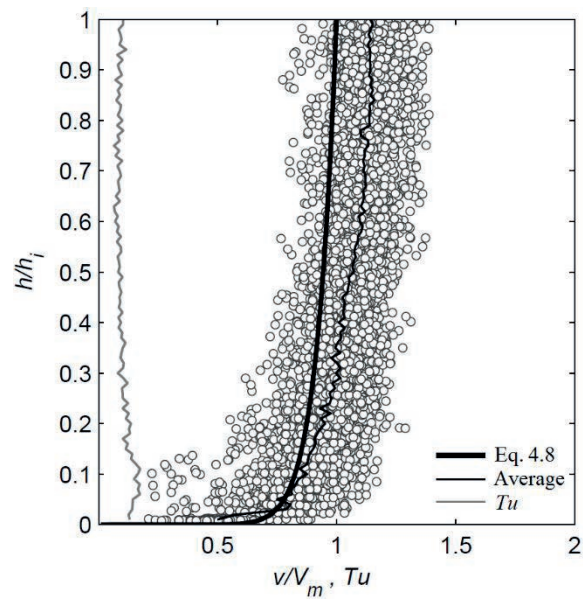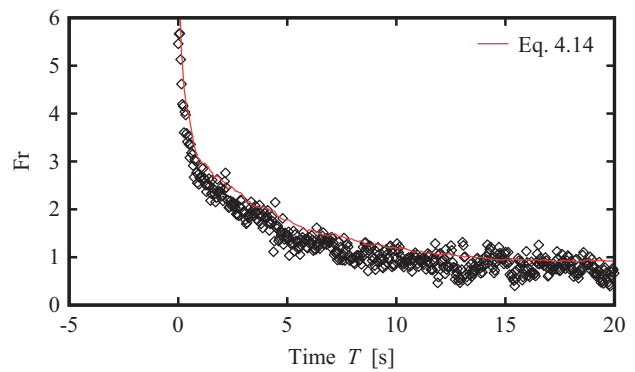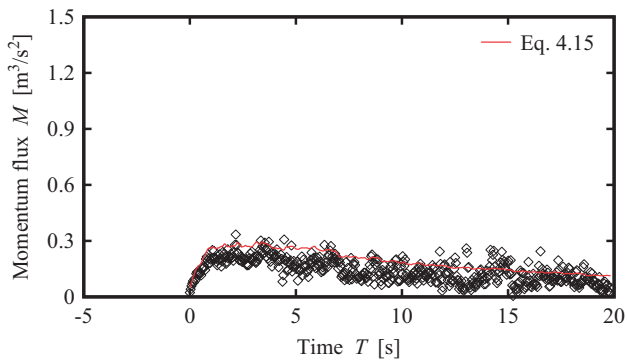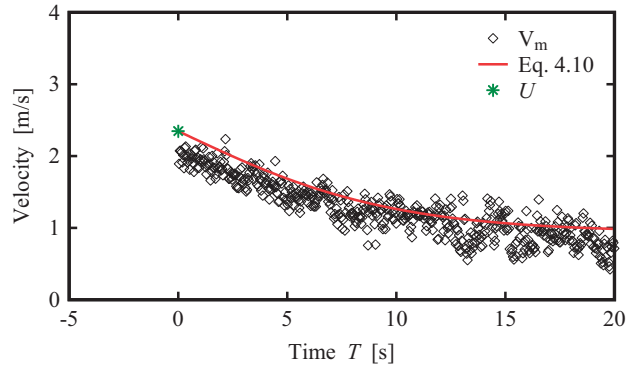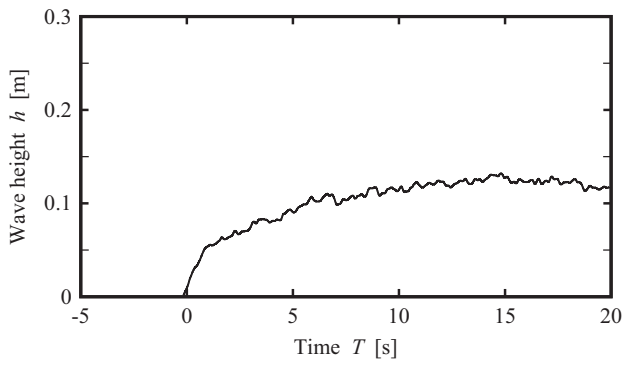
WAVE PARAMETERS

Wave type		Dry bed surge	
Name		WD2	
Repetitions		4	
Impoundment depth	d_0	0.63	[m]
Initial still water depth	h_0	-	[m]
Maximum wave height	h_{max}	0.162	[m]
Plateau height	h_2	-	[m]
Front celerity	U	3.114	[m/s]
Maximum momentum flux	M_{max}	0.708	[m³/s²]
	χ	1	[-]
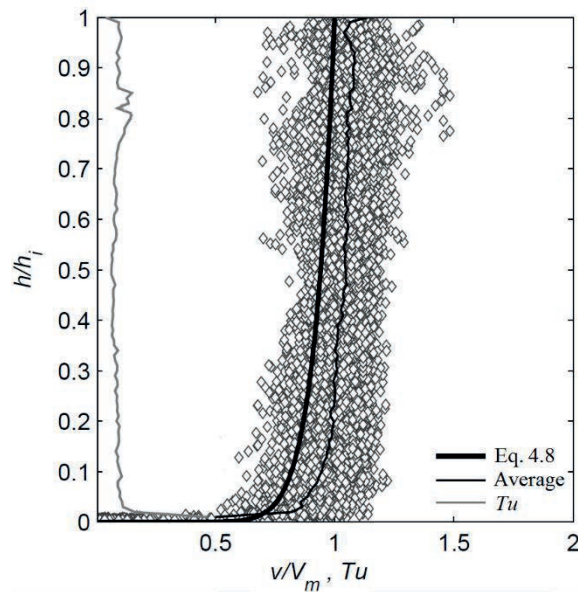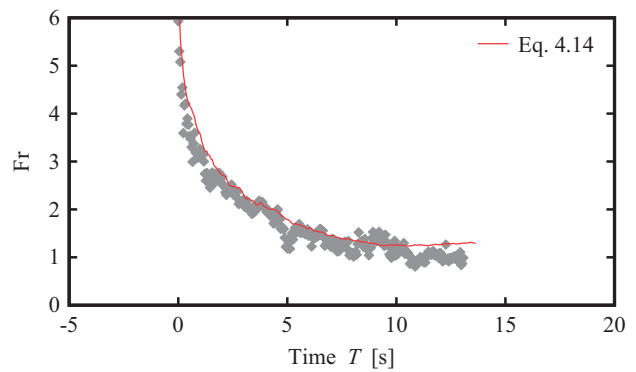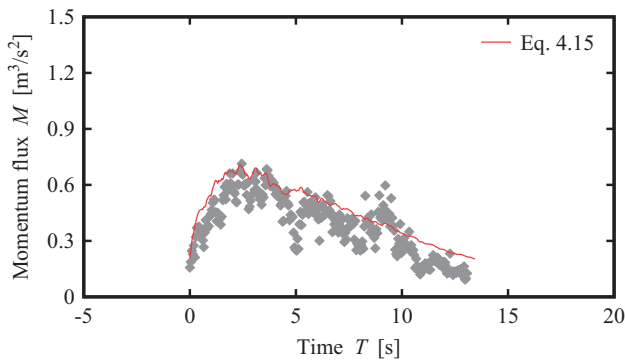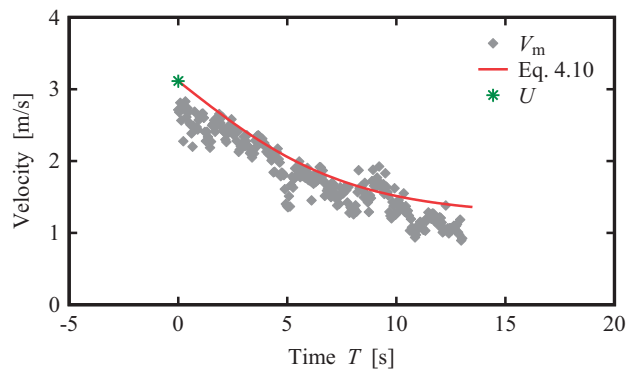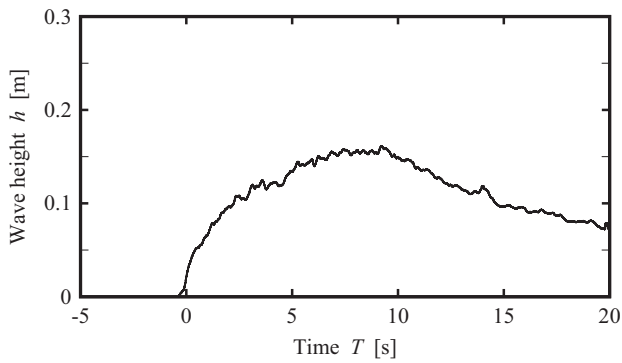
WAVE PARAMETERS

Wave type		Dry bed surge	
Name		WD3	
Repetitions		11	
Impoundment depth	d_0	0.82	[m]
Initial still water depth	h_0	-	[m]
Maximum wave height	h_{max}	0.181	[m]
Plateau height	h_2	-	[m]
Front celerity	U	3.556	[m/s]
Maximum momentum flux	M_{max}	1.218	[m³/s²]
	χ	1	[-]
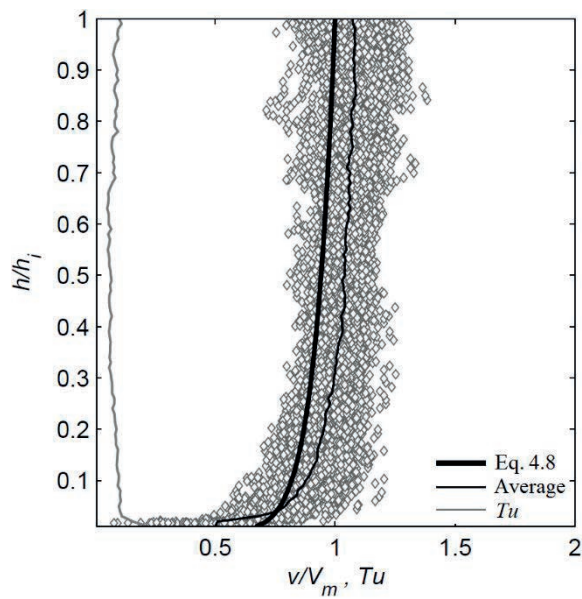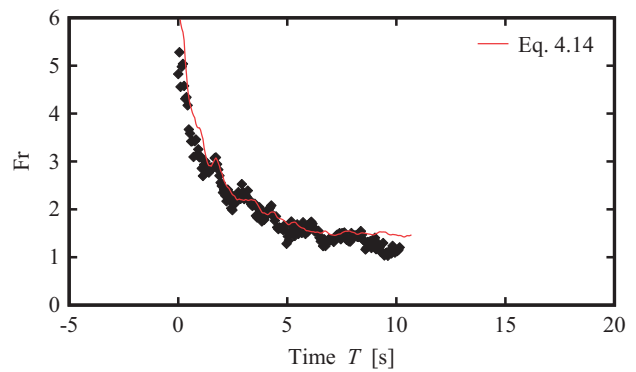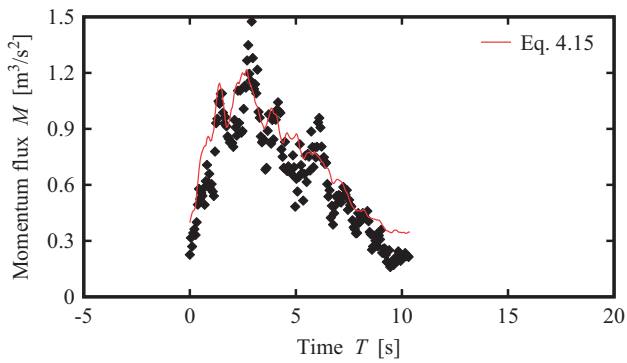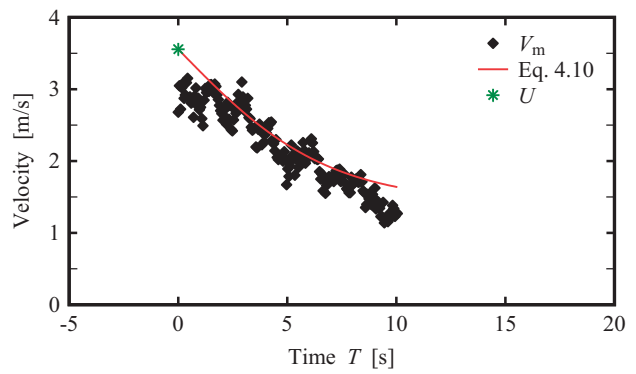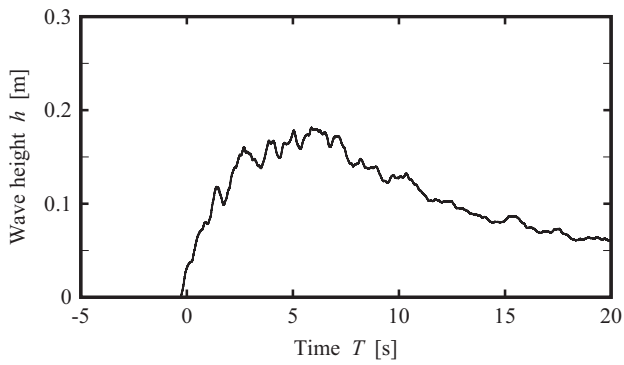
WAVE PARAMETERS

Wave type		Dry bed surge	
Name		WDH	
Repetitions		1	
Impoundment depth	d_0	0.82	[m]
Initial still water depth	h_0	~ 0.001	[m]
Maximum wave height	h_{max}	0.184	[m]
Plateau height	h_2	-	[m]
Front celerity	U	3.417	[m/s]
Maximum momentum flux	M_{max}	1.172	[m³/s²]
	χ	1	[-]
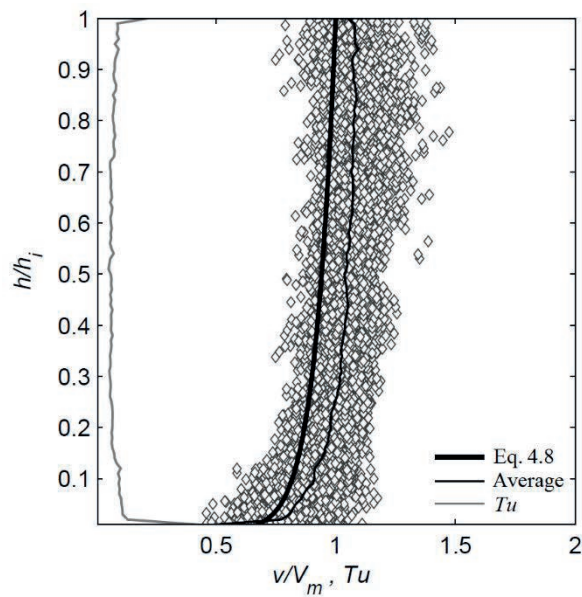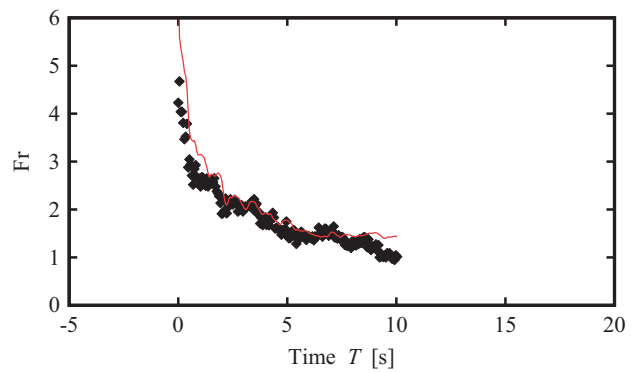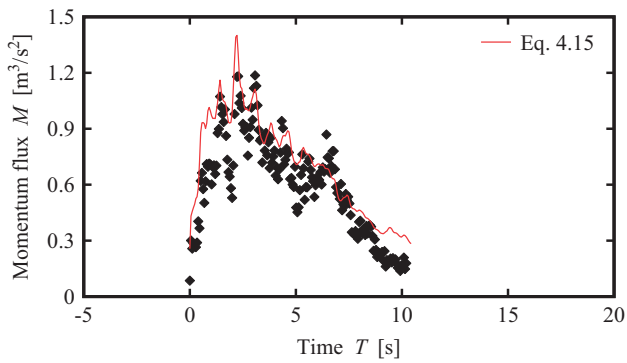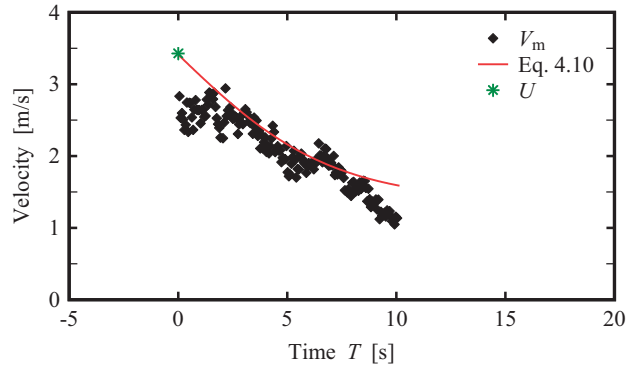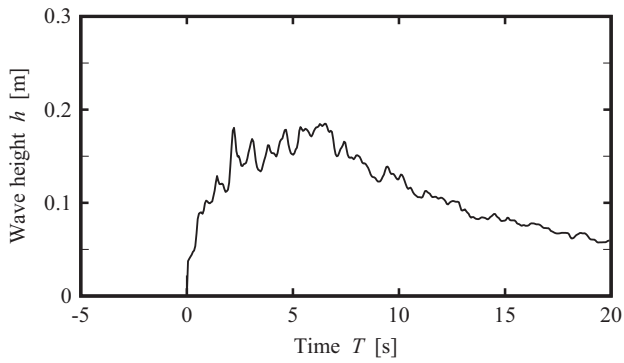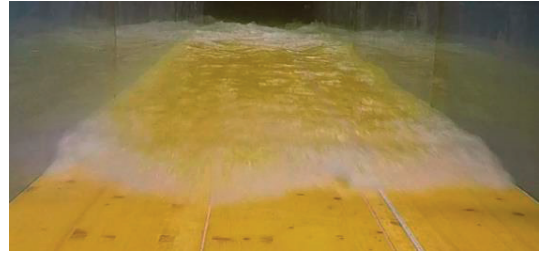
WAVE PARAMETERS

Wave type		Wet Bed Bore	
Name		WW1_1P	
Repetitions		3	
Impoundment depth	d_0	0.400	[m]
Initial still water depth	h_0	0.010	[m]
Maximum wave height	h_{max}	0.135	[m]
Plateau height	h_2	0.094	[m]
Front celerity	U	2.104	[m/s]
Maximum momentum flux	M_{max}	0.366	[m³/s²]
	χ	0.895	[-]
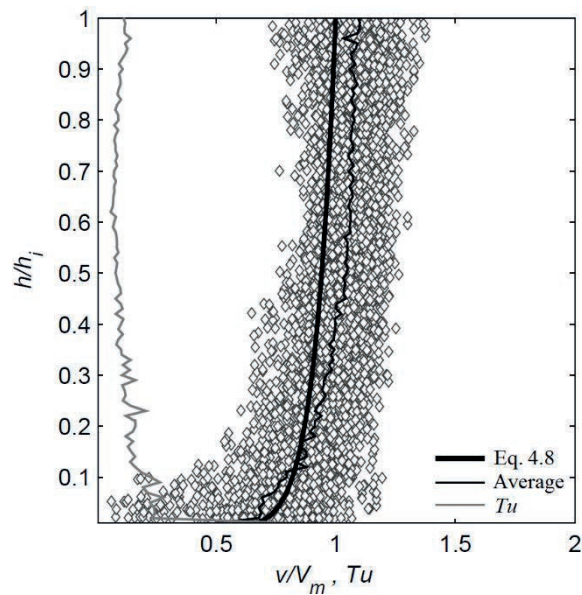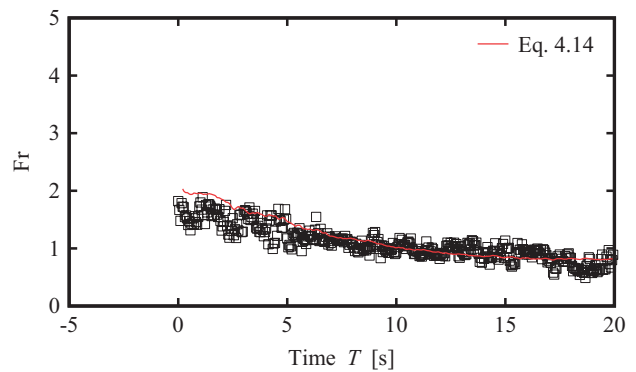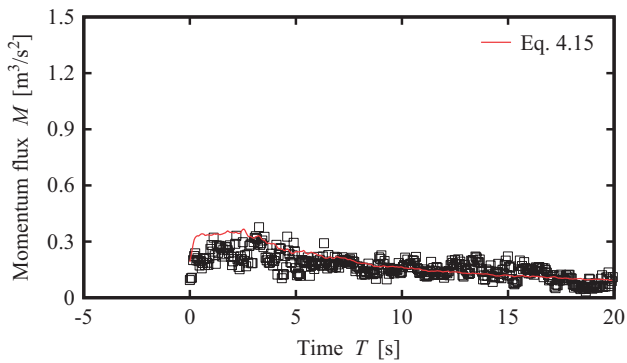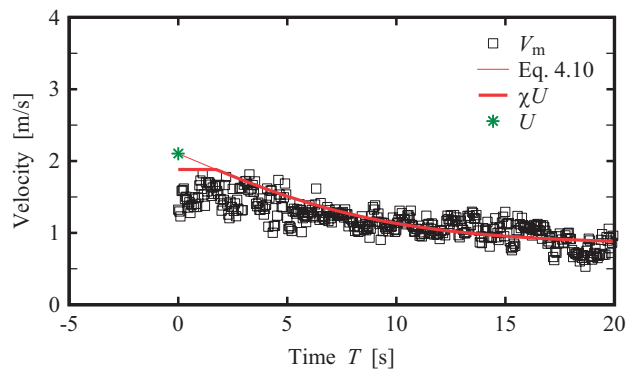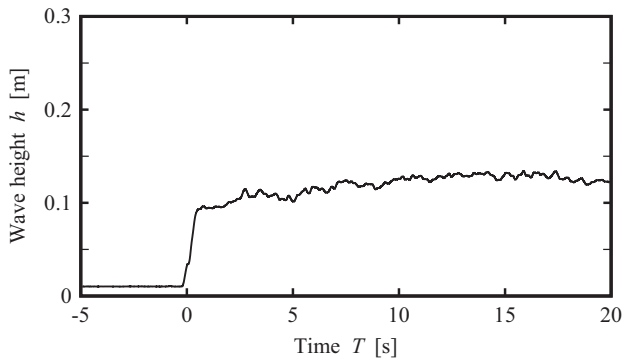
WAVE PARAMETERS

Wave type		Wet Bed Bore	
Name		WW1_2P	
Repetitions		3	
Impoundment depth	d_0	0.630	[m]
Initial still water depth	h_0	0.010	[m]
Maximum wave height	h_{max}	0.167	[m]
Plateau height	h_2	0.125	[m]
Front celerity	U	2.702	[m/s]
Maximum momentum flux	M_{max}	0.774	[m³/s²]
	χ	0.918	[-]
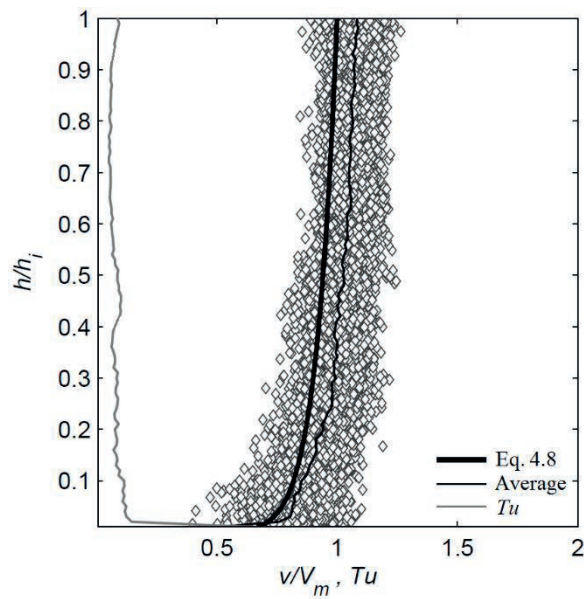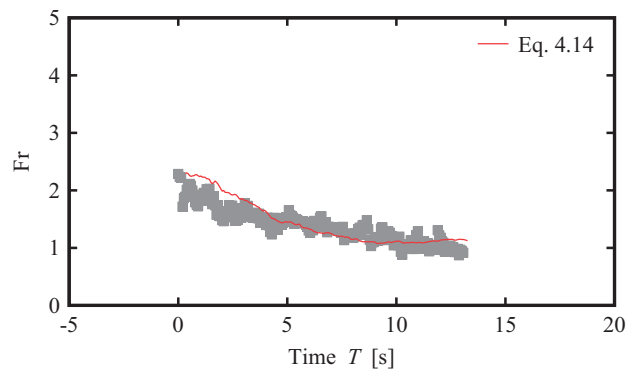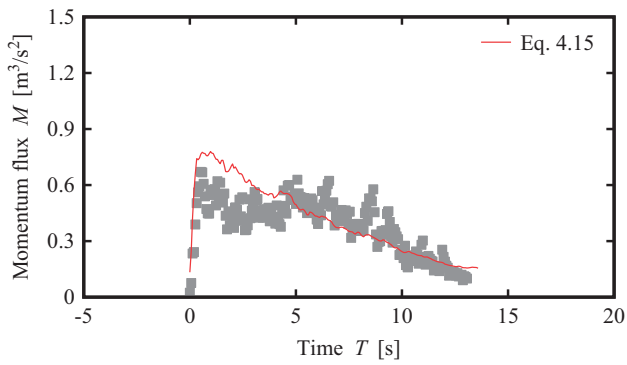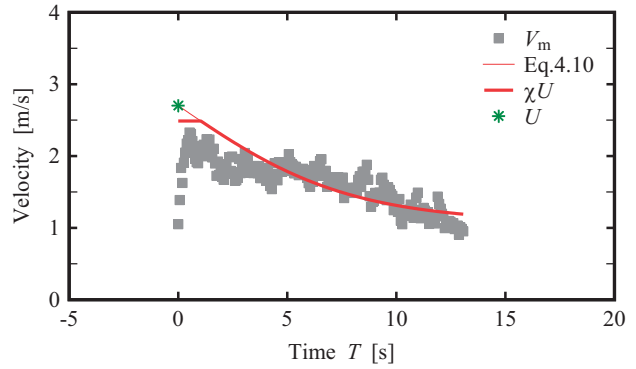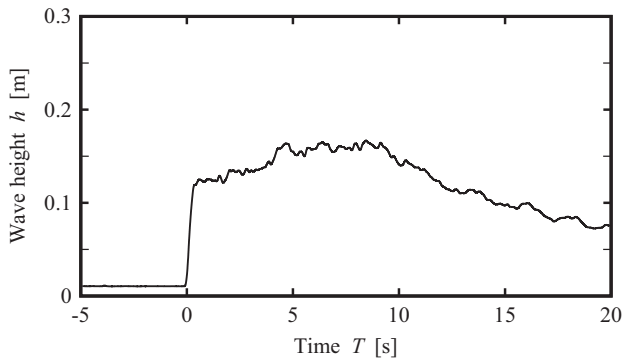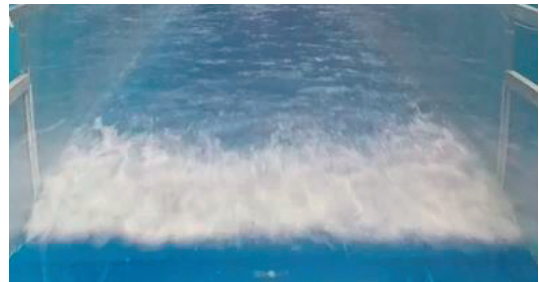
WAVE PARAMETERS

Wave type		Wet Bed Bore	
Name		WW1_3P	
Repetitions		5	
Impoundment depth	d_0	0.820	[m]
Initial still water depth	h_0	0.010	[m]
Maximum wave height	h_{max}	0.190	[m]
Plateau height	h_2	0.149	[m]
Front celerity	U	3.074	[m/s]
Maximum momentum flux	M_{max}	1.175	[m³/s²]
	χ	0.933	[-]
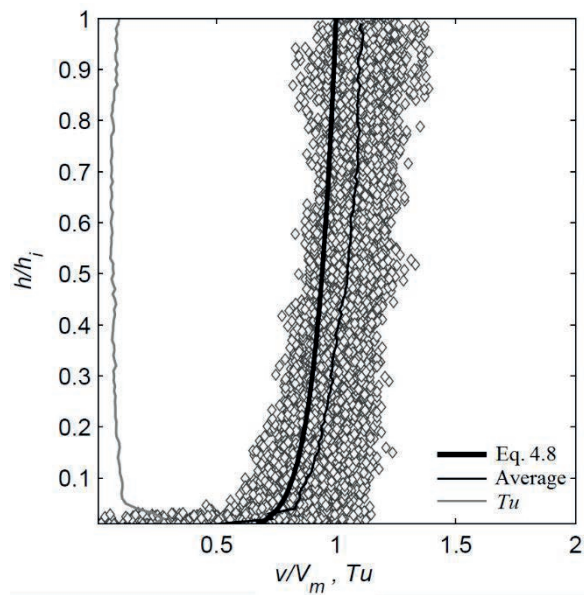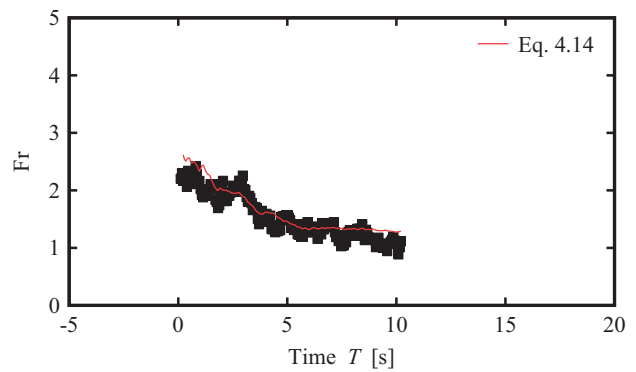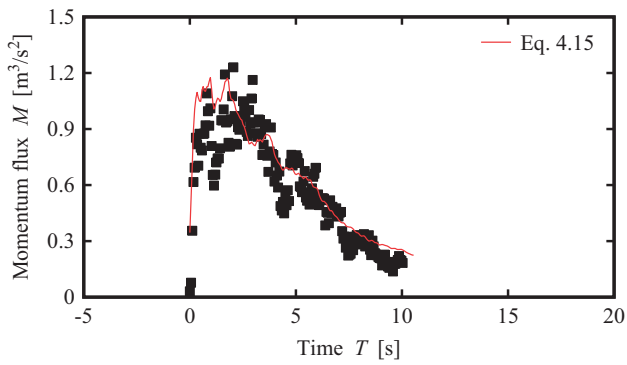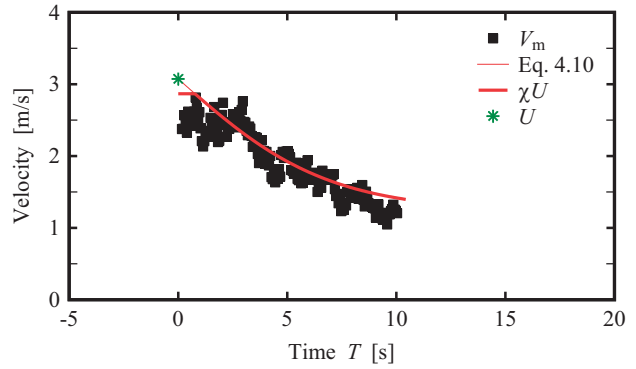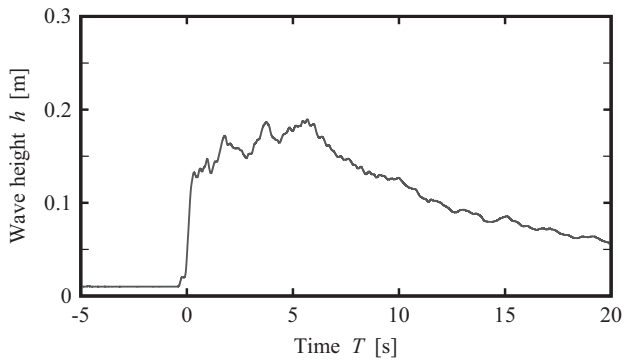
WAVE PARAMETERS

Wave type		Wet Bed Bore	
Name		WW3_1P	
Repetitions		3	
Impoundment depth	d_0	0.400	[m]
Initial still water depth	h_0	0.030	[m]
Maximum wave height	h_{max}	0.158	[m]
Plateau height	h_2	0.212	[m]
Front celerity	U	1.971	[m/s]
Maximum momentum flux	M_{max}	0.351	[m³/s²]
	χ	0.790	[-]
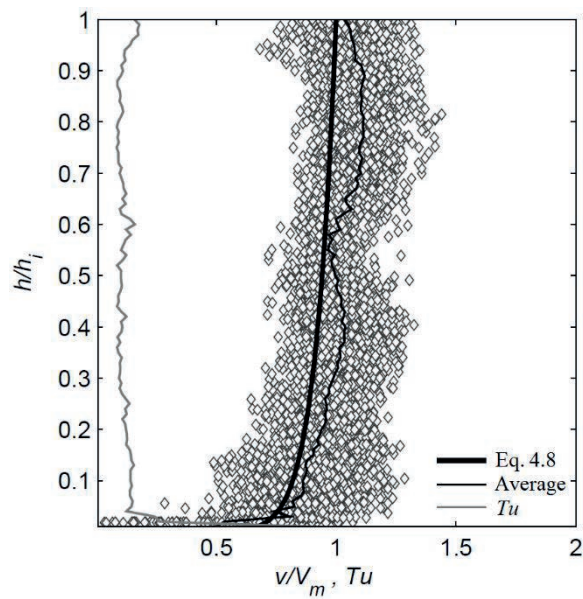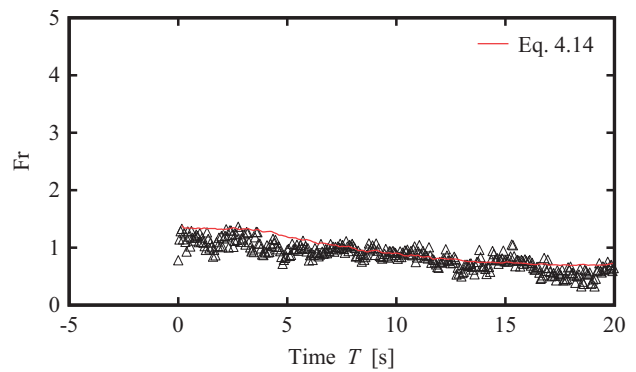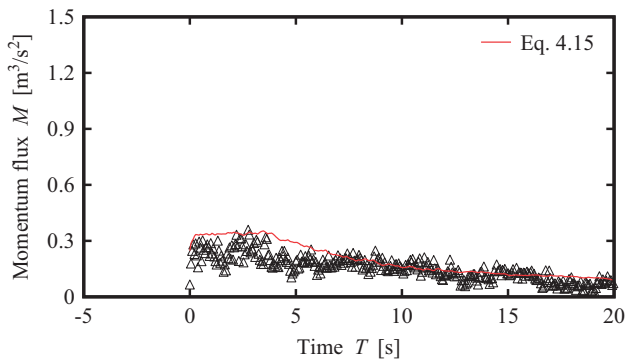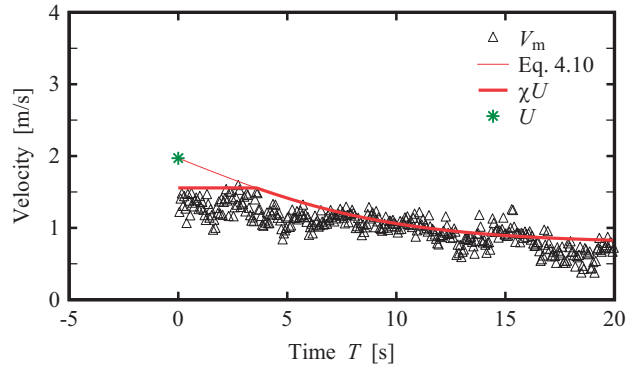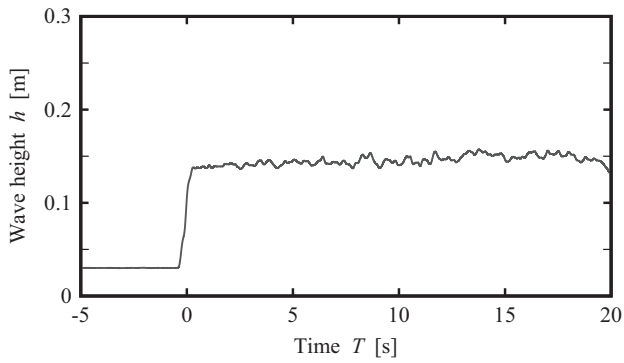
WAVE PARAMETERS

Wave type		Wet Bed Bore	
Name		WW3_2P	
Repetitions		4	
Impoundment depth	d_0	0.630	[m]
Initial still water depth	h_0	0.030	[m]
Maximum wave height	h_{max}	0.200	[m]
Plateau height	h_2	0.189	[m]
Front celerity	U	2.518	[m/s]
Maximum momentum flux	M_{max}	0.834	[m³/s²]
	χ	0.842	[-]
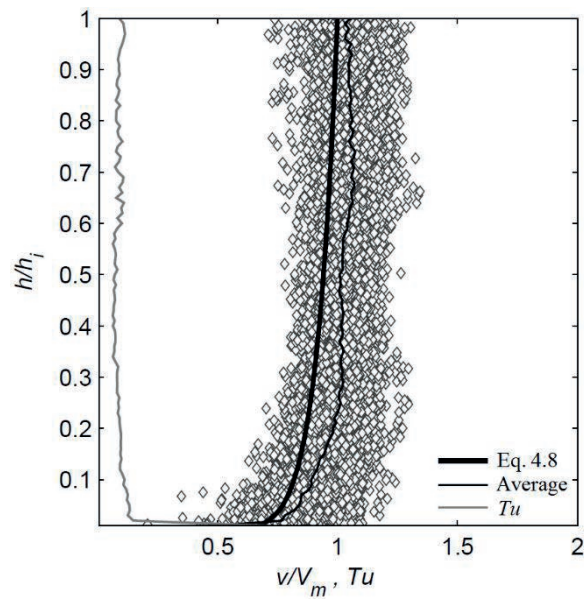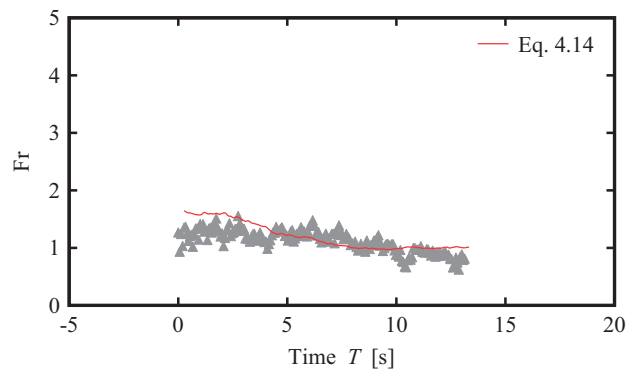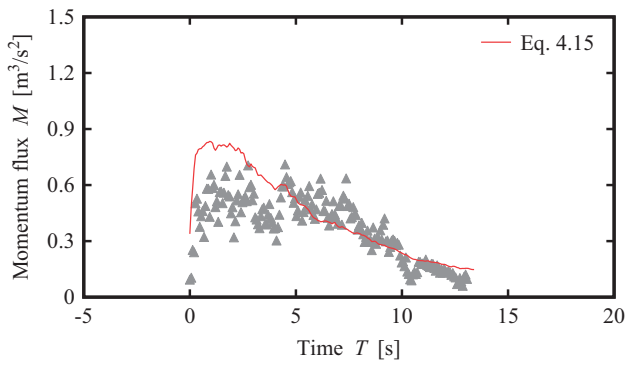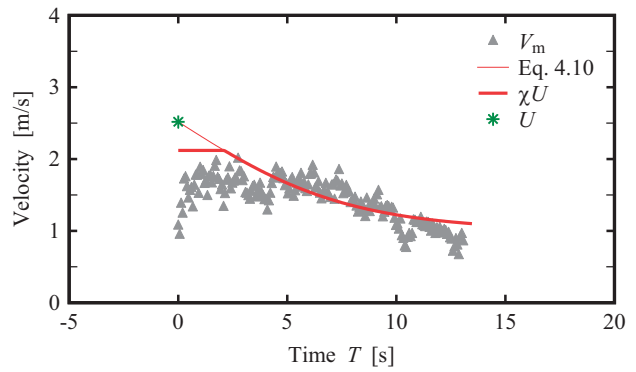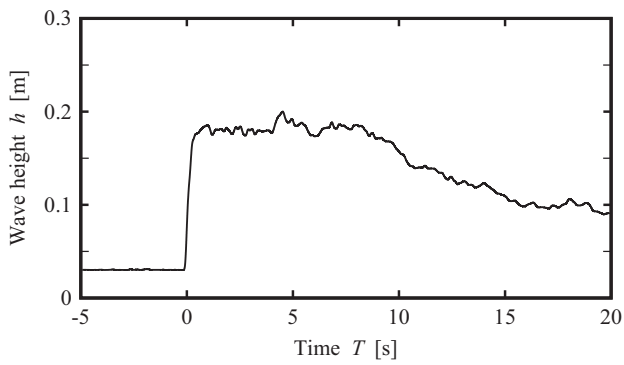
WAVE PARAMETERS

Wave type		Wet Bed Bore	
Name		WW3_3P	
Repetitions		6	
Impoundment depth	d_0	0.820	[m]
Initial still water depth	h_0	0.030	[m]
Maximum wave height	h_{max}	0.231	[m]
Plateau height	h_2	0.222	[m]
Front celerity	U	2.810	[m/s]
Maximum momentum flux	M_{max}	1.312	[m³/s²]
	χ	0.866	[-]
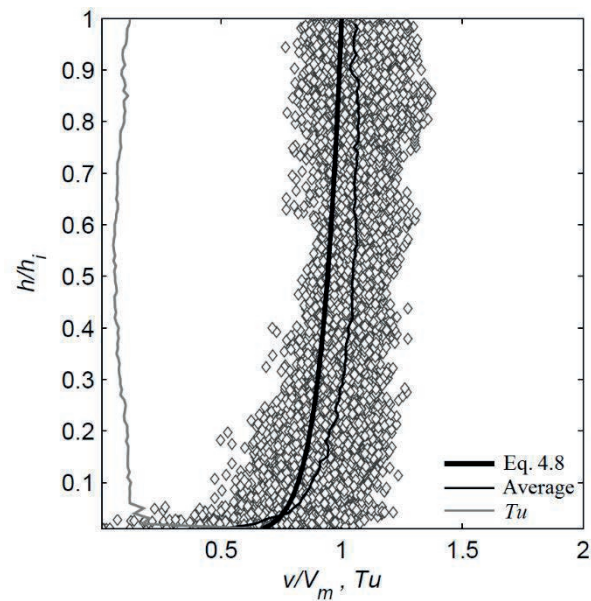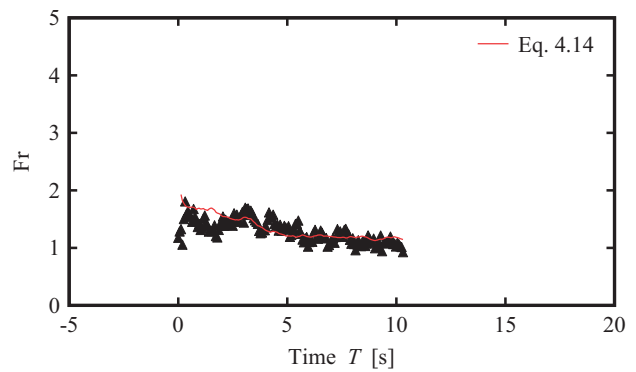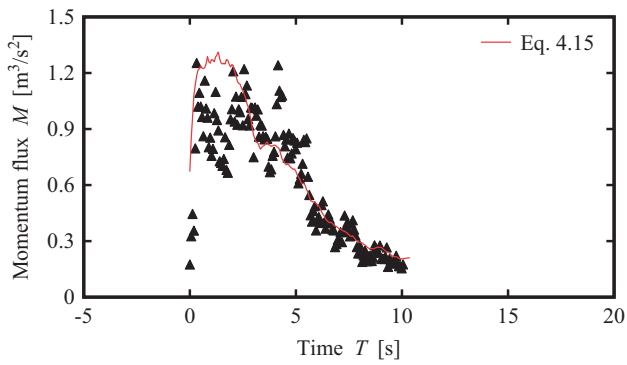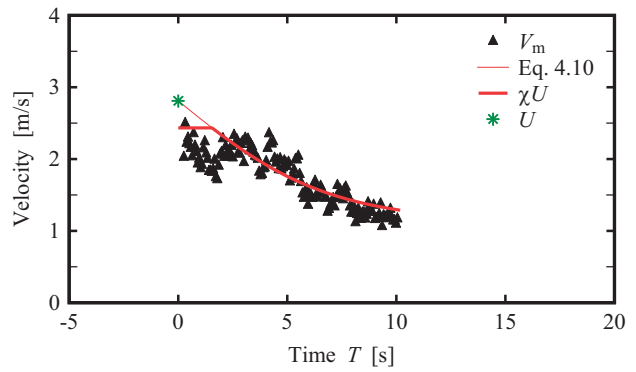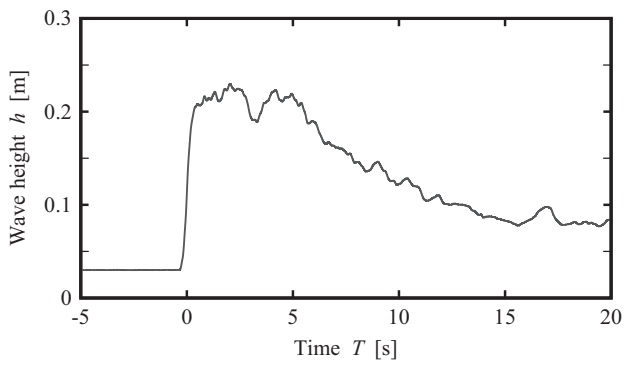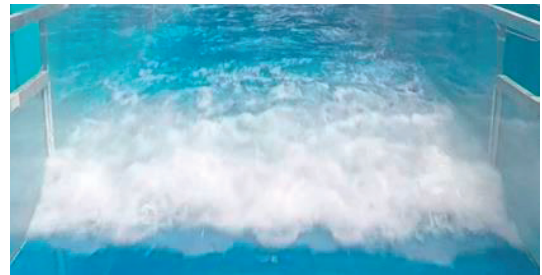
WAVE PARAMETERS

Wave type		Wet Bed Bore	
Name		WW5_1P	
Repetitions		3	
Impoundment depth	d_0	0.400	[m]
Initial still water depth	h_0	0.050	[m]
Maximum wave height	h_{max}	0.177	[m]
Plateau height	h_2	0.172	[m]
Front celerity	U	1.933	[m/s]
Maximum momentum flux	M_{max}	0.332	[m³/s²]
	χ	0.710	[-]
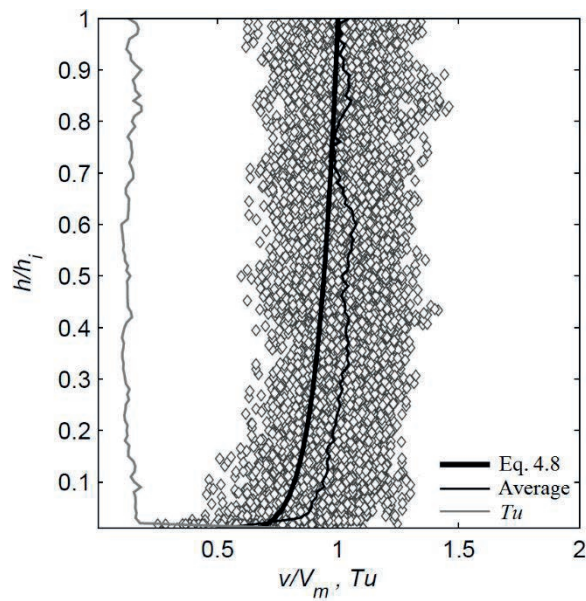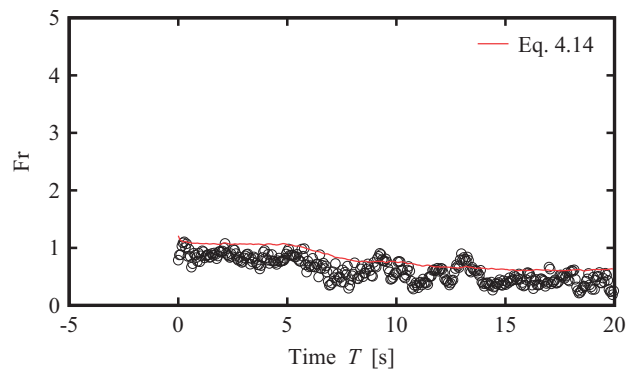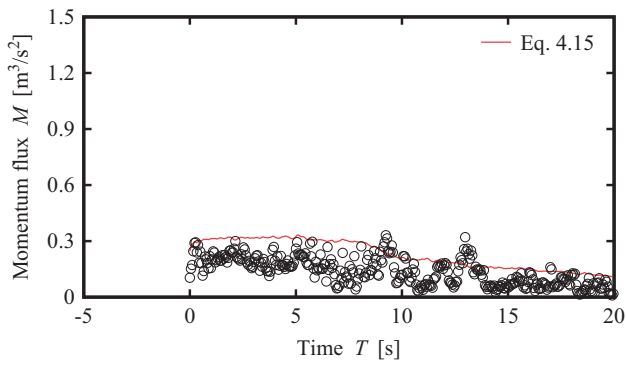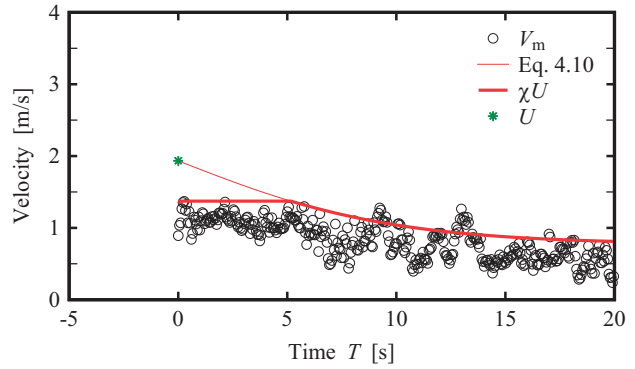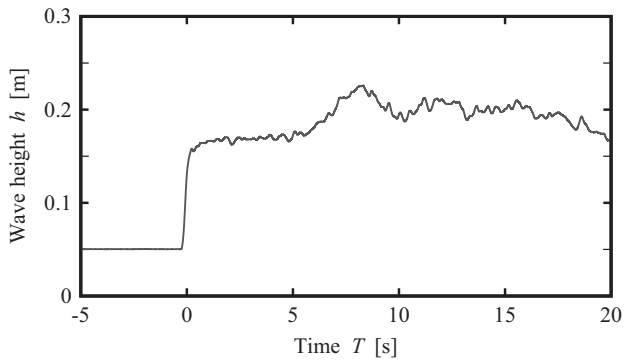
WAVE PARAMETERS

Wave type		Wet Bed Bore	
Name		WW5_2P	
Repetitions		3	
Impoundment depth	d_0	0.630	[m]
Initial still water depth	h_0	0.050	[m]
Maximum wave height	h_{max}	0.224	[m]
Plateau height	h_2	0.230	[m]
Front celerity	U	2.437	[m/s]
Maximum momentum flux	M_{max}	0.810	[m³/s²]
	χ	0.782	[-]
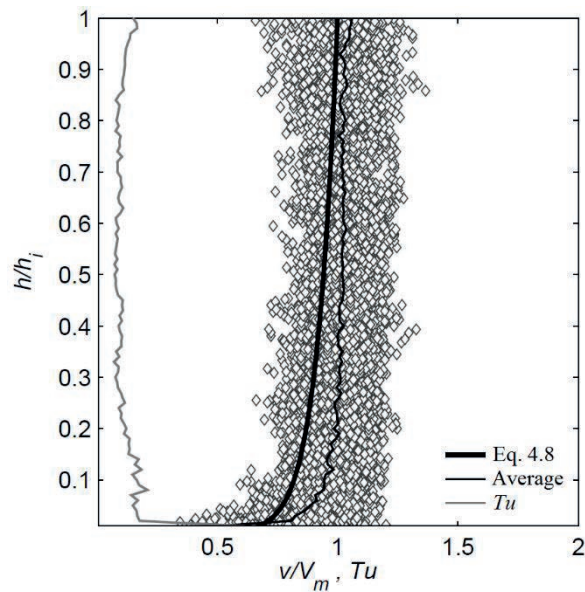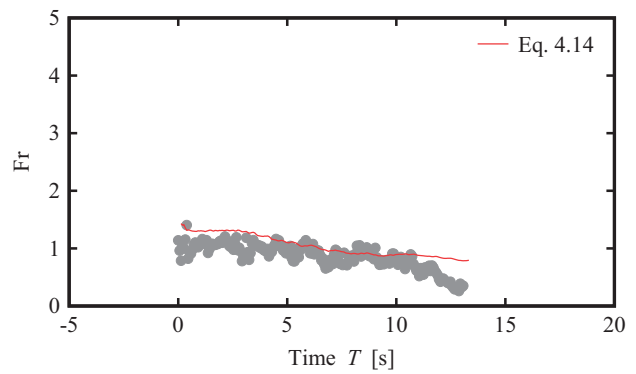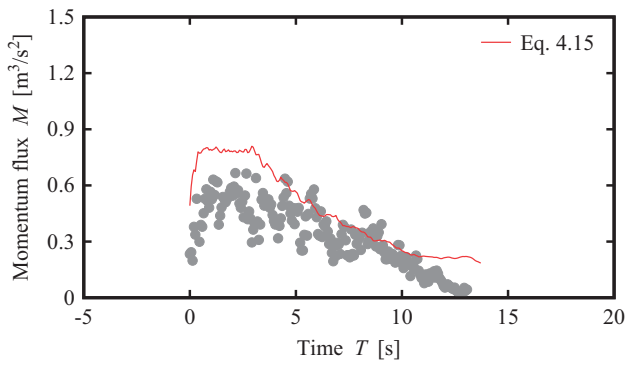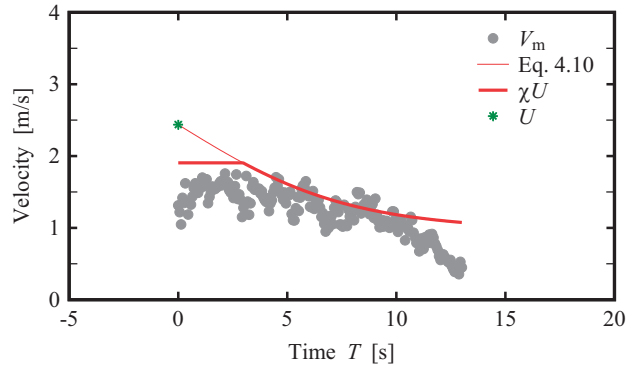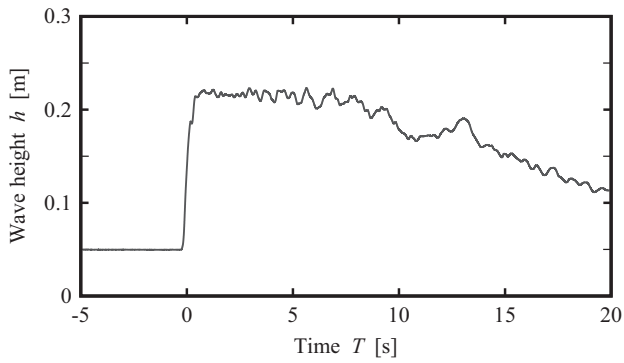
WAVE PARAMETERS

Wave type		Wet Bed Bore	
Name		WW5_3P	
Repetitions		3	
Impoundment depth	d_0	0.820	[m]
Initial still water depth	h_0	0.050	[m]
Maximum wave height	h_{max}	0.259	[m]
Plateau height	h_2	0.271	[m]
Front celerity	U	2.755	[m/s]
Maximum momentum flux	M_{max}	1.295	[m³/s²]
	χ	0.815	[-]
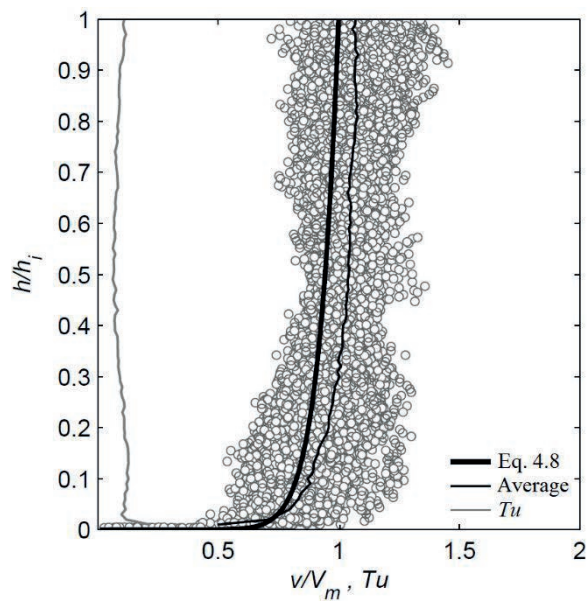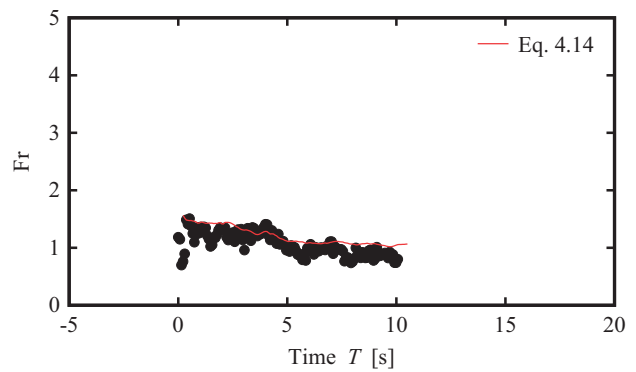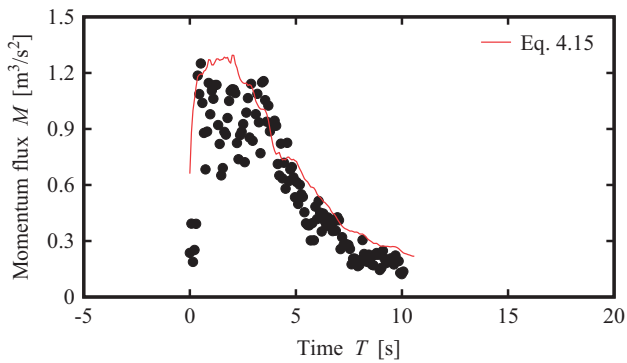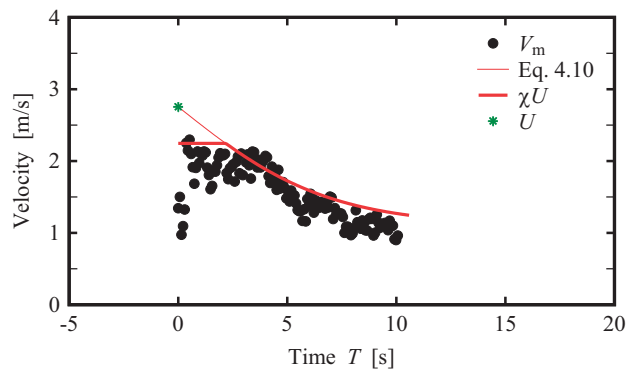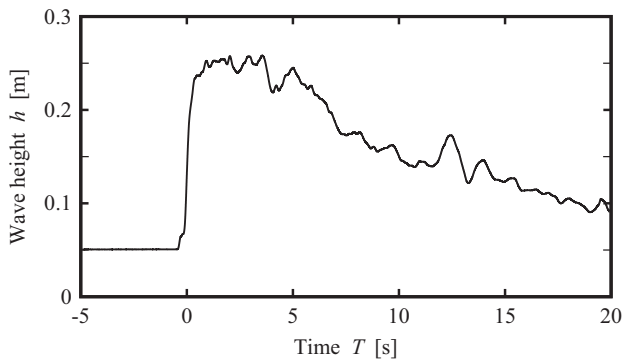
WAVE PARAMETERS

Wave type		Wet Bed Bore	
Name		WW10_3P	
Repetitions		1	
Impoundment depth	d_0	0.820	[m]
Initial still water depth	h_0	0.100	[m]
Maximum wave height	h_{max}	0.349	[m]
Plateau height	h_2	0.350	[m]
Front celerity	U	2.661	[m/s]
Maximum momentum flux	M_{max}	1.241	[m^3/s^2]
	χ	0.751	[-]
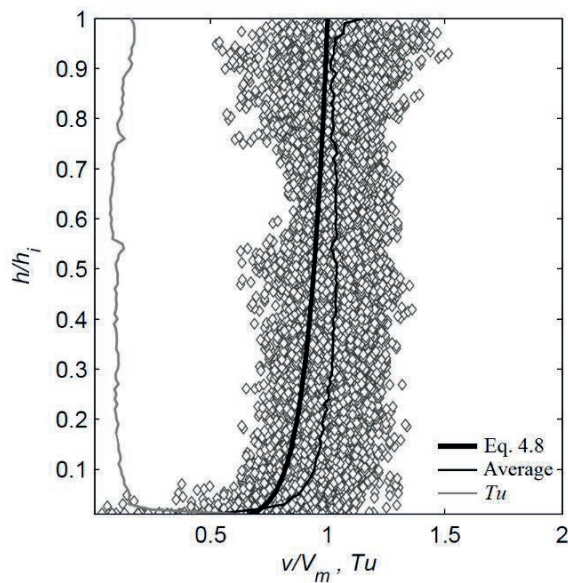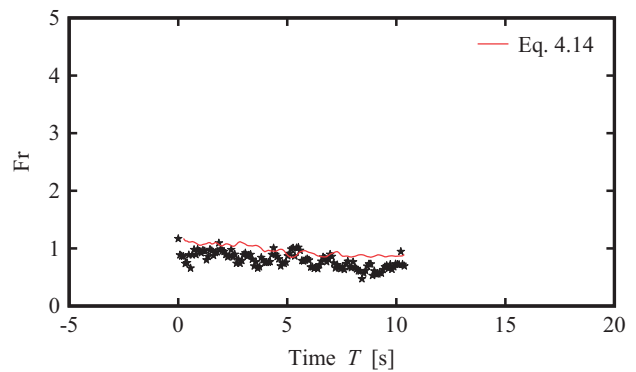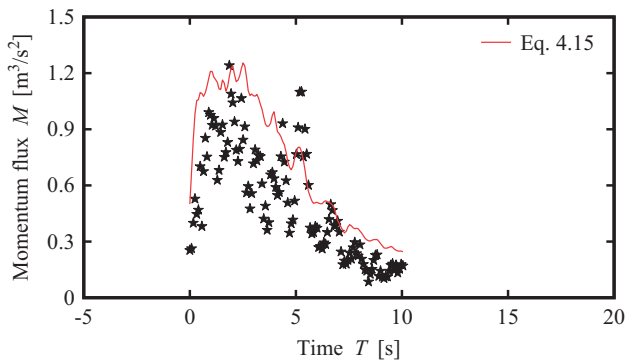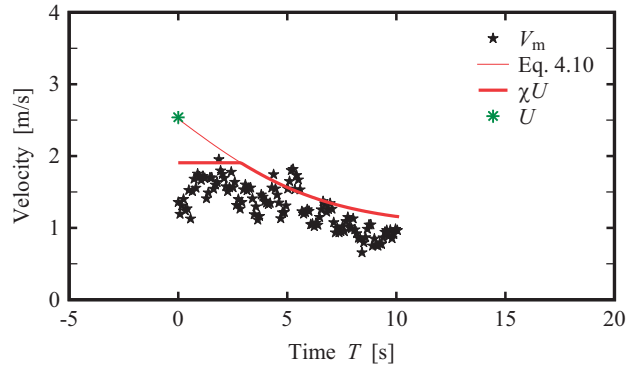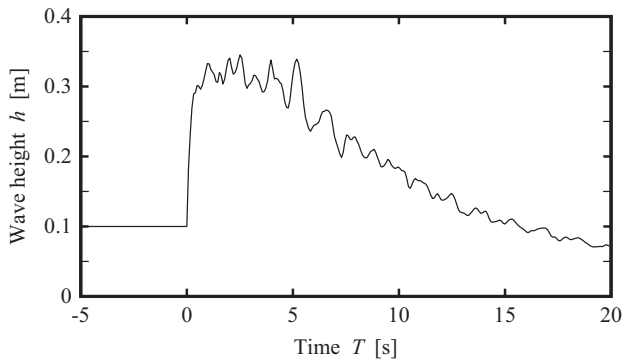
E Testsheets: impact on buildings

This Appendix contains the results of the tests performed during this research, on the impact of surges and bores on buildings with and without openings. The main parameters used in the present study are defined in Figures E.1 and E.2.

Selected examples of testsheets summarizing the main results are presented in this report. The complete collection of testsheets for all configurations is available on-line (DOI: 10.5075/epfl-thesis-8116) on:

https://infoscience.epfl.ch/

Note:

- $P_{h,max}$ is the surface porosity defined between $0 < z < h_{max}$.
- P_{tot} is the surface porosity defined between $0 < z < H_B$.
- h_{max} is the maximum wave height, measured without the building (Table D.1).
- H_{max} is the maximum run-up height, measured with the building.
- $F_{x,D,max}$ is the maximum horizontal force, computed using Eq. 7.5.
- The computed force $F_{x,D}$ is obtained with Eq. 7.4.
- C_R is the resistance coefficient at $T = \tau_{max}$, obtained experimentally.
- L_z is the cantilever arm, defined as $L_z = M_y/F_x$.
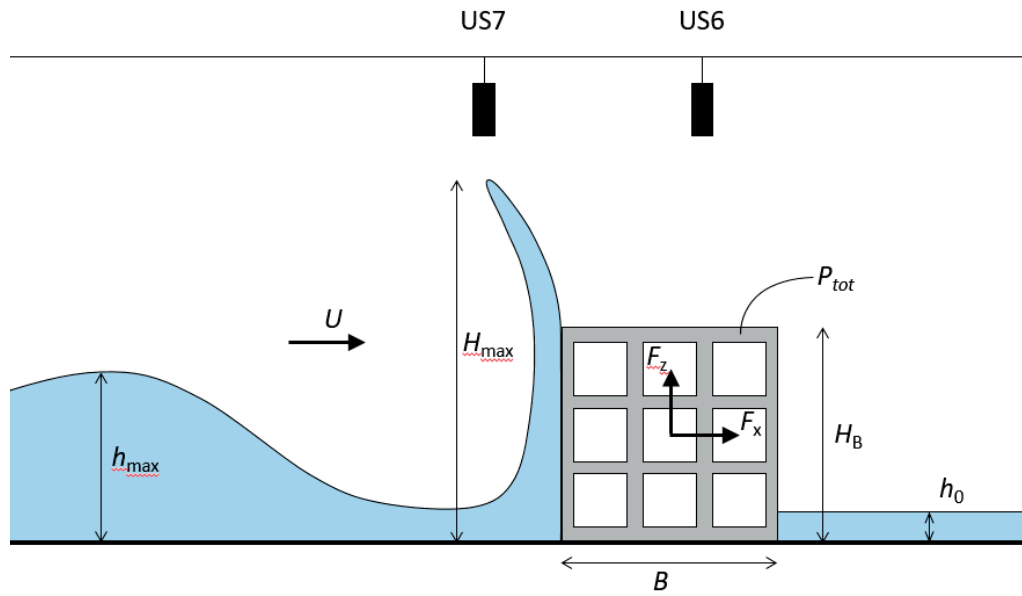
Figure E.1 – Definition sketch of the main parameters during the wave impact
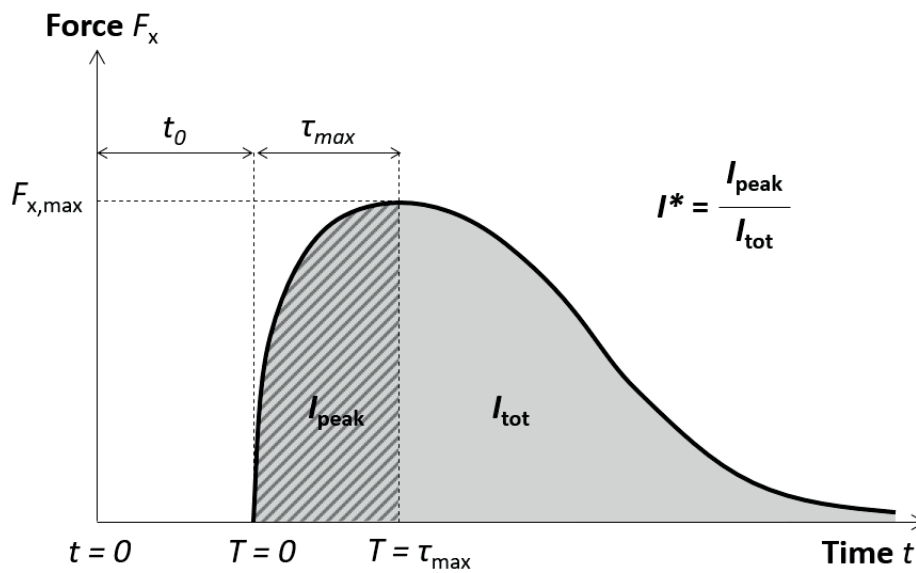
Figure E.2 – Definition sketch of the main force parameters

Test name	Configuration	Porosity	Wave type	Page
B0_H_WD1	Reference (H_B = 0.6m)	0	WD1	online
B0_H_WD2	Reference (H_B = 0.6m)	0	WD2	page 208
B0_H_WD3	Reference (H_B = 0.6m)	0	WD3	online
B0_H_WW1_1P	Reference (H_B = 0.6m)	0	WW1_1P	online
B0_H_WW1_2P	Reference (H_B = 0.6m)	0	WW1_2P	online
B0_H_WW1_3P	Reference (H_B = 0.6m)	0	WW1_3P	online
B0_H_WW3_1P	Reference (H_B = 0.6m)	0	WW3_1P	online
B0_H_WW3_2P	Reference (H_B = 0.6m)	0	WW3_2P	online
B0_H_WW3_3P	Reference (H_B = 0.6m)	0	WW3_3P	online
B0_H_WW5_1P	Reference (H_B = 0.6m)	0	WW5_1P	online
B0_H_WW5_2P	Reference (H_B = 0.6m)	0	WW5_2P	online
B0_H_WW5_3P	Reference (H_B = 0.6m)	0	WW5_3P	online
B0_0_WD1	Reference (H_B = 0.3m)	0	WD1	online
B0_0_WD2	Reference (H_B = 0.3m)	0	WD2	page 210
B0_0_WD3	Reference (H_B = 0.3m)	0	WD3	online
B0_0_WW1_1P	Reference (H_B = 0.3m)	0	WW1_1P	online
B0_0_WW1_2P	Reference (H_B = 0.3m)	0	WW1_2P	online
B0_0_WW1_3P	Reference (H_B = 0.3m)	0	WW1_3P	online
B0_0_WW3_1P	Reference (H_B = 0.3m)	0	WW3_1P	online
B0_0_WW3_2P	Reference (H_B = 0.3m)	0	WW3_2P	online
B0_0_WW3_3P	Reference (H_B = 0.3m)	0	WW3_3P	online
B0_0_WW5_1P	Reference (H_B = 0.3m)	0	WW5_1P	online
B0_0_WW5_2P	Reference (H_B = 0.3m)	0	WW5_2P	online
B0_0_WW5_3P	Reference (H_B = 0.3m)	0	WW5_3P	online
B17_0_WD1	All porous (0)	17	WD1	online
B17_0_WD2	All porous (0)	17	WD2	page 212
B17_0_WD3	All porous (0)	17	WD3	online
B17_0_WW1_1P	All porous (0)	17	WW1_1P	online
B17_0_WW1_2P	All porous (0)	17	WW1_2P	online
B17_0_WW3_1P	All porous (0)	17	WW3_1P	online
B17_0_WW3_2P	All porous (0)	17	WW3_2P	online
B17_0_WW5_1P	All porous (0)	17	WW5_1P	online
B17_0_WW5_2P	All porous (0)	17	WW5_2P	online
B17_F_WD1	Impervious sides (F)	17	WD1	online
B17_F_WD2	Impervious sides (F)	17	WD2	online
B17_F_WD3	Impervious sides (F)	17	WD3	online
B17_F_WW1_1P	Impervious sides (F)	17	WW1_1P	online
B17_F_WW1_2P	Impervious sides (F)	17	WW1_2P	online
B17_F_WW3_1P	Impervious sides (F)	17	WW3_1P	online
B17_F_WW3_2P	Impervious sides (F)	17	WW3_2P	online

B17_F_WW5_1P	Impervious sides (F)	17	WW5_1P	online
B17_F_WW5_2P	Impervious sides (F)	17	WW5_2P	online
B17_B_WD1	Impervious back (B)	17	WD1	online
B17_B_WD2	Impervious back (B)	17	WD2	online
B17_B_WD3	Impervious back (B)	17	WD3	online
B17_B_WW1_1P	Impervious back (B)	17	WW1_1P	online
B17_B_WW1_2P	Impervious back (B)	17	WW1_2P	online
B17_B_WW3_1P	Impervious back (B)	17	WW3_1P	online
B17_B_WW3_2P	Impervious back (B)	17	WW3_2P	online
B17_S_WD1	With side buildings (S)	17	WD1	online
B17_S_WD2	With side buildings (S)	17	WD2	online
B17_S_WD3	With side buildings (S)	17	WD3	online
B17_S_WW1_1P	With side buildings (S)	17	WW1_1P	online
B17_S_WW1_2P	With side buildings (S)	17	WW1_2P	online
B17_S_WW3_1P	With side buildings (S)	17	WW3_1P	online
B17_S_WW3_2P	With side buildings (S)	17	WW3_2P	online
B31.34_0_WD1	All porous (0)	31.34	WD1	online
B31.34_0_WD2	All porous (0)	31.34	WD2	page 214
B31.34_0_WD3	All porous (0)	31.34	WD3	online
B31.34_0_WW1_1P	All porous (0)	31.34	WW1_1P	online
B31.34_0_WW1_2P	All porous (0)	31.34	WW1_2P	online
B31.34_0_WW3_1P	All porous (0)	31.34	WW3_1P	online
B31.34_0_WW3_2P	All porous (0)	31.34	WW3_2P	online
B31.34_0_WW5_1P	All porous (0)	31.34	WW5_1P	online
B31.34_0_WW5_2P	All porous (0)	31.34	WW5_2P	online
B31.34_F_WD1	Impervious sides (F)	31.34	WD1	online
B31.34_F_WD2	Impervious sides (F)	31.34	WD2	online
B31.34_F_WD3	Impervious sides (F)	31.34	WD3	online
B31.34_F_WW1_1P	Impervious sides (F)	31.34	WW1_1P	online
B31.34_F_WW1_2P	Impervious sides (F)	31.34	WW1_2P	online
B31.34_F_WW3_1P	Impervious sides (F)	31.34	WW3_1P	online
B31.34_F_WW3_2P	Impervious sides (F)	31.34	WW3_2P	online
B31.34_F_WW5_1P	Impervious sides (F)	31.34	WW5_1P	online
B31.34_F_WW5_2P	Impervious sides (F)	31.34	WW5_2P	online
B31.34_S_WD1	With side buildings (S)	31.34	WD1	online
B31.34_S_WD2	With side buildings (S)	31.34	WD2	online
B31.34_S_WD3	With side buildings (S)	31.34	WD3	online
B31.34_S_WW1_1P	With side buildings (S)	31.34	WW1_1P	online
B31.34_S_WW1_2P	With side buildings (S)	31.34	WW1_2P	online
B31.34_S_WW3_1P	With side buildings (S)	31.34	WW3_1P	online
B31.34_S_WW3_2P	With side buildings (S)	31.34	WW3_2P	online
B34_0_WD1	All porous (0)	34	WD1	online

B34_0_WD2	All porous (0)	34	WD2	page 216
B34_0_WD3	All porous (0)	34	WD3	online
B34_0_WW1_1P	All porous (0)	34	WW1_1P	online
B34_0_WW1_2P	All porous (0)	34	WW1_2P	online
B34_0_WW3_1P	All porous (0)	34	WW3_1P	online
B34_0_WW3_2P	All porous (0)	34	WW3_2P	online
B34_0_WW5_1P	All porous (0)	34	WW5_1P	online
B34_0_WW5_2P	All porous (0)	34	WW5_2P	online
B34_F_WD1	Impervious sides (F)	34	WD1	online
B34_F_WD2	Impervious sides (F)	34	WD2	online
B34_F_WD3	Impervious sides (F)	34	WD3	online
B34_F_WW1_1P	Impervious sides (F)	34	WW1_1P	online
B34_F_WW1_2P	Impervious sides (F)	34	WW1_2P	online
B34_F_WW3_1P	Impervious sides (F)	34	WW3_1P	online
B34_F_WW3_2P	Impervious sides (F)	34	WW3_2P	online
B34_F_WW5_1P	Impervious sides (F)	34	WW5_1P	online
B34_F_WW5_2P	Impervious sides (F)	34	WW5_2P	online
B34_B_WD1	Impervious back (B)	34	WD1	online
B34_B_WD2	Impervious back (B)	34	WD2	online
B34_B_WD3	Impervious back (B)	34	WD3	online
B34_B_WW1_1P	Impervious back (B)	34	WW1_1P	online
B34_B_WW1_2P	Impervious back (B)	34	WW1_2P	online
B34_B_WW3_1P	Impervious back (B)	34	WW3_1P	online
B34_B_WW3_2P	Impervious back (B)	34	WW3_2P	online
B34_S_WD1	With side buildings (S)	34	WD1	online
B34_S_WD2	With side buildings (S)	34	WD2	online
B34_S_WD3	With side buildings (S)	34	WD3	online
B34_S_WW1_1P	With side buildings (S)	34	WW1_1P	online
B34_S_WW1_2P	With side buildings (S)	34	WW1_2P	online
B34_S_WW3_1P	With side buildings (S)	34	WW3_1P	online
B34_S_WW3_2P	With side buildings (S)	34	WW3_2P	online
B42.24_0_WD1	All porous (0)	42.24	WD1	online
B42.24_0_WD2	All porous (0)	42.24	WD2	page 218
B42.24_0_WD3	All porous (0)	42.24	WD3	online
B42.24_0_WW1_1P	All porous (0)	42.24	WW1_1P	online
B42.24_0_WW1_2P	All porous (0)	42.24	WW1_2P	online
B42.24_0_WW3_1P	All porous (0)	42.24	WW3_1P	online
B42.24_0_WW3_2P	All porous (0)	42.24	WW3_2P	online
B42.24_0_WW5_1P	All porous (0)	42.24	WW5_1P	online
B42.24_0_WW5_2P	All porous (0)	42.24	WW5_2P	online
B42.24_F_WD1	Impervious sides (F)	42.24	WD1	online
B42.24_F_WD2	Impervious sides (F)	42.24	WD2	online

B42.24_F_WD3	Impervious sides (F)	42.24	WD3	online
B42.24_F_WW1_1P	Impervious sides (F)	42.24	WW1_1P	online
B42.24_F_WW1_2P	Impervious sides (F)	42.24	WW1_2P	online
B42.24_F_WW3_1P	Impervious sides (F)	42.24	WW3_1P	online
B42.24_F_WW3_2P	Impervious sides (F)	42.24	WW3_2P	online
B42.24_F_WW5_1P	Impervious sides (F)	42.24	WW5_1P	online
B42.24_F_WW5_2P	Impervious sides (F)	42.24	WW5_2P	online
B42.24_B_WD1	Impervious back (B)	42.24	WD1	online
B42.24_B_WD2	Impervious back (B)	42.24	WD2	online
B42.24_B_WD3	Impervious back (B)	42.24	WD3	online
B42.24_B_WW1_1P	Impervious back (B)	42.24	WW1_1P	online
B42.24_B_WW1_2P	Impervious back (B)	42.24	WW1_2P	online
B42.24_B_WW3_1P	Impervious back (B)	42.24	WW3_1P	online
B42.24_B_WW3_2P	Impervious back (B)	42.24	WW3_2P	online
B42.24_S_WD1	With side buildings (S)	42.24	WD1	online
B42.24_S_WD2	With side buildings (S)	42.24	WD2	online
B42.24_S_WD3	With side buildings (S)	42.24	WD3	online
B42.24_S_WW1_1P	With side buildings (S)	42.24	WW1_1P	online
B42.24_S_WW1_2P	With side buildings (S)	42.24	WW1_2P	online
B42.24_S_WW3_1P	With side buildings (S)	42.24	WW3_1P	online
B42.24_S_WW3_2P	With side buildings (S)	42.24	WW3_2P	online
B60_0_WD1	All porous (0)	60	WD1	online
B60_0_WD2	All porous (0)	60	WD2	page 220
B60_0_WD3	All porous (0)	60	WD3	online
B60_0_WW1_1P	All porous (0)	60	WW1_1P	online
B60_0_WW1_2P	All porous (0)	60	WW1_2P	online
B60_0_WW3_1P	All porous (0)	60	WW3_1P	online
B60_0_WW3_2P	All porous (0)	60	WW3_2P	online
B60_0_WW5_1P	All porous (0)	60	WW5_1P	online
B60_0_WW5_2P	All porous (0)	60	WW5_2P	online
B60_F_WD1	Impervious sides (F)	60	WD1	online
B60_F_WD2	Impervious sides (F)	60	WD2	page 222
B60_F_WD3	Impervious sides (F)	60	WD3	online
B60_F_WW1_1P	Impervious sides (F)	60	WW1_1P	online
B60_F_WW1_2P	Impervious sides (F)	60	WW1_2P	online
B60_F_WW3_1P	Impervious sides (F)	60	WW3_1P	online
B60_F_WW3_2P	Impervious sides (F)	60	WW3_2P	online
B60_F_WW5_1P	Impervious sides (F)	60	WW5_1P	online
B60_F_WW5_2P	Impervious sides (F)	60	WW5_2P	online
B60_B_WD1	Impervious back (B)	60	WD1	online
B60_B_WD2	Impervious back (B)	60	WD2	page 224
B60_B_WD3	Impervious back (B)	60	WD3	online

B60_B_WW1_1P	Impervious back (B)	60	WW1_1P	online
B60_B_WW1_2P	Impervious back (B)	60	WW1_2P	online
B60_B_WW3_1P	Impervious back (B)	60	WW3_1P	online
B60_B_WW3_2P	Impervious back (B)	60	WW3_2P	online
B60_S_WD1	With side buildings (S)	60	WD1	online
B60_S_WD2	With side buildings (S)	60	WD2	page 226
B60_S_WD3	With side buildings (S)	60	WD3	online
B60_S_WW1_1P	With side buildings (S)	60	WW1_1P	online
B60_S_WW1_2P	With side buildings (S)	60	WW1_2P	online
B60_S_WW3_1P	With side buildings (S)	60	WW3_1P	online
B60_S_WW3_2P	With side buildings (S)	60	WW3_2P	online
B84_F_WD1	Impervious sides (F)	84	WD1	online
B84_F_WD2	Impervious sides (F)	84	WD2	online
B84_F_WD3	Impervious sides (F)	84	WD3	online
B84_F_WW1_1P	Impervious sides (F)	84	WW1_1P	online
B84_F_WW1_2P	Impervious sides (F)	84	WW1_2P	online
B84_F_WW3_1P	Impervious sides (F)	84	WW3_1P	online
B84_F_WW3_2P	Impervious sides (F)	84	WW3_2P	online
B84_F_WW5_1P	Impervious sides (F)	84	WW5_1P	online
B84_F_WW5_2P	Impervious sides (F)	84	WW5_2P	online

Table E.1 – Experimental program of all the tests conducted in the present research

TEST PARAMETERS

Name		B0_H_WD2_2	
Repetitions		3	
Configuration		Reference	
Total porosity	P_{tot}	0	[%]
Porosity at h_{max}	$P_{h,max}$	0	[%]
Building height	H_B	0.6	[m]
Wave type		Surge (WD2)	
Impoundment depth	d_0	0.630	[m]
Initial still water depth	h_0	0.000	[m]
Front celerity	U	3.070	[m/s]
Maximum wave height	h_{max}	0.162	[m]
Maximum run-up height	H_{max}	0.519	[m]

FRONT VIEW	TOP VIEW

Wave
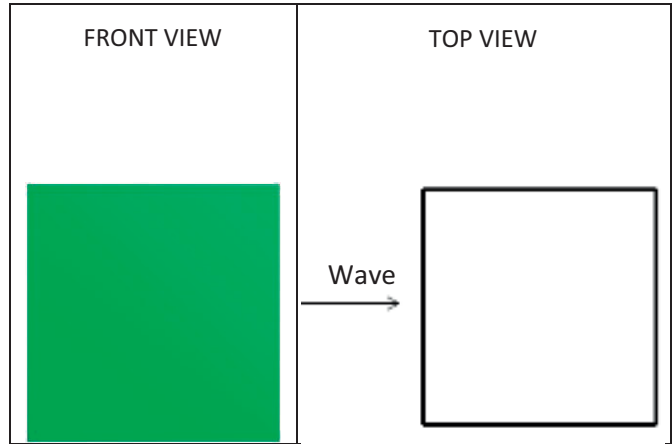
IMPACT PARAMETERS

	Min	Max	Unity
F_x	-6.153	204.381	[N]
F_y	-22.457	16.698	[N]
F_z	-13.339	8.215	[N]
M_x	-3.821	4.966	[Nm]
M_y	-2.139	41.691	[Nm]
M_z	-1.872	1.698	[Nm]

|			
Predicted Force	$F_{x,D,max}$	212.377	[N]
Initial time	t_0	4.956	[s]
Time to peak	τ_{max}	3.321	[s]
Total impulse	I_{tot}	2134.957	[Ns]
Peak Impulse	I_{peak}	464.765	[Ns]
Relative impulse	I^*	0.230	[-]
Wave height at $F_{x,max}$	h_M	0.718	[-]
Resistance coefficient	C_R	1.933	[-]

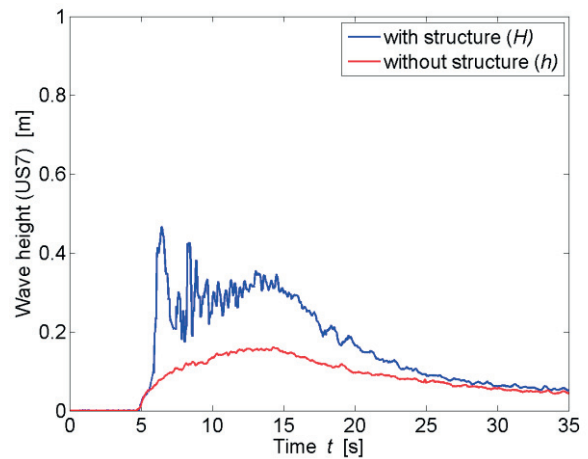* All parameters are presented and defined at the beginning of the Appendix
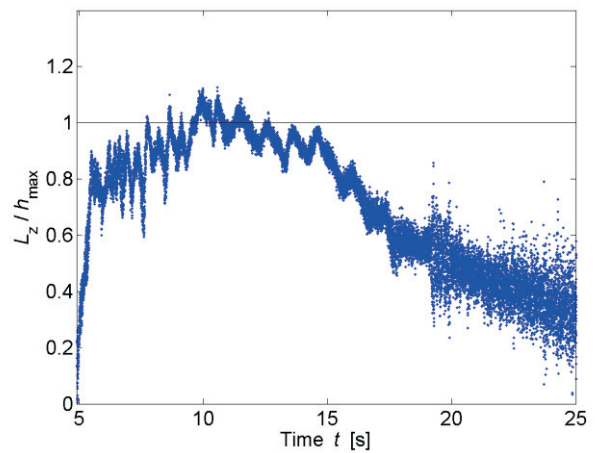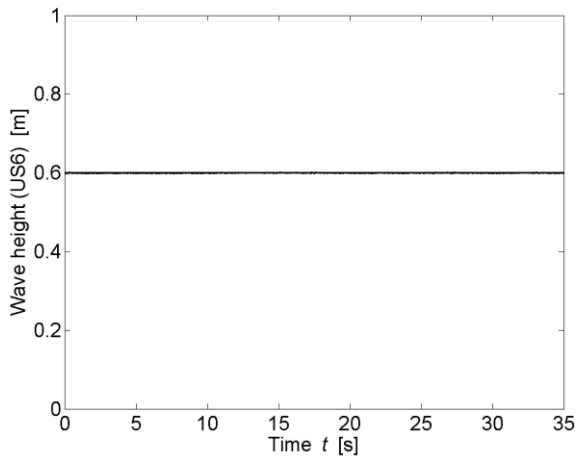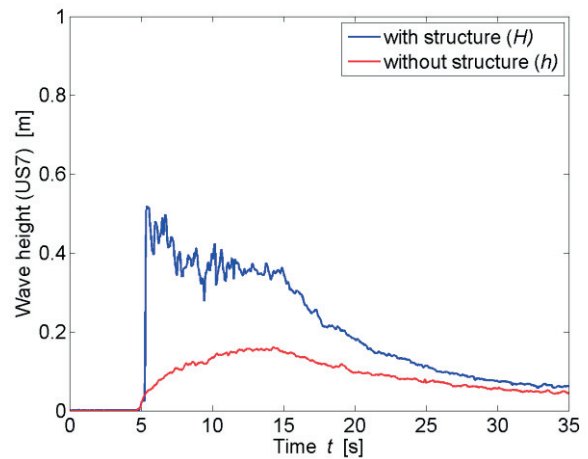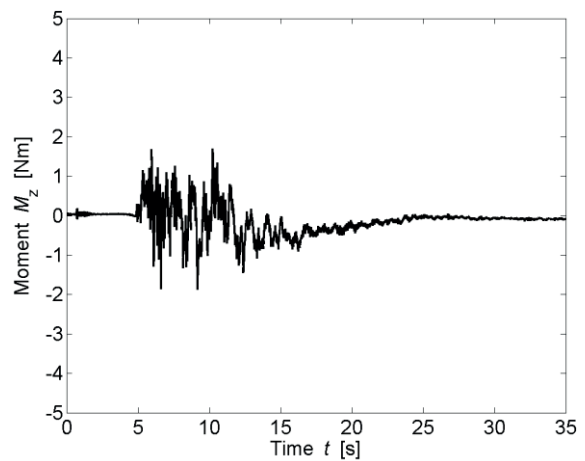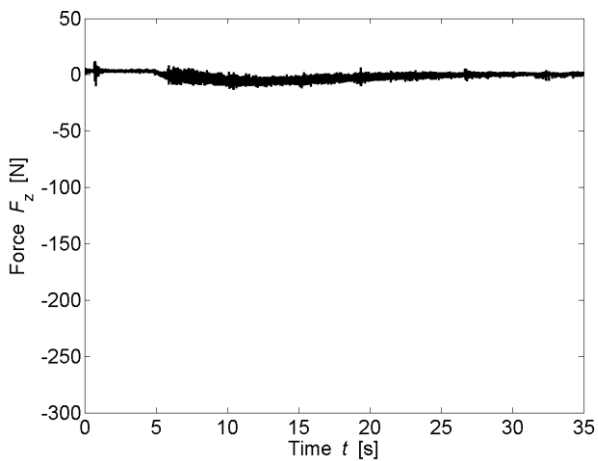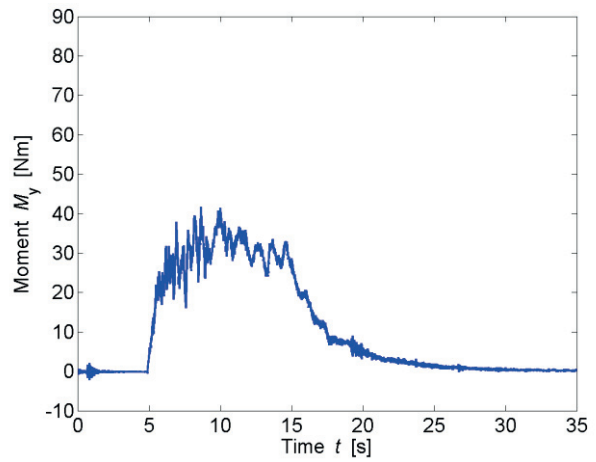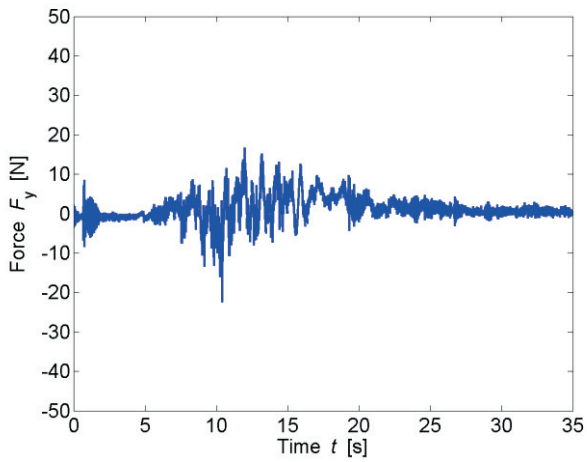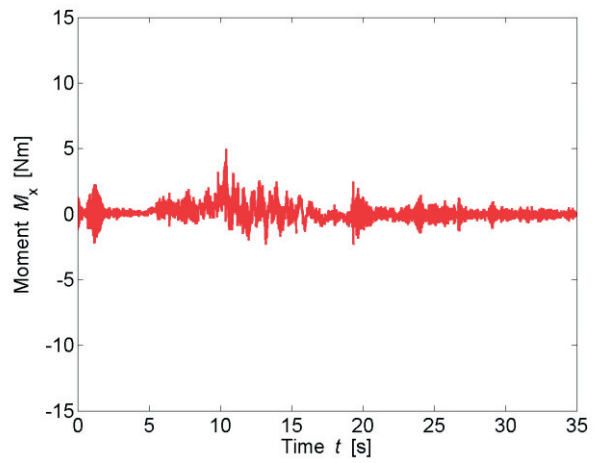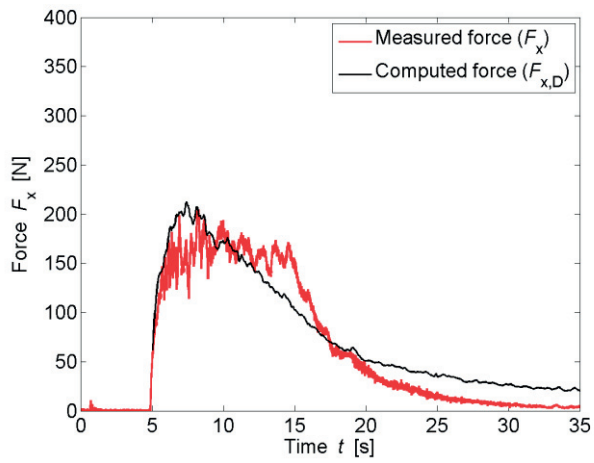
TEST PARAMETERS

Name		B0_0_WD2_2	
Repetitions		2	
Configuration		Reference	
Total porosity	P_{tot}	0	[%]
Porosity at h_{max}	$P_{h,max}$	0	[%]
Building height	H_B	0.3	[m]
Wave type		Surge (WD2)	
Impoundment depth	d_0	0.63	[m]
Initial still water depth	h_0	0.00	[m]
Front celerity	U	3.07	[m/s]
Maximum wave height	h_{max}	0.16	[m]
Maximum run-up height	H_{max}	0.63	[m]

FRONT VIEW	TOP VIEW

Wave →
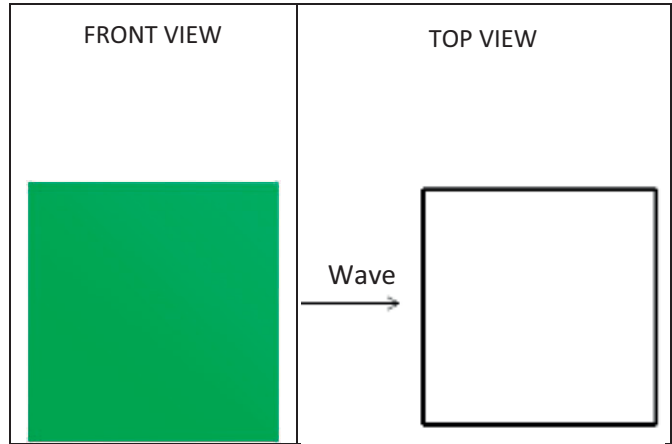
IMPACT PARAMETERS

	Min	Max	Unity
F_x	-5.690	196.062	[N]
F_y	-19.109	28.294	[N]
F_z	-41.249	2.608	[N]
M_x	-4.832	4.171	[Nm]
M_y	-1.582	36.674	[Nm]
M_z	-1.834	2.404	[Nm]

Predicted Force	$F_{x,D,max}$	212.377	[N]
Initial time	t_0	5.012	[s]
Time to peak	τ_{max}	3.110	[s]
Total impulse	I_{tot}	2031.836	[Ns]
Peak Impulse	I_{peak}	419.846	[Ns]
Relative impulse	I^*	0.218	[-]
Wave height at $F_{x,max}$	h_M	0.730	[-]
Resistance coefficient	C_R	1.833	[-]

210

* All parameters are presented and defined at the beginning of the Appendix
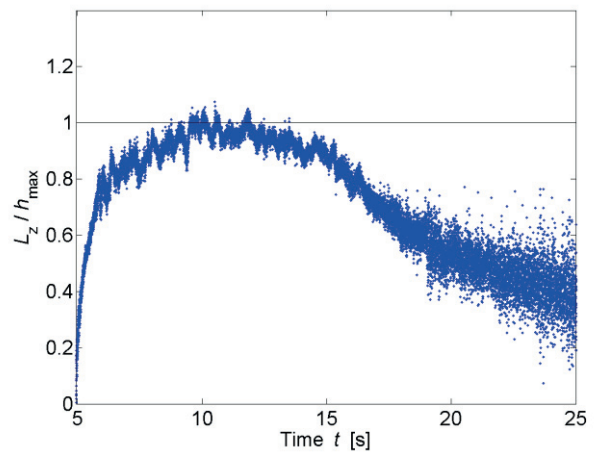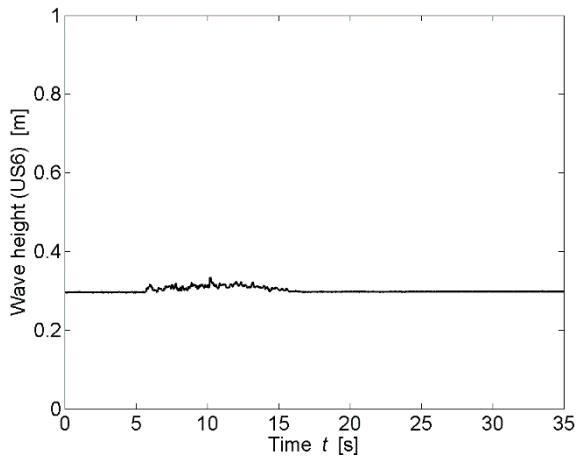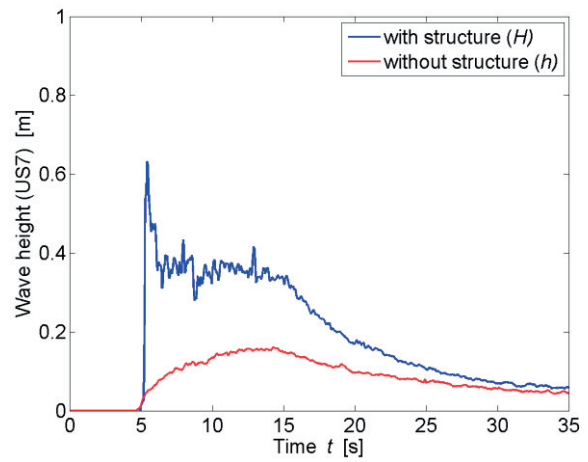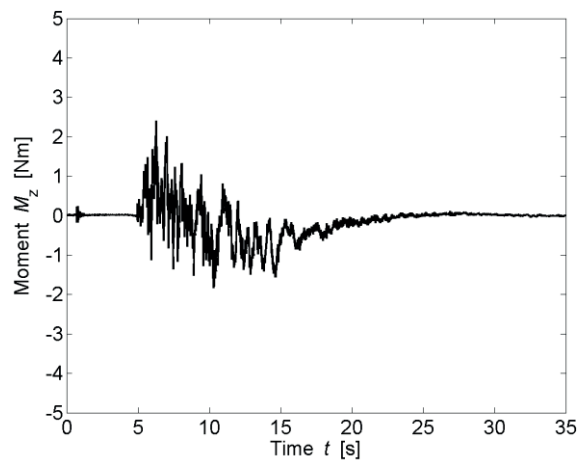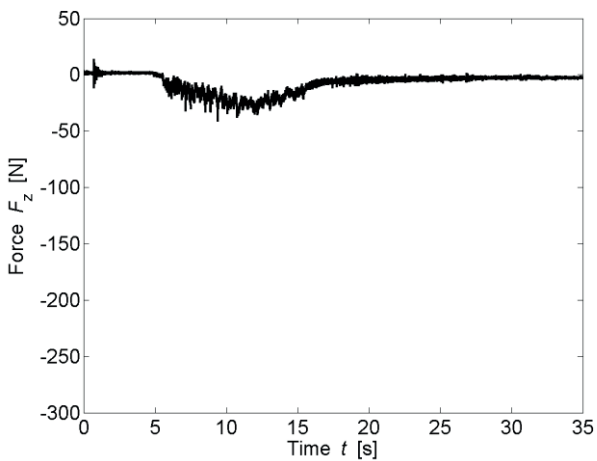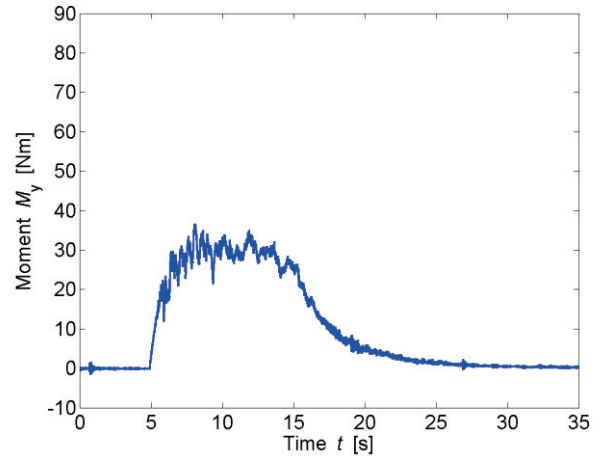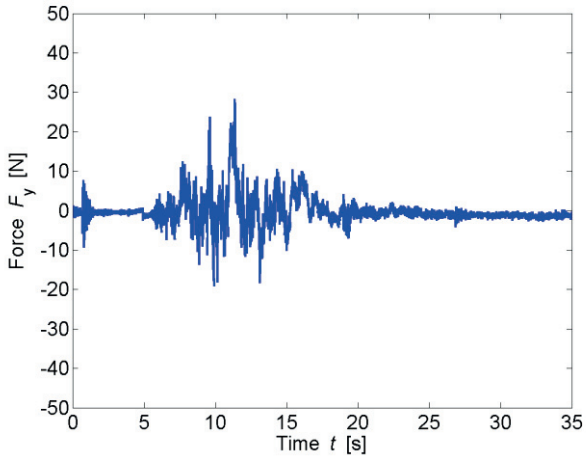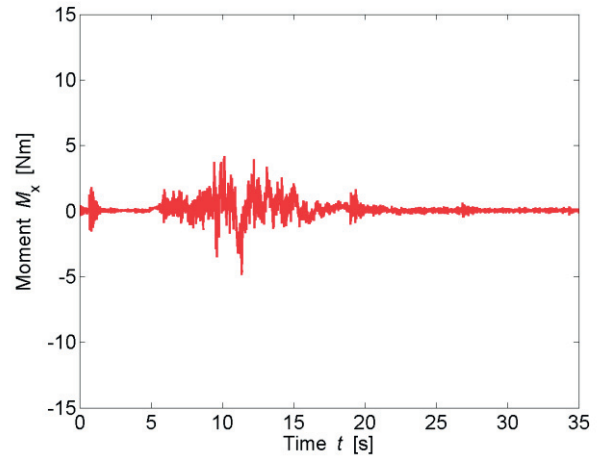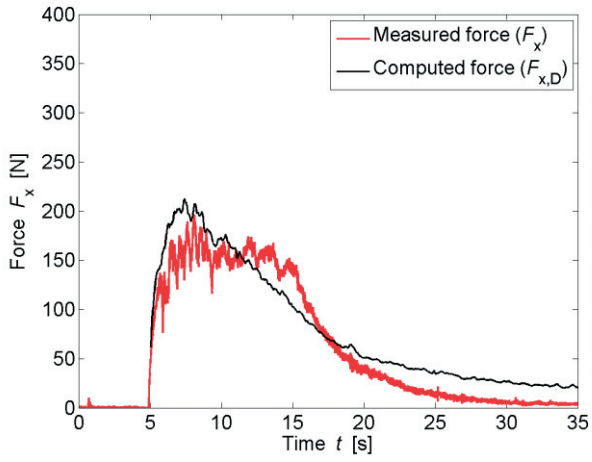
TEST PARAMETERS

Name		B17_0_WD2_ 1	
Repetitions		1	
Configuration		All Porous (0)	
Total porosity	P_{tot}	17	[%]
Porosity at h_{max}	$P_{h,max}$	16.68	[%]
Building height	H_B	0.3	[m]
Wave type		Surge (WD2)	
Impoundment depth	d_0	0.630	[m]
Initial still water depth	h_0	0.000	[m]
Front celerity	U	3.087	[m/s]
Maximum wave height	h_{max}	0.162	[m]
Maximum run-up height	H_{max}	0.543	[m]

FRONT VIEW   TOP VIEW

Wave
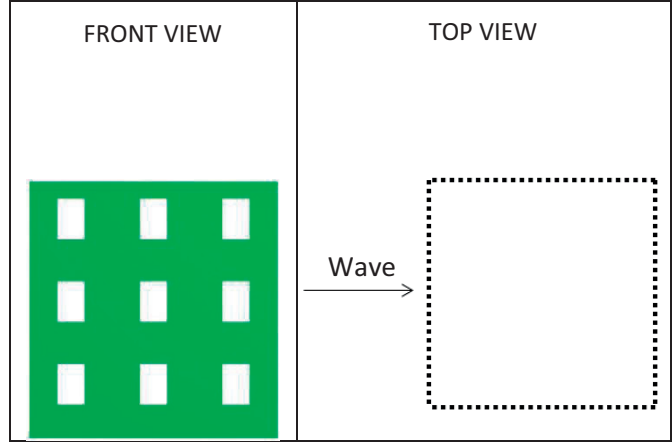
IMPACT PARAMETERS

	Min	Max	Unity
F_x	-2.714	166.884	[N]
F_y	-9.907	21.711	[N]
F_z	-236.075	16.103	[N]
M_x	-4.157	2.986	[Nm]
M_y	-0.892	33.458	[Nm]
M_z	-2.076	0.974	[Nm]

Predicted Force	$F_{x,D,max}$	176.948	[N]
Initial time	t_0	5.002	[s]
Time to peak	τ_{max}	2.867	[s]
Total impulse	I_{tot}	1601.965	[Ns]
Peak Impulse	I_{peak}	324.536	[Ns]
Relative impulse	I^*	0.212	[-]
Wave height at $F_{x,max}$	h_M	0.641	[-]
Resistance coefficient	C_R	1.568	[-]
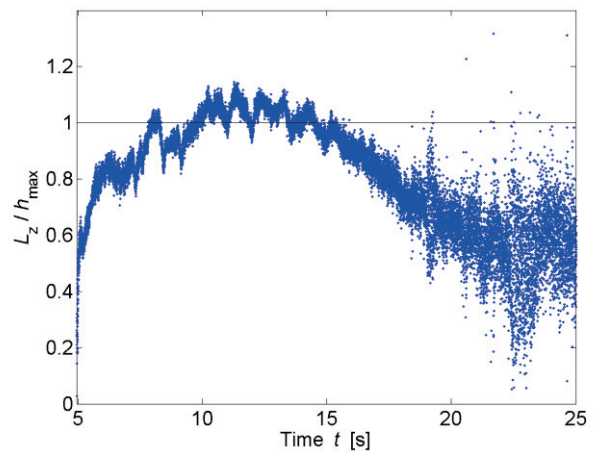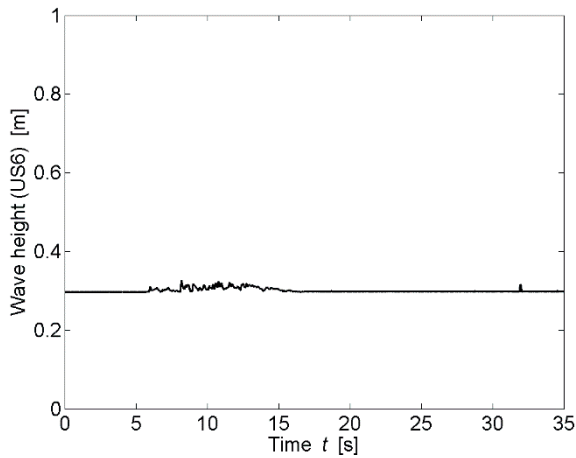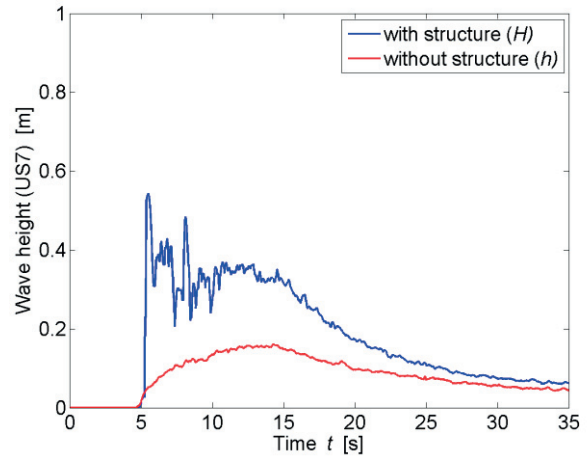
---

* All parameters are presented and defined at the beginning of the Appendix
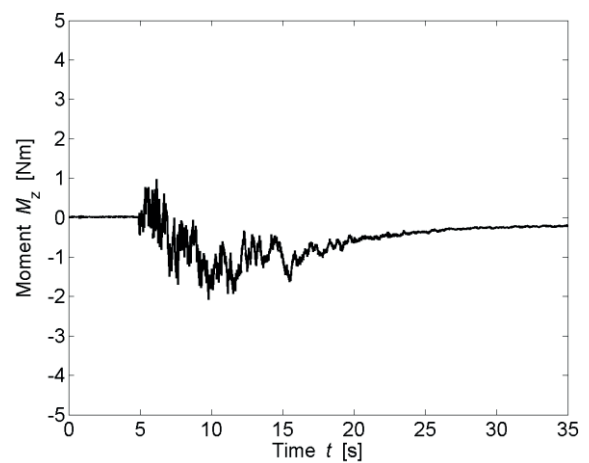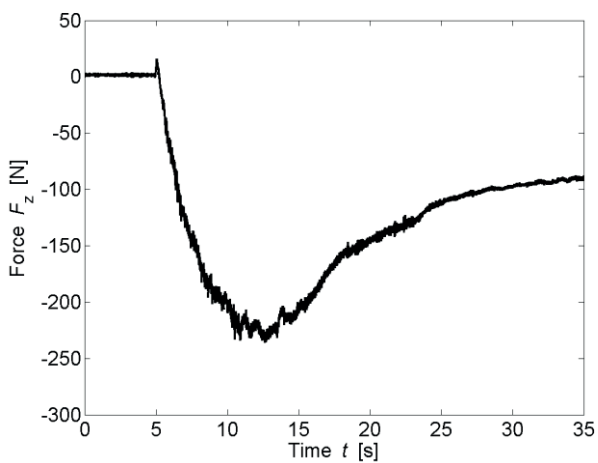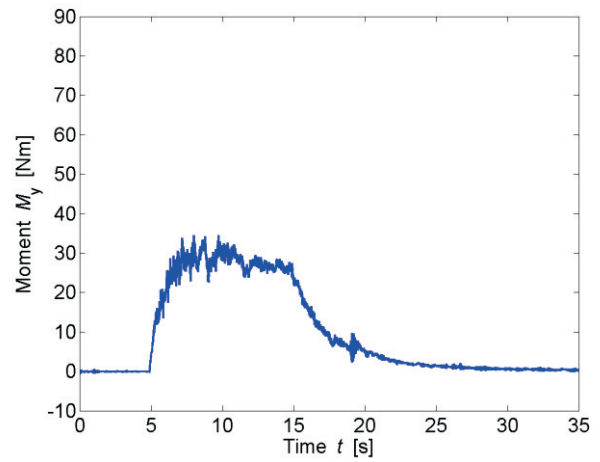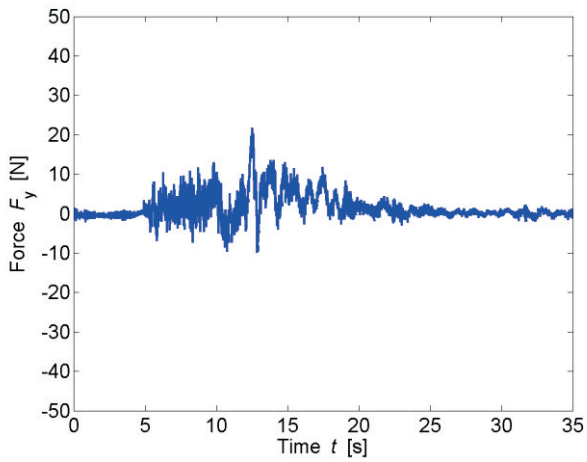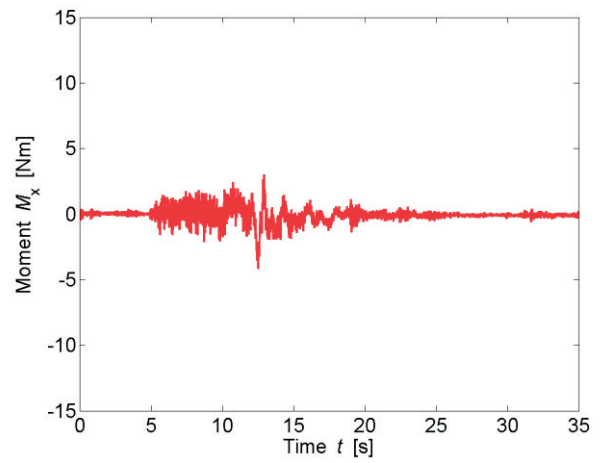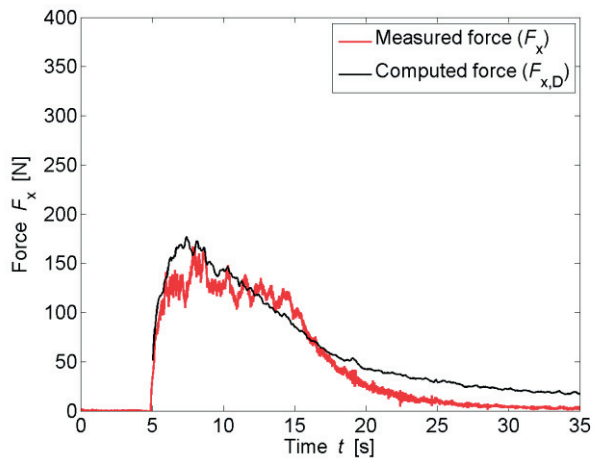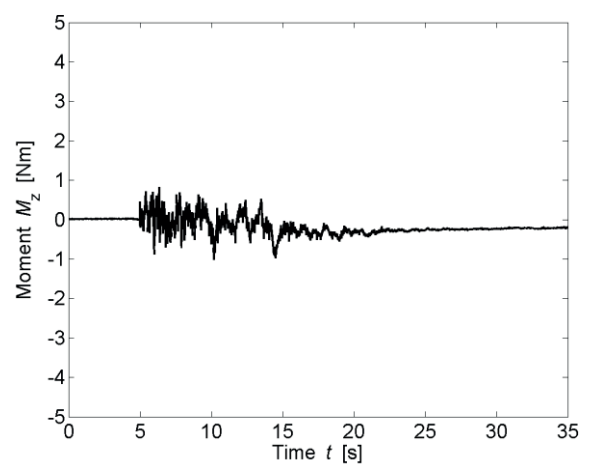
TEST PARAMETERS

Name		B31.34_0_WD2_1	
Repetitions		1	
Configuration		All Porous (0)	
Total porosity	P_{tot}	31.34	[%]
Porosity at h_{max}	$P_{h,max}$	44.08	[%]
Building height	H_B	0.3	[m]
Wave type		Surge (WD2)	
Impoundment depth	d_0	0.630	[m]
Initial still water depth	h_0	0.000	[m]
Front celerity	U	3.059	[m/s]
Maximum wave height	h_{max}	0.162	[m]
Maximum run-up height	H_{max}	0.466	[m]

FRONT VIEW TOP VIEW Wave
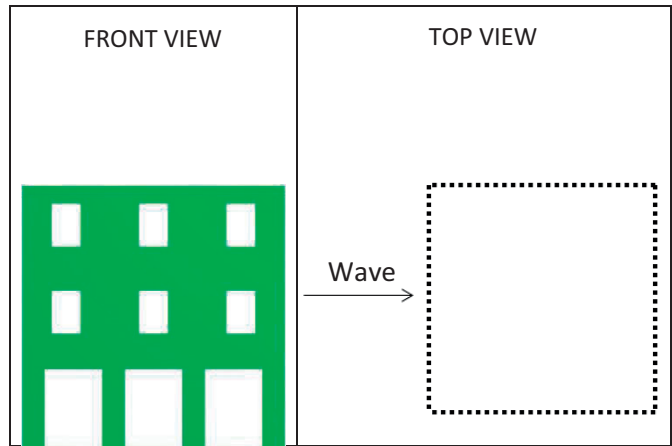
IMPACT PARAMETERS

	Min	Max	Unity
F_x	-2.641	134.513	[N]
F_y	-13.823	11.947	[N]
F_z	-241.229	2.327	[N]
M_x	-2.004	3.218	[Nm]
M_y	-1.198	26.849	[Nm]
M_z	-2.051	0.106	[Nm]

Predicted Force	$F_{x,D,max}$	118.765	[N]
Initial time	t_0	4.936	[s]
Time to peak	τ_{max}	3.224	[s]
Total impulse	I_{tot}	1222.613	[Ns]
Peak Impulse	I_{peak}	235.797	[Ns]
Relative impulse	I^*	0.200	[-]
Wave height at $F_{x,max}$	h_M	0.737	[-]
Resistance coefficient	C_R	1.239	[-]
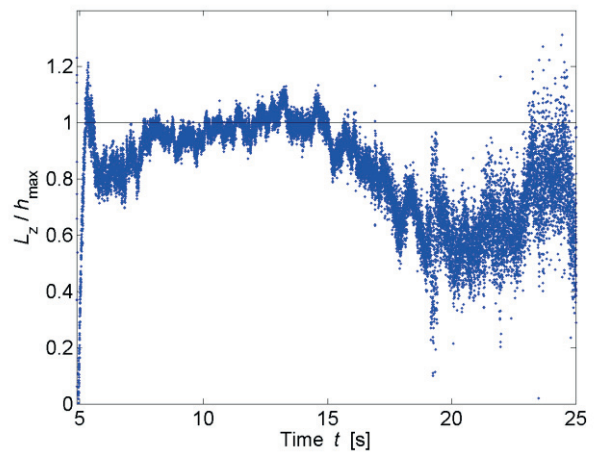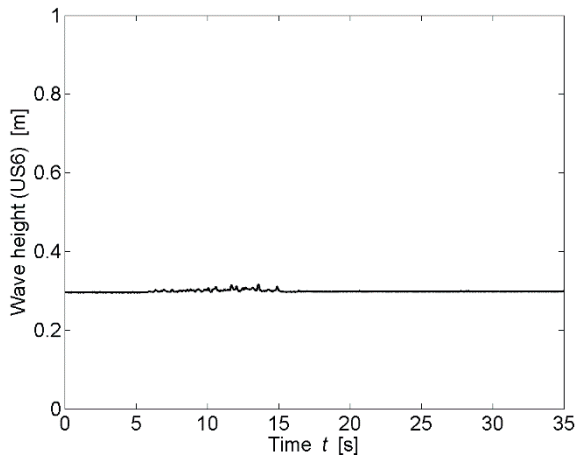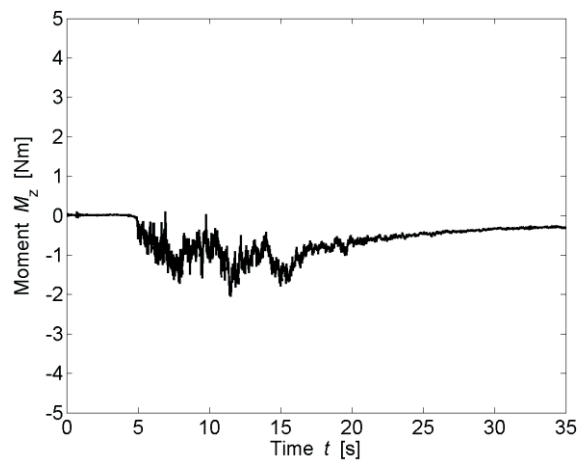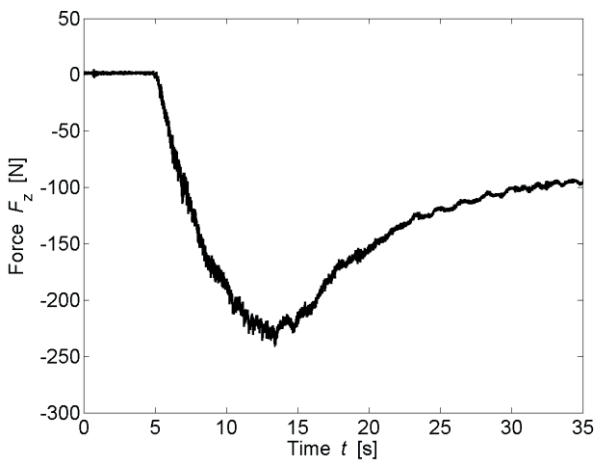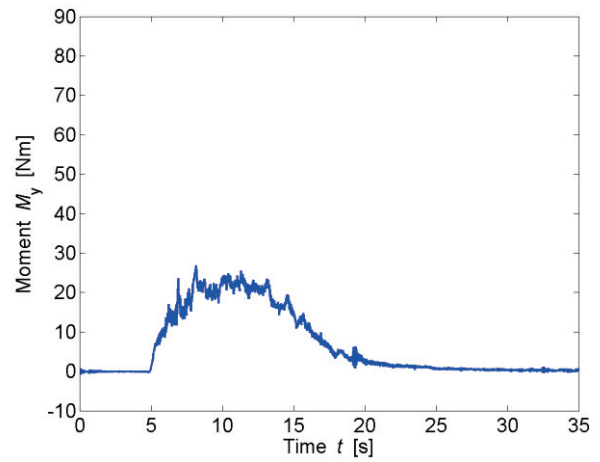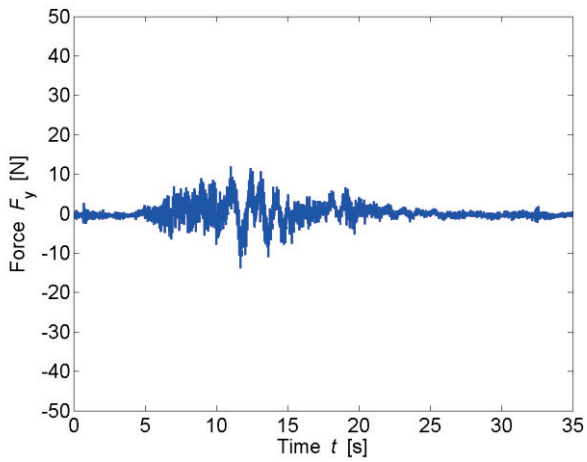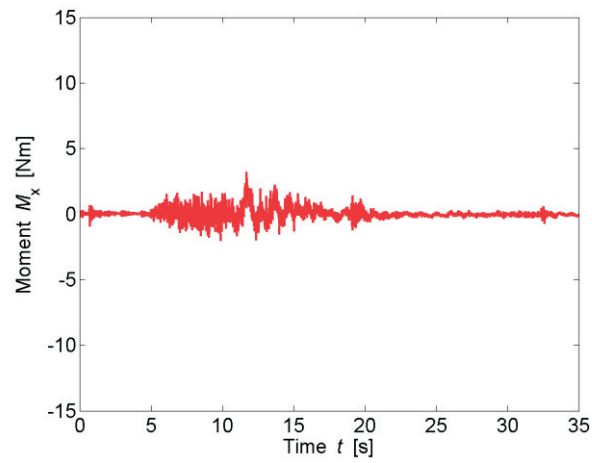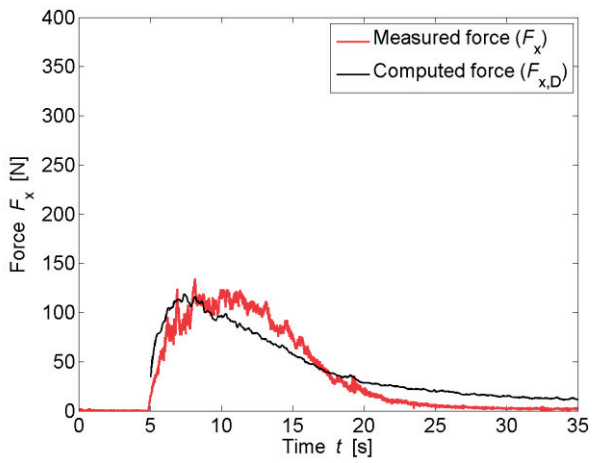
TEST PARAMETERS

Name		B34_0_WD2_1	
Repetitions		2	
Configuration		All Porous (0)	
Total porosity	P_{tot}	34	[%]
Porosity at h_{max}	$P_{h,max}$	33.36	[%]
Building height	H_B	0.3	[m]
Wave type		Surge (WD2)	
Impoundment depth	d_0	0.630	[m]
Initial still water depth	h_0	0.000	[m]
Front celerity	U	3.058	[m/s]
Maximum wave height	h_{max}	0.162	[m]
Maximum run-up height	H_{max}	0.464	[m]

FRONT VIEW	TOP VIEW

Wave →
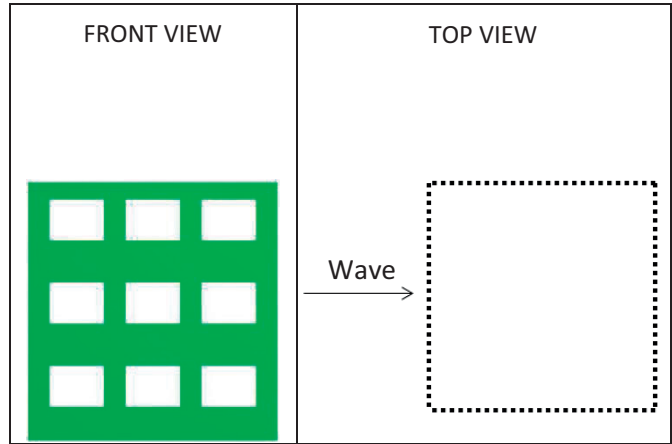
IMPACT PARAMETERS

	Min	Max	Unity
F_x	-2.133	140.755	[N]
F_y	-5.820	11.604	[N]
F_z	-235.044	28.472	[N]
M_x	-1.725	2.188	[Nm]
M_y	-0.680	27.163	[Nm]
M_z	-1.098	0.913	[Nm]

Predicted Force	$F_{x,D,max}$	141.527	[N]
Initial time	t_0	4.979	[s]
Time to peak	τ_{max}	2.572	[s]
Total impulse	I_{tot}	1348.108	[Ns]
Peak Impulse	I_{peak}	246.057	[Ns]
Relative impulse	I^*	0.190	[-]
Wave height at $F_{x,max}$	h_M	0.670	[-]
Resistance coefficient	C_R	1.291	[-]

216
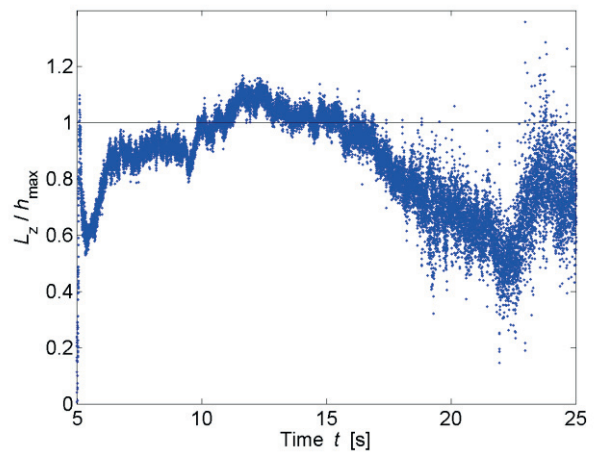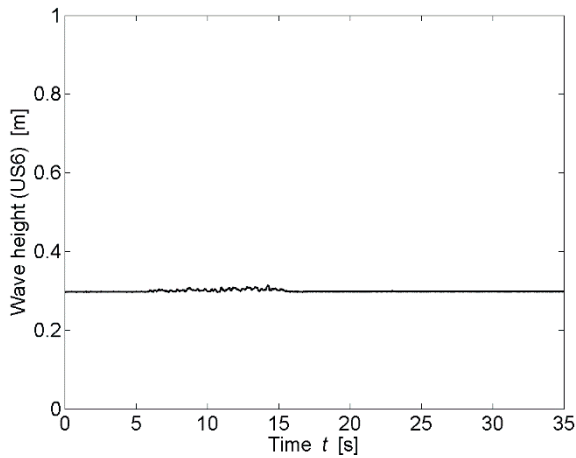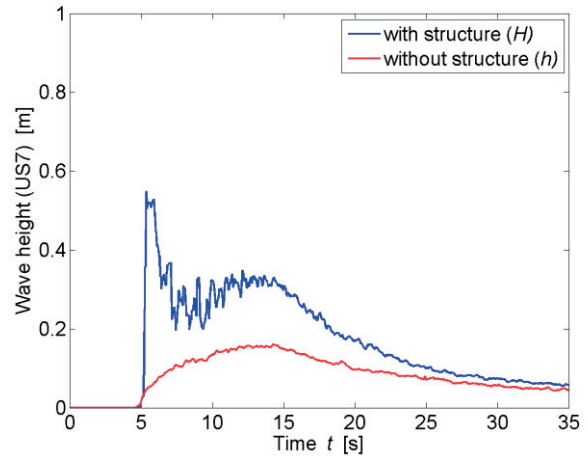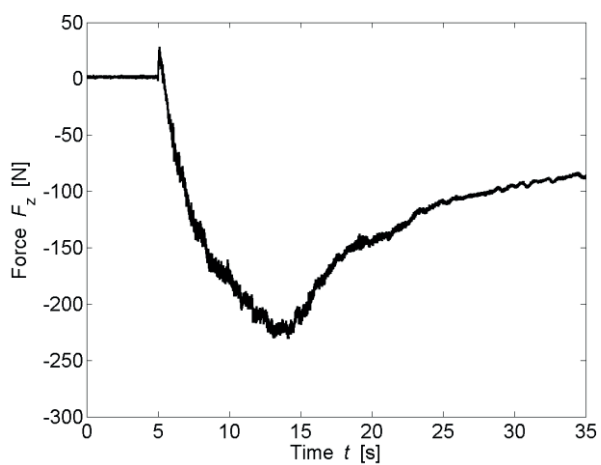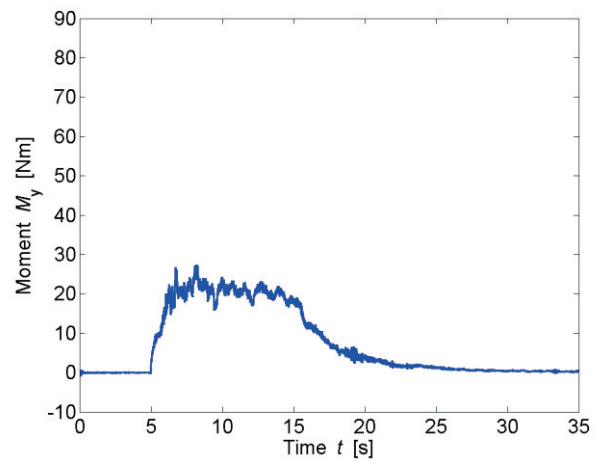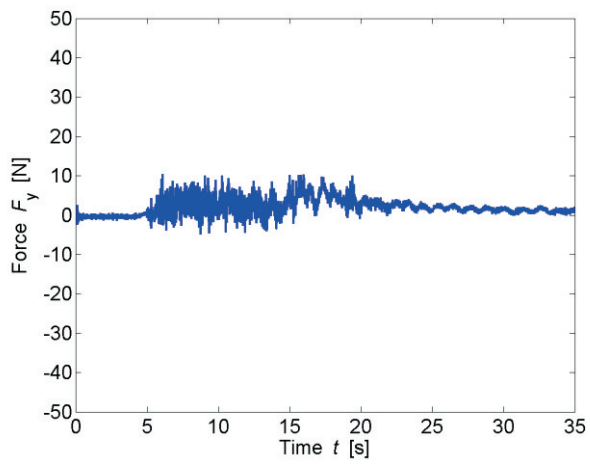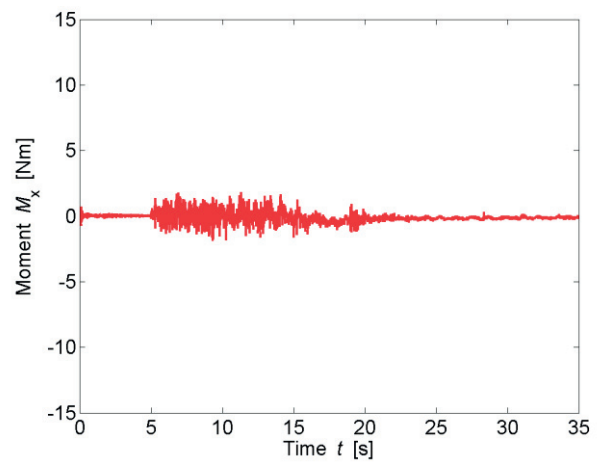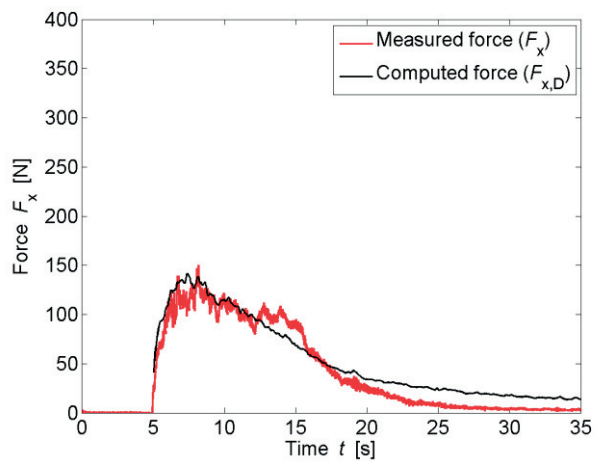
TEST PARAMETERS

Name		B42.24_0_WD2_1	
Repetitions		2	
Configuration		All Porous (0)	
Total porosity	P_{tot}	42.24	[%]
Porosity at h_{max}	$P_{h,max}$	49.71	[%]
Building height	H_B	0.3	[m]
Wave type		Surge (WD2)	
Impoundment depth	d_0	0.630	[m]
Initial still water depth	h_0	0.000	[m]
Front celerity	U	3.069	[m/s]
Maximum wave height	h_{max}	0.162	[m]
Maximum run-up height	H_{max}	0.440	[m]

FRONT VIEW   TOP VIEW

Wave
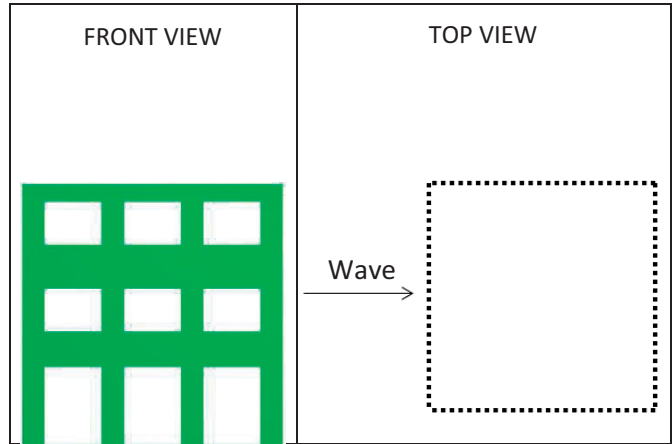
IMPACT PARAMETERS

	Min	Max	Unity
F_x	-3.149	115.255	[N]
F_y	-13.798	8.741	[N]
F_z	-231.296	0.921	[N]
M_x	-1.819	2.608	[Nm]
M_y	-1.295	24.442	[Nm]
M_z	-1.306	0.936	[Nm]

Predicted Force	$F_{x,D,max}$	106.796	[N]
Initial time	t_0	4.928	[s]
Time to peak	τ_{max}	3.463	[s]
Total impulse	I_{tot}	957.653	[Ns]
Peak Impulse	I_{peak}	239.385	[Ns]
Relative impulse	I^*	0.253	[-]
Wave height at $F_{x,max}$	h_M	0.736	[-]
Resistance coefficient	C_R	1.094	[-]

* All parameters are presented and defined at the beginning of the Appendix
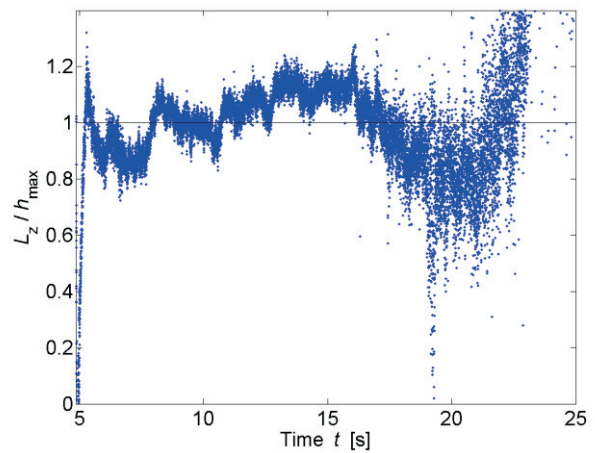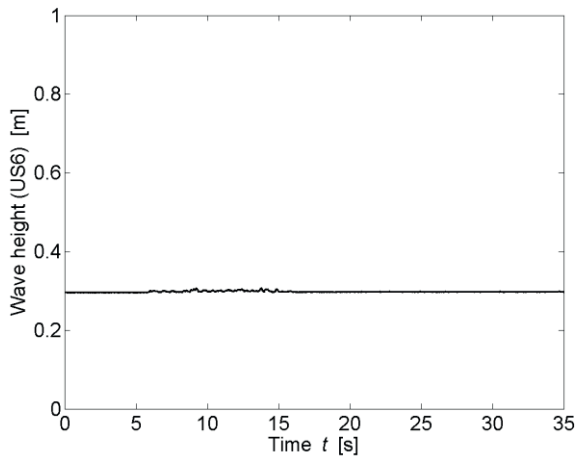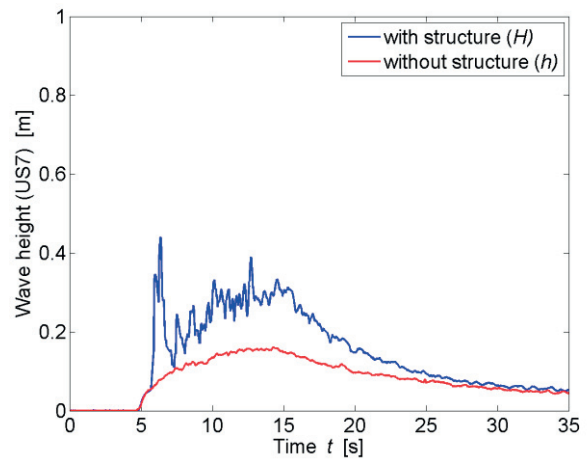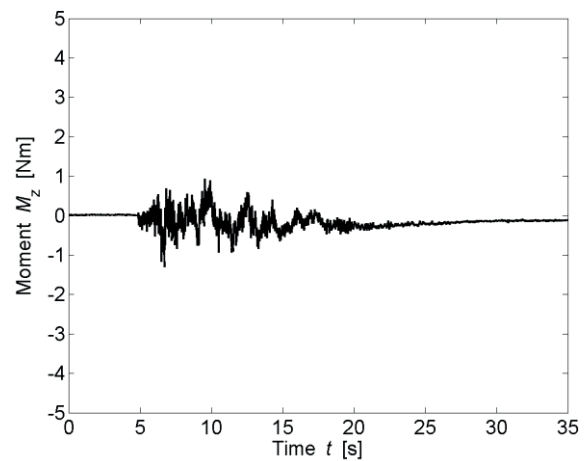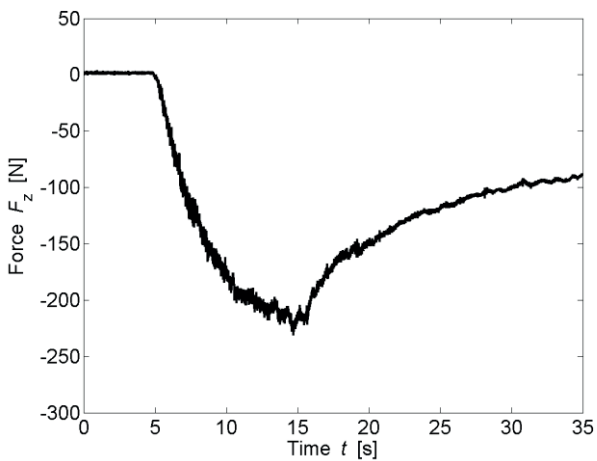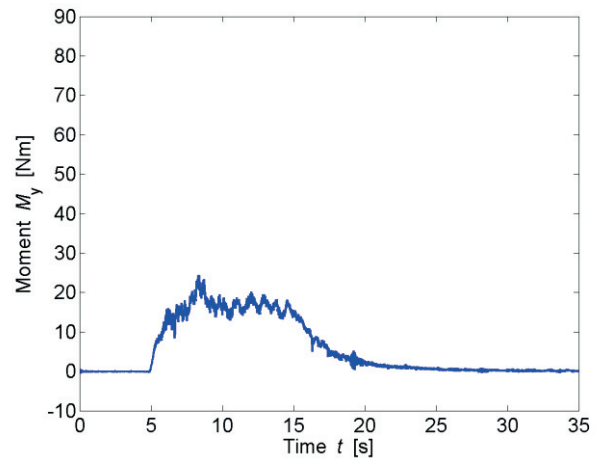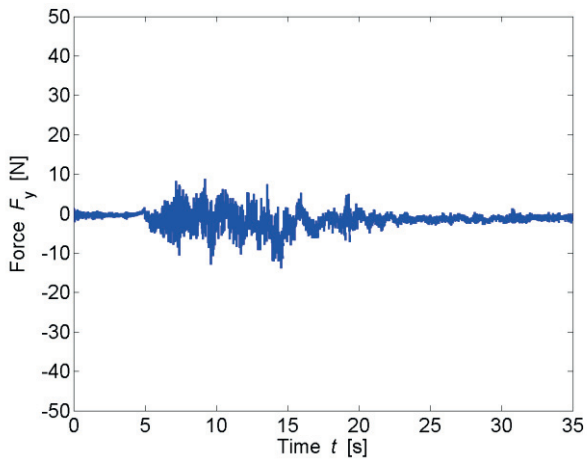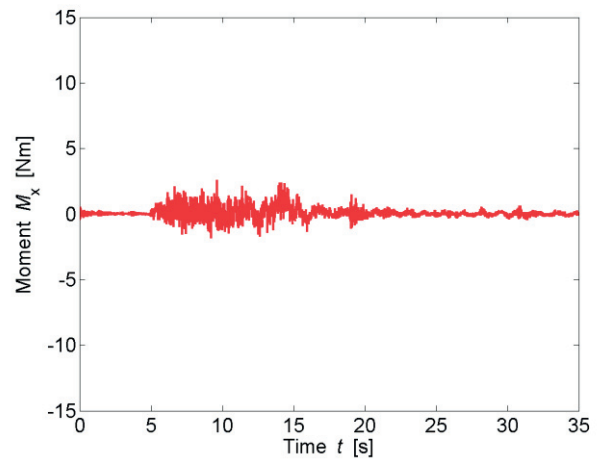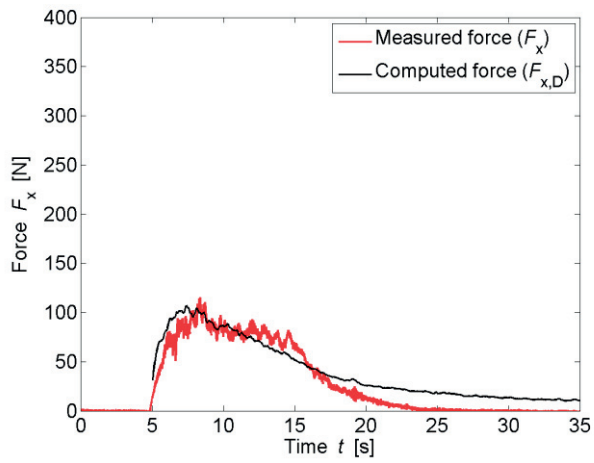
TEST PARAMETERS

Name		B60_0_WD2_ 1	
Repetitions		1	
Configuration		All Porous (0)	
Total porosity	P_{tot}	60	[%]
Porosity at h_{max}	$P_{h,max}$	62.17	[%]
Building height	H_B	0.3	[m]
Wave type		Surge (WD2)	
Impoundment depth	d_0	0.630	[m]
Initial still water depth	h_0	0.000	[m]
Front celerity	U	3.080	[m/s]
Maximum wave height	h_{max}	0.162	[m]
Maximum run-up height	H_{max}	0.507	[m]

FRONT VIEW   TOP VIEW

Wave
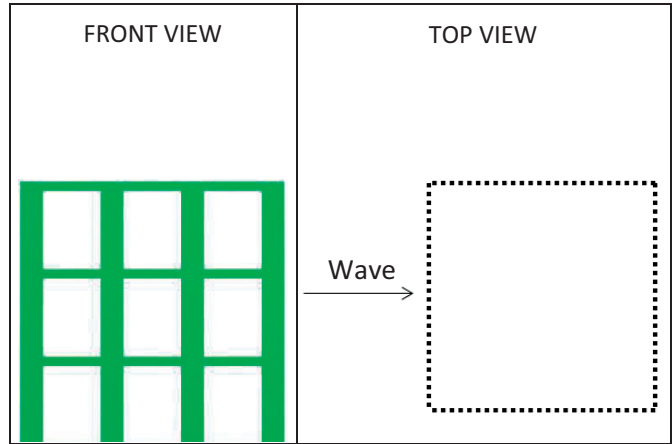
IMPACT PARAMETERS

	Min	Max	Unity
F_x	-4.359	84.359	[N]
F_y	-7.068	13.733	[N]
F_z	-190.625	6.263	[N]
M_x	-1.866	1.566	[Nm]
M_y	-1.614	17.527	[Nm]
M_z	-0.526	0.954	[Nm]

Predicted Force	$F_{x,D,max}$	80.338	[N]
Initial time	t_0	4.986	[s]
Time to peak	τ_{max}	5.952	[s]
Total impulse	I_{tot}	796.182	[Ns]
Peak Impulse	I_{peak}	388.098	[Ns]
Relative impulse	I^*	0.501	[-]
Wave height at $F_{x,max}$	h_M	0.904	[-]
Resistance coefficient	C_R	0.965	[-]

* All parameters are presented and defined at the beginning of the Appendix
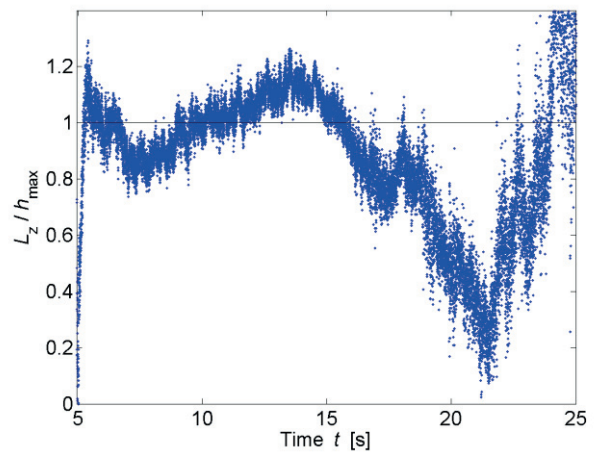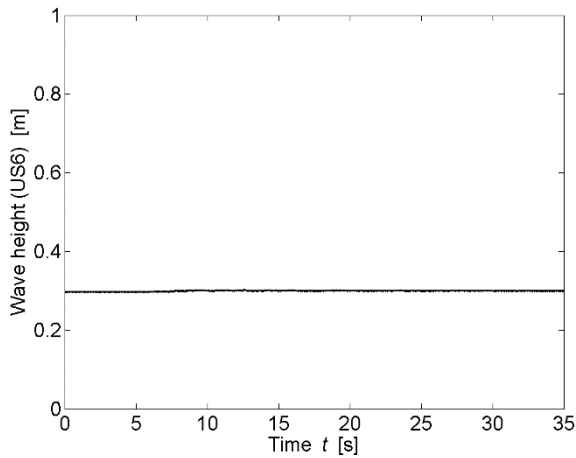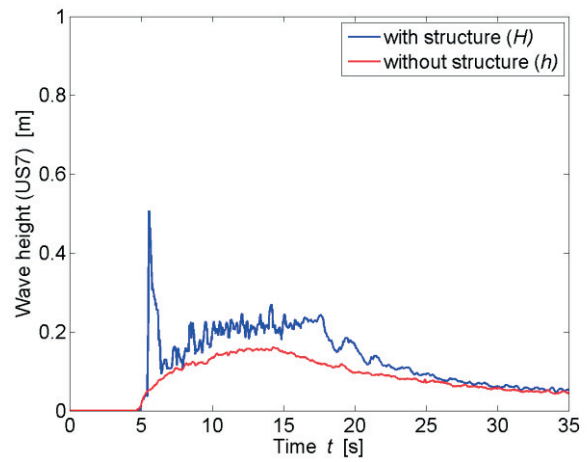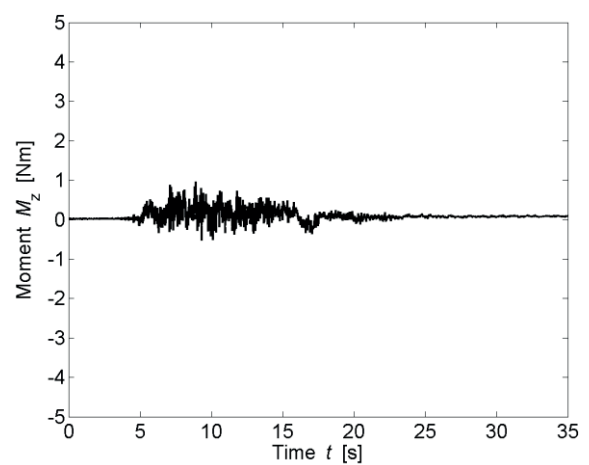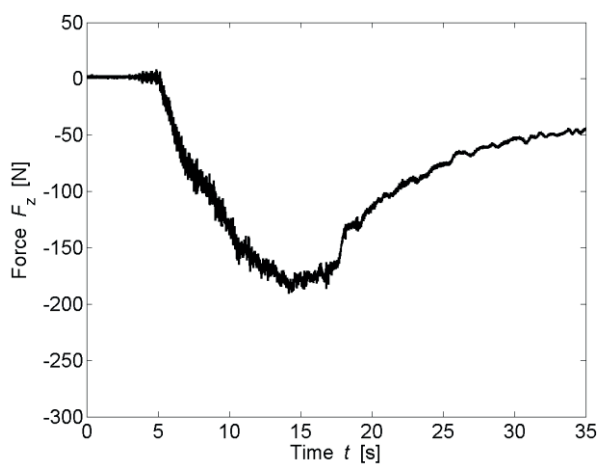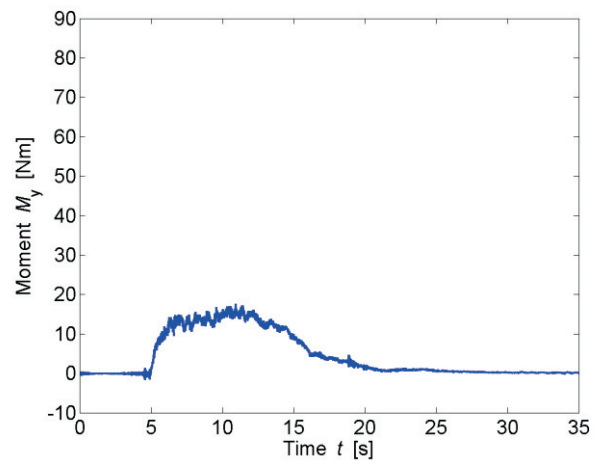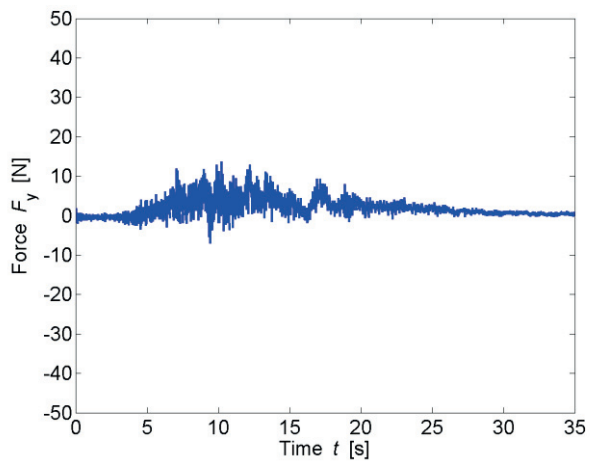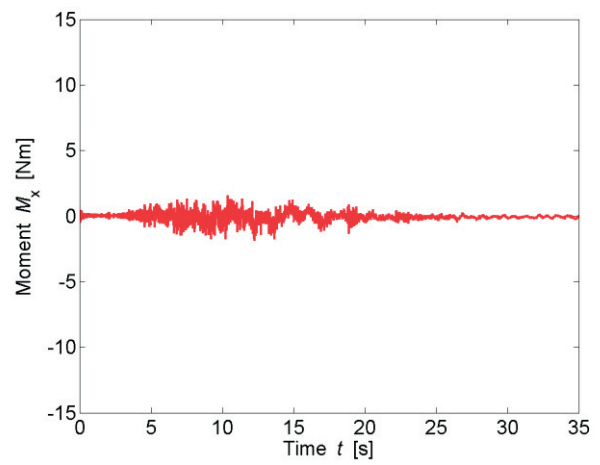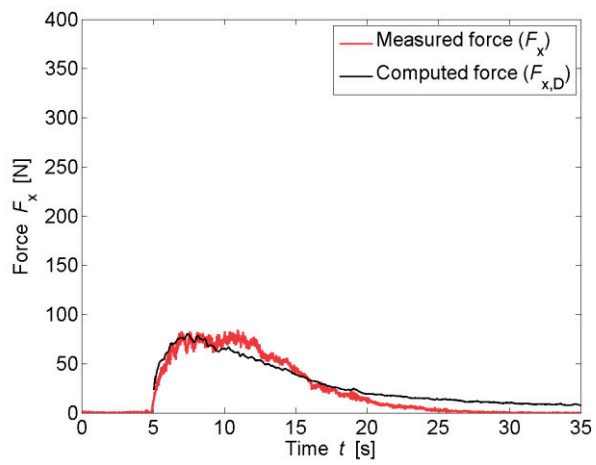
TEST PARAMETERS

Name		B60_F_WD2_ 2	
Repetitions		2	
Configuration		Impervious sides (F)	
Total porosity	P_{tot}	60	[%]
Porosity at h_{max}	$P_{h,max}$	62.17	[%]
Building height	H_B	0.3	[m]
Wave type		Surge (WD2)	
Impoundment depth	d_0	0.630	[m]
Initial still water depth	h_0	0.000	[m]
Front celerity	U	3.062	[m/s]
Maximum wave height	h_{max}	0.162	[m]
Maximum run-up height	H_{max}	0.471	[m]

FRONT VIEW   TOP VIEW

Wave →
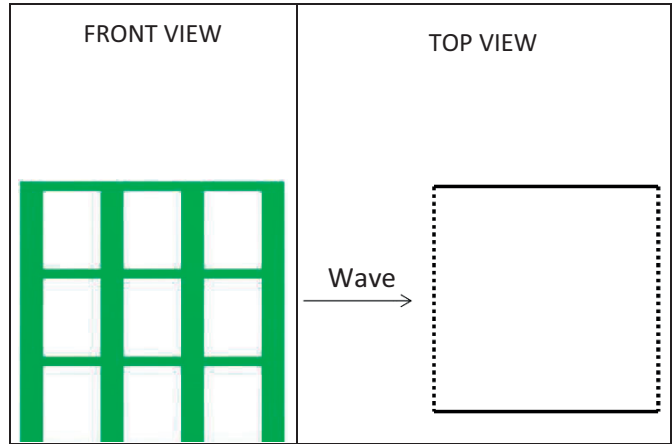
IMPACT PARAMETERS

	Min	Max	Unity
F_x	-5.593	70.932	[N]
F_y	-18.693	24.207	[N]
F_z	-218.176	0.000	[N]
M_x	-4.634	4.270	[Nm]
M_y	-1.444	16.489	[Nm]
M_z	-0.344	1.628	[Nm]

Predicted Force	$F_{x,D,max}$	80.338	[N]
Initial time	t_0	5.127	[s]
Time to peak	τ_{max}	3.343	[s]
Total impulse	I_{tot}	638.838	[Ns]
Peak Impulse	I_{peak}	173.718	[Ns]
Relative impulse	I^*	0.275	[-]
Wave height at $F_{x,max}$	h_M	0.729	[-]
Resistance coefficient	C_R	0.665	[-]

---

* All parameters are presented and defined at the beginning of the Appendix
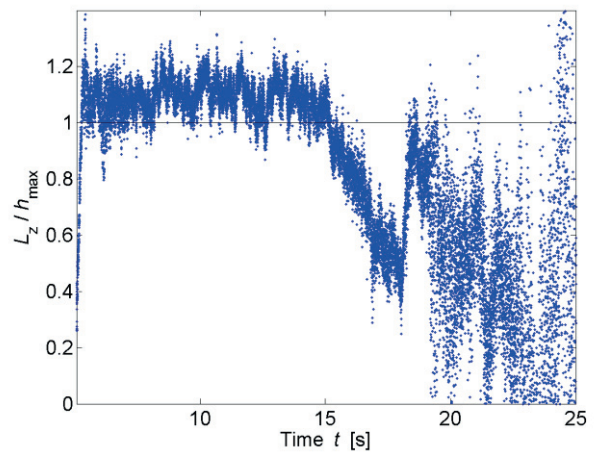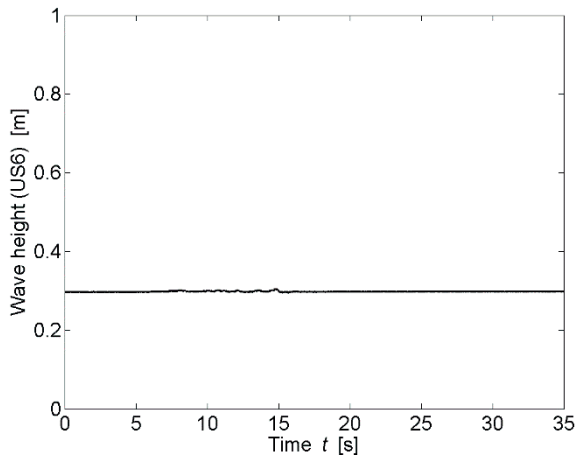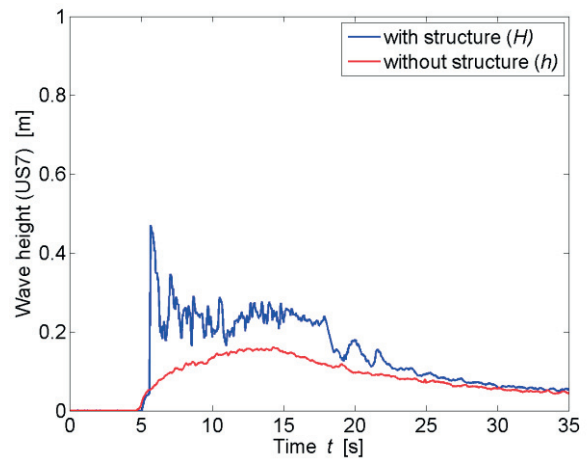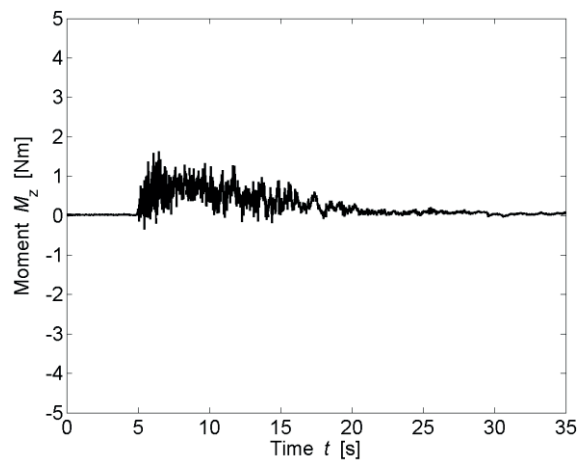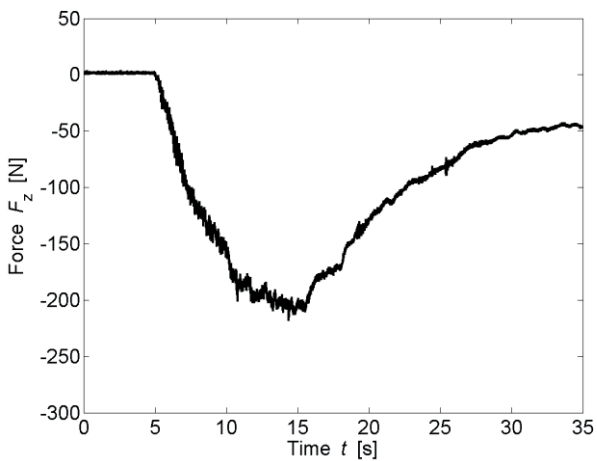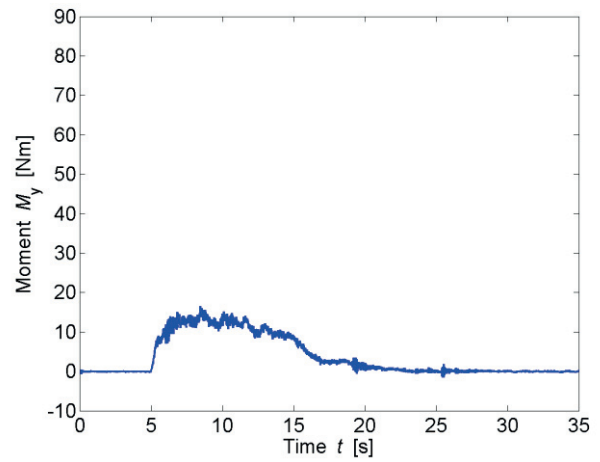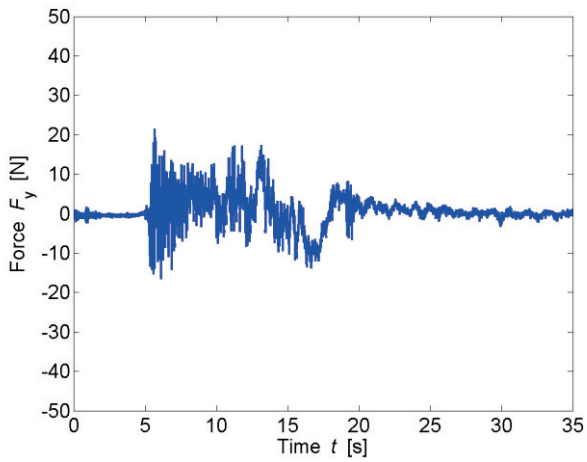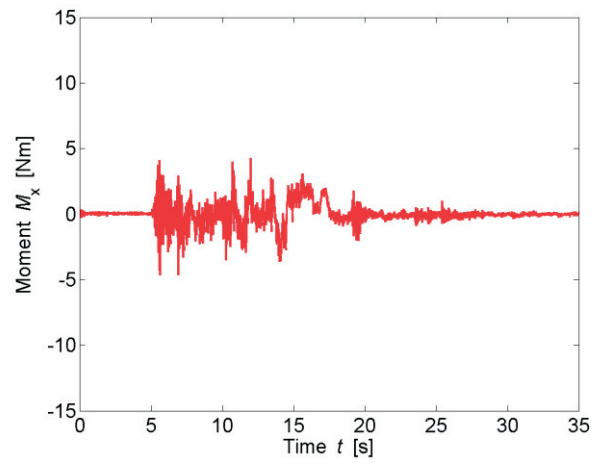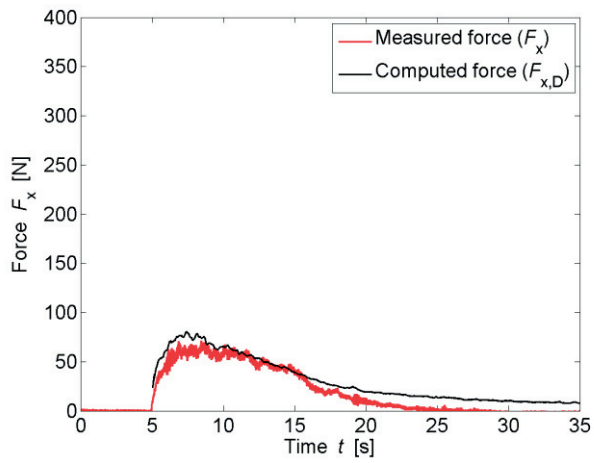
TEST PARAMETERS

Name		B60_B_WD2_4	
Repetitions		5	
Configuration		Impervious back (B)	
Total porosity	P_{tot}	60	[%]
Porosity at h_{max}	$P_{h,max}$	62.17	[%]
Building height	H_B	0.3	[m]
Wave type		Surge (WD2)	
Impoundment depth	d_0	0.630	[m]
Initial still water depth	h_0	0.000	[m]
Front celerity	U	3.044	[m/s]
Maximum wave height	h_{max}	0.162	[m]
Maximum run-up height	H_{max}	0.481	[m]

FRONT VIEW	TOP VIEW

Wave →
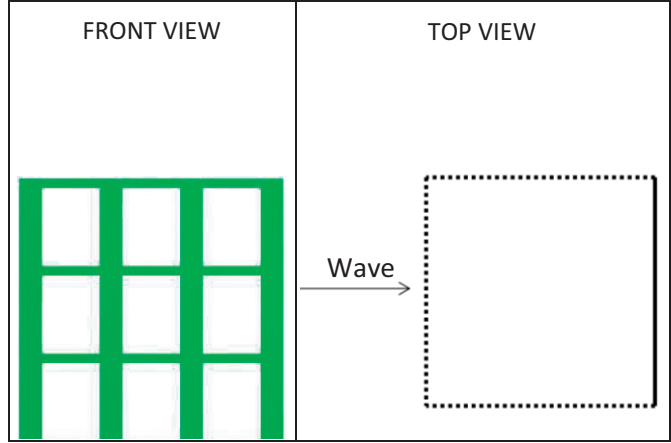
IMPACT PARAMETERS

	Min	Max	Unity
F_x	-6.077	188.369	[N]
F_y	-11.400	11.628	[N]
F_z	-260.159	0.000	[N]
M_x	-1.900	2.147	[Nm]
M_y	-1.520	34.900	[Nm]
M_z	-2.085	0.951	[Nm]

Predicted Force	$F_{x,D,max}$	212.377	[N]
Initial time	t_0	5.139	[s]
Time to peak	τ_{max}	2.643	[s]
Total impulse	I_{tot}	2034.984	[Ns]
Peak Impulse	I_{peak}	333.434	[Ns]
Relative impulse	I^*	0.174	[-]
Wave height at $F_{x,max}$	h_M	0.649	[-]
Resistance coefficient	C_R	1.861	[-]
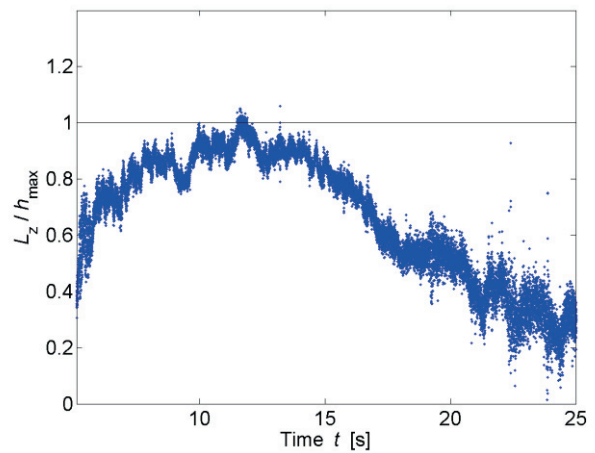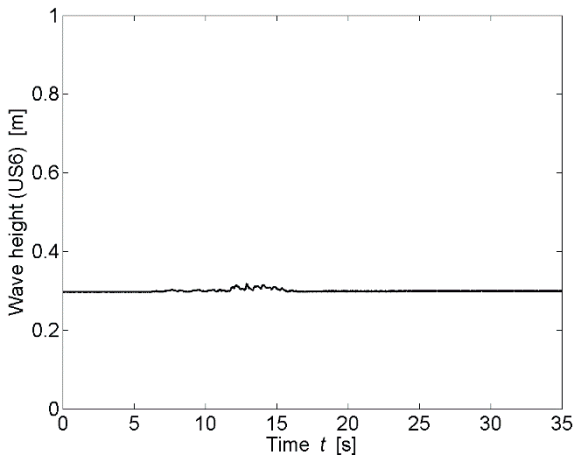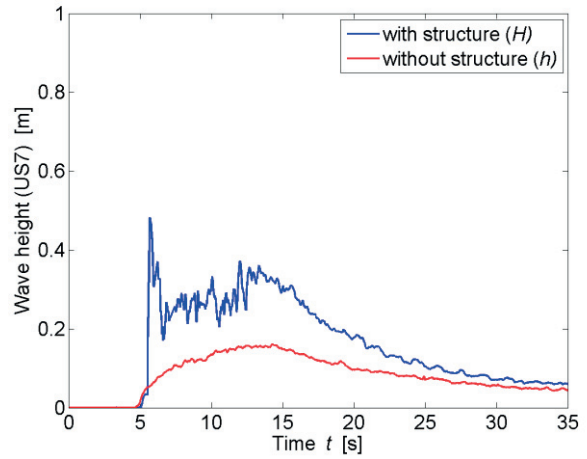
224

* All parameters are presented and defined at the beginning of the Appendix
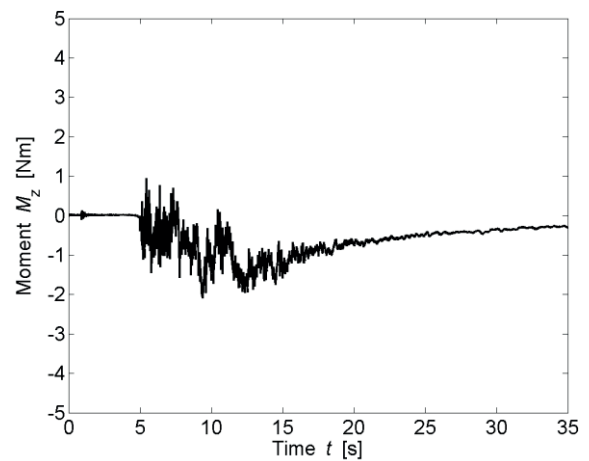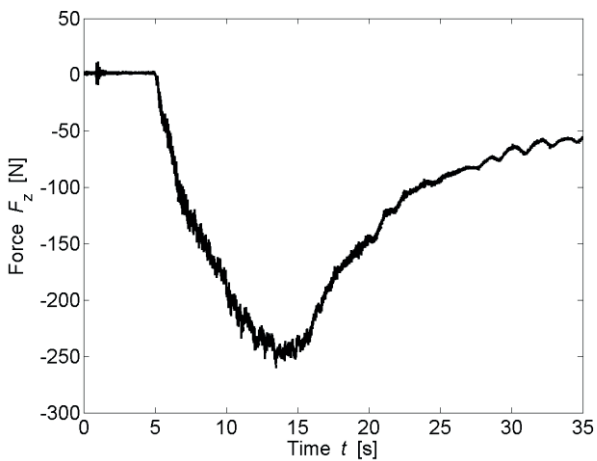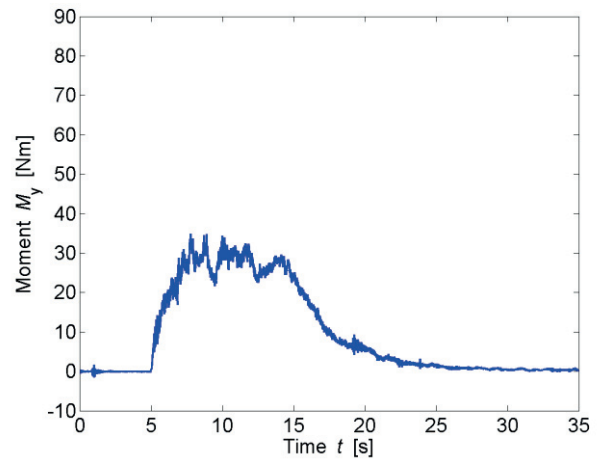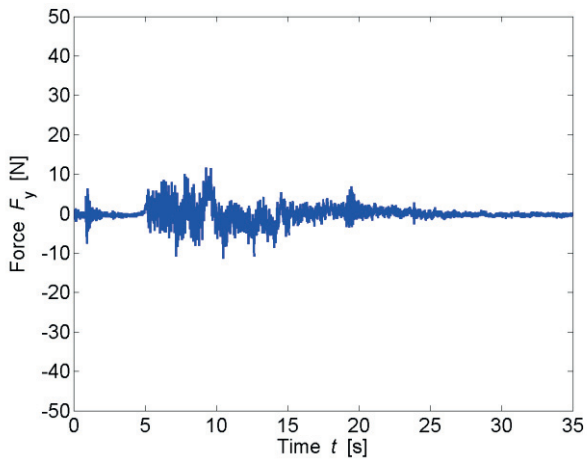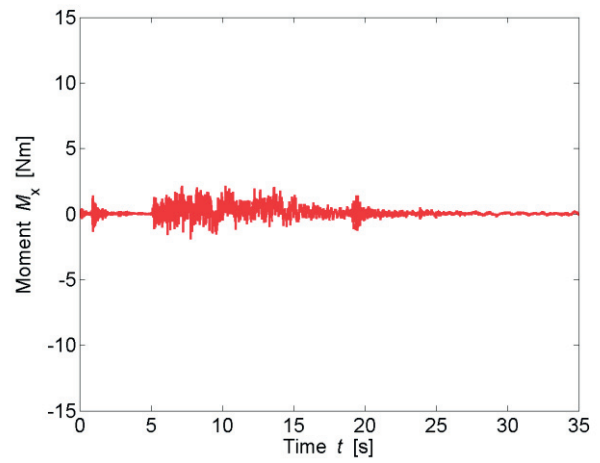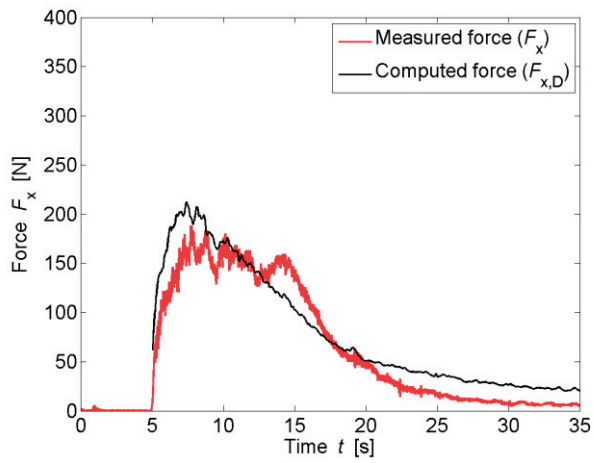
TEST PARAMETERS

Name		B60_S_WD2_ 1	
Repetitions		1	
Configuration		With side building (S)	
Total porosity	P_{tot}	60	[%]
Porosity at h_{max}	$P_{h,max}$	62.17	[%]
Building height	H_B	0.3	[m]
Wave type		Surge (WD2)	
Impoundment depth	d_0	0.630	[m]
Initial still water depth	h_0	0.000	[m]
Front celerity	U	3.088	[m/s]
Maximum wave height	h_{max}	0.162	[m]
Maximum run-up height	H_{max}	0.501	[m]

FRONT VIEW	TOP VIEW
	Wave →
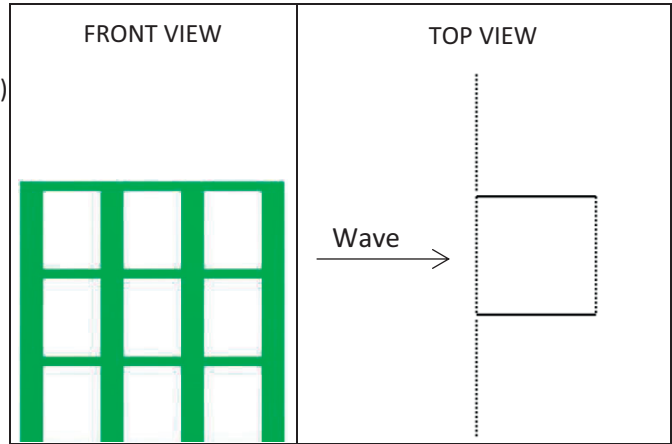
IMPACT PARAMETERS

	Min	Max	Unity
F_x	-4.504	94.497	[N]
F_y	-21.140	32.846	[N]
F_z	-252.756	0.734	[N]
M_x	-5.314	5.089	[Nm]
M_y	-1.334	18.794	[Nm]
M_z	-1.607	0.969	[Nm]
Predicted Force	$F_{x,D,max}$	96.002	[N]
Initial time	t_0	5.029	[s]
Time to peak	τ_{max}	2.123	[s]
Total impulse	I_{tot}	817.431	[Ns]
Peak Impulse	I_{peak}	123.056	[Ns]
Relative impulse	I^*	0.156	[-]
Wave height at $F_{x,max}$	h_M	0.596	[-]
Resistance coefficient	C_R	0.875	[-]

227

* All parameters are presented and defined at the beginning of the Appendix
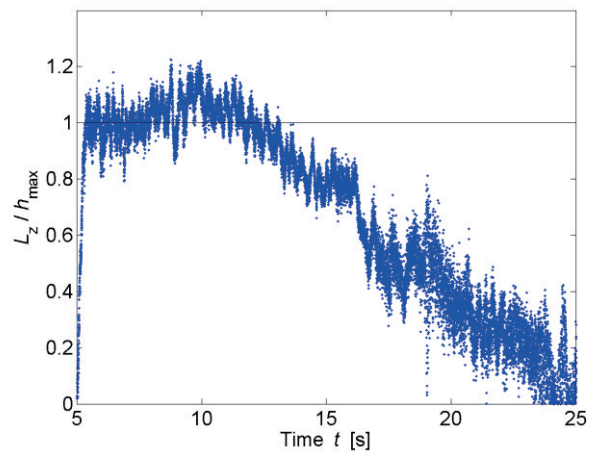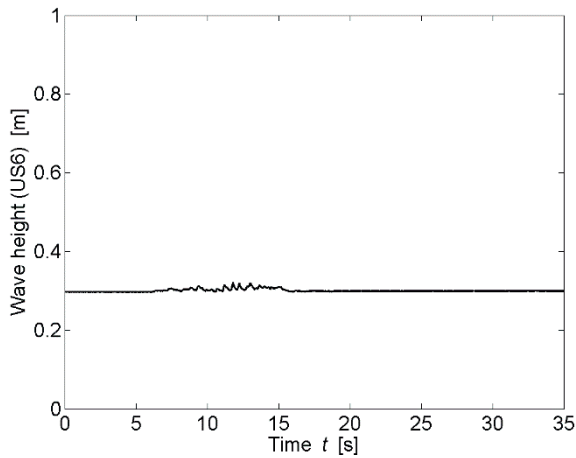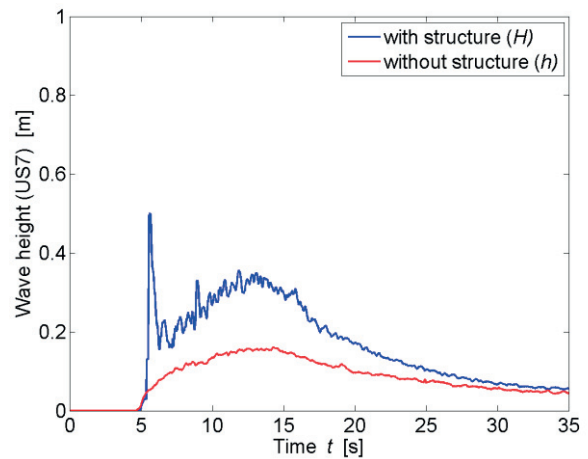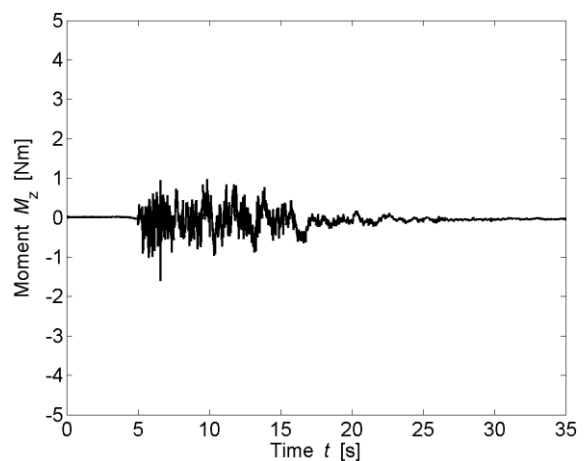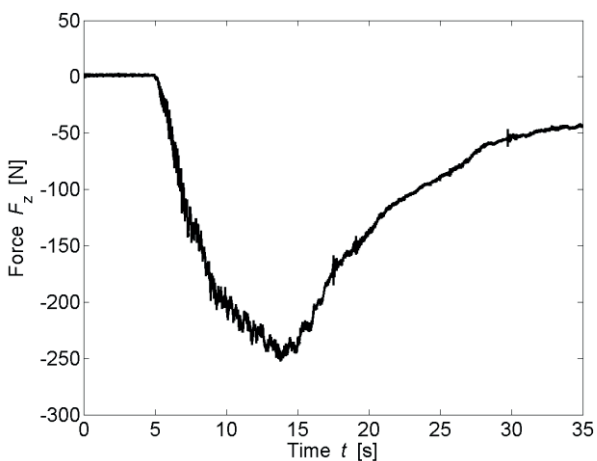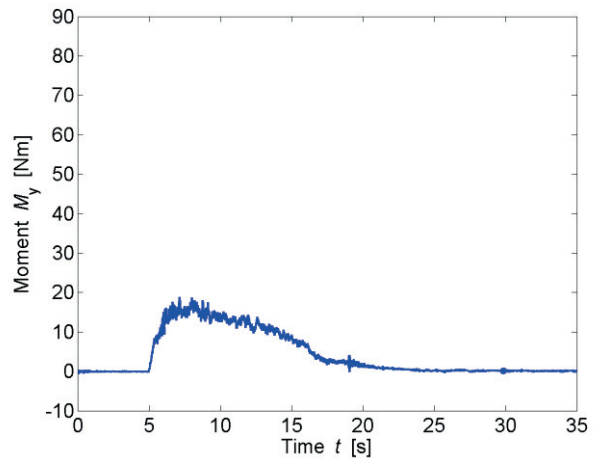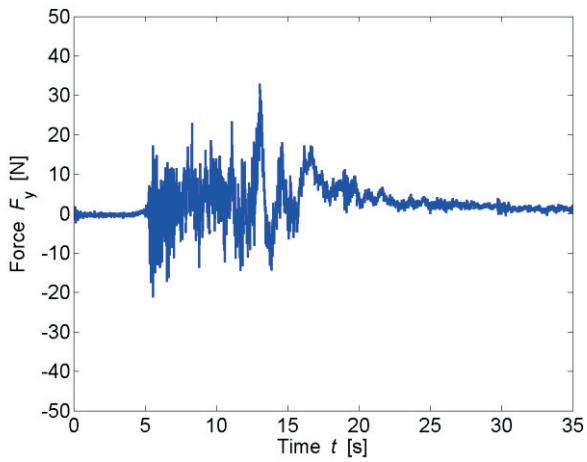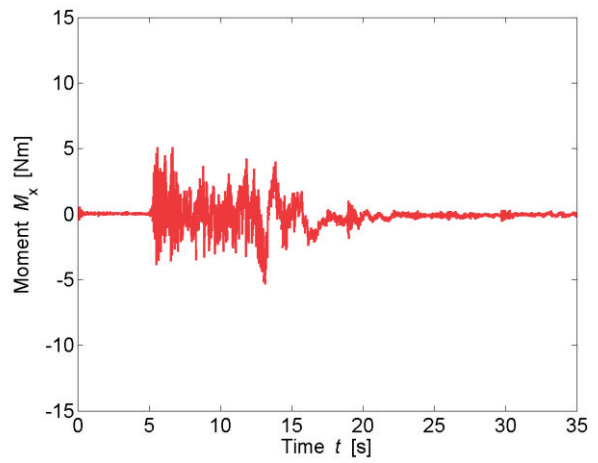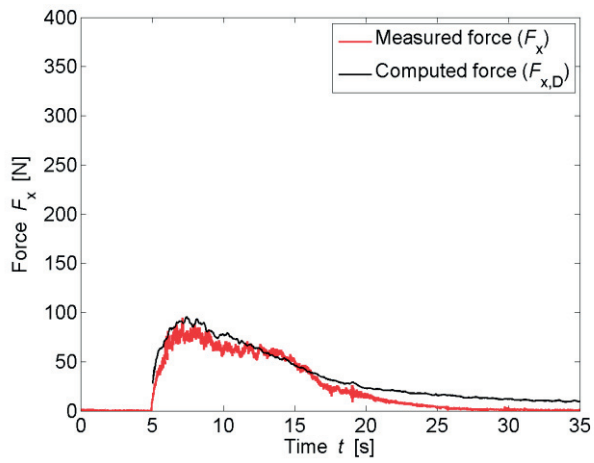
Bibliography

Al-Faesly, T., Palermo, D., Nistor, I., and Cornett, A. (2012). Experimental modeling of extreme hydrodynamic forces on structural models. *International Journal of Protective Structures*, 3(4):477–506.

Ali, A. (1999). Climate change impacts and adaptation assessment in Bangladesh. *Climate research*, 12(2/3):109–116.

Allsop, W., Chandler, I., and Zaccaria, M. (2014). Improvements in the physical modelling of tsunamis and their effects. *Proceeding of the 5th International Conference on Application of Physical Modelling to Port and Coastal Protection (Coastlab14)*, Varna, Bulgaria, 29 Septembre - 2 Octobre.

Arnason, H. (2005). Interactions between an incident bore and a free-standing coastal structure. *PhD Thesis*, University of Washington, Seattle, USA, 172 pages.

Arnason, H., Petroff, C., and Yeh, H. (2009). Tsunami bore impingement onto a vertical column. *Journal of Disaster Research*, 4(6):391–403.

Asakura, R., Iwase, K., Ikeya, T., Takao, M., Kaneto, T., Fujii, N., and Omori, M. (2000). An experimental study on wave force acting on on-shore structures due to overflowing tsunamis. *Proceedings of Coastal Engineering JSCE*, 47:911–915.

ASCE7-06 (2016). Minimum design loads for buildings and other structures. *ASCE/SEI 7-16*, Reston (VA) USA, 66 pages.

Benjamin, T. B. (1956). On the flow in channels when rigid obstacles are placed in the stream. *Journal of Fluid Mechanics*, 1(2):227–248.

Blanckaert, K. and Lemmin, U. (2006). Means of noise reduction in acoustic turbulence measurements. *Journal of Hydraulic Research*, 44(1):3–17.

Blevins, R. D. (1984). Applied fluid dynamics handbook. *Van Nostrand Reinhold Co.*, New York, USA, 568 pages.

Bryant, E. (2001). Tsunami: the underrated hazard. *Springer-Verlag*, Germany, 222 pages.

Bibliography

Bullock, G., Crawford, A., Hewson, P., Walkden, M., and Bird, P. (2001). The influence of air and scale on wave impact pressures. *Coastal Engineering*, 42(4):291–312.

Bullock, G., Obhrai, C., Peregrine, D., and Bredmose, H. (2007). Violent breaking wave impacts. part 1: Results from large-scale regular wave tests on vertical and sloping walls. *Coastal Engineering*, 54(8):602–617.

CCH (2000). City and County of Honolulu Building Code (CCH). *Department of Planning and Permitting of Honolulu Hawaii*, Chapter 16, Article 11, 5 pages.

Chandler, I., Allsop, W., Barranco-Granged, I., and McGovern, D. (2016). Understanding wave generation in pneumatic tsunami simulators. *Proceedings of the 6th International Conference on the Application of Physical Modelling in Coastal and Port Engineering and Science (Coastlab16)*, Ottawa, Canada, 10-13 May.

Chanson, H. (2004). The hydraulics of open channel flow: an introduction. *Elsevier Ltd.*, Oxford, UK, 581 pages.

Chanson, H. (2005a). Applications of the saint-venant equations and method of characteristics to the dam break wave problem. *Report CH55/05*, University of Queensland, 90 pages.

Chanson, H. (2005b). Le tsunami du 26 décembre 2004: un phénomène hydraulique d'ampleur internationale. premiers constats. *La Houille Blanche*, 1(2):25–32.

Chanson, H. (2006). Tsunami surges on dry coastal plains: Application of dam break wave equations. *Coastal Engineering Journal*, 48(4):355–370.

Chanson, H. (2009). Application of the method of characteristics to the dam break wave problem. *Journal of Hydraulic Research*, 47(1):41–49.

Chanson, H. (2011). Hydraulic jumps: turbulence and air bubble entrainment. *La Houille Blanche*, 3:5–16.

Chanson, H. (2012). Tidal bores, aegir, eagre, mascaret, pororoca: Theory and observations. *World Scientific Publishing Co.*, Singapore, 220 pages.

Chanson, H., Aoki, S., and Maruyama, M. (1999). Air bubble entrainment at plunging breakers and its effect on long period waves: an experimental study. *Coastal/Ocean Engineering Report No. COE99-1*, Toyohashi University of Technology, Japan, 42 pages.

Chanson, H., Aoki, S., and Maruyama, M. (2000). Experimental investigation of wave runup downstream of nappe impact: applications to flood wave resulting from dam overtopping and tsunami wave run-up. *Coastal/Ocean Engineering Report No. COE00-2*, Toyohashi University of Technology, Japan, 38 pages.

Chanson, H., Aoki, S., and Maruyama, M. (2002). Unsteady air bubble entrainment and detrainment at a plunging breaker: dominant time scales and similarity of water level variations. *Coastal Engineering*, 46(2):139–157.

230

Chanson, H., Aoki, S., and Maruyama, M. (2003). An experimental study of tsunami runup on dry and wet horizontal coastlines. *Science of Tsunami Hazards*, 20(5):278–293.

Chen, X., Hassan, W., Uijttewaal, W., Verwaest, T., Verhagen, H. J., Suzuki, T., and Jonkman, S. N. (2012). Hydrodynamic load on the building caused by overtopping waves. *Proceedings of the 33rd International Conference on Coastal Engineering (ICCE)*, Santander, Spain, 1-6 July.

Chinnarasri, C., Thanasisathit, N., Ruangrassamee, A., Weesakul, S., and Lukkunaprasit, P. (2013). The impact of tsunami-induced bores on buildings. *Proceedings of the ICE-Maritime Engineering*, 166(1):14–24.

Chock, G. (2015). The asce 7 tsunami loads and effects design standard. *Structures Congress 2015*, ASCE:1446–1456.

Chock, G., Robertson, I., Kriebel, D., Francis, M., and Nistor, I. (2012). Tohoku japan tsunami of march 11, 2011 – performance of structures. *American Society of Civil Engineers (ASCE)*, 348 pages.

Chock, G. Y. (2016). Design for tsunami loads and effects in the asce 7-16 standard. *Journal of Structural Engineering*, 142(11):04016093.

Choufi, L., Kettab, A., and Schleiss, A. J. (2014). Effet de la rugosité du fond d'un réservoir rectangulaire à faible profondeur sur le champ d'écoulement. *La Houille Blanche*, 5:83–92.

Chow, V. (1959). Open channel hydraulics. *McGraw-Hill Book Company Inc.*, New York, USA, 680 pages.

Cross, R. H. (1967). Tsunami surge forces. *Journal of the Waterways and Harbors Division*, 93(4):201–231.

Dames and Moore (1980). Design and construction standards for residential construction in tsunami-prone areas in Hawaii. *Federal Emergency Management Agency (FEMA)*, Washington DC, USA.

Dean, R. G. and Dalrymple, R. A. (1991). Water wave mechanics for engineers and scientists. *World Scientific Publishing Co.*, Singapore, 368 pages.

Dias, P., Dissanayake, R., and Chandratilake, R. (2006). Lessons learned from tsunami damage in Sri-Lanka. *Proceedings of the Institution of Civil Engineers-Civil Engineering*, 159(2):74–81.

Dias, W. and Mallikarachchi, H. (2006). Tsunami-planning and design for disaster mitigation. *Structural Engineer*, 84(11):25.

Dressler, R. (1952). Hydraulic resistance effect upon the dam-break functions. *Journal of Research of the National Bureau of Standards*, 49(3):217–225.

Bibliography

Dressler, R. (1954). Comparison of theories and experiments for the hydraulic dam-break wave. *International Association Scientific Hydrology*, 3(38):319–328.

Duricic, J., Erdik, T., Pektaş, A. O., and van Gelder, P. H. (2013). Mean normalized force computation for different types of obstacles due to dam break using statistical techniques. *Water*, 5(2):560–577.

English, E. C., Friedland, C. J., and Orooji, F. (2017). Combined flood and wind mitigation for hurricane damage prevention: Case for amphibious construction. *Journal of Structural Engineering*, 143(6):06017001.

Esteban, M., Glasbergen, T., Takabatake, T., Hofland, B., Nishizaki, S., Nishida, Y., Stolle, J., Nistor, I., Bricker, J., and Takagi, H. (2017). Overtopping of coastal structures by tsunami waves. *Geosciences*, 7(4):121.

Evers, F. M. and Hager, W. H. (2015). Impulse wave generation: Comparison of free granular with mesh-packed slides. *Journal of Marine Science and Engineering*, 3(1):100–110.

Favre, H. (1935). Etude théorique et expérimentale des ondes de translation dans les canaux découverts. *Dunod*, Paris, France, 215 pages.

FEMA55 (2000). Coastal Construction Manual. *Federal Emergency Management Agency (FEMA)*, Chapter 8 - Washington DC, USA, 82 pages.

Foster, A., Rossetto, T., and Allsop, W. (2017). An experimentally validated approach for evaluating tsunami inundation forces on rectangular buildings. *Coastal Engineering*, 128:44–57.

Freeman, J. and LéMehauté, B. (1964). Wave breakers on a beach and surges in a dry bed. *Journal of the Hydraulics Division*, 90(2):187–216.

Fritz, H. (2002). Initial phase of landslide generated impulse waves. *ETH PhD Thesis (No. 14871) and VAW Mitteilung 178*, (Ed. H.E. Minor), Zürich, Switzerland, 254 pages (ISSN 0374-0056).

Fritz, H., Hager, W., and Minor, H. (2004). Near field characteristics of landslide generated impulse waves. *Journal of Waterway, Port, Coastal, and Ocean Engineering*, 130(6):287–302.

Fritz, H., Phillips, D., Okayasu, A., Shimozono, T., Liu, H., Mohammed, F., Skanavis, V., Synolakis, C., and Takahashi, T. (2012). The 2011 japan tsunami current velocity measurements from survivor videos at kesennuma bay using lidar. *Geophysical Research Letters*, 39:1–6.

Fritz, H. M. and Okal, E. A. (2008). Socotra Island, Yemen: field survey of the 2004 Indian Ocean tsunami. *Natural Hazards*, 46(1):107–117.

Fuchs, H. (2013). Solitary impulse wave run-up and overland flow. *ETH PhD Thesis (No. 21174) and VAW Mitteilung 221*, (Ed. R. Boes), Zürich, Switzerland, 178 pages (ISSN 0374-0056).

Fuchs, H. and Hager, W. H. (2015). Solitary impulse wave transformation to overland flow. *Journal of Waterway, Port, Coastal, and Ocean Engineering*, 141(5):04015004.

Fuchs, H., Heller, V., and Hager, W. H. (2010). Impulse wave run-over: experimental benchmark study for numerical modelling. *Experiments in fluids*, 49(5):985–1004.

Fujima, K., Achmad, F., Shigihara, Y., and Mizutani, N. (2009). Estimation of tsunami force acting on rectangular structures. *Journal of Disaster Research*, 4(6):404–409.

Fukui, Y., Nakamura, M., Shiraishi, H., and Sasaki, Y. (1963). Hydraulic study on tsunami. *Coastal Engineering in Japan*, 6:67–82.

Fukuyama, H., Kato, H., Ishihara, T., Tajiri, S., Tani, M., Okuda, Y., and Nakano, Y. (2011). Structural design requirement on the tsunami evacuation buildings. *Japan Structural Consultants Association (JSCA)*, Tokyo, Japan.

Goseberg, N., Stolle, J., Derschum, C., and Nistor, I. (2017). Swing gate generated dam-break waves. *Proceedings of the 37th IAHR World Congress*, Kuala Lumpur, Malaysia, 13 - 18 August.

Goseberg, N., Wurpts, A., and Schlurmann, T. (2013). Laboratory-scale generation of tsunami and long waves. *Coastal Engineering*, 79:57–74.

Green, G. (1837). On the motion of waves in a canal of variable depth. *Cambridge Philosophical Transasctions*, 6:457–462.

Gupta, V. P. and Goyal, S. C. (1975). Hydrodynamic forces on bridge piers. *Journal of the Institution of Engineers (India)*, Civil Engineering Division 56:12–16.

Hartana and Murakami, K. (2015). Numerical and experimental simulation of two-phase tsunami flow through buildings with openings. *Journal of Earthquake and Tsunami*, 9(3):1550007.

Hayashi, S. and Koshimura, S. (2013). The 2011 Tohoku tsunami flow velocity estimation by the aerial video analysis and numerical modeling. *Journal of Disaster Research*, 8(4):561–572.

Heller, V. (2007). Landslide generated impulse waves: Prediction of near field characteristics. *ETH PhD Thesis (No. 17531) and VAW Mitteilung 204*, (Ed. H.E. Minor), Zürich, Switzerland, 178 pages (ISSN 0374-0056).

Heller, V. (2011). Scale effects in physical hydraulic engineering models. *Journal of Hydraulic Research*, 49(3):293–306.

Henderson, F. (1966). Open channel flow. *MacMillan Company*, New York, USA, 522 pages.

Hinwood, J. B. and Mackenzie, N. (2011). Design for tsunami resistance: Flume experiments on arrays of buildings. *Proceedings of the 34th IAHR World Congress*, Brisbane, Australia, 26 - 30 June.

Bibliography

Huber, A. (1980). Schwallwellen in Seen als Folge von Felsstürzen (Impulse waves following rockfalls). *PhD Thesis*, ETH/VAW, Zürich, Switzerland, 222 pages (in German).

Hunt, B. (1982). Asymptotic solution for dam-break problem. *Journal of the Hydraulics Division*, 108(1):115–126.

Iizuka, H. and Matsutomi, H. (2000). Damage due to flood flow of tsunami. *Proceedings of the Coastal Engineering of JSCE*, 47:381–385.

Jaffe, B., Goto, K., Sugawara, D., Richmond, B., Fujino, S., and Nishimura, Y. (2012). Flow speed estimated by inverse modeling of sandy tsunami deposits: results from the 11 March 2011 tsunami on the coastal plain near the Sendai Airport, Honshu, Japan. *Sedimentary Geology*, 282:90–109.

Karim, M. F. and Mimura, N. (2008). Impacts of climate change and sea-level rise on cyclonic storm surge floods in Bangladesh. *Global Environmental Change*, 18(3):490–500.

Kirkoz, M. (1983). Breaking and run-up of long waves, tsunamis: their science and engineering. *Proceedings of the 10th IUGG International Tsunami Symposium*, Hamburg, Germany, 19 - 21 August.

Kisacik, D., Troch, P., and Van Bogaert, P. (2012). Description of loading conditions due to violent wave impacts on a vertical structure with an overhanging horizontal cantilever slab. *Coastal Engineering*, 60:201–226.

Koch, C. and Chanson, H. (2009). Turbulence measurements in positive surges and bores. *Journal of Hydraulic Research*, 47(1):29–40.

Kolmogoroff, A. (1931). Über die analytischen Methoden in der Wahrscheinlichkeitsrechnung. *Mathematische Annalen*, 104(1):415–458.

Koshimura, S., Oie, T., Yanagisawa, H., and Imamura, F. (2009). Developing fragility functions for tsunami damage estimation using numerical model and post-tsunami data from Banda Aceh, Indonesia. *Coastal Engineering Journal*, 51(3):243–273.

Kreibich, H., Thieken, A. H., Petrow, T., Müller, M., and Merz, B. (2005). Flood loss reduction of private households due to building precautionary measures–lessons learned from the elbe flood in august 2002. *Natural Hazards and Earth System Science*, 5(1):117–126.

Kremer, K., Simpson, G., and Girardclos, S. (2012). Giant Lake Geneva tsunami in ad 563. *Nature Geoscience*, 5(11):756–757.

Lauber, G. and Hager, W. H. (1998). Experiments to dambreak wave: Horizontal channel. *Journal of Hydraulic Research*, 36(3):291–307.

Leng, X. and Chanson, H. (2015). Breaking bore: Physical observations of roller characteristics. *Mechanics Research Communications*, 65:24–29.

Leng, X. and Chanson, H. (2017a). Unsteady turbulence, dynamic similarity and scale effects in bores and positive surges. *European Journal of Mechanics-B/Fluids*, 61:125–134.

Leng, X. and Chanson, H. (2017b). Unsteady velocity profiling in bores and positive surges. *Flow Measurement and Instrumentation*, 54:136–145.

Li, Y. and Raichlen, F. (2003). Energy balance model for breaking solitary wave runup. *Journal of Waterway, Port, Coastal, and Ocean Engineering*, 129(2):47–59.

Linton, D., Gupta, R., Cox, D., van de Lindt, J., Oshnack, M. E., and Clauson, M. (2012). Evaluation of tsunami loads on wood-frame walls at full scale. *Journal of Structural Engineering*, 139(8):1318–1325.

Liu, P. (2008). Advanced numerical models for simulating tsunami waves and run-up. *Advances In Coastal and Ocean Engineering*, 10.

Longuet-Higgins, M. S. and Turner, J. (1974). An 'entraining plume' model of a spilling breaker. *Journal of Fluid Mechanics*, 63(1):1–20.

Lukkunaprasit, P., Ruangrassamee, A., and Thanasisathit, N. (2009a). Tsunami loading on buildings with openings. *Science of Tsunami Hazards*, 28(5):303–310.

Lukkunaprasit, P., Thanasisathit, N., and Yeh, H. (2009b). Experimental verification of fema p646 tsunami loading. *Journal of Disaster Research*, 4(6):410–418.

Madsen, P. A., Fuhrman, D. R., and Schäffer, H. A. (2008). On the solitary wave paradigm for tsunamis. *Journal of Geophysical Research: Oceans (1978–2012)*, 113(C12).

Marche, C., Beauchemin, P., and El Kayloubi, A. (1995). Etude numerique et experimentale des ondes secondaires de favre consecutives à la rupture d'un barrage. *Canadian Journal of Civil Engineering*, 22(4):793–801.

Margaritondo, G. (2005). Explaining the physics of tsunamis to undergraduate and non-physics students. *European Journal of Physics*, 26(3):401–407.

Matsutomi, H. and Okamoto, K. (2010). Inundation flow velocity of tsunami on land. *Island Arc*, 19(3):443–457.

Matsutomi, H., Sakakiyama, T., Nugroho, S., and Matsuyama, M. (2006). Aspects of inundated flow due to the 2004 Indian Ocean tsunami. *Coastal Engineering Journal*, 48(2):167–195.

Meile, T. (2007). Influence of macro-roughness of walls on steady and unsteady flow in a channel. *EPFL PhD Thesis (No. 3952) and LCH Communication 36*, (Ed. A.J. Schleiss), Lausanne, Switzerland, 414 pages (ISSN 1661-1179).

Meile, T., Boillat, J. L., and Schleiss, A. J. (2011). Water-surface oscillations in channels with axi-symmetric cavities. *Journal of Hydraulic Research*, 49(1):73–81.

Bibliography

Meile, T., Boillat, J. L., and Schleiss, A. J. (2013). Propagation of surge waves in channels with large-scale bank roughness. *Journal of Hydraulic Research*, 51(2):195–202.

Meile, T., De Cesare, G., Blanckaert, K., and Schleiss, A. J. (2008). Improvement of acoustic doppler velocimetry in steady and unsteady turbulent open-channel flows by means of seeding with hydrogen bubbles. *Flow Measurement and Instrumentation*, 19(3):215–221.

Montes, S. (1998). Hydraulics of open channel flow. *American Society of Civil Engineers (ASCE)*, Baltimore (MD), USA, 697 pages.

Morison, J. R., Johnson, J. W., and Schaaf, S. A. (1950). The force exerted by surface waves on piles. *Journal of Petroleum Technology*, 2(5):149–154.

Murty, T. S., Flather, R. A., and Henry, R. (1986). The storm surge problem in the Bay of Bengal. *Progress in Oceanography*, 16(4):195–233.

Nagler, F. A. (1918). Obstruction of bridge piers to the flow of water. *Proceedings of the American Society of Civil Engineers (ASCE)*, 43(5):815–846.

Nakano, Y. (2008). Design load evaluation for tsunami shelters based on damage observations after Indian Ocean tsunami disaster due to the 2004 Sumatra earthquake. *The 14th World Conference on Earthquake Engineering*, Beijing, China, 12 - 17 October.

Nistor, I., Palermo, D., Nouri, Y., Murty, T., and Saatcioglu, M. (2009). Tsunami-induced forces on structures. *Handbook of Coastal and Ocean Engineering.*, World Scientific Co., Singapore, pages 261-286.

Nouri, Y., Nistor, I., Palermo, D., and Cornett, A. (2010). Experimental investigation of tsunami impact on free standing structures. *Coastal Engineering Journal*, 52(1):43–70.

OCADI (2009). Technical Standards and Commentaries for Port and Harbour Facilities in Japan. *The Overseas Coastal Area Development Institute of Japan, Ports and Harbours Bureau*, Tokyo, Japan, 981 pages.

O'Donoghue, T., Pokrajac, D., and Hondebrink, L. (2010). Laboratory and numerical study of dambreak-generated swash on impermeable slopes. *Coastal Engineering*, 57(5):513–530.

Okada, T., Sugano, T., Ishikawa, T., Ohgi, T., Takai, S., and Hamabe, C. (2005). Structural design method of buildings for tsunami resistance. *Building Technology Research Institute, Building Centre for Japan*, 15, Tokyo, Japan.

Peregrine, D., Bredmose, H., Bullock, G., Obrhai, C., Müller, G., and Wolters, G. (2005). Water wave impact on walls and the role of air. *Coastal Engineering*, 4:4005–4017.

Pfister, M. and Chanson, H. (2012). Scale effects in physical hydraulic engineering models. discussion. *Journal of Hydraulic Research*, 50(2):244–246.

236

Qi, Z., Eames, I., and Johnson, E. (2014). Force acting on a square cylinder fixed in a free-surface channel flow. *Journal of Fluid Mechanics*, 756:716–727.

Rahman, S., Akib, S., Khan, M., and Shirazi, S. (2014). Experimental study on tsunami risk reduction on coastal building fronted by sea wall. *The Scientific World Journal*, 7 pages.

Raju, K., Rana, O., Asawa, G., and Pillai, A. (1983). Rational assessment of blockage effect in channel flow past smooth circular cylinders. *Journal of Hydraulic Research*, 21(4):289–302.

Ramsden, J. D. (1993). Tsunami-forces on a vertical wall caused by long waves, bores and surges on a dry bed. *PhD Thesis*, California Institute of Technology, Pasadena, California, 218 pages.

Ramsden, J. D. (1996). Forces on a vertical wall due to long waves, bores, and dry-bed surges. *Journal of Waterway, Port, Coastal, and Ocean Engineering*, 122(3):134–141.

Ritter, A. (1892). Die Fortpflanzung der Wasserwellen. *Zeitschrift Verein Deutscher Ingenieure*, 36(33):947–954.

Robertson, I. N. (2016). Tsunami loads and effects: Guide to the tsunami design provisions of asce 7-16. *American Society of Civil Engineers (ASCE)*, Reston (VA), USA.

Robertson, I. N., Pacskowski, K., Riggs, H. R., and Mohamed, A. (2013). Experimental investigation of tsunami bore forces on vertical walls. *Journal of Offshore Mechanics and Arctic Engineering*, 135(2):1–8.

Roeber, V. and Bricker, J. D. (2015). Destructive tsunami-like wave generated by surf beat over a coral reef during typhoon haiyan. *Nature communications*, 6:7854.

Rossetto, T., Allsop, W., Charvet, I., and Robinson, D. I. (2011). Physical modelling of tsunami using a new pneumatic wave generator. *Coastal Engineering*, 58(6):517–527.

Rossetto, T., Peiris, N., Pomonis, A., Wilkinson, S., Del Re, D., Koo, R., and Gallocher, S. (2007). The Indian Ocean tsunami of December 26, 2004: observations in Sri Lanka and Thailand. *Natural Hazards*, 42(1):105–124.

Santo, J. and Robertson, I. (2010). Lateral loading on vertical structural elements due to a tsunami bore. *Report No. UHM/CEE/10-02*, University of Hawaii, Honolulu, 64 pages.

Schüttrumpf, H. and Oumeraci, H. (2005). Scale and model effects in crest level design. *Proceedings of the 2nd International Coastal Symposium in Iceland*, Höfn, Iceland, 5-8 June.

Shafiei, S., Melville, B. W., and Shamseldin, A. Y. (2016). Experimental investigation of tsunami bore impact force and pressure on a square prism. *Coastal Engineering*, 110:1–16.

Snodgrass, F., Rice, E., and Hall, M. (1951). Wave forces on piling. *University California Berkeley*, 35:1–9.

Bibliography

Soares-Frazão, S. and Zech, Y. (2002). Undular bores and secondary waves-experiments and hybrid finite-volume modelling. *Journal of Hydraulic Research*, 40(1):33–43.

St. Venant, B. (1871). Théorie du mouvement non permanent des eaux. *Institute de France, Académie des sciences, Comptes rendus*, 73:147–237.

Stoker, J. J. (1957). Water waves: The mathematical theory with applications. *Interscience*, New York, USA, 567 pages.

Terrier, S., Bieri, M., Cesare, G. D., and Schleiss, A. J. (2013). Surge wave propagation in a common tailrace channel for two large pumped-storage plants. *Journal of Hydraulic Engineering*, 140(2):218–225.

Thusyanthan, N. I. and Madabhushi, S. P. G. (2008). Tsunami wave loading on coastal houses: a model approach. *Proceedings of the ICE-Civil Engineering*, 161(2):77–86.

Triatmadja, R. and Nurhasanah, A. (2012). Tsunami force on buildings with openings and protection. *Journal of Earthquake and tsunami*, 6(4):1250024.

Ursell, F. (1953). The long-wave paradox in the theory of gravity waves. *Mathematical Proceedings of the Cambridge Philosophical Society*, 49(4):685–694.

Van de Lindt, J. W., Gupta, R., Garcia, R. A., and Wilson, J. (2009). Tsunami bore forces on a compliant residential building model. *Engineering Structures*, 31(11):2534–2539.

Wang, H. and Chanson, H. (2015). Air entrainment and turbulent fluctuations in hydraulic jumps. *Urban Water Journal*, 12(6):502–518.

Whitham, G. (1955). The effects of hydraulic resistance in the dam-break problem. *Proceedings of the Royal Society of London. Series A. Mathematical and Physical Sciences*, 227(1170):399–407.

Whittingham, H. (1958). The bathurst bay hurricane and associated storm surge. *Bureau of Meteorology*, Brisbane, Australia, 23 pages.

Wilson, J. S., Gupta, R., Van de Lindt, J. W., Clauson, M., and Garcia, R. (2009). Behavior of a one-sixth scale wood-framed residential structure under wave loading. *Journal of Performance of Constructed Facilities*, 23(5):336–345.

Wüthrich, D. (2017). Impact of a dry bed surge against structures with and without openings. *Proceedings of the 37th IAHR World Congress, p. 3775-3784,*, Kuala Lumpur, Malaysia, 13 - 18 August.

Wüthrich, D., Pfister, M., De Cesare, G., and Schleiss, A. J. (2016a). Velocity profile measurements in bore waves. *Proceedings of the 10th International Symposium on Ultrasonic Doppler Methods for Fluid Mechanics and Fluid Engineering*, Tokyo, Japan, 28-30 September.

Wüthrich, D., Pfister, M., Manso, P., Constantinescu, G., and Schleiss, A. J. (2016b). Surface turbulence on bores and surges propagating on smooth and rough beds. *Proceedings of the 6th International Conference on the Application of Physical Modelling in Coastal and Port Engineering and Science (Coastlab16)*, Ottawa, Canada, 10-13 May.

Wüthrich, D., Pfister, M., Nistor, I., and Schleiss, A. J. (2018a). Experimental study of tsunami-like waves on dry and wet bed generated with a vertical release technique. *Journal of Waterway, Port, Coastal, and Ocean Engineering*, (accepted for publication, DOI: 10.1061/(ASCE)WW.1943-5460.0000447).

Wüthrich, D., Pfister, M., Nistor, I., and Schleiss, A. J. (2018b). Experimental study on forces on free-standing buildings with openings. *Coastal Engineering*, (under review).

Wüthrich, D., Pfister, M., Nistor, I., and Schleiss, A. J. (2018c). Experimental study on the hydrodynamic impact of tsunami-like waves against impervious free-standing buildings. *Coastal Engineering Journal*, (under review).

Wüthrich, D., Pfister, M., and Schleiss, A. J. (2016c). Example of wave impact on a residential house. *Proceedings of the 4th IAHR Europe Congress*, Liege, Belgium, 27-29 July.

Yarnell, D. L. (1934). *Bridge piers as channel obstructions*, volume Technical Bulletin 442, Deptartment of Agriculture, USA, 80 pages.

Yeh, H. (2006). Maximum fluid forces in the tsunami run-up zone. *Journal of Waterway, Port, Coastal, and Ocean Engineering*, 132(6):496–500.

Yeh, H. (2007). Design tsunami forces for onshore structures. *Journal of Disaster Research*, 2(6):531–536.

Yeh, H., Liu, P., and Synolakis, C. (1996). Long-wave run-up models. *World Scientific Publishing Co.*, Singapore, 403 pages.

Yeh, H. and Mok, K. (1990). On turbulence in bores. *Physics of Fluids A: Fluid Dynamics (1989-1993)*, 2(5):821–828.

Yeh, H., Robertson, I., and Preuss, J. (2005). Development of design guidelines for structures that serve as tsunami vertical evacuation sites. *Open File Report 2005-4*, Washington State Department of Natural Resources, Division of Geology and Earth Resources, USA, 42 pages.

Yeh, H. H., Ghazali, A., and Marton, I. (1989). Experimental study of bore run-up. *Journal of Fluid Mechanics*, 206:563–578.

Acknowledgements

In primis, I would like to thank my thesis director, Prof. Anton J. Schleiss for giving me the opportunity to conduct this Ph.D. at LCH. I owe him gratitude for believing in my abilities and for his support throughout the thesis.

This work would have not been the same without the contribution of my co-supervisor, Prof. Michael Pfister, whose knowledge and experience in the domain of hydraulic structures were essential.

I would also like to express my deepest gratitude to Prof. Ioan Nistor (University of Ottawa, Canada) for coming to EPFL as a visiting professor, for advising me throughout the thesis and for hosting me as visiting Ph.D. student at uOttawa. His precious suggestions in both research and at a personal level were a spur for the pursuit of the thesis and a source of inspiration for whatever will come next.

I would like to thank Prof. Nils Goseberg (TU Braunschweig) and Prof. Willi H. Hager (ETH Zürich) for being part of the jury and Prof. Eugen Brühwiler (EPFL) for accepting to be the president. All comments received contributed to increase the scientific quality of this work. Helpful discussions with Dr. Giovanni De Cesare, Dr. Pedro Manso, Prof. Mário Franca (IHE Delft) and Prof. Hubert Chanson (University of Queensland) are also acknowledged.

As all experimental works, a big thanks goes to the technical support received from Cédric Bron, Michel Teuscher, Marc-Eric Pantillon (PanPam) and all the people in the workshop. Their professionalism and availability in solving last-minute problems was fundamental to ensure the optimal functionality of the experimental set-up. Indispensabile anche il supporto burocratico di Aldo.

Time goes by, but memories remain and I have to be thankful to my wonderful colleagues, without whom the time spent at LCH would have not been this awesome: Aaron, Alain, Azin,

Acknowledgements

Carmelo, Clàudia, David, Dora, Felix, Fränz, Irene, Ivan, Matthias, Mona, Nicolas, Paloma, Pierre, Sabine (*Chancy*), Samuel, Sebastián, Sebastian, Shun, Stephane, Zé Pedro in addition to all interns and students. A special thanks also goes to Jacob Stolle, from uOttawa, for the support during my stay in Canada and for the constructive discussions.

Among all colleagues, a special appreciation goes to my office mates Alex and Sara, who supported me in the most difficult times and whose ears were always ready to listen and provide constructive feedbacks. A special mention also goes to Severin for making LCH more dynamic. Grazie a Jessica per il supporto morale durante gli ultimi mesi: ce l'abbiamo fatta!!! Elena e Gaetano: è stato un immenso piacere conoscervi e la nostra amicizia è andata ben oltre il tipico rapporto tra colleghi. Condividere con voi gioie, tristezze, news, commenti e pettegolezzi è stata una continua fonte di motivazione ed ispirazione.

On ne peut pas bien travailler si on n'habite pas avec un entourage sympathique et stimulant; pour cela un grand merci va à mes colocs Aline, Ben, Céline (×2), Guillaume, Remco et Vincent. Mes remerciements vont aussi aux amis hors de l'EPFL, pour m'avoir toujours fourni plain de distractions: Benjamin, Daniel, Dimitris, Haroun, Jonathan, Laura, Matteo et Olivia. During the Ph.D. I also had the opportunity to discover the world with some wonderful people: thank you Annie, Elena V., Emmanuel and Francesca for accompanying me and for sharing experiences together. Nei weekend a Torino ho sempre trovato conforto in grandi amicizie che persistono nonostante la lontananza geografica, vero Giacomo, Elda, Vicky e Matte?

Dulcis in fundo, il mio più sentito ringraziamento va a mia sorella Monica ed ai miei genitori, Ernesto e Carlotta, per il vostro supporto incondizionato e per tutte le opportunità che mi avete sempre dato, fin da quanto ero piccolo. Vi voglio bene.

Lausanne, 22nd December 2017

D.W.

Davide WÜTHRICH

Nationality	Swiss and Italian
Date of birth	28 June 1988
Contact	davide.wuthrich@alumni.epfl.ch

EDUCATION

2014-2018 **Ph.D. in Hydraulic Engineering**
Laboratory of Hydraulic Constructions (LCH)
Ecole Polytechnique Fédérale de Lausanne (EPFL), Switzerland

2011-2013 **Master of Science (M.Sc.) in Civil Engineering**
École Polytechnique Fédérale de Lausanne (EPFL), Switzerland
Focus: Hydraulic engineering

2007-2010 **Bachelor of Science (B.Sc.) in Civil Engineering**
Politecnico di Torino, Italy
Final grade: 110/110

2002-2007 **Maturità Scientifica PNI**
Liceo Scientifico Statale "*Galileo Ferraris*", Torino, Italy
Final grade: 100/100

2005-2006 **High School Diploma**
Kirkwood High School, St. Louis, Missouri, USA

AWARDS

2019 Nomination for **2019 EPFL Doctorate Award**
The award honours a candidate who performed a remarkable thesis as to its originality, the impact of the results and presentation of the work.

2015 **EDCE Mobility Award**
Award assigned to encourage Ph.D. students to go for an academic visit to an external research institution (University of Ottawa)

2014 **IM Prize** (IM Maggia Engineering)
Rewards the *M.Sc.* thesis performed at the University of Queensland, Australia.

2007 **Gold K Award**
Kirkwood High School *Gold K* Award to academic excellence.

LANGUAGES

Italian	Native language
English	Fluent
French	Fluent
Spanish	Intermediate
German	Beginner

COMPUTER SKILLS

Numerical Computation	HEC-RAS, Basement
Programming	Matlab
Computer-aided Design	AutoCAD, Inventor
Office	MS Office (Word, Excel, PowerPoint), LATEX, DPlot

PROFESSIONAL EXPERIENCE

2014-2018   **Laboratory of Hydraulic Constructions (LCH)**, EPFL, Switzerland
Ph.D. student and scientific assistant on applied research projects (supervisors Prof. Anton Schleiss and Prof. Michael Pfister, since 2014)
<u>Applied Research</u>: *Scour protection of the Chancy-Pougny dam stilling basin* (2013-2017).
<u>Teaching</u>: Assistant for the following courses: *Aménagement hydrauliques 1* (BA6), *Barrages et ouvrages hydrauliques annexes* (MA3). Followed 3 Master projects and numerous semester projects of both graduate and undergraduate students of the School of Architecture, Civil and Environmental Engineering (ENAC) at EPFL.

2017   **University of Ottawa (uOttawa)**, Ottawa, Canada
Visiting Ph.D. student (supervisor Prof. Ioan Nistor, 3 months)

2013   **University of Queensland (UQ)**, Brisbane, Australia
M.Sc. Project (supervisor Prof. Hubert Chanson, 25 weeks)
"*Air-water flow properties and energy dissipation performances on flat and gabion stepped spillways*"

2012   **Stucky SA**, Renens, Switzerland & **Stucky Caucasus Ltd**, Tbilisi, Georgia
Internship (8 weeks)
Numerical modelling of rivers and related hydraulic structures; initial design of dam spillways and dam failure analysis.

2002-2007   **Applied HydroEconomics and Alpine environmental Dynamics (AHEAD)**, EPFL, Switzerland
Internship (supervisor Prof. Paolo Perona, 6 months)
River Engineering and solid transport – Merging of 3D surfaces, water simulations and data analysis; statistical analysis of river anabranching patterns.

2005-2006   **Italian National agency for new technologies, Energy and sustainable economic development (ENEA)**, Rome, Italy
B.Sc. Project (supervisors Prof. Marco Masoero and Dr Gabriella Funaro, 6 months)
Development of a numerical model for energy simulations aiming at minimizing the consumptions of a Vertical Farm. This research was part of an international project "*Skyland*", between Italy and the city of Abu Dhabi (UAE).

PEER-REVIEWD SCIENTIFIC PUBLICATIONS

Perona, P., Molnar, P., Crouzy, B., Perucca, E., Jiang, Z., McLelland, S., **Wüthrich, D.**, Edmaier, K., Francis, R., Camporeale, C. and Gurnell, A. (**2012**). Biomass selection by floods and related timescales: Part 1. Experimental observations. *Advances in Water Resources*, Vol. 4, p.85.96.

Wüthrich, D. and Chanson, H. (**2014**). Hydraulics, Air Entrainment, and Energy Dissipation on a Gabion Stepped Weir. *ASCE Journal of Hydraulic Engineering,* Vol.140, n. 9, 04014046

Wüthrich, D. and Chanson, H. (**2015**). Aeration performances of a gabion stepped weir with and without capping. *Environmental Fluid Mechanics,* Vol.15, n.4, p.711-730.

Wüthrich, D., Chamoun, S., Bollaert, E., De Cesare, G, and Schleiss, A.J. (**2017**). Hybrid Modelling Approach to Study Scour Potential at Chancy-Pougny Dam Stilling Basin. *Advances in Hydroinformatics.* (accepted for publication).

Wüthrich, D., Pfister, M. Nistor, I. and Schleiss, A.J. (**2018**). Experimental study of tsunami-like waves on dry ad wet bed generated with a vertical release technique. *ASCE Journal of Waterways, Port, Coastal and Ocean Engineering* (accepted for publication).

Wüthrich, D., Pfister, M., Nistor, I. and Schleiss, A.J. (**2018**). Experimental study on the hydrodynamic impact of tsunami-like waves against impervious free-standing buildings. *Coastal Engineering Journal* (under review).

Wüthrich, D., Pfister, M., Nistor, I. and Schleiss, A.J. (**2018**). Experimental study on forces exerted on buildings with openings due to extreme hydrodynamic events. *Coastal Engineering* (under review).

Wüthrich, D., Pfister, M., Nistor, I. and Schleiss, A.J. (**2018**). Effect of overflow on wave-induced loads on impervious free-standing structures. *Journal of Hydraulic Research* (under review).

CONFERENCE PROCEEDINGS

Wüthrich, D. and Chanson, H. (**2014**). Air entrainment and energy dissipation on Gabion stepped weirs. *5th IAHR International Symposium on Hydraulic Structures*, Brisbane, Australia, 25-27 June.

Crouzy, B., **Wüthrich, D.**, Perona, P. and D'Odorico, P. (**2014**). Ecomorphodynamic conditions for the emergence of river anabranching patterns. *7th International Conference on Fluvial Hydraulics (River Flow)*, Lausanne, Switzerland, 3-5 September.

Canale, L. and **Wüthrich, D.** (**2014**). Dam Break Analysis for Serra degli Ulivi Dam. *Hydro 2014 - Building on Recent Development Progress*, Cernobbio, Italy, 13-15 October.

Wüthrich, D., Pfister, M., Nistor I and Schleiss, A.J. (**2015**). Experimental generation of tsunami-like waves. *Coastal Structures Conference*, Boston, USA, 9-11 September.

Wüthrich, D., Zordan, J., Baehler, M., Gaudenz, M., Pasquier R., and Stylo, M. (**2015**). Hydropower plants: price and prejudice. *Hydro 2015 - Advancing police and practice*, Bordeaux, France, 26-28 October.

Wüthrich, D., Pfister, M., Manso, P., Constantinescu, G. and Schleiss, A.J. (**2016**). Surface Turbulence on Bores and Surges propagating on Smooth and Rough Beds. *6th International Conference on the Application of Physical Modelling in Coastal and Port Engineering and Science (Coastlab16),* Ottawa, Canada, 7-9 May.

Wüthrich, D., Pfister, M. and Schleiss, A.J. (**2016**). Example of wave impact on a residential house. *4th IAHR Europe Congress*, Liege, Belgium, 27-29 July.

Wüthrich, D., Pfister, M., De Cesare, G. and Schleiss, A.J. (**2016**). Velocity profile measurements in bore waves. *10th International Symposium on Ultrasonic Doppler Methods for Fluid Mechanics and Fluid Engineering*, Tokyo, Japan, 28-30 September.

Wüthrich, D., Chamoun, S., Bollaert, E., De Cesare, G. and Schleiss, A.J. (**2017**). Hybrid modelling approach to study scour potential at Chancy-Pougny Dam Stilling Basin. *SimHydro 2017: choosing the right model in applied hydraulics*, Sophia Antipolis, France, 14-16 June.

Wüthrich, D. (**2017**). Impact of a dry bed surge against structures with and without openings. *37th IAHR World Congress*, Kuala Lumpur, Malaysia, 13-18 August.

Wüthrich, D., Pfister, M., Nistor, I. and Schleiss, A.J. (**2017**). Estimation of wave propagation velocity on a channel with smooth and rough bed. *37th IAHR World Congress*, Kuala Lumpur, Malaysia, 13-18 August.

Wüthrich, D., Chamoun, S., De Cesare G. and Schleiss, A.J. (**2017**). Protection de la fosse de dissipation du barrage de Chancy-Pougny avec prismes an béton. *Hydraulique des barrages et des digues*, Chambéry, France, 29-30 November. (in French)

Wüthrich, D., Chamoun, S., De Cesare G. and Schleiss, A.J. (**2018**). Behaviour of a scour protection overlay with randomly distributed concrete prisms in plunge pools downstream of mobile barrages for exceptional operation conditions. *7th IAHR International Symposium on Hydraulic Structures*, Aachen, Germany, 15-18 May. (accepted for oral presentation)

Yllas Arbòs, C., **Wüthrich, D.**, Pfister, M. and Schleiss, A.J. (**2018**). Wave impact on oriented impervious buildings. *5th IAHR Europe Congress: New challenges in hydraulic research and engineering*, Trento, Italy, 12-14 June. (submitted)

SCIENTIFIC REPORTS

Wüthrich, D. and Chanson, H. (2014). Aeration and energy dissipation over stepped Gabion spillways: a physical study. *Hydraulic Model Report No. CH92/13*, School of Civil Engineering, The University of Queensland, Brisbane, Australia, 171 pages.

Chamoun, S., **Wüthrich D.**, De Cesare, G. and Schleiss, A.J. (2017). Barrage de Chancy-Pougny, Erosion à l'aval du barrage: Essais sur modèle physique. *Rapport LCH 02/2017*, Laboratoire de Constructions Hydrauliques (LCH), EPFL, Switzerland, 97 pages. (in French)